Nitric Oxide and pH Measurement with AlGaN/GaN Based ISFETs

DISSERTATION

Zur Erlangung des akademischen Grades
Doktoringenieur (Dr.-Ing.)

Vorgelegt der Fakultät für Elektrotechnik und
Informationstechnik der Technischen Universität Ilmenau

Von MSEE Mary Jocelyn Donahue
Geboren am 14.03.1980 in Alamogordo, NM

Gutachter: Univ.-Prof. Dr. rer. nat. habil. Andreas Schober
Technische Universität Ilmenau
Univ.-Prof. Dr. rer. nat. habil Hannes Töpfer
Technische Universität Ilmenau
Prof. Dr. Richard Gale, PE
Texas Technical University

Eingereicht am: 13. Jan 2016
Verteidigt am: 10. Mai 2016

urn:nbn:de:gbv:ilm1-urn:nbn:de:gbv:ilm1-2016000368

Acknowledgements

I would firstly like to thank my advisor Prof. Dr. Andreas Schober for the possibility to work in the interesting field of biosensors. I would like to express my appreciation for the relaxed/open research atmosphere as well as a great deal of freedom to manage personal scheduling. I would additionally like to thank Prof. Dr. Oliver Ambacher for the initial opportunity to come to Germany, to be introduced into the realm of III-Nitride research and of course to learn a new culture and lifestyle.

My appreciation also goes to those from (or alumni of) the nano-biosystem technology group, with particular emphasis on Mario Kittler, whose programming skills, measurement assistance and general solid state device knowledge was very helpful; Ben Lübber(z) for pervious work and development of the sensor-related aspects; Katja Tonisch, also for previous work and the introduction to device development; Karin Friedel for the time spent in the SEM room on my behalf; Maren Klett for the continuous supply of PBS solutions. Additionally, thanks to Sukhdeep Singh and Michael Gebinoga for assistance in the chemical field and discussion of ideas regarding NO sensing.

I would also like to thank those from other groups or institutes for the friendly, straightforward cooperation: Michael Fischer, Marcel Himmerlich, Alex Schulz, Sven Radeberger, Gundis Bauer, and Ranjith Vellacheri. My appreciation also goes to Brett Moore for the great increase of oxford commas in this work. A special thanks to those in the cleanroom, whose help, fabrication advice and extremely open minds and atmosphere for testing new processes and ideas made the research fun and interesting. In particular, Birgitt Hartmann for the fun in Nasschemie, Thomas Stauden, Ilona Marquardt, Jutta Uziel, and Joachim Döll, for the fun in the rest of the cleanroom.

Although not directly related to this work, I would like to extend thanks to my brothers and sister for everything in life previous to studies, as well as the continuing friendship. To my father for his patience, always interesting conversations… and shared love for brewing. Lastly, I would like to express my gratitude to my mother for her support throughout my life, not necessarily in times of difficulty for me, but more significantly, in difficult times for herself. She sacrificed a great deal to make opportunities possible for her children.

Particular gratitude is expressed to Thomas Stauden, who has been a great friend from the first days when we arrived in Ilmenau, until final days, when he even took care of the physical submission of this document as I could not personally be there.

Special thanks to Ilona and Uli Marquardt for much more than I can summarize in a few sentences! I believe the phrase *my house is your house* has rarely been epitomized the way it was by them. Extra thanks to Itch1, who even hung and folded our laundry as I worked.

I want to express my very deep gratitude (jodagranularkölnvasidilitator!) to my ZMNBGWs (including der Ösi-B), das ***tolle*** Büro 315 (Ilona, Gernot, Lars, Liele) und seine Besucher (Jörg, Elvira, Henry, Stubi…), and the two important Adams in my life. This group made daily life interesting, fun and more than I could have expected. The first Adam, and those who attended the small-round research lectures, comprised a part of my weeks from which I learned many new and interesting science and/or life lessons which I will never forget.

The second Adam that I would like to thank is of course my fantastic husband and best friend, who supported me a great deal in everything since I have known him. Specifically, during the work in the following pages, he was a valuable resource for scientific discussion, a friend during leisure time and an exceptional father for our four amazing kids, spending a great deal of quality time with them when 'mommy had to work.'

Finally, these amazing four kids, Noah, Daphne, Hazel and Leontes, I would like to thank the most for making life so unbelievably interesting and fun. You five together make my life complete. ☺

Abstract

What is nitric oxide (NO)? Under standard temperature and pressure conditions in a chemistry class, NO is described as a colorless gas. When considering environmental emissions, NO is described as an unavoidable product in power plants and automobile engines during the combustion of fossil fuels. In physiology NO is described a strong vasodilator and a central signaling molecule involved in cellular processes. All of this makes NO a molecule of high interest for sensor applications. This thesis firstly deals with the optimization of Aluminum-gallium nitride/gallium nitride (AlGaN/GaN) ion sensitive field effect transistors (ISFETs), including the material parameters associated with fabrication, and secondly the implementation of these optimized sensors for the detection of NO, regardless of application.

As the sensors will be used in fluidic environments, the demands regarding the chemical and mechanical stability of passivation systems are quite different to standard Si-transistor technology. This passivation development was a key step in maintaining device functionality while additionally providing good insulation. It was demonstrated that polyimide exhibits the best insulating properties for these transistors in comparison to the well-known 'hard passivation' materials Si_3N_4 or SiO_2. In order to employ polyimide as the passivation material, a unique ECR plasma process was developed to enable patterning while protecting the active sensor area of each of the AlGaN/GaN devices. Only a few nm beneath the surface of this active area is the so-called two-dimensional electron gas (2DEG), which is spontaneously formed between AlGaN and GaN and could be compared to the inversion layer in standard silicon-based transistors. The ECR plasma step delivers the essential anisotropic polyimide etching to insulate each ISFET with no measureable damage to the active 2DEGs. Furthermore, it was demonstrated that a contamination free surface was attained through the use of this fabrication process, providing good device functionality from the initial measurement-state of the ISFET, without the need of the additional cleaning procedures previously used. This accomplishment leads to stable process conditions allowing for further functionalization and testing of AlGaN/GaN ISFET sensors for detection of desired analytes.

Regarding NO, a number of new technological processes were developed involving AlGaN/GaN ISFET gate area functionalization to enable NO measurement and will be discussed in detail. A complete analysis of the sensor performance based on these utilized functionalization methods is included, which shows tungsten trioxide (WO3) and graphene functionalization techniques to be the most useful and compatible of those considered. These experiments also encompass verification of NO sensitivity in contrast to known interfering substances. Very interestingly it was possible to make simultaneous pH and NO measurements via a suitable reduction of pH sensitivity of the functionalized transistors. Preliminary investigations of physiological related concentrations of NO and initial biocompatibility were demonstrated using L929 (mouse fibroblast) cells. With large scale devices sensitivities of up to 57.0 mV/pH (values extremely near the theoretical Nernstian limit of 58.2 mV/pH at 20 °C) for $W/L = 1$ at $V_{DS} = 1V$ could be achieved.

Finally, a miniaturized AlGaN/GaN ISFET array was developed, competitive in size and performance to comparable reduced sensor size arrays reported in literature. In this work, a sensor size reduction and pitch size of 10 µm x 10 µm and 100 µm x 100 µm, respectively, was employed to improve precision for in vitro cell culture or tissue related experiments. Combining the pH sensitivity reduction of NO sensors and the small-scale arrays, future work could enable simultaneous NO and pH measurement on a single chip across a local gradient in physiological applications.

Zusammenfassung

Was ist Stickstoffmonoxid (NO)? Aus dem Chemieunterricht kennt man NO unter Standardbedingungen für Temperatur und Druck als farbloses Gas. Im Zusammenhang mit Umweltemissionen ist NO ein unvermeidbares Abfallprodukt von Kraftwerken und Automotoren bei der Verbrennung von fossilen Brennstoffen. In der Physiologie ist NO für seine stark gefäßerweiternde Wirkung und als zentrales Signalmolekül bei zellulären Prozessen bekannt. All dies erklärt den starken Bedarf an NO-Sensoren. Diese Arbeit befasst sich zunächst mit der Optimierung von Aluminium-Gallium-Nitrid/Gallium-Nitrid (AlGaN/GaN) -Ionen-sensitiven-Feldeffekttransistoren (ISFETs), einschließlich der zur Prozessierung notwendigen Materialparameter. Im zweiten Teil der Arbeit wird unabhängig von seinem letztendlichen Anwendungsgebiet die Implementierung des Sensors zur Detektion von NO behandelt.

Durch den angestrebten Einsatz der Transistoren in Flüssigkeiten werden an die Passivierung des Systems, bezüglich der chemischen und mechanischen Stabilität, andere Anforderungen gestellt als bei einer Standard-Si-Transistor Technologie. Die Entwicklung einer geeigneten Passivierung war daher der Schlüssel, um eine gute Isolierung zu gewährleisten und gleichzeitig die Funktionalität der Bauteile zu erhalten. Im Vergleich mit den bekannten ‚harten' Passivierungsmaterialien wie Si_3N_4 oder SiO_2 konnte gezeigt werden, dass Polyimid zwar die besten Isolationseigenschaften für diese Transistoren aufweist. Um aber Polyimid als Passivierung einzusetzen, musste ein neuartiger ECR (Electron Cyclotron Resonance) Plasmaprozess entwickelt werden, der einerseits die AlGaN/GaN-Elemente strukturiert und gleichzeitig den aktiven Sensorbereich schützt. Denn wenige nm unter der Oberfläche dieses Sensorbereichs befindet sich das sogenannte zweidimensionale Elektronengas (2DEG), das sich spontan zwischen der AlGaN- und GaN-Schicht ausbildet, vergleichbar mit der Inversionsschicht eines Standard Si-basierten Transistors. Der ECR Plasmaschritt ermöglicht das notwendige anisotrope Ätzen zur Isolierung der ISFETs gegeneinander ohne eine messbare Degeneration des 2DEG. Weiterhin wurde gezeigt, dass dieser Prozess eine kontaminationsfreie Oberfläche hinterlässt und damit die vorher benötigten Reinigungsschritte überflüssig macht. Diese Prozessabfolge schafft die Grundlage für eine stabile Prozessierung, welche eine weitere Funktionialisierung erlaubt sowie Tests mit AlGaN/GaN-Sensoren zur Detektion der gewünschten Analyten.

Hinsichtlich der Detektion von NO wurde eine Reihe neuer technologischer Prozesse entwickelt, wie etwa die entsprechende Gate-Funktionalisierung des AlGaN/GaN-ISFET, die in dieser Arbeit ausführlich beschrieben wird. Diese Arbeit beinhaltet auch eine vollständige Anlayse des Sensorverhaltens in Abhängigkeit von der verwendeten Funktionalisierungsmethode. Dabei stellte sich Wolframtrioxid und Graphen als die besten der untersuchten Funktionalisierungen heraus. Diese Experimente umfassen auch den Nachweis der NO-Sensitivität gegenüber bekannten störenden Substanzen. Interessanterweise war es über die Verringerung der pH-Sensitivität des funktionalisierten Transistors möglich, eine gleichzeitige Messung des pH-Wertes und NO durchzuführen. Es wurden sowohl Versuche zur Messbarkeit von physiologischen Konzentrationen des NO als auch erste Tests zur Biokompatibilität des Systems durchgeführt, letzteres mit der Hilfe von L929-Zellen (Maus-Fibroblasten). Für größere Sensoren kann dabei für ein W/L = 1 und V_{DS} = 1V eine Sensitivität von bis zu 57.0 mV/pH (nahe am theoretischen Nernst´schen Verhalten mit 58.2 mV/pH bei 20 °C) erreicht werden.

Zuletzt wurde ein miniaturisiertes AlGaN/GaN-ISFET-Array entwickelt, das in Größe und Leistungsfähigkeit zu den in der Literatur beschriebenen Sensorarrays konkurrenzfähig ist. Es konnte eine Miniaturisierung und Pitch von 10 µm x 10 µm beziehungsweise 100 µm x 100 µm erreicht und angewendet werden, um die Genauigkeit für *in vitro* Zellkulturen oder Gewebe-basierte Experimente zu erhöhen. Die Kombination von miniaturisierten Arrays und der

Verringerung der pH-Sensitivität könnte in zukünftigen Arbeiten eine simultane NO- sowie pH-Messung auf einem Chip über einen lokalen Gradienten physiologischer Anwendungen ermöglichen.

Contents

Symbols and Acronyms

α	sensitivity parameter
β	geometric sensitivity parameter
β_{int}	intrinsic buffering capacity
λ	electromagnetic wavelength
λ_D	Debye length
μ	electron mobility
$\bar{\mu}$	partial molar free energy
μ_0	permeability constant
μ_i	chemical potential of species i
μ_r	relative permeability
ϕ	phase angle of the complex impedance
Φ_0	surface potential
Φ_e	potential in the electrolyte solution
Φ_{OHP}	potential at the OHP
Φ_M	work function of a metal, M
σ^0	surface charge density
σ^P	polarization-induced charge density
σ^{2DEG}	2DEG charge density
σ^{EDL}	EDL charge density
σ^m	charge density at the electrode
σ^s	charge density in solution
χ^{sol}	surface dipole potential of the solvent
ψ	chemical input parameter of the system
τ	time constant of the PPC decay
α_i	ionic activity
B	magnetic field
c	concentration
C_{dif}	differential capacitance
C_i	insulator capacitance
G	Gibbs free enrgy
d	atomic spacing
d_i	insulator thickness
E	electric field
E_{ad}	reaction quotient adsorption energy
f	activity coefficient
f	frequency
Id, I_{DS}	drain current
k_B	Boltzmann's constant, $1.38064852 \times 10^{-23}$ m^2 kg s^{-2} K^{-1}
K	equilibrium constant
K_a, K_b	acid, base dissociation constant
L	gate length
N_A	Avogadro constant (6.02×10^{23} mol^{-1})
N_d	impurity concentration
N_s	total 2DEG sheet charge density
n_s	2DEG sheet charge density
N_{ss}	total density of available surface sites
P	pressure
P_{PE}	piezoelectric polarization
P_{SP}	spontaneous polarization

pH_B	bulk pH-value
pH_S	surface pH-value
pH_{PZC}	pH-value at point of zero charge
pK_+, pK_-	dissociation constants of surface hydroxyl groups (logarithmic)
pK_a	acid dissociation constant (logarithmic)
q	elementary charge
Q	electric charge
Q	reaction quotient
Q	Mulliken charge
Q_B	depletion charge of the silicon
Q_{ox}	accumulated charge in the oxide
Q_{ss}	accumulated charge at the oxide-silicon interface
R	equivalent resistance
R	gas constant (8.314 J mol^{-1} K^{-1})
$t_{1/2}$	half-life
T	absolute temperature
V_{ac}	ac voltage
V_{bias}	bias voltage
V_{DS}	drain-source voltage
V_{FB}	flatband voltage
V_{GS}	gate-source voltage
V_{ref}	reference electrode voltage
V_T	threshold voltage
W	gate width
µTAS	micro-total analysis system
2DEG	two-dimensional electron gas
ACh	acetylcholine
AD	Alzheimer's disease
AES	Auger electron spectroscopy
AFM	atomic force microscopy
AKI	acute kidney injury
APTES	3-Aminopropyl triethoxysilane
ALD	atomic layer deposition
ALS	amyotrophic lateral sclerosis
ChemFET	chemically sensitive field-effect transistors
cGMP	cyclic guanosine monophosphate
CPA	constant potential amperometry
CPE	constant phase element
CV	capacitance-voltage
DBNBS	3,5,-dibromo-4-nitrosobenzene
DIW	deionised water
DMPO	5,5-dimethyb-pyrrobine-N-oxide
DMSO	dimethylsulfoxide
DNA	deoxyribonucleic acid
DNA-FET	DNA-modified field-effect transistor
DNPA	differential normal pulse amperometry
EBC	exhaled breath condensate
ECR	electron cyclotron resonance
EDL	electric double layer
EIS	electrochemical impedance spectroscopy
EIHS	electrolyte-insulator-heterostructure

emf	electromotive force E
EnFET	enzyme-modified field-effect transistor
EPR	electron paramagnetic resonance
EQE	external quantum efficiencies
FBS	fetal blood sampling
FWHM	full width at half maximum
HEMT	high electron mobility transistors
EDHF	endothelium dependent hyperpolarizing factor
EDRF	endothelium-derived relaxing factor
EGFET	electrolyte-gated field effect transistor
FI	flow injection
Gox	glucose oxidase
HD	Huntington's disease
HEMT	high-electron mobility transistors
HRXRD	high resolution x-ray diffraction
ICP	inductively coupled plasma
IMFET	immuno-field-effect transistor
IRF-1	interferon regulatory factor-1
IVP	impedance voltage profiling
KIM-1	kidney injury molecule-1 antibody
LED	light-emitting diode
LOD	limit of detection
M	mol L^{-1}
MBE	molecular beam epitaxy
MIHS	metal-insulator-heterostructure
MIS	metal-insulator-semiconductor
MNP	2-methyl-2-nitrosopropane
MOCVD	metal organic chemical vapour deposition
MOSFET	metal-oxide-semiconductor field-effect transistor
MQW	multi quantum-well
MS	multiple sclerosis
NF-κβ	nuclear factor κβ
NMDA	N-methyl-D-aspartate
NO	nitric oxide
eNOS, NOS3	endothelial nitric oxide synthase
iNOS, NOS2	inducible nitric oxide synthase
nNOS, NOS1	neuronal nitric oxide synthase
OCP	open-circuit potential
OCS	Octadecyltrimethoxysilane
OHP	outer Helmholtz plane
PBS	phosphate buffer solution
PC	pulsed coulometry
PCB	printed circuit board
PD	Parkinson's disease
PDMS	polydimethylsiloxane
PEEK	polyether ether ketone
pH	negative common logarithm of the hydronium activity
PGI_2	prostacyclin
POCT	point-of-care-testing
PPC	persistent photoconductivity
PMMA	poly(methyl methacrylate)

PSA	prostate specific antigen
PSL	porous silicon layer
QRE	quasi-reference electrode
REFET	pH-insensitive reference ISFET
RIE	reactive ion etching
rms	root mean square
RTP	rapid thermal process
SAM	self-assembled monolayer
SAW	surface acoustic wave
Si-NW	silicon nanowires
sGC	soluble gualnylate cyclase
SEM	scanning electron microscopy
SOD	superoxide dismutase
SMU	source-meter unit
SNR	signal to noise ratio
SQW	single quantum-well
SWCNT	single wall carbon nanotube
TEGa	triethylgallium
TMAl	trimethylaluminum
UV	ultra-violet
WF-FET	work-function field-effect transistor

1. INTRODUCTION

Bio-medical and -chemical sensing devices represent an evolving field in which considerable progress has been made over several decades. Although chemical sensor development dates back to the beginning of the 20th century with work on the first hydrogen-sensitive glass electrode, significant advancement in this field flourished in the 1960s [1, 2]. The beginning of this decade marked the first reported biosensor [3]. Since, the field has steadily developed; more recently, emphasis has been placed on miniaturization, low cost, and high analyte sensitivity/selectivity to produce the Lab-on-a-Chip and micro-total analysis solutions (µTAS). Due to the demanding nature of these systems, many intrinsic problems of these sensors have yet to be resolved. Devices built on various sensing approaches have been developed in attempts to overcome these difficulties. Some ideas, such as metal oxide semiconductor (MOS) capacitor-based sensors, chemically-sensitive Schottky barrier diodes, and solid electrolyte based sensors, have been abandoned due to complexity of signal read-out or issues involving the integration into fabrication processes. Integrated systems, such as surface acoustic wave (SAW) sensing and its more complex signal transduction show promise in selectivity, sensitivity, and response time. However, these integrated systems require complicated measurement setups and complicate production.

Given these limitations, promising alternative approaches in the field include thin-film sensors, ion-sensitive field effect transistors (ISFETs), and chemically sensitive field effect transistors (ChemFETs). Since the ISFET and ChemFET are based on the field effect transistor, they inherently possess advantages of signal amplification and impedance transformation, in addition to the necessary potential for bridging electrical and biochemical realms [4]. Enhancement of this electrical-biochemical interface is one means of increasing sensitivity, as well as specificity for target analytes. A wide variety of techniques can be applied in order to establish such an interface; the functionalization methods range from supplementary material layers (which can increase the electrochemical response to specific ions or molecules) to gels for the entrapment of biological catalysts or selective membranes. These structural modification techniques open the possibility of sensing a multitude of analytes separately, but also include the ability to simultaneously measure multiple parameters once the requisite mass fabrication processes are brought into play.

Miniaturized sensor arrays are an ideal way to realize small-area, multi-parameter measurement systems; these systems efficiently manage space while performing *in vitro* or *in vivo* cellular physiological and pathophysiological analysis, when biocompatible materials are made use of during production. Electrolyte gated field effect transistors (EGFETs), which can also include ISFETs and ChemFETs, present a platform which has received a great deal of attention and success in biochemical sensing. Much of the development of EGFETs, sensor arrays, and other transistor technologies is founded on well-developed silicon-based devices. These devices, however, are often unsuitable for biological applications due to long-term stability issues of standard gate insulator materials, such as Si_3N_4 and SiO_2 in a fluid environment [5, 6, 7]. III-V heterostructures, particularly III-nitrides, on the other hand, frequently demonstrate higher chemical stability and biocompatibility; accordingly, a significant increase in investigation of this material system has occurred over the past two decades [7]. Initial interest, as well as efforts to begin development of group III-nitride based systems, dates back to the 1970s; however, fabrication limitations due to the lack of electronic grade metalorganic precursors severely limited progress [7, 8, 9, 10, 11]. Following advancements in the fields of metal organic chemical vapor deposition (MOCVD) and molecular beam epitaxy (MBE), high quality epitaxial film growth became possible, and the advantages of these material systems (wide band gap, superior piezoelectric and spontaneous polarization properties, and chemical stability) could be exploited, making them prime candidates for bio-chemical sensors. Additional advantages over silicon-based devices include noise reduction and – particularly in the case of the AlGaN/GaN heterostructure – optical transparency, a property that enables optical analysis or measurement [7, 12].

Aluminum gallium nitride/gallium nitride (AlGaN/GaN) based systems represent an example of wide bandgap III-Nitride heterostructures (structures containing two or more semiconductor layers) exhibiting high breakdown voltage and thermal stability. A detailed structural and electrical analysis of this material has been reported by Ambacher, et al. [13]; their work presents a focus on high-voltage, high-power applications for high-electron mobility transistors (HEMTs). Specifically, the authors examined the various structural properties and their influences on the two-dimensional electron gas (2DEG) that develops within the heterostructure. Extending that work, Steinhoff et al. studied the use of AlGaN/GaN heterostructures as the foundation for ISFETs and EGFETs. Following studies involving lipid membranes demonstrated promising results regarding the applicability of this system for bio-sensing applications [7].

Considerable progress has been made in the last decade in the characterization and optimization of AlGaN/GaN ISFETs for pH measurement [14, 15]. This development, along with recent improvements in sensor stability, presents exciting new opportunities for exploring the detection of other analytes [15, 16]. One such prospect is nitric oxide (NO), an important signaling molecule in biological systems. NO is particularly interesting due to its paradoxical role: the molecule can serve as a gaseous messenger in certain contexts and as a cytotoxic agent in others. The role of NO as the first known gaseous mediator was discovered though the work of Furchgott, et al. in 1987, proving that the endothelium-derived relaxing factor (EDRF) and NO are in fact one and the same [17]. This fairly recent finding along with immune system and neurotransmission related functions signify the way in which detection and measurement of NO at physiologically relevant concentrations may benefit, for example, neuroscience, pharmacology, and cardiology. Thus far, sensing applications for NO have been studied to limited degree; however, exploration of ISFET NO sensing systems has not been well researched. In particular, promising III-nitride material systems are notable in their lack of examination [18].

Additionally, many contemporary NO sensors rely on optical measurement techniques and the burdensome analysis setup requirements associated with those methods. FET-based electrochemical (i.e. non-optical) NO detection systems lack those difficulties and offer a more straight-forward approach. This advantage, together with the potential of H^+ measurement (the initial and most often studied ion during ISFET development) utilizing the same sensor chip, is attractive from the biological standpoint. H^+ is an important parameter for many biological processes; it is the main ion for metabolic activity and must be tightly regulated within living organisms.

Detection of NO and H^+ (and other ions or molecules of interest) in a biological context inherently require passivation of conductive contacts/materials to ensure proper function in aqueous environments. Here, sensor passivation presents a substantial challenge due to the demanding conditions of biological media. Passivation has not often been studied or emphasized, despite its importance in preserving sensor integrity [4]. Regardless, passivation must be considered and applied to facilitate precise, reproducible analyte measurement – in this case pH or NO. Accordingly, various passivation materials and techniques were investigated and characterized in AlGaN/GaN FET systems in order to achieve robust measurement conditions. This research focuses on this objective, as well as other adjacent topics, interests and issues. The work is divided as follows:

- study of various passivation materials in order to provide a stable foundation for AlGaN/GaN based ISFETs and the further development of biosensors,
- functionalization of the GaN active area of the ISFET to enable nitric oxide measurement, and
- miniaturization and sensitivity analysis of AlGaN/GaN ISFETs to for the development of multi-analyte sensor arrays

Advancement in the above areas allows stable and reliable simultaneous measurement of multiple parameters. In addition, miniaturization of the sensors, and therefore reduction of required space for the sensor array, also facilitates analysis with extremely low sample volumes.

2 AlGaN/GaN Heterostructure

To establish a foundation for the III-nitride based pH and nitric oxide (NO) detection system studied in this research, the AlGaN/GaN material system will first be presented. This discussion covers crystal growth, as well as the polarization effects within the heterostructure utilized in these NO detection applications.

2.1 Growth of Group III-Nitrides

2.1.1 Background

Epitaxial growth of group III-nitride material systems is accomplished through various techniques, including sputtering, chemical transport, metalorganic chemical vapor deposition (MOCVD), and molecular beam epitaxy (MBE) [10, 19, 20, 21]. Although experiments utilizing III-V and specifically III-nitride material systems date back to the 1970s, progress was initially limited due to the lack of electronic-grade metal-organic precursors or plasma sources for nitrogen radicals compatible with MBE systems. As a result of the low quality material growth, highly degenerate layers with impurity concentrations in the ($N_d = 10^{18}$ to 10^{20} cm^{-3}) range [22] were observed. The high background concentrations of electrons were presumed to be due to point-defects such as nitrogen vacancies, as well as contamination by oxygen, silicon or carbon in the obtained crystal lattice [23]. An additional issue hindering progress in this field included the lack of a suitable substrate material. Achieving a good lattice match is important in this respect and, as subsequent research has demonstrated, the crystal structure of epitaxial nitrides is strongly influenced by the orientation and material of the substrate [4, 24, 25, 26, 27]. Finally, the inability to produce p-type material made the development of light emitting device applications impossible, one of the most promising benefits from this material system with photoluminescence possibilities in the blue and UV range. Until high-quality epitaxial growth became possible such devices based on III-nitride material systems were not feasible.

The early 1990s brought about the first display of a distinct improvement in III-nitride layers on sapphire substrates by metal organic techniques [10, 19, 28]. This can be attributed to general advancements in crystal growth technology in combination with the use of an AlN nucleation layer to alleviate obstacles involving the substrate [9]. This buffer layer made GaN growth with a flat surface on a sapphire substrates possible without macroscopic defects such as cracking or pitting. Although silicon carbide (SiC) is better matched regarding thermal expansion and lattice constants (~3.5% mismatch to GaN versus ~13.9% for sapphire), the high cost has prevented these substrates from being the main choice to this point. The use of an AlN nucleation layer was therefore a significant advancement in solving the substrate issue; subsequently, improvement of the structural and electronic properties occurred over the following years. As a result, a decrease in the background electron concentration and an improvement of mobility were observed, as well as the realization of p-type GaN [10, 29].

2.1.2 Applications

The growth technology advancements yielding improved electronic properties of III-nitrides have granted opportunities to exploit promising characteristics long sought in these material systems. Favorable properties include the optical properties of InN, GaN and AlN, as well as the high thermal and chemical stability of these III-nitrides that make them prime candidates for various optoelectronic applications. Particularly advantageous is the wide tunable direct bandgap range covered by the ternary compounds (i.e. compound containing three different elements). As can be seen in figure 2.1, this tunable bandgap covers the range of 1.9 eV to 3.4

eV to 6.2 eV for α-InN, α-GaN and α-AlN, respectively and 1.7 eV to 3.2 eV to 4.9 eV for β-InN, β-GaN and β-AlN, respectively [30, 31, 32, 33, 34, 35]. Indium nitride (InN) and its compounds mainly contribute to the visible and infrared (IR) portion of the electromagnetic spectrum. However, InN did not initially receive much attention due to difficulties in growth and its low thermal stability, which made high temperature growth impossible in III-nitride based systems [10]. Furthermore, the bandgap of InN (and other possible ternary compounds) is well covered by alternative semiconductors [11]. $Al_xGa_{x-1}N$, on the other hand, with its tunable wide direct bandgap in the visible blue and violet and the ultraviolet (UV) range, makes it ideal for optical applications in this region of the spectrum.

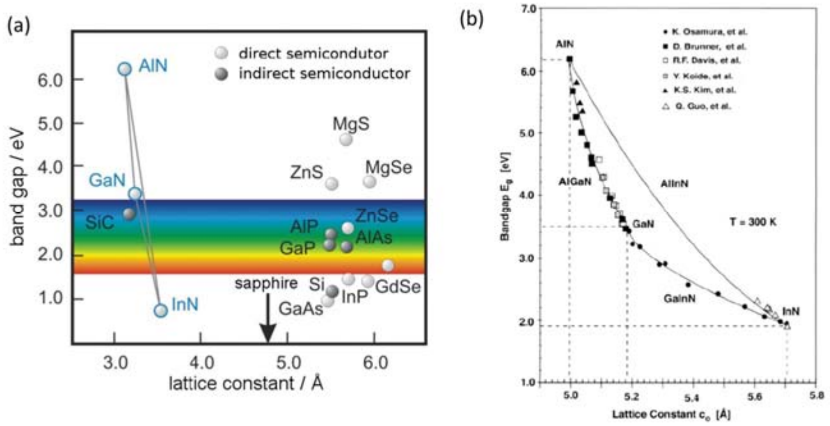

Figure 2.1: Semiconductors and the respective bandgaps, with particular focus on III-nitrides: a) theoretical and b) experimental results correlation

Emission at wavelengths in this range has been actively pursued, and potential for this tunable bandgap has been viewed favorably. Substantial progress has been made in this area with GaN-based light emitting devices, which were the first optoelectronic application to be successfully developed and commercialized, the first example a blue p-n LED in 1994 [36]. In following years, a variety of III-Nitride systems were developed with AlN-, AlGaN/GaN- and GaN-based devices helping to make a range of applications for UV emission possible. The shortest emitted wavelength to this point has been an AlN-based UV-C LED with an output of 210 nm by Taniyasu in 2006 [37]. Advancements involving system optimization, such as output power of GaN based UV LEDs, have also been achieved with external quantum efficiencies (EQEs) up to 43% at near UV and UV-A wavelengths and 2.78% in the deep UV range, while blue-violet LEDs range up to 52-73% [38, 39, 40, 41, 42, 43]. The EQE of most UV-C range LEDs however, still typically lies at 2% or below as defect densities in AlGaN layers continue to hinder emission power and efficiency. Many of the pioneers of GaN growth optimization continue work on the reduction of the defect density, and consistent progress has been made [28, 325, 326]. In fact, the Nobel Prize in 2014 went to three of these early pioneers in the field Isamu Akasaki, Hiroshi Amano, and Shuji Nakamura, for the research and development on the blue LED. Much of their recent work still relies on the uniform, low defect density growth that begins at the interface with the substrate.

In addition to the interesting optical properties of III-nitride based systems, the development of high-power, high-voltage HEMTs has progressed greatly. Devices exploiting the high thermal stability, large peak electron and saturation velocities, and the ability to form quantum wells and two-dimensional electron gases (2DEGs) have found many applications as advancement has been made. As the growth of III-nitrides has progressed and devices based on AlGaN/GaN heterostructures have become more established, these are also looked to for the next generation of wireless communication systems and are being used more often for biological applications

[7, 14, 44, 45, 46]. The formation of the 2DEG, which is taken advantage of for many of these purposes, will be discussed in the following section.

2.2 Two -Dimensional Electron Gas

Studies have been conducted to assess the structural and electrical characteristics of the two-dimensional electron gas (2DEG) that forms within the AlGaN/GaN heterostructure [20, 21, 47]. These studies directed attention to surface properties, passivation, and electron sheet confinement effects. The majority of progress in III-nitride growth quality has been achieved using MOCVD or PIMBE technology. Since the epitaxial growth of the device heterostructures utilized in this research was performed with MOCVD, this technique will receive the focus of discussion in this section. Likewise, the spontaneous and piezoelectric polarization within the epitaxially grown layers, as well as the formation and confinement of the 2DEG, are described.

Cubic zincblende and hexagonal wurtzite crystal structures are possible for group III-nitrides; both possess spontaneous and piezoelectric polarization properties. The wurtzite (α-phase) is the more stable phase in this case; since this form of GaN and AlGaN is noncentrosymmetric, it exhibits crystallographic polarity and may be grown either N-face or Ga(Al)-face. This property indicates the atomic stacking sequence and, therefore, the orientation of the spontaneous polarization; however, this does not identify which atom terminates the layer growth. Like other noncentrosymmetric structures, the polarity of the crystal affects both the bulk and surface characteristics. Here, the Ga-faced crystal typically exhibits higher structural quality and better electron transport properties [48, 49, 50]. This orientation, which may only be determined experimentally, is illustrated in figure 2.2 with corresponding examples of GaN/AlGaN/GaN heterostructures. Table 2.1 summarizes the spontaneous polarization and piezoelectric and dielectric constants, some of which are also represented in figure 2.1, which may be used to determine the polarization or bound charge densities shown.

This table is a compilation from Ambacher, et al. in 1999, in which a comprehensive description of the formation of the 2DEG and the effects of various structural properties on this are described [21]. Here, the dependence of the 2DEG on both the spontaneous and piezoelectric polarization is demonstrated. The spontaneous polarization may be determined following for the range from GaN to AlN covered by $Al_xGa_{1-x}N$ as a function of x, the percentage of Al contained in the ternary film [51]:

$$P_{SP} = (-0.029 - 0.052x)\frac{C}{m^2}. \qquad 2.1$$

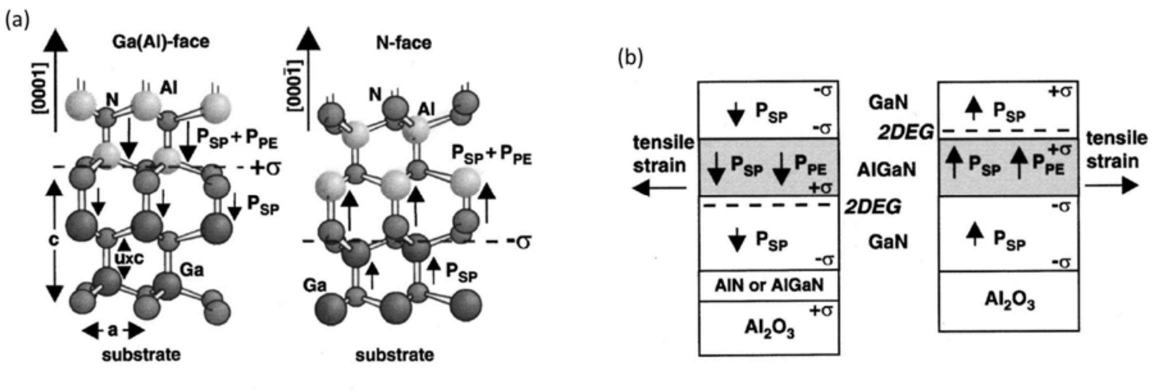

Figure 2.2: Spontaneous and piezoelectric polarization in Ga(Al)- and N-faced GaN or AlN layers and corresponding GaN/AlGaN/GaN heterostructures [21]

Table 2.1: Crystal properties of AlN, GaN and InN [21]

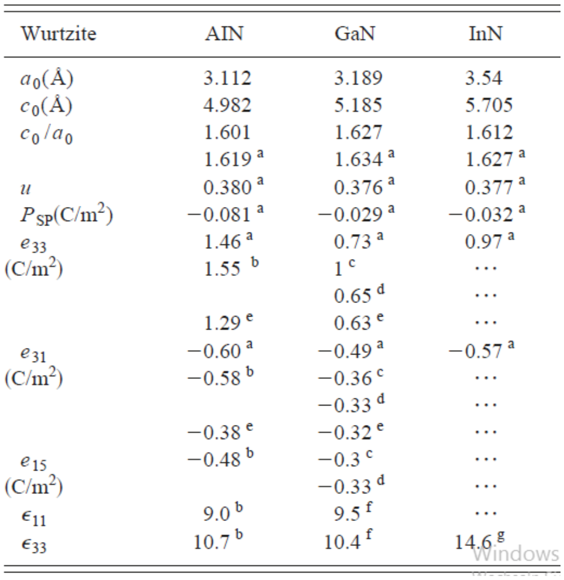

Wurtzite	AlN	GaN	InN
a_0(Å)	3.112	3.189	3.54
c_0(Å)	4.982	5.185	5.705
c_0/a_0	1.601	1.627	1.612
	1.619 [a]	1.634 [a]	1.627 [a]
u	0.380 [a]	0.376 [a]	0.377 [a]
P_{SP}(C/m^2)	−0.081 [a]	−0.029 [a]	−0.032 [a]
e_{33}	1.46 [a]	0.73 [a]	0.97 [a]
(C/m^2)	1.55 [b]	1 [c]	⋯
		0.65 [d]	⋯
	1.29 [e]	0.63 [e]	⋯
e_{31}	−0.60 [a]	−0.49 [a]	−0.57 [a]
(C/m^2)	−0.58 [b]	−0.36 [c]	⋯
		−0.33 [d]	⋯
	−0.38 [e]	−0.32 [e]	⋯
e_{15}	−0.48 [b]	−0.3 [c]	⋯
(C/m^2)		−0.33 [d]	⋯
ϵ_{11}	9.0 [b]	9.5 [f]	⋯
ϵ_{33}	10.7 [b]	10.4 [f]	14.6 [g]

For the piezoelectric polarization, this calculation involves the piezoelectric tensor, from which two components are relevant when describing the polarization induced along the c-axis:

$$P_{PE} = e_{33}\epsilon_z + e_{31}(\epsilon_x + \epsilon_y), \tag{2.2}$$

for which

$$\epsilon_z = \frac{(c-c_0)}{c_0}, \tag{2.3}$$

$$\epsilon_x = \epsilon_y = \frac{(a-a_0)}{a_0}. \tag{2.4}$$

Here, ϵ_z is the strain along the c-axis and the in-plane strain is assumed to be isotropic; hence, $\epsilon_x = \epsilon_y$. e_{33} and e_{33} are piezoelectric constants, and a and c are the lattice constants for the wurtzite hexagonal cell – all of which can be found in table 2.1 for the binary III-nitrides. The variation for the $Al_xGa_{1-x}N$ case may be determined through the use of the elastic coefficients C_{13} and C_{33} which compensate for the variation in the lattice constants:

$$P_{PE} = 2\frac{a-a_0}{a_0}\left(e_{31} - e_{33}\frac{C_{13}}{C_{33}}\right). \tag{2.5}$$

With the use of Equations (1) - (5), and Vegard's law, and linear interpolation over x to account for $Al_xGa_{1-x}N$, the piezoelectric and spontaneous polarization, as well as the induced sheet charge density at the interface between AlGaN and GaN may be quantified. The heterostructures of interest are grown on a c-plane sapphire [0001] substrate with a thin AlN nucleation layer (i.e. Ga-face), and a thick (~1.5 µm) GaN bulk layer. AlGaN barrier dimensions are always held below the critical layer relaxation thickness. Consequently, the tensile strain within the AlGaN layer depicted in figure 2.2 is always relevant. Additionally, it has been shown that the piezoelectric polarization over the entire composition range of $Al_xGa_{1-x}N$ has the same sign for tensile strain (negative) or compressive strain (positive) [51]. This property signifies that both the Ga-faced and N-faced heterostructures are relevant to the case in which both the spontaneous and piezoelectric polarization within the film point in the same direction, yielding a total polarization defined by:

$$P = P_{PE} + P_{SP}. \tag{2.6}$$

As the piezoelectric constant and the spontaneous polarization increase from GaN to AlN, (see table 2.1), the total polarization of a strained or unstrained (i.e. $P_{PE} = 0$) AlGaN layer is higher than that of the relaxed GaN buffer layer. The polarization orientation and induced bound sheet charges at each interface are shown in figure 2.2. Additionally, the resulting 2DEG near the lower AlGaN/GaN or upper GaN/AlGaN interface for the case of Ga-faced or N-faced layer growth, respectively, in GaN/AlGaN/GaN heterostructures is shown. This 2DEG is induced due to the polarization pointing toward (Ga-face) or away (N-face) from the substrate. The confined sheet charges σ_P appearing at the interface relevant to the heterostructures grown in this work (Ga-face, $Al_{0.3}Ga_{0.7}N$) are found to be approximately $\sigma_{P_{SP}GaN} = 1.8\, x\, 10^{13}\, cm^{-2}$ at the upper GaN bulk layer boundary and $\sigma_{P_{SP}GaN} = 2.8\, x\, 10^{13}\, cm^{-2}$ at the lower boundary of the $Al_{0.3}Ga_{0.7}N$ layer. The additive piezoelectric polarization charge attributed to the tensile strain within AlGaN contributing to the total polarization within the barrier layer has a value of approximately $\sigma_{P_{PE}GaN} = 6\, x\, 10^{12}\, cm^{-2}$ [52]. An uncompensated charge at the lower AlGaN boundary is thus present, which in turn leads to the formation of the 2DEG at the upper boundary of the GaN bulk layer with sheet carrier densities (n_s) which can be great than 1 x 10^{13} cm^{-2}. The development of the quantum well may also be visualized through the band diagram in figure 2.3. The formation of the 2DEG in response to the establishment of a quantum well at the AlGaN/GaN interface may be observed at the point where the energy drops below the fermi level.

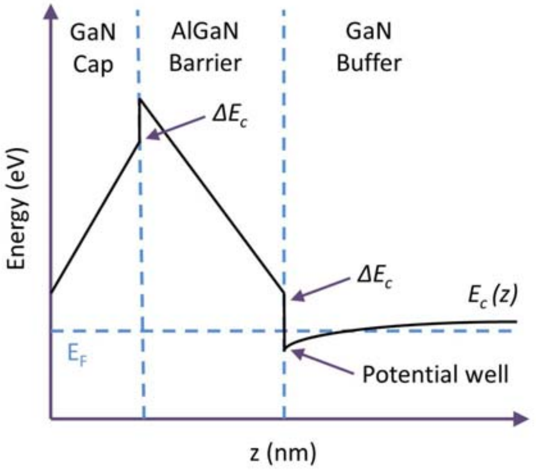

Figure 2.3: Valence band energy levels demonstrating 2DEG formation due to polarization induced sheet charges confined at the GaN/AlGaN/GaN interfaces

Buchheim et. al. demonstrated that the compensation of the resulting polarization induced bound charges is not complete, and a resulting electric field within the AlGaN barrier for an uncapped (upper GaN layer excluded) is on the order of -300kV/cm [52]. This field leads to a positive surface potential Φ_0 at the AlGaN/air interface of approximately 0.7 V, which is reduced to 0.3V with the addition of the GaN cap layer – although this value may vary depending upon growth conditions [53].

The described 2DEGs formed in AlGaN/GaN heterostructures are utilized for a wide range of applications through the modulation of the electron gas carrier density. Example applications include HEMTs, optical devices (such as those covered in section 2.1.2), along with the developed biosensors in this research, and the previously developed fluid sensors for which further optimization has been carried out previously, as well as in this study, to improve heterostructure and measurement conditions [15, 16].

2.3 Heterostructure and Measurement Optimization for Stability in Aqueous Environments

Defect density and chemical surface stability are two examples of the various structural properties that depend on growth conditions, substrate material and the orientation of epitaxial films. These properties have been considered in the optimization of the AlGaN/GaN heterostructure growth accomplished with MOCVD. Additionally, measurement conditions for developed devices in aqueous (i.e. a solution with water as the solvent) environments, have been studied [15, 16, 54]. The heterostructure represented in figure 2.4 is a general illustration of that used in much of the previous related work, as well as the devices developed here. The 500 nm GaN bulk layer utilized in [54, 55] was necessary for the development of resonators; however, the 1.2 – 1.5 µm thick GaN used here results in fewer structural defects within the GaN layer [15, 16]. This defect reduction has also been demonstrated in the literature with validation by high resolution x-ray diffraction (HRXRD) measurement, as well as an increase in electron mobility from 250 cm^2/Vs to 550 cm^2/Vs for an increase of the GaN bulk layer thickness from 1 µm to 2.5 µm [21].

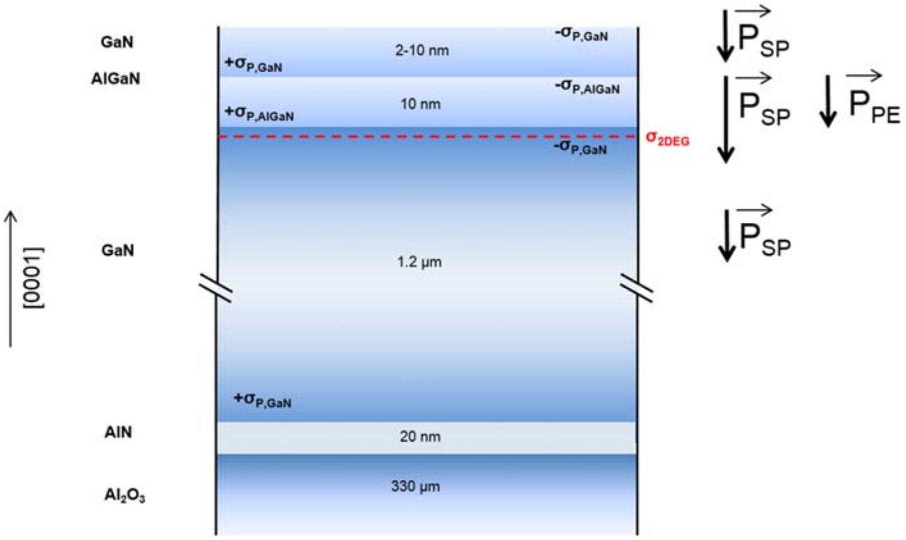

Figure 2.4: GaN/AlGaN/GaN Heterostructure with spontaneous and piezoelectric fields and induced bound sheet charges [56].

In an effort to continue improvement of heterostructure integrity through the reduction of issues that relate to the defect types which are present, including dislocations, stacking faults, grain boundaries and boundaries in general, defect related phenomena were analyzed. Persistent photoconductivity (PPC) is one of the main defect-related problems and is observable through a drawn-out decay of the photoconductivity after darkening, as shown in figure 2.5. This effect has been attributed to deep level defects within the bandgap and was previously demonstrated for AlGaAs as well as AlGaN/GaN heterostructures [57, 58, 59, 60]. The drawn-out decay has also been shown to exist as a result of defects in both the GaN and AlGaN film through the investigation of n-type, p-type, and undoped GaN, GaN photodetectors and AlGaN/GaN heterostructures [60, 61, 62, 63, 64]. Such defects result in additional energy levels present within the forbidden bandgap and present an additional energy barrier for the charge carrier generation/recombination process. It should be noted that although more homogeneous films have been demonstrated by MOCVD growth, it has been made evident that the PPC has a reduced effect in comparable MBE films [16]. This signifies that despite the decrease of structural defects during metal-organic growth, the resulting intrinsic and extrinsic point defects and varying types of contamination between the two growth techniques play a major role.

To better understand the effects of PPC and how the drawn out photocurrent decay plays a role in the devices under investigation, various studies have been carried out [15, 16, 58, 59, 64,].

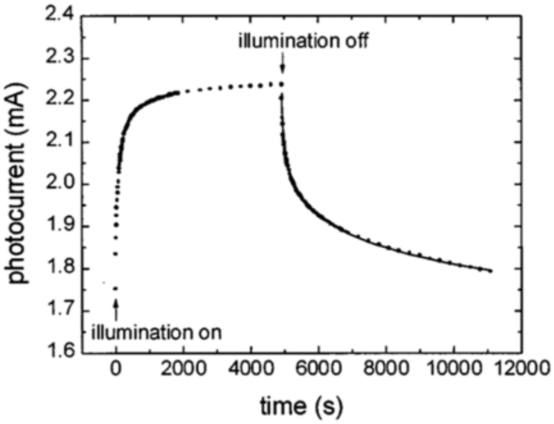

Figure 2.5: Drawn out current decay as a result of the PPC effect [64]

The PPC drawn out decay was shown to be well described by the stretched exponential function:

$$I(t) = I_{dark} + (I_o - I_{dark})e^{\left(\left(-\frac{t}{\tau}\right)^{\beta}\right)}, \qquad 2.7$$

where I_{dark} represents the current without illumination, I_o the current upon illumination, τ the time constant, and β the decay exponent which lies in the range $0 < \beta < 1$ with reported values from 0.2 to 0.4 [16, 58, 59, 64]. Significant time constants of 1×10^3 s to 1×10^4 s are typical upon switching off ambient light or monochromatic light in the range of 2-3 eV [16, 64]. This PPC is detrimental to the development of stable devices as the resulting drift makes accurate measurement of desired analytes extremely difficult. Previous measures taken in an effort to reduce this effect include Si-doping near the AlGaN/GaN interface, constant illumination with an LED, and reference circuits to calculate out the measurement instability due to the drift influence.

Doping with Si is employed at approximately 50 nm below the AlGaN barrier and has demonstrated a reduction of the effects due to illumination by up to a factor of 3. This improvement is achieved by increasing the magnitude of the sheet carrier concentration N_s and reducing the proportion of photo-induced charge carriers to the overall concentration of charge carriers. The utilization of additional reference sensors in a differential circuit has also demonstrated an additional successful factor 5 reduction of disturbance due to PPC.

Utilization of violet and red LEDs as continuous illumination sources during measurement was based on previous measurement results on the changes in drain current of AlGaN/GaN based ISFETs when ambient light was removed, leaving only LED illumination [16]. Wavelengths near that of the GaN band gap showed the smallest change in drain current and therefore a violet LED (λ = 400nm) was first chosen. However, due to reports on photochemical etching of III-Nitrides, the surface of the GaN cap layer was studied and comparative measurements were made with a red LED [65, 66, 67, 68, 69]. The difference in violet and red LED use was easily observable as comparative measurement series were carried out over extended periods of time. As may be seen in figure 2.6, impedance voltage profiling (IVP) was used for analysis of the illumination influence. Here, capacitance/conductance profiles versus bias voltage, V_{BIAS}, demonstrate drift upon continuous illumination, as well as a distortion of the shape of the profile curves. The initial measurement is made in darkness (black line) followed by multiple measurements with the activated red or violet LED, the first of these represented by the red curve. Although the drift is demonstrated, the benefit of the red LED (figure 2.6, right) is already quite evident upon observation of the extreme two-fold distortion behavior with the use of the violet LED (figure 2.6, left) and within a much shorter amount of time (measurement numbers are indicated in the insets). In addition, the loss of a clear peak in the phase measurement contributes to this indication.

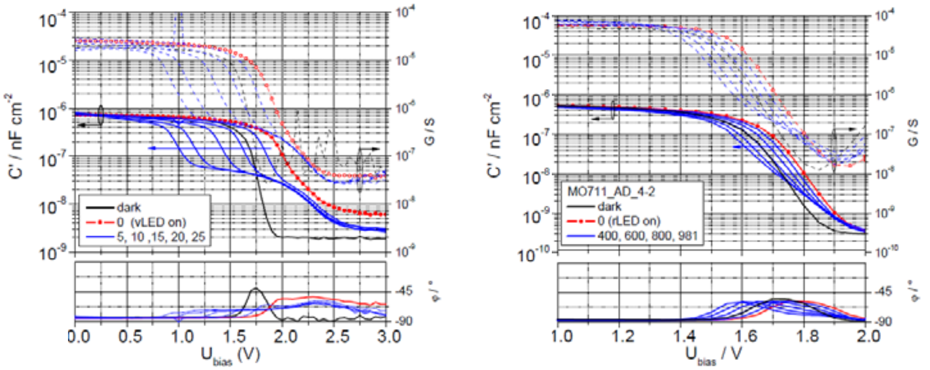

Figure 2.6: IVP of GaN/$Al_{0.3}Ga_{0.7}N$/GaN heterostructures with a 2nm GaN cap layer under violet (left) and red (right) LED illumination [15]

Furthermore, measurement series in which only one measurement was made under violet LED illumination (followed by many hours of measurement in darkness) demonstrated a decreased time for settling of the PPC drift (~12 hours). However, such measurements also showed the inability to reproduce the initially recorded dark curve. These findings, along with the deformation of the IVP curves, indicate an irreversible process has occurred and demonstrate that this effect is much more pronounced for the measurements with violet LED illumination. Photochemical etching was found to be the cause of the drift seen here. The variation of the measurement profiles over time is a consequence of changes (i.e. reduction of surface area) in the upper GaN cap layer as the etching takes place. Scanning electron microscopy (SEM) analysis provided more insight into this issue by visually demonstrating corrosion of the surface, as well as displaying a difference between the etching under violet illumination (fig. 2.7b, deep vertical pitting) and that with red lighting (fig 2.7c, shallow horizontal etching). This may be compared to the unused GaN surface (fig 2.7a), where the defects are also evident; however, no etching has taken place. As previously mentioned, the existence of these structural defects is well known and typically originates at the interface with the substrate and run through the entire heterostructure. Although GaN is known to be extremely stable, it is also known that these defect sites are vulnerable to etching [70]. This vulnerability is confirmed here, as it is clearly seen that these sites are attacked. Etched corrosion sites resulting from the use of violet light have a diameter of 30-50 nm, demonstrate anisotropic vertical etching, and have a pit density of 2×10^{10} cm^{-2}. Red light defect etching brought about shallower pits with increased diameter and a density of approximately 1×10^{10} cm^{-2}, which corresponding well to the values in literature [15].

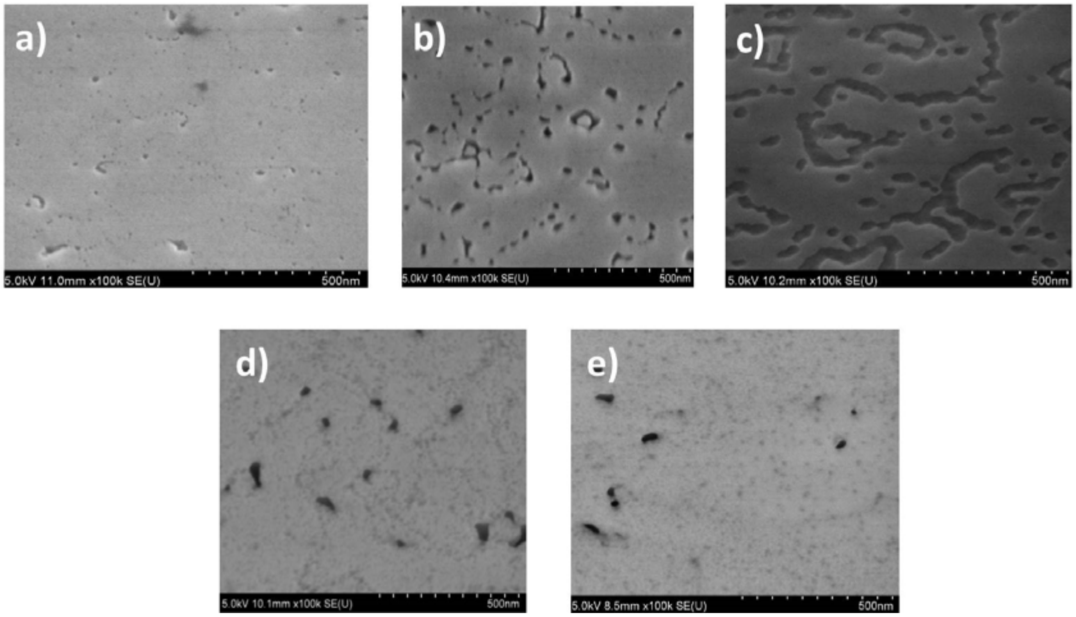

Figure 2.7: SEM images of a) unused, b) violet LED utilization resulting in narrow/deep pits, c) red LED use resulting in wide/shallow pits, d) increased cap layer with violet LED exposure, e) increased cap layer thickness and lower Al % with violet LED use [15]

In an effort to increase the device stability and reduce photochemical etching, heterostructure modifications, including increased GaN cap layer and decreased Al content in the barrier film, were tested. SEM images of structures including these variations visually demonstrate a beneficial effect. Supplementary IVP analysis also demonstrated the advantages of these modifications. Table 2.2 presents an overview of the drift due to the violet or red LED illumination and heterostructure modifications. This improvement is demonstrated in terms of variation over the threshold voltage of the capacitance and conductance profiles, V_{thC}, V_{thG}, and the derived total sheet carrier concentration N_S, and absolute value of the capacitance and conductance at zero bias voltage, C'_0 and G'_0.

Table 2.2: Overview of illumination and heterostructure modification effect on drift stability [15]

Parameter	**Direct succession - violet LED**	**45 Min pause - violet LED**	**Dark**	**Red LED**	**Violet LED – 10nm Cap**	**Violet LED – 10nm Cap/20%Al**
V_{thC} (mV)	-51.7	-52.3	-0.1	-0.14	-8.1	-1.0
V_{thG} (mV)	-48.2	-50.6	-0.1	-0.18	-5.1	0.1
N_s (10^9 cm^{-2})	-148.6	-173.0	-0.4	-0.66	-12.2	1.3
C'_0 (nF cm^{-2})	6.6	6.8	-0.01	0.01	2.4	0.8
G_0 (µS)	-0.8	-1.5	-0.03	0.04	0.3	-0.1

To ensure that the discussed corrosion is independent of time and principally due to the number of measurements, measurement series were made in direct succession as well as with a 45-minute rest. The drift variations are negligibly higher for the series with a rest, showing that a very small part of the corrosion effect may be based solely on light-induced etching. However, the majority of corrosion is due to the measurement process under illumination and is therefore photoelectrochemical etching of the surface. Utilization of the red LED resulted in a significant reduction of the drift magnitude during the measurement process. In this case the drift is brought to a level only slightly higher (less than a factor of 2) than measurements without light.

The increase of the GaN cap layer and reduction of Al in the barrier layer included in the structural variation demonstrated better chemical stability of the heterostructure surface in electrolyte solution. Taking advantage of red illumination and/or the optimization options for the AlGaN/GaN heterostructure, utilization of sensors based on this heterostructure may benefit from lower drift level and increased overall stability. This optimization, in addition to the improvement due to Si-doping, provides the advantage of a solid basis as far as GaN/AlGaN/GaN growth and heterostructure characterization is concerned. With this advancement the improved stability of this material system is evident and the possibility to look towards further applications is feasible.

Many types of bio-functionalization on a wide variety of materials and devices have been developed over the past 50-60 years, some of which are considered in the Chapter 3. One of the three main topics of this research is aimed at functionalization of the AlGaN/GaN heterostructure for multi-parameter bio-sensing, including nitric oxide and pH. As measurement of these analytes also takes place in aqueous environments, the described optimization steps are of great importance and are made use of for this investigation. The importance of pH and nitric oxide measurement, along with a brief summary of biosensors will be covered in the following sections.

3. Biochemical Sensing

Development of biosensors began more than half a century ago, with the first reported biosensor from Clark and Lyons in 1962 [3]. This sensor consisted of an enzymatic layer, glucose oxidase (Gox), immobilized over an oxygen electrode to monitor the consumption of glucose through variations in oxygen levels. The oxygen electrode comprised a platinum cathode and anode covered by a polyethylene membrane, based on previous work by Clark [71]. The membrane allows for a limited diffusion of oxygen (i.e. preventing depletion of O_2 in the sample) while measurement of oxygen levels due to reduction reactions at the cathode takes place. Additionally, the polyethylene serves a protective function as the surface of metal electrodes is often poisoned upon contact with fluid environments, particularly in biological media such as blood, known as "biofouling" [72]. The combination of the enzymatic Gox layer with this sensor fit the initial classical "biosensor" definition in which a molecular biological recognition unit, such as an enzyme, antibody, etc., is used in combination with a transducing element in order to obtain information about a particular analyte. Currently, this definition is often expanded to include sensors which do not incorporate this type of recognition element, however are operated in biological samples to obtain information about the chemical makeup of the sample, for example the Clark oxygen electrode itself when utilized for detection of biological oxygen levels, as well as microvoltammetric methods for electrochemical detection small or electroactive molecules, such as catecholamines, or non-enzymatic, fluorescence-based ion selective sensors [73, 74]. The latter definition will be taken here when the term biosensor is applied. Since the time of the Clark sensor a great deal of progress has been made in this area, including the development of a broad range of measurement and sensing techniques as well as a wide variety of technologies and materials. As the main topics of this work involve pH and NO sensors, this chapter will focus on the history and theory of these analytes, as well as an overview of pertinent biochemical sensing possibilities.

3.1 pH Value

The pH value, or more accurately the activity of hydronium ions, is an important parameter relevant to numerous biochemical processes and one which must be tightly regulated within living organisms. Slight deviation from the typical blood pH value of 7.35-7.45 signifies a problem with acid-base homeostasis and may indicate a respiratory or metabolic deficiency [75]. Here, a brief history of the pH value, the associated theory and the relevance to biological applications will be covered. Much of the theory in the following sections is based on *General chemistry* by Ebbing and Gammon and *Prentice Hall Chemistry* by Wibraham, et al. [76].

3.1.1 pH Value - History

pH measurement has a broad range of applications and corresponding performance requirements depending on the field of application. A few examples of fields in which the pH value is relevant include medicine, pharmacy, biology, chemistry, agriculture, food science, environmental science, oceanography, and water treatment [72, 77, 78, 79, 80, 81, 82, 83, 84, 85]. The practice of pH related measurement dates back to the 16th century where violet extract was used by alchemists as an acid indicator. The mid-18th century brought about the first documented use of a chemical indicator as Gabriel Venel made use of this extract in titration experiments to determine the alkalinity of water [86]. This colored indicator technique is similar to the pH laboratory strips currently used for approximate pH determination. However, nearly a century and a half passed before notable advances were made in the study of the pH value through electrometric measurement of the hydrogen ion concentration by some of the "founding fathers" of this field: Hoff, Arrhenius, Ostwald and Nernst [84, 85]. At this time the work of Arrhenius on the ionization of salts, acids and bases in water by assessment of the conductivity in dilute solutions inspired Ostwald to develop the measurement of hydrogen ion concentration using the hydrogen gas electrode, which would later provide the thermodynamic electrochemical reference point for all other electrode potentials [87]. Utilizing experimental work on this hydrogen electrode, the osmotic pressure theory of Hoff, and the ionic theory of Arrhenius, Walther Nernst, a student of Ostwald, derived the theoretical relationship between ionic concentration and electrode potential [88, 89].

Shortly following the experimental work of Henderson, et al. in the early 1900s regarding physiological acid-base equilibria and the mechanism of its adjustment, specification of the "pH" concept was presented by Søren Sørensen in 1909 [79, 80, 90]. The concept of ionic activity evolved in subsequent years as a more accurate replacement for ionic concentration [91]. Although this represents an important advancement in understanding of the electromotive force in chemical cells, it also created confusion concerning the terminology and straightforward comprehension of the pH value [92]. As the general understanding progressed in the two decades after the formulation of the pH value, differing techniques involving its electrometric measurement also arose. These typically involved utilizing a platinum electrode, hydrogen gas and a reference electrode within systems of various complexities [93, 94, 95]. During this development period Hasselbalch also made the first accurate blood pH measurements employing his work on the Hendersen-Hasselbalch equation and the bicarbonate buffer system [96, 97]. This was achieved in spite of the complicated and/or unstable measurement methods present during this time period, particularly in the case of blood which requires special attention for the gases present in solution [84, 85]. Some years later, in 1930, an exceptionally stable pH measurement design was first attained when Andrew Beckman introduced the glass electrode (fig 3.1a) [98]. Since this time many systems have evolved, continually making more accurate measurement as well as less demanding and/or inexpensive approaches possible. The combination glass electrode is an example of this development, whose clear advantage, based on size alone, may be observed in figure 3.1b [99]. This has enabled simple pH quantification for application in food industry as well as sophisticated solutions for electrophysiology and bio-chemical purposes as will be further discussed in the following sections.

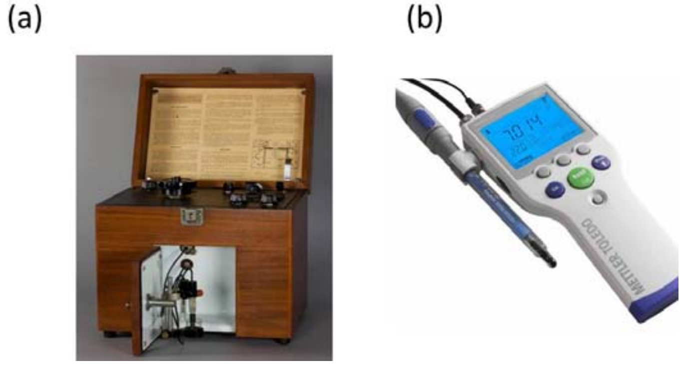

Figure 3.1: Examples of pH measurement systems: a) the first glass pH electrode introduced by Andrew Beckman in 1930 and b) an example of a typical present-day handheld Toledo® pH meter [99]

3.1.2 pH Value - Theory

Generally speaking, the pH value is a measure of the concentration, or more precisely the activity, of hydronium ions [H_3O^+] in a solution. This is directly related to the definition of acids and bases and the calculation of their strength. Looking first at how an acid or base is described, one finds three common definitions: the Arrhenius, the Brønsted-Lowry, and the Lewis definition. The first is based on the demonstration by Arrhenius showing the dissociation of acids, bases or salts to create an electrolyte solution with mobile ions and therefore an ionic current. The resulting general equation of Arrhenius for the dissociation of acids and bases in solution is as follows:

$$HA + H_2O \rightleftharpoons H_3O^+ + A^- \tag{3.1}$$

$$B + H_2O \rightleftharpoons BH^+ + OH^- \tag{3.2}$$

with neutralization of one or the other taking place through the production of water:

$$H_3O^+_{(aq)} + OH^-_{(aq)} \rightleftharpoons 2H_2O_{(l)}. \tag{3.3}$$

This theory is limited however, due to the explicit designation of an aqueous solution in which the H_3O^+ or OH^- ions are of interest. A generalization which accounts for solvents other than water, or the absence of a solvent altogether, is the Brønsted–Lowry Theory of acids and bases. This states that an acid and base react to form their conjugated base and acid, respectively, by proton transfer. Using the above notation this may be written as:

$$HA + B \rightleftharpoons A^- + HB^+ \tag{3.4}$$

This theory does not involve the constraint of dissociation of an acid to give hydronium ions or a base to yield hydroxyl ions, and it additionally accounts for amphoteric substances, which are molecules or ions that may react as either an acid or base. Water is the most obvious example of these, as may be observed above in equation 3.3. The Lewis Theory further generalizes by defining an acid to be an electron pair acceptor while a base is an electron pair donor. This definition makes it possible to take into account reactions in which no hydrogen ions are present. Ultimately, however, the Brønsted–Lowry Theory is the most widely accepted theory and will also be employed here.

Once the general acid/base definition has been given, details regarding these substances, such as how strong or weak the acid or base is, may be discussed. A strong acid or base defined as one which completely dissociates in solution. The dissociation constant is used to quantify this strength, which is written as follows for an acid or base, respectively:

$$K_a = \frac{\alpha_{H_3O^+}\alpha_{A^-}}{\alpha_{HA}\alpha_{H_2O}},\ K_b = \frac{\alpha_{BH^+}\alpha_{OH^-}}{\alpha_B\alpha_{H_2O}} \tag{3.5}$$

with the ionic activity α which may be defined by:

$$\alpha_i = f_i c_i, \tag{3.6}$$

where *f* is the dimensionless activity coefficient and *c* the ion concentration. As the activity coefficient tends towards unity at low ionic concentrations, the ionic activity is often simply replaced by the concentration; in the case of the hydronium ion the resulting notation would be $[H_3O^+]$. In addition, the hydrogen ion H^+ is often substituted for H_3O^+ in literature for simplicity, although it only exists in the hydrated form and therefore the correct form is in fact the hydronium ion. As this substitution is standard and the interionic interaction is negligible, H^+ will also be the adopted notation here and should be interpreted as interchangeable with H_3O^+. Taking these substitutions into account, along with the further assumption that the activity of H_2O at low ionic strength can be approximated to 1, the resulting acid and base dissociation constants are

$$K_a = \frac{[H^+][A^-]}{[HA]},\ K_b = \frac{[BH^+][OH^-]}{[B]}. \tag{3.7}$$

These may be related through the dissociation constant of water:

$$K_w = [H^+][OH^-], \tag{3.8}$$

which is equal to 1.0 x 10^{-14} at 25° C. The concentrations here use the definition of molarity, M, which is defined by mol/L. As the values resulting from the calculations of the dissociation constants may traverse several orders of magnitude, the logarithmic scale is employed to make the relationship between various substances more convenient. This is calculated by:

$$pK_a = \ log_{10} \frac{[HA]}{[H^+][A^-]}. \tag{3.9}$$

This formulation is particularly well known in regard to the description of the activity of hydrogen ions, commonly known as the pH value. The precise definition of this quantity is the negative logarithm of this activity of H^+ ions, which may be simplified in the same way as the previous constants to give

$$pH = \ -log_{10}[H^+]. \tag{3.10}$$

This value is a measure of the acidity or alkalinity of a solution with lower values representing more acidic and higher values more alkaline solutions. This value typically spans a range of 0 to 14, as may be seen in figure 3.2 for various common and biologically relevant substances. Negative values or greater than 14 are also possible, however outside of the pH 2-12 range special measurement preparation is necessary to obtain correct results.

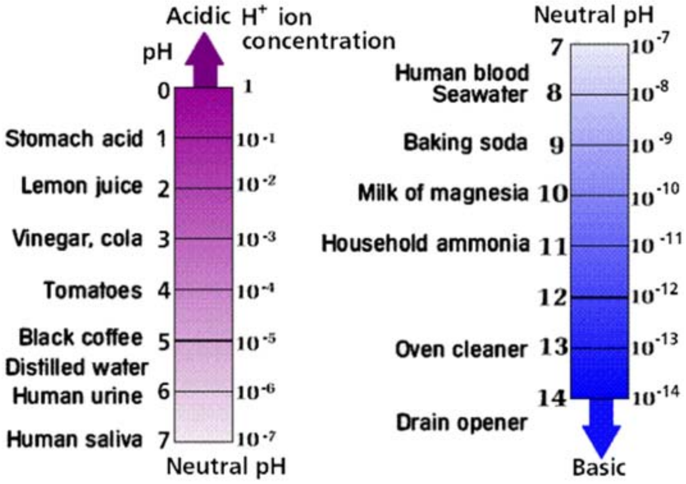

Figure 3.2: pH values of various familiar items [100]

The pH value along with the concept of dissociation and conjugated acids/bases become especially important for buffer solutions. These are made up of a weak acid and its conjugate base or a weak base and its conjugate acid. The purpose of buffer solutions is to resist change in pH upon addition of another solution or dilution of the original sample. pH buffer solutions are therefore particularly important for biological research where the pH level must be maintained within a narrow range to allow proper function in organisms. Most laboratory experiments for biologically relevant measurement employ phosphate buffer solutions (PBS) in order to sustain a constant pH value, as is the case throughout this work.

3.1.3 pH Value - Measurement

As a result of the wide range of fields requiring pH measurement, a wide variety of pH sensors are currently available. A representation of the various sensing methods and the abundant assortment of sensor classes within these methods is shown in figure 3.3. The electrochemical methods, particularly those based on the glass electrode and ISFETs, will be of particular interest here.

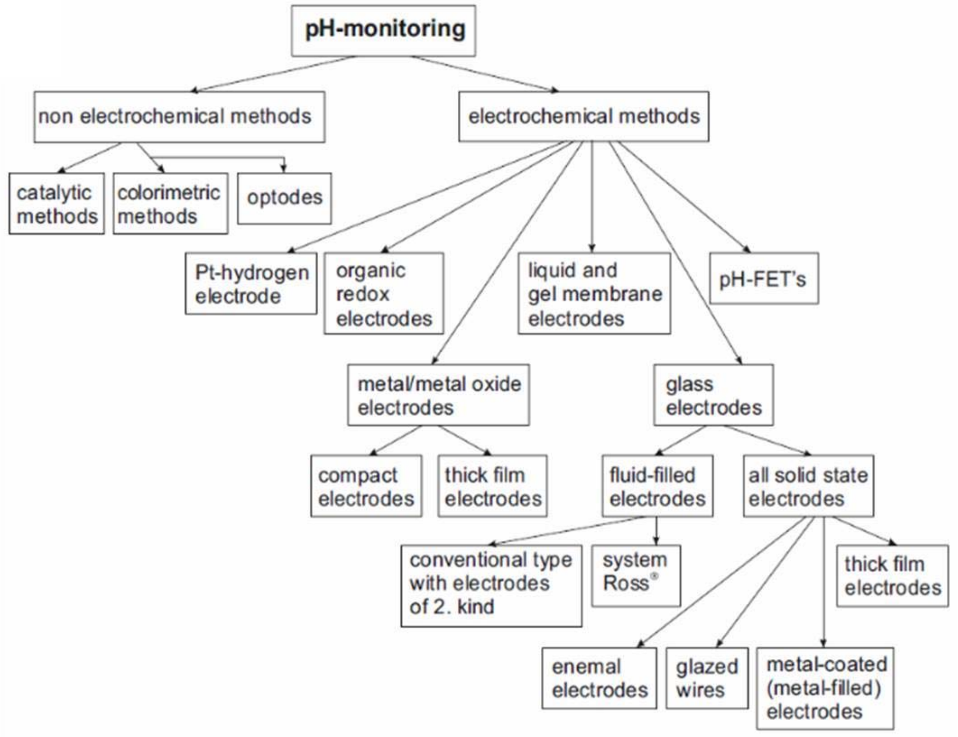

Figure 3.3: Methods for pH monitoring [101]

The glass electrode alternative was the first published pH sensor, a potentiometric sensing device demonstrated by Haber and Klemensiewicz in 1909 [102]. An example schematic for a modern pH sensitive glass electrode, based on this initial work, is shown in figure 3.4. This includes a glass bulb at the bottom, which is the H^+ sensitive element, a reference system making use of buffered filling solutions, stable electrode materials, and junctions between the various phases of the measurement cell in order to complete the electrochemical circuit. This type of electrode may vary in respect to the material used, the type of inner electrolyte employed, and the size or shape of the electrode and the junctions between phases. These variations make adaption to the environment in which the desired measurement will take place possible, allowing for analysis, for example, in highly basic or acidic conditions, extreme temperature environments or precise measurement under biological conditions. An example of the shorthand galvanic cell notation describing this entire electrochemical cell may be simply written as follows

Reference electrode|Reference Solution|Test Solution||Filling Solution|Reference electrode

which, for the commonly utilized silver/silver chloride (Ag/AgCl) reference electrode, would be as follows

$$Ag(s)|AgCl(s)|KCl(aq), H^+|glass|H^+(test\ solution)||KCl(aq)|AgCl(s)|Ag(s)$$

with phase interfaces represented by vertical lines and commas; this notation will be further described in the following section [103].

In this example KCl is utilized as the reference solution, typically buffered to pH 7, on the inside of the H^+ sensitive glass bulb, as well as the reference solution labeled 6 in figure 3.4. Although KCl is the most common filling solution, other solutions may also be used, containing ions corresponding to the given electrode material. The choice of electrolyte is determined in an attempt to reduce liquid junction potentials or contamination at interfaces where some ion/electrolyte flow into the test solution is necessary, as well as to avoid interference from other ions [104, 105].

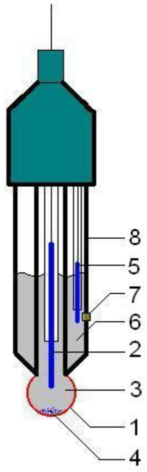

Figure 3.4: Typical Glass pH Electrode [106]

The ISFET may be employed in a similar approach; however the transistor is used in place of the glass bulb, incorporating an H^+ sensitive layer at the gate of the device. The principles of electrochemistry necessary to completely understand the mechanism by which this system functions will be presented in the following section followed by a detailed discussion of the pH sensor working principle, along with other various biosensors in section 3.4.

3.2 Electrochemical Cells

Having presented some of the fundamental concepts related to ions, electrolytes and the determination of pH it is now fitting to move onto electrochemical properties which are relevant to this work. These involve the chemical and electrochemical potential, the dependence of the energy within the system on these and the correlations which may be applied to the electrodes and ISFETs utilized here. The concepts and relationships provided here correspond for the most part to those demonstrated in Allen Bard's *Electrochemical Methods Fundamentals and Applications*, in *Electrochemical Systems* by Newman and Thomas-Alyea and by Sergio Trasatti in *The Absolute Electrode Potential: An Explanatory Note* [103, 107, 108].

The electrochemical potential of a system depends on temperature, pressure, composition and electrical state. In some instances, such as in the case of electrostatics, the chemical interactions of a system may be ignored and the "idealized electrical potential" is then described. This is accordingly employed as an ideal limit of the electrochemical potential. Although this is useful for some calculations or approximations, in many instances both the chemical and electrical interactions of a system are important. This includes the interface of two phases of differing chemical composition, at which the factors affecting the charge transport at the phase boundary are of interest. In an electrochemical cell this often consists of the electrode/electrolyte interface such as that in the example shown in the following section in figure 3.4. This type of a single interface is the simplest case to hypothetically examine when considering the potential difference of two phases of differing chemical composition. In actuality at least two interfaces are required to construct a complete electrochemical cell which can be measured. For the initial consideration of the electrode/electrolyte interface, however, the more straightforward single interface as two various phases are brought into contact with one another will be considered.

3.2.1 Electrochemistry - Theory

In order to understand the fundamentals of processes within an electrochemical cell, it is beneficial to begin with the Gibbs free energy of the system. This is a thermodynamic quantity which combines entropy (S) and enthalpy (H) and depending on the sign indicates whether the give reaction occurs spontaneously ($\Delta G < 0$) or requires energy to be given to the system ($\Delta G > 0$). At temperature T this is given by

$$\Delta G = \Delta H - T\Delta S. \tag{3.11}$$

This free energy may also be defined at constant temperature and pressure as

$$\Delta G = -nFE \tag{3.12}$$

where *n* is the number of moles of electrons, *F* is Faraday's constant. *E* is the potential between electrodes or *half-cells*; also termed the electromotive force (emf). This free energy relationship describes the electrical energy of an electrochemical cell where charge is transferred through redox reactions. When taking this type of system into consideration, the spontaneous (negative) instance corresponds to a galvanic cell in which chemical free energy is converted into electrical energy, which may be measured as a potential with proper electrical connections within the cell. The non-spontaneous case, on the other hand, represents the electrolytic case, in which a potential must be applied to introduce electrical energy into the system, thus providing the driving force for chemical reactions, i.e. the change in the free chemical energy.

A further generalization, involving the formulation which relates the Gibb's free energy to the reaction quotient (Q) or equilibrium constant (K) of the species involved in the chemical reactions within the cell, is as follows

$$\Delta G = \Delta G^0 + RTlnQ \tag{3.13}$$

where R is the universal gas constant and ΔG^0 is the standard-state free energy. The standard state case infers a concentration of 1 M, a pressure of 1 atm for any gases involved and a temperature of 298K. The reaction quotient for a generalized process

$$aA + bB \rightleftharpoons \mathrm{cC} + \mathrm{dD} \tag{3.14}$$

is given by

$$Q = \frac{[C]^c[D]^d}{[A]^a[B]^b}, \tag{3.15}$$

where x is the stoichiometric constant for species X.

As Q → K the reaction reaches equilibrium and the equilibrium constant may be then be calculated by

$$K_{eq} = \frac{[C]_{eq}^c[D]_{eq}^d}{[A]_{eq}^a[B]_{eq}^b}. \tag{3.16}$$

As previously discussed, it is more accurate to describe the activities of the species within the system, in which case the concentration of X, [X] is replaced by the activity represented with curly brackets by {X}. Utilizing these thermodynamic relationships, the Nernst equation may be obtained through the combination of equations 3.12 and 3.13

$$E = E^0 + \frac{RT}{nF}\ln Q. \tag{3.17}$$

This relates the electrochemical cell potential to its standard emf, E^0, and arises from chemical thermodynamics of equilibrium. The calculation or quantification of the cell potential at various concentrations may be carried out through the use of this relationship. For a temperature of 298

K and *n* = *1* the well-known Nernstian potential of 59.16 mV is found, which represents the theoretical thermodynamic limit for a given reaction within the cell or for the ion-flux of a specific ion across a membrane.

The Nernst equation may also be analogously derived from the thermodynamic measure of the chemical potential or partial molar free energy, $\bar{\mu}$, which can be described as the difference between energy barriers for reduction and oxidation at an electrode in an electrochemical cell. The traditionally accepted chemical potential is governed by the concentration of the potential determining ion (RTln[X]). When two mixed phases or two volumes of varying concentration separated by a barrier are brought together, chemical reactions or the spontaneous flow of the ions takes place until the chemical potential of the components are in equilibrium

$$\mu_I^x = \mu_{II}^x. \qquad 3.18$$

For an electrode submerged into a solution containing its own ions the resulting possibilities are demonstrated in figure 3.5. Depending on the relation of the chemical potential of the metal ion in solution, $\mu_{Me^{Z+}(aq)}$, to its potential as a solid, $\mu_{Me^{Z+}(s)}$, the tendency for ions to leave the surface of the electrode and go into solution or to leave the solution and join the metal electrode will vary. Figure 3.5a demonstrates the case for $\mu_{Me^{Z+}(s)} > \mu_{Me^{Z+}(aq)}$ in which metal ions spontaneously go into the solution leaving behind a net negative charge consisting of a thin layer of electrons at the surface of the electrode. The reaction for this process is written as

$$Me^{Z+}{}_{(aq)} + Ze^- \rightleftharpoons Me_{(s)} \qquad 3.19$$

and the corresponding shorthand notation representing the interface for this interface is

$$Me|Me^{Z+}(c) \qquad 3.20$$

in which the vertical line is used to represent a phase boundary and *c* specifies the concentration of the ion. Other symbols used for notation in electrochemical cells, which are not yet used in this simple example, include: a comma separating two components in the same phase, and a double slash which represents a phase boundary whose potential is regarded as a negligible component of the overall cell potential. These symbols may be seen, however, in the notation describing the glass pH electrode previously shown in figure 3.4. When the rate of ions leaving the surface is equal to that of ions rejoining dynamic equilibrium is reached and the resulting potential difference corresponds to E^0 from the thermodynamic relationships. For the case in which $\mu_{Me^{Z+}(s)} < \mu_{Me^{Z+}(aq)}$ the equilibrium potential polarity is simply reversed as the tendency for ions to rejoin the electrode exceeds the movement of ions away from the surface (fig 3.5b).

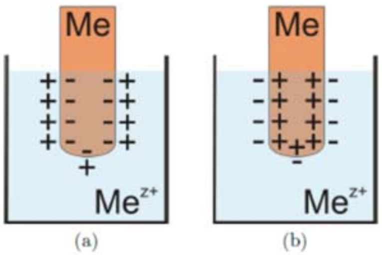

Figure 3.5: Development of potential difference at the electrode/electrolyte interface due to differing chemical potential of the metal ion in solution of in solid form along with the thermodynamic requirement for equilibrium [16]

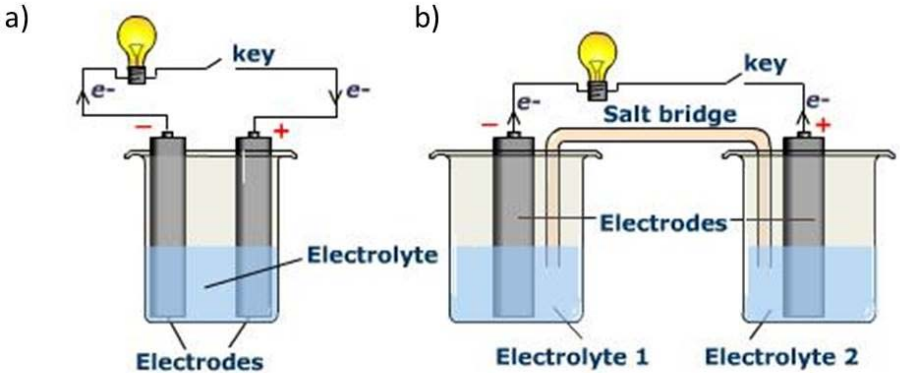

Figure 3.6: Examples of electrochemical cells using a) one electrolyte or b) two separate electrolyte solutions connected via a salt bridge permeable to ions [109]

The ensuing charged layer of the electrolyte which develops at the immediate electrode surface is referred to as the electrical double layer (EDL). Since this phenomenon affects the interface of devices such as those used in this work it will be discussed in more detail in the following section. The resulting potential at the phase boundary cannot be measured on its own and it is thus referred to as a *half-cell*, whereas the complete electrochemical cell consists of at least two such interfaces which may then be connected to complete the circuit. This may involve two electrodes submerged in the same electrolyte or two separate solutions connected by an ionic conductor such as salt bridge; both arrangements are represented in figure 3.6.

In this situation two half reactions are present and the overall cell potential or thermodynamic electrochemical potential is dependent on all interfaces present in the system. The electrode at which oxidation takes place is the anode of the system and reduction occurs at the cathode. The potential difference which may be measured between these electrodes is the emf of the cell. Under standard conditions (P = 1atm, c = 1 M, T = 298K) the standard cell potential which results at equilibrium is obtained.

3.2.2 Electrochemistry – Electrode Interactions

Two types of processes occur at the electrodes in electrochemical systems; the first are *faradaic processes* which receive their name as they are governed by Faraday's Law, relating the amount of electric charge (*Q*) transferred at an electrode to the mass transfer due to the chemical process taking place. Specifically, this states that, for a one-electron reaction, 1 mol of product/reactant are produced/consumed for 96485.4 C of charge passed, with 1 C equivalent to 6.24 x 10^{18} electrons. When quantifying results of such charge transfer processes at an electrode a current-potential plot (*i vs. E*) is often used, providing useful information regarding the system, electrolyte and interfaces of the varying phases.

The second type of electrode interface interaction involves the electric double layer (EDL), which is made up of an array of charged species and oriented dipoles existing at the metal-solution interface which develops when no transfer of electrons occurs at the electrode. This has been shown to behave like a capacitor as two charged layers arise and result in capacitive current, i.e. non-faradaic, effects at the electrode surface. The resulting charged planes are depicted in figure 3.7, typically termed the inner/outer Helmholtz planes (IHP/OHP) after Helmholtz who, in the 1850s, was the first to realize that this process takes place. His analysis of the EDL, however, failed to take into account effects due to diffusion, mixing, adsorption at the electrode surface and dipole interactions. In order to consider these influences, additional models were developed by Gouy-Chapman and later by Stern. These aid in the description of the capacitive dependence of the EDL on applied potential, despite the irrelevance of potential for typical capacitors. The resulting most accurate model of the EDL involves a charge density at the electrode, σ^m ($\mu C/cm^2$), and several layers of ions/molecules which are involved in the balancing of this charge. The innermost layer (IHP) is said to be specifically adsorbed with a charge density σ^i and is made up of solvent molecules or ions whose distance from the electrode is defined by the radius of the molecule or ion. The OHP is made up of hydrated ions whose interaction with the electrode only entails long range electrostatic forces and is therefore for the most part independent of the chemical properties of the ion. The distance of the OHP from the electrode is defined by the radius of the ions with a sphere of solvation (fig 3.7a). This layer is said to be nonspecifically adsorbed and may be combined with the third region termed the diffuse or Gouy-Chapman layer. This extends into the electrolyte bulk and has a charge density σ^i. The charge density at the solution side of the double layer may then be given by

$$\sigma^S = \sigma^{IHP} + \sigma^{OHP} = -\sigma^M . \qquad 3.21$$

The ionic strength of the solution directly influences the thickness of the Gouy-Chapman as may be seen in the definition the Debye length λ_D for (monovalent) electrolytes or colloidal suspensions

$$\lambda_D = \sqrt{\frac{\varepsilon_0 \varepsilon_r k_B T}{2 N_A e^2 I}} \qquad 3.22$$

where the permittivity of free space and relative permittivity are given by ε_0 and ε_r, respectively, k_B is Boltzmann's constant, N_A is Avagadro's number and I is the ionic strength. The Debye length may range from less than 1 nm for solutions of high ionic strength (> 100 mM) to more than 10 nm for dilute solutions. In the latter case the effects due to the thickness of this layer must be taken into account, whereas for high ionic strength it can be neglected.

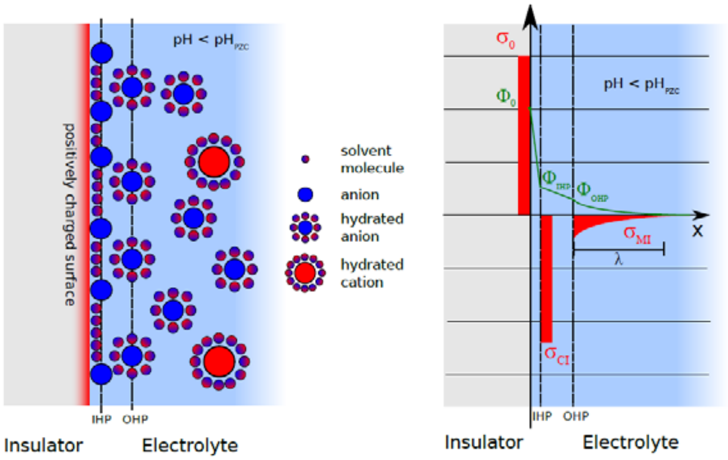

Figure 3.7: Depiction of the electric double layer for a positively charged electrode surface [15]

The importance of the EDL arises from the prospective electrode processes which may be affected by the potential drop across the IHP and diffuse layer. An electroactive species which is not specifically adsorbed may not come closer to the electrode than the OHP due to the specifically adsorbed molecules and ions. It is only possible, therefore, for this species to experience a potential Φ_{OHP} due to the potential drop of $\Phi^S - \Phi_{IHP}$ which exists across the adsorbed layer. The potential drop across the IHP and OHP into the diffuse layer is schematically illustrated in figure 3.7b.

The electrode interface reactions and effects upon these are particularly significant in sensing applications, especially for biochemical sensors in which the sensing mechanism is based on this electrode/electrolyte interface. In the following sections this topic will be further considered as it pertains to the developed sensor devices.

3.3 Nitric Oxide

Nitric oxide (NO) is an example of a significant messenger molecule, particularly interesting due to its conflicting yet crucial biological roles involving cytotoxicity and as an intercellular messenger [110]. This simple uncharged molecule has an unpaired electron in the outer antibonding π-orbital, making it a free radical. This characteristic, along with the short half-life of NO, contribute to the commonly believed concept that NO is highly reactive. This is, however, not always the case as will be discussed in the following sections along with its relevance to the fields of cardiovascular physiology, pharmacology, and neurology.

3.3.1 Background

Advantageous utilization of the effects of NO and nitrate/nitrite (NO_3^-/NO_2^-) production dates as far back as the meat curing techniques of the Romans, or perhaps even back to the time of the Sumerians [111, 112]. An observed reddening appearance due to the salting of meats during this time has now been attributed to formation of NO from nitrates and the consequent regulation of bacteria in the meat under anaerobic conditions follows. More recently, although also utilized for more than a century and a half, the therapeutic effects of nitrovasodilators such as nitroglycerin have been taken advantage of for human treatment of cardiovascular disorders. This medicinal effect was realized by Albert Nobel through the relief of angina pectoris symptoms from workers in his dynamite factory during the workweek [113]. Although such effects of NO have been exploited for many years it was only within the last decades that the biological importance of this molecule became apparent.

More than 30 years ago the accidental discovery of the endothelium-derived relaxing factor (EDRF) took place during studies involving vasoactive drugs in which preparation of rabbit thoracic aorta had varied [114]. In the involved experiments it became evident that the procedure for rabbit aorta preparation demonstrated relaxation due to muscarinic agonists such as acetylcholine (ACh) and carbachol where vasoconstriction was expected as had been observed in previous research. It was subsequently realized that the preparation in one case had involved a perfusion step which consisted of bubbles running over the intimal surface of the aorta and the endothelium layer had been unknowingly mechanically removed. When proper care was taken during preparation of the tissue, the initially expected (in 1953) relaxation of the aorta was demonstrated in addition to the fact that this vasodilation was endothelium-dependent; resulting in the term EDRF [115]. Following this discovery Furchgott also hypothesized, among other things, that the EDRF stimulates the soluble guanylate cyclase (sGC) of the vascular smooth muscle cell causing an increase in cyclic guanosine monophosphate (cGMP) This theory was based on a previous study demonstrating a relationship between cGMP increase and vascular relaxation [116, 117, 118, 119]. Shortly thereafter it was suggested by various groups in 1986 that the EDRF and NO are identical. Its function as the EDRF is indeed one of the main three functions carried out by NO, as was subsequently proven by three separate labs in the same year [17, 120, 121]. In addition to this role in the control of vascular tone and blood pressure, NO is also involved in the pathogenesis and control of infectious disease and tumors [122, 123] as well as performing intracellular messenger functions in neurotransmission [124, 125].

The discovery of NO as the first known gaseous mediator and its variety of biologically relevant functions, whereas previously this molecule was only known for environmental toxicity in pollution, led to it being named molecule of the year in 1992. Six years later in 1998 the Nobel

Prize was awarded to Robert F. Furchgott, PhD, Louis J. Ignarro, PhD, and Ferid Murad, MD, PhD for the discovery of NO and its signaling roles [126]. Presently, NO is known to be produced by L-arginine, that its production takes place in adventitial nerve fibers, neurons, epithelia and interstitial cells, in addition to the endothelium cell formation, and that it is one of three gaseous signaling molecules, the others being carbon monoxide (CO) and hydrogen sulfide (H_2S) [127]. All three of these gaseous molecules are recognized anti-inflammatories, vasodilators, and promoters of neovascular growth [128]. Through these effects NO plays an important part in cardiovascular disease and the regulation of thrombosis and platelet aggregation, however in other instances NO switches, as described by Schmidt [129], from "friend to foe." In this scenario a cytotoxic function is carried out as μM concentrations of NO are released, which may be beneficial when activated by macrophages in order to work against microbes, tumor cells or alloantigens within the immune system [130, 131, 132]. In other cases the high levels of NO make it the only molecule at physiological concentrations that can outcompete superoxide dismutase (SOD) for a diffusion limited reaction with superoxide ($O_2^{\cdot-}$), which is produced in large amounts by aerobic metabolism [133]. This reaction of superoxide with NO produces peroxynitrite, $ONOO^-$, which is thermodynamically stable (i.e. the reaction is irreversible) and capable of direct oxidative toxicity [134]. This indirect toxic effect of NO is also exhibited through other oxidative mediators, accounting for many of the toxin related mechanisms of NO in table 3.1, which gives an overview of the various roles of NO throughout the body.

Table 3.1: Messenger, immune system and toxic functions of NO [129]

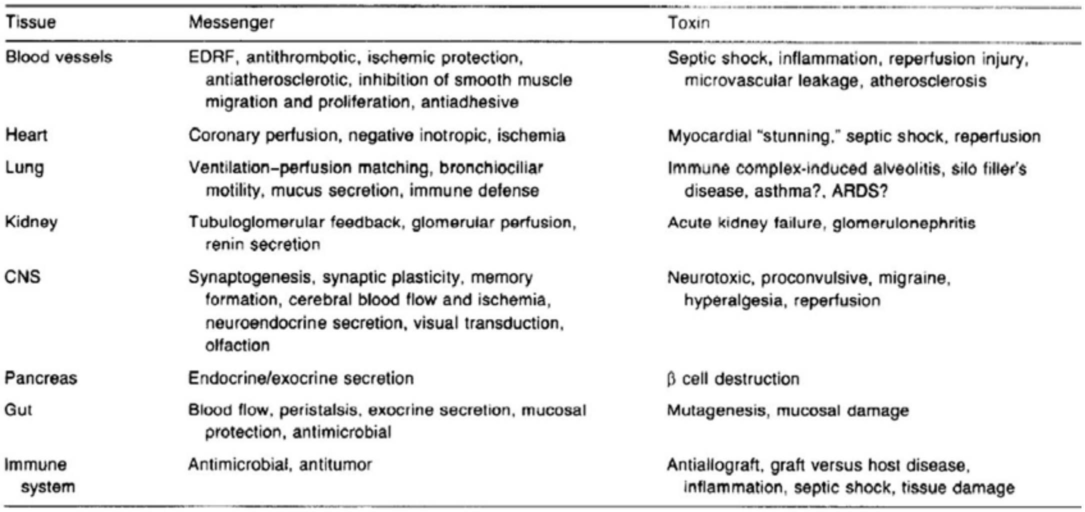

Tissue	Messenger	Toxin
Blood vessels	EDRF, antithrombotic, ischemic protection, antiatherosclerotic, inhibition of smooth muscle migration and proliferation, antiadhesive	Septic shock, inflammation, reperfusion injury, microvascular leakage, atherosclerosis
Heart	Coronary perfusion, negative inotropic, ischemia	Myocardial "stunning," septic shock, reperfusion
Lung	Ventilation–perfusion matching, bronchiociliar motility, mucus secretion, immune defense	Immune complex-induced alveolitis, silo filler's disease, asthma?, ARDS?
Kidney	Tubuloglomerular feedback, glomerular perfusion, renin secretion	Acute kidney failure, glomerulonephritis
CNS	Synaptogenesis, synaptic plasticity, memory formation, cerebral blood flow and ischemia, neuroendocrine secretion, visual transduction, olfaction	Neurotoxic, proconvulsive, migraine, hyperalgesia, reperfusion
Pancreas	Endocrine/exocrine secretion	β cell destruction
Gut	Blood flow, peristalsis, exocrine secretion, mucosal protection, antimicrobial	Mutagenesis, mucosal damage
Immune system	Antimicrobial, antitumor	Antiallograft, graft versus host disease, inflammation, septic shock, tissue damage

Since the discovery of the various biological roles of NO, many efforts have been made to model the diffusion versus reactivity of this molecule, to determine whether it acts in a paracrine or autocrine fashion and also to investigate its synthesis and the differing enzymes responsible for this production. The reports regarding diffusion related properties tend to refer back to the benchmark paper in 1993 by Malinski, et al. in which the concentration of NO at various locations was measured in reference to a single NO producing cell. Pertinent details on the production, diffusion characteristics and the biological importance of these are covered in the following section. Multiple reviews are also available, such as those from Bredt and Snyder [135], Nathan and Xie [131] and Moncada and Higgs [110], which provide a more comprehensive description of NO and its biological functions.

Synthesis

The production of NO typically takes place through the enzymatic conversion of L-arginine by NO synthase (NOS), which catalyzes the 5 electron oxidation of the guanidino nitrogen of arginine and molecular oxygen. NOS exists in three isoforms, all of which function through the stoichiometric conversion of the amino acid arginine to NO and citrulline (fig 3.8) [136].

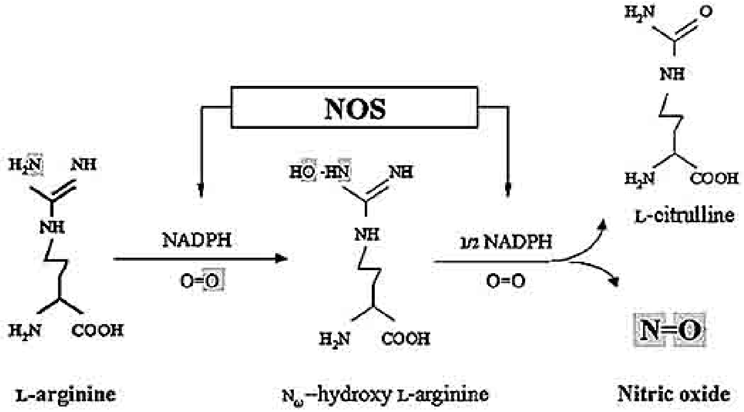

Figure 3.8: Production of NO and L-citrulline by NOS [136]

The isoforms are named in order of their cloning: neuronal NOS (nNOS, NOS1), inducible NOS (iNOS, NOS2) and endothelial NOS (eNOS, NOS3). In the case of nNOS and eNOS, the synthesis of NO is constitutive, cytosolic Ca^{2+}/calmodulin dependent and these synthases are therefore also labeled cNOS [131]. As the intracellular Ca^{2+} levels rise pM concentrations of NO are released over a period of several minutes. This takes place in the brain, for instance, in response to the binding of glutamate at the N-methyl-D-aspartate (NMDA) receptor, causing an influx of calcium ions (Ca^{2+}). These ions in turn bind to calmodulin, activating cNOS, in this instance nNOS, and resulting in the production of NO [137] (fig 3.9a). This often activates sGC to produce cGMP, as is the case in the cerebellum. It has been demonstrated, however, that localizations of sGC and NOS differ in other parts of the brain, indicating that NO most likely has other targets as well [137].

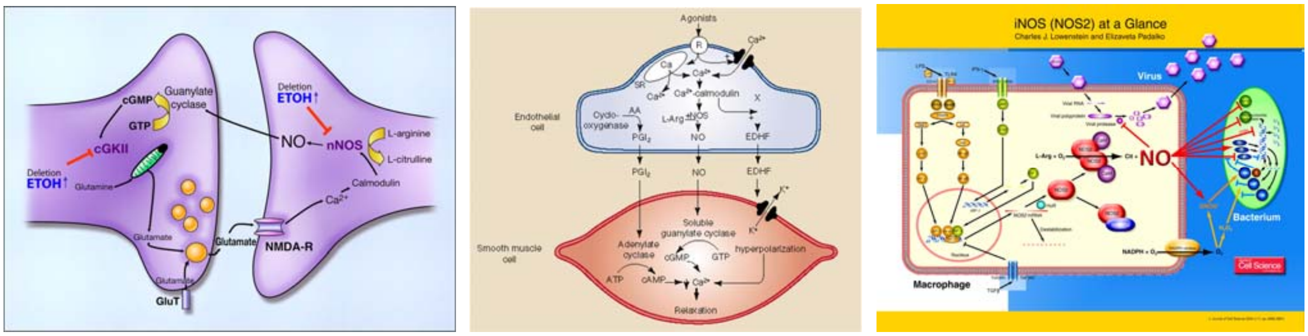

Figure 3.9: Isoforms of NOS and their corresponding functions [138, 139, 140]

Ca^{2+} inflow and subsequent binding to calmodulin is also responsible for the activation of eNOS, however for endothelial cells this is due to binding of, for example, ACh, thrombin or bradykinin at receptors. The resulting vasodilation effects are due to diffusion of produced NO which may then reach neighboring smooth muscle cells. This concerns the EDRF role of NO, which may also be carried out through other substances and processes, as is schematically portrayed in figure 3.9b, although NO is best characterized to date. It is currently believed that NO is one of three mediators, each of which predominates in various physiological circumstances. As shown in this illustration, the other two vasodilator substances are prostacyclin (PGI_2) and an endothelium dependent hyperpolarizing factor (EDHF), believed to be K^+ [138]. In addition to the EDRF function, the inhibition of platelet adhesion and aggregation are also carried out through the vasculatory regulation pathway of NO production.

The iNOS isoform is independent of Ca^+ levels due to constitutive interaction with calmodulin [141, 142] and is activated by immunological challenge resulting in NO production over a time period of multiple days. This process, depicted in figure 3.9c, occurs as a result of inflammatory stimuli such as endotoxin, interferon regulatory factor-1 (IRF-1) or nuclear factor κβ (NF-κβ), enabling tumoricidal and bacteriacidal functions of macrophages [137, 131, 142]. Cytokine activation of macrophages in mice and subsequent oxidative injury inflicted on tumor cells or fungi was demonstrated in 1990 by Hibbs, et al. [143]. This oxidative damage partially results from the reaction of NO with superoxide, giving rise to the production of the powerful oxidant peroxynitrite ($ONOO^-$). It has been shown that $ONOO^-$ can potentially oxidize and nitrate DNA and may cause single strand breaks through attack on the sugar-phosphate backbone [144]. Nitrous anhydride (N_2O_3) is another potential conversion product of NO, which may indirectly alkylate DNA after production of *N*-nitrosamines. A more direct cytotoxic role of NO has to do with the inactivation of iron-sulfur (Fe-S) centers of tumor cells or the binding to Fe-S proteins which are sensitive targets of NO. Cytotoxicity due to intracellular iron loss entailing the inhibition of various Fe-S enzymes, such as aconitase, a citric acid cycle enzyme, may also result from binding of NO [122, 130, 133]. These are only a few examples of how NO plays an important and versatile role within the immune system as a result of long-term production by the iNOS isoform. Numerous additional examples of the function of iNOS derived NO in immunological and pathological instances exist in addition to the suggested role of NO in various neurodegenerative diseases which exhibit oxidative stress, such as Parkinson's disease (PD), Huntington's disease (HD), Alzheimer's disease (AD), amyotrophic lateral sclerosis (ALS), multiple sclerosis (MS) and ischemia [145, 146, 147, 148].

Although the discussed NOS isoforms are responsible for the majority of NO production, in some specific cases the synthesis may be carried out through other methods. Enzymatic production may also take place through the xanthine oxidase pathway or H_2O_2 and L-arginine may create in NO via a non-enzymatic process [142, 149]. The reduction of nitrites to NO may also occur in acidic or reducing environments, which is the case, for example, during ischemic processes [150, 142].

Reactivity and diffusion characteristics

NO is often reported to have a short half-life of a few seconds, however this is in fact strongly dependent on its concentration and surroundings. As shown in table 3.2, for an oxygen dependent reaction (i.e. without a NO scavenger such as oxyhemoglobin present) this time varies from close to half of a second at concentrations approaching saturation (at room temperature) to more than half of a day at nM concentrations. The inversely proportional dependence of the half-life of NO on its concentration in water is as follows

$$t_{1/2} = \frac{ln2[NO]}{k_f} \tag{3.23}$$

with $k_f = 2x10^{-6} M^{-2} s^{-1}$. This is due to the requirement for two NO molecules to collide with one oxygen molecule in order to create NO_2 (a strong and toxic oxidant) through the following reaction

$$2NO + O_2 \rightarrow 2NO_2 \tag{3.24}$$

with a rate of formation dependence on the square of the NO concentration:

$$\frac{d[NO]}{dt} = 4k_3[O_2][NO]^2. \tag{3.25}$$

As physiological concentrations of NO range from a few nM (enough to activate sGC) to approximately 4μM (during cerebral ischemia), reaction with oxygen and production of cytotoxic NO_2 are not significant [133, 151, 152, 153]. The toxicity due to NO_2 has been often overestimated during in vitro testing where no drain for NO is provided. In vivo, however, the rapid diffusion of NO to nearby blood vessels results in a largely increased scavenging rate of NO through the destruction by oxyhemoglobin to produce nitrate (NO_3^-). This reaction along with the binding to and activation of sGC, an enzyme involved in vasodilation and the only known receptor for NO [154, 155, 156], and the reaction with superoxide ($O_2^{\cdot -}$) to form peroxynitrite ($ONOO^-$) make up the most important biologically relevant reactions of NO, all of which are represented in figure 3.10 [133, 157].

Table 3.2: NO half-life dependency on concentration in O_2 saturated fluid [133]

NO, μM	Half-Life, s
1,000	0.56
100	5.6
10	56
1	560
0.1	5,600
0.01	56,000

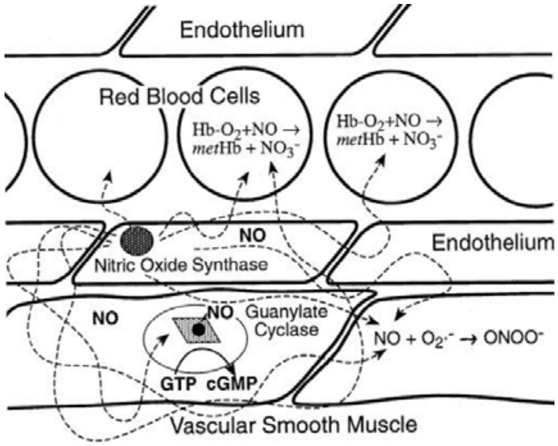

Figure 3.10: Principle biologically relevant reactions of nitric oxide [133]

In order to understand the effects of the various reactions, as well as the diffusion versus reactivity relationship of NO and how this is affected by the concentration at a point in space, Lancaster, et al. performed various experiments with rat hepatocytes in culture and have also written a thorough review in [158] on this subject. A main topic in this review is the uniqueness of NO due to the movement within biological systems based solely on free diffusion. This means that the probability for movement in all directions is the same, and therefore the net probability of movement of any one molecule of NO is zero. The Smoluchowski-Einstein equation may therefore be utilized here to describe the diffusion distance of the molecules,

$$\langle \Delta x \rangle^2 = 2Dt \tag{3.26}$$

where *t* is the elapsed time and *D* is the diffusion constant, which is inversely proportional to the molecular radius when neglecting dipole effects of nonelectrolytes such as NO. This implies that NO is not slowed by a surrounding solvent cage and electrostatic interactions when moving through solution. As NO is very small, one of the 10 smallest existing molecules, the resulting D is rather large, determined experimentally to be 3300 $\mu m^2/s$ under physiological conditions [152]. It is typically assumed that this value is spatially invariant since NO is uncharged and approximately 9 times more soluble in hydrophobic solvents than in aqueous solutions, indicating that restrictions on movement due to, for example, cell membranes do not pertain [159, 160]. This has also been confirmed experimentally showing that the diffusion constant is approximately the same in water as in biological systems (although small modeling modifications for heterogeneous diffusion effects due to bone or cartilage could be included for higher accuracy) [161]. Neglecting these minor influences, however, the concentration dependence on NO diffusion may be described utilizing Fick's second law of diffusion for a single production source as follows:

$$[NO]_x = [NO]_0 \, exp\left[\frac{(-\ln 2)(\Delta x)}{\sqrt{2Dt_{\frac{1}{2}}}}\right]. \tag{3.27}$$

As a result of the high diffusion constant, the spatial distribution function, known as the "diffusional spread," describing the NO concentration when multiple cells are producing NO and the diffusion paths overlap one another is of interest. This distribution depends not only on the magnitude of the diffusion constant of NO and the rate at which it is produced or at which it reacts with other oxygen species or cellular components, but also on the physical distance to and the reaction rate with scavengers which provide a "sink" for NO. Many of these reactions with scavengers, such as red blood cells due to the extremely fast reaction rate of NO with oxyhemoglobin to produce methemoglobin and nitrate, are limited only by the diffusion rate of NO to the scavenger [158]. It has been shown that NO may diffuse up to 300 μm, as may be seen in figure 3.11 which summarizes the diffusion distance through the root mean square (rms) net displacement of NO over its half-life.

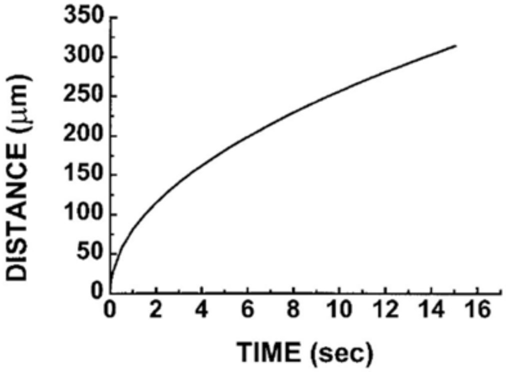

Figure 3.11: NO diffusion distance under physiological conditions [158]

This spatial correlation has been demonstrated experimentally and has been modelled to represent various numbers of NO-producing cells distributed homogeneously and non-homogeneously among non-NO-producing cells. Additionally, the effect of a NO sink at various diffusions distances from the producing cell has been taken into account [161]. In 1992 Malinski, et al., first experimentally demonstrated the effect of NO diffusion using a muscle cell 100μm away from the NO source, a single endothelial cell [151]. In addition, Schuman and Madison published on the spatial distribution in 1994 through NO-induced synaptic potentiation of paired neurons and synapses (approx. 100μm apart in hippocampal slices) [162]. Following in 1996 Leone, et al. made use of high transmission microscopy a high-sensitivity photon counting camera to demonstrate NO diffusion spread of up to 175μm [163]. The results from both of these following studies correlate well with the original study by Malinski, et al.

Due to this wide spread diffusion, the significance of the effects of NO scavengers, even at substantial distances from the producing cells must be considered. Lancaster, et al. have carried out thorough modelling efforts in an effort to understand how far NO may diffuse from the site of production and how the contribution of various NO producing cells affects the overall concentration at a certain point [161]. Additionally, complications due to drains for NO, such as scavenging by hemoglobin in neighboring lumen when production is carried out in endothelial cells, have been considered. An overview of the influence of hemoglobin at distances of a few up to 200 μm away from NO producing cells is given in figure 3.12 [158]. Here it may be seen directly that the effect of hemoglobin at physiological concentrations (~2mM) is substantial. In figure 3.12a-c the locations of NO-producing cells are indicated by upward arrows, while hemoglobin scavenging sites are designated by downward arrows. The hemoglobin concentration is indicated through various symbols shown at the right-hand side of each graph. In figure 3.12d the concentration profiles resulting from of a single site of NO production at the distance specified on the right in relation to a single scavenging site are presented [161].

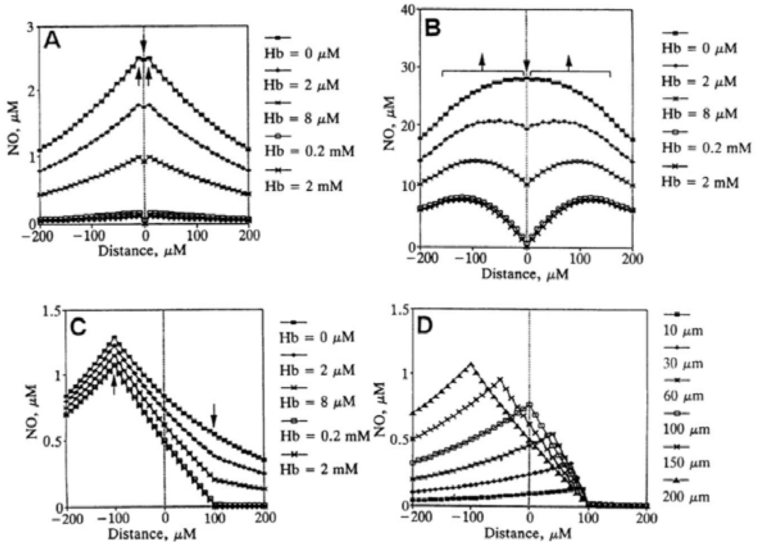

Figure 3.12: NO concentration profiles based on varying distances between NO-production and scavenging sites [161]

This modeling along with that of the diffusional spread of NO for various numbers of producing cells within a specific tissue volume has been used to speculate on whether NO acts in mainly a paracrine or autocrine fashion. The results of Lancaster, et al. have been examined in order to confirm correlation with experimental measurements [164]. It has been demonstrated that NO indeed works over a wide diffusion range and that the effects are much more related to the number of NO producing cells in a particular region than on where these cells are located within the tissue volume, i.e. primarily paracrine signaling function [158].

Research continues on these topics for NO production in various tissues; however advancement in sensors for *in vitro*/*in vivo* testing possibilities continues to be important in order to be able to answer many questions with more certainty. Such questions may involve, for example, differences in various NOS isoform production resulting in a quickly established raised steady state concentration of NO (iNOS) or “bursts” of NO production on the millisecond timescale due to Ca^{2+} fluctuations (eNOS, nNOS) [158]. More definitive information on the local benefit or potential toxicity of NO is also necessary in order to further pursue therapeutic and pharmacological applications of NO. The current status, accomplishments and limitation regarding sensors which could provide such information will be discussed in the following section.

3.3.2 Methods of Detection

Many reasons for the necessity and desire for improvement in NO detection have been mentioned. Due to the role NO plays in various physiological and pathophysiological processes, this aspiration for further sensor development is ongoing. The current most utilized possibilities for NO measurement include: chemiluminescence, entrapment by nitroso-compounds or reduced hemoglobin and subsequent detection through electron paramagnetic resonance (EPR), fluorescence, spectroscopy used to detect NO as it oxidizes reduced hemoglobin to methemoglobin and electrochemically active microelectrodes [152, 153, 165, 166, 167, 168]. As can be expected, each of these methods possesses inherent advantages and disadvantages. Many rely on secondary products such as nitrate, nitrite or NO-adducts. Additionally, complicated setups are necessary for many of the measurement techniques, making *in vivo* or even *in vitro* testing impossible. Electrochemical methods can provide an exception to these issues, however may lack in sensitivity or selectivity to NO.

The chemiluminescence procedure, which typically relies on the idea that NO reacts with ozone to generate light through the reaction

$$NO + O_3 \rightarrow NO_2 + O_2 + hv, \qquad 3.28$$

has been shown to be extremely sensitive (detection limit ~20-50 pM), however also very complex and requires the stripping of NO from the solution into the gas phase [169, 170, 166, 121, 171, 172]. This can be useful in some cases and allows for a very rapid time response, but is not useful for many biological applications and requires a great deal of equipment and a complex setup. Utilization of EPR also been demonstrated to provide a low detection limit (~1 nM). This is carried out following chemical entrapment of NO by nitroso-compounds or reduced hemoglobin to form a stable adduct. This adduct is then detectable via the formed triplet signal which can be characterized by its line width and hyperfine coupling constant [165, 173]. Due to hydrolysis, nitroso spin traps such as 2-methyl-2-nitrosopropane (MNP) and 3,5,-dibromo-4-nitrosobenzene (DBNBS) were shown to demonstrate a more specific detection of NO than the nitrones such as 5,5-dimethyb-pyrrobine-N-oxide (DMPO) [173, 174]. Hemoglobin has been demonstrated as a useful spin trap due to the easily detectable nitrosyl-hemoglobin (NO-Hb) by EPR as well as the commercial availability of Hb-agarose gels which may be used in quartz columns for EPR [175]. An advantage of EPR detection of NO-Hb over chemiluminescence is the ability to detect NO in blood, which has been exploited, for example, in experiments involving human forearm ischemia and venous blood of rats with endotoxic shock [175, 176, 177]. EPR equipment is, however, expensive and requires a great deal of skill/experience in comparison to the chemiluminescence technique.

A further spectroscopic method utilizing hemoglobin is based on the characteristic shift in the Soret absorbance peak due to the rapid oxidation of reduced hemoglobin (Fe^{2+}) to methemoglobin (Fe^{3+}) by NO by the following reaction

$$NO + Hb(Fe^{2+})O_2 \rightarrow \mathrm{Hb}(Fe^{3+}) + NO_3^-. \qquad 3.29$$

A shift from 433 nm to 406 nm may be observed, specific to the binding of NO as the oxidation to oxyhemoglobin by O_2 exhibits a different absorbance peak (416 nm) [165, 173 174]. Advantages of this method include the reported detection limit down to 1 nM and the wide availability of spectrometers. Utilization of this methemoglobin spectrophotometry assay method has been carried out via a dual wavelength, double-beam spectrophotometer with a flow-through cell to provide real-time biological analysis of endothelial cell NO production due to introduction of bradykinin [165, 120, 178]. Although a real-time solution is therefore feasible, disadvantages of this measurement technique lie in the possible interference of other nitrosyl groups present as well as complicated measurement equipment and setups [165].

Alterative attempted non-electrochemical NO detection techniques include the diazotization assay and mass spectroscopy. In the diazotization method an NO containing sample is added to 4N HCl. This is subsequently incubated for 10 minutes with a mixture of 2 N HC1 and sulfanilicacid (2 mg/ml). N-(1-naphthyl)ethylenediamine (1 mg/ml) is added and following a 30-minute period the absorbance at 548 nm is measured. Through comparison to a NO absorption/calibration curve the concentration of NO may be determined. A significant issue presents itself in the form of sample contamination, however, due to O_2 through the conversion of NO to NO_2^-, even in supposedly O_2-free gases [165]. This contamination in combination with the necessary time required and a higher detection limit of 0.1 – 1 μM have made this assay far less popular for NO detection. Mass spectroscopy, which was carried out following the entrapment of exhaled breath into a degassed aqueous solution of 15 nM thioproline, has also been relatively unsuccessful due to the equivalent possibility to make this measurement using chemiluminescence [179].

A wide variety of electrochemical NO sensors have been developed with measurement methods including constant potential amperometry (CPA), pulsed coulometry (PC), differential normal pulse amperometry (DNPA) and flow injection (FI). Amperometric microelectrodes have demonstrated detection limits as low as 10^{-20} M. The first well known electrochemical microprobe for NO detection was designed by Shibuki in 1990; consisting of a glass micro-pipette with a chloroprene rubber seal, a Teflon coated Pt wire in NaCl/HCl near this seal acting as the cathode and a silver wire counter electrode. The Teflon seal enhances selectivity by only allowing the passage of low molecular weight gases, the Pt wire is utilized as the working electrode and is held at 0.9 V vs the silver wire, which is grounded. At this potential a current is produced due to oxidation of NO at the Pt cathode, which is proportional to NO concentration. The reported linear range for this device is, however, quite small; approximately 1-3 μM [180, 181]. Nevertheless, Shibuki demonstrated measurement of NO release in rat cerebellar tissue with alleged nanomolar NO sensitivity and a rapid response time in the seconds range.

Since the time of the first electrochemical NO sensor several concepts have been investigated. Some examples of these include taking advantage of the fact that NO avidly binds to metals such as Fe, Cu, Co and Mn to form metal nitrosyl complexes by using an electropolymerized film of metal ethylenebis(salicylideneiminate) [(M(salen), M=Co, Fe, Cu and Mn] [157, 182]; utilizing hemoglobin immobilization onto TiO_2 or SnO_2 electrodes [183]; Nafion coated multi-walled carbon nanotube electrodes [184]; and an electroformed tetrasulfonated nickel phthalocyanine (NiTSPc) layer on carbon microelectrodes. Many of these techniques have demonstrated improvements in some form, however still suffer from high detection limits or limited application possibility *in vivo* or *in vitro*. One of the most promising electrochemical method to date remains that demonstrated by Malinski and Taha in 1992, involving electrochemical deposition of a thin polymeric porphyrin layer onto thermally sharpened carbon fibers suitable for measurement with single cells. The application of metalloporphyrins was based on previous work by the same group showing that they catalyze the oxidation of NO [185, 186]. The microelectrode is covered with a Nafion film which results in slightly a lower current response, however the selectivity against anions, such as NO_2^- or NO_3^-, which may significantly interfere in authentic NO detection is significantly increased. This sensor was successfully employed to measure NO production from a single cell following introduction of bradykinin to the system. This concept has also been made commercially available by world precision instruments (WPI) with their ISO-NO series including variations on the selective polymer film as well as modifications on the size and setup depending on the desired application.

As described, successful NO detection has been demonstrated though various methods, with differing characteristic advantages and disadvantages. The electrochemical-based microelectrode has exhibited the most elegant solution, especially for biological applications. The redox current generated by these electrodes is typically very small; however, on the order of physiologically relevant NO concentration changes [187]. This area for improvement, along with the potential of electrochemical techniques for biological *in vivo* or *in vitro* applications, make the combination of unique NO recognition with the inherent signal-amplification properties of transistors an ideal solution. This concept has been made use of here in order to develop a sensor array for pH and NO measurement. In the section 3.4 a brief background of biochemical sensing devices will be presented with particular attention given to the ISFET and related transistor based devices.

3.4 History of Biochemical Sensing

The focus in this section will be on the most successful device structures for bio-electrochemical measurement without complex read-out requirements: thin film transistors, ISFETs and ChemFETs. Particular attention will be paid to III-Nitride based systems and especially to the AlGaN/GaN heterostructure due to the superior chemical and biological properties, and the relevance to the developed sensors here.

3.4.1 Thin Film Sensors

A wide variety of devices for biochemical measurement and analysis are based on conductivity modulation upon variations in concentration changes or introduction of a specific chemical substance. The thin film sensor is one of the simplest approaches used to realize this type of device, with the working principle based on resistive changes within the chemically sensitive film due to variations of specific chemical substances within the sample. This variation results in an increase or decrease in the conductivity of the film, which can in turn be read out in a simple manner as a voltage or current. An example of this is shown in figure 3.13, in this case a tin oxide (SnO_2) sensor to detect hazardous gases such as H_2, CH_4, CO, H_2S or NO_x, the most popular and commercially successful of this device type [188, 189, 190].

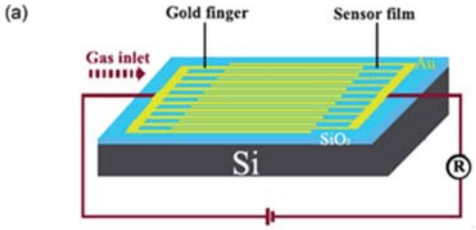

Figure 3.13: Thin film Pt-doped SnO_2 sensor for hazardous gases [188]

In this specific case the thin film consists of a platinum (Pt)-doped SnO_2 sensitive layer, deposited onto interdigitated gold contacts; all of which are based upon a standard Si/SiO_2 substrate. In general, the dopants used and the crystal structure of the films are very important in order to create sensitivity to specific analytes. In addition, the surface area of the sensitive film is obviously an important parameter through which sensitivity may be enhanced by the use of micro-/ or nano-structured films [189]. Since thin film sensors are based on surface interaction with a chemical species, the higher the surface area and the ratio of this with respect to the film volume, the more sensitive the device becomes. Conversely, with increasing film volume the overall change as a result of variation of the analyte will be too small to produce a significant enough change in the overall conductivity, resulting in low sensitivity.

Thin film sensors have been successfully implemented in temperature or strain gauges, as well as applications in which thin film technology is highly desired due to the small size and low power consumption [189]. The robust nature of several typically employed thin film materials, such as gallium oxide, has also made them attractive for applications such as monitoring automotive exhaust [191]. Thin films are also frequently utilized for biological sensors, however many times in a transistor format such as thin film transistors (TFTs) or in combination with FETs in order to benefit from amplification properties.

3.4.2 The Ion-Sensitive Field Effect Transistor and Related FETs

The idea of employing an ISFET for electrochemical sensing was presented by Bergveld in 1970 in a short communication [192] and followed by a full description of the concept in 1972 [193]. The initial application for which the ISFET was intended was in the realm of electrophysiological measurement, specifically for the recording of biological events such as action potentials [194]. This aim was based on the relatively small possible dimensions of ISFETs, along with the expected signal transduction possibilities and signal to noise ratio (SNR). Extracellular monitoring of activity from smooth muscle fibers of the guinea pig taenia coli as well as action potential recordings from the flexor tibialis of a Locust were indeed demonstrated utilizing the ISFET in 1972 and 1976, respectively [193, 195]. Although the legitimacy of some of these results has been questioned due to leaky passivation issues at the relatively high voltage bias that was used, the resulting measurements demonstrate the typical shape of monophasic neuro-active cell activity [4, 193, 195, 196]. Additionally, subsequent similar recordings from cardiomyocytes were presented by Steinhoff in 2005 with AlGaN/GaN based ISFETs as well as the successful demonstration of action potential recordings from cultured cerebral rat neurons with Si-based FETs by Offenhäuser, et al. in 1995 and 1997 [197, 198, 199].

Despite accomplishments regarding physiological recording, a particular difficulty regarding the commercial success of ISFETs has been present since the beginning of development which lies in the miniaturization of the reference electrode [4, 194, 196]. Substantial research has been carried out involving appropriate micro-reference systems, including the miniaturization of conventional Ag/AgCl electrodes, miniature liquid junction electrodes, and reference field effect transistors (REFETs) which are essentially ISFETs covered with a chemically insensitive film and operated in differential mode to remove drift light and temp sensitivity [200, 201, 202]. Significant progress has been made, even resulting in Si-technology compatible solutions such as a porous silicon layers (PSLs) over a micromachined cavity into which the reference solution may be loaded or an isotropically etched cavity through the entire wafer which allows for contact to the reference solution at both sides, while impeding efflux of the electrolyte into the sample solution due to the small pore opening and the use of a hydrogel [202]. These examples show the potential for possible micro-reference systems, however much advancement is still necessary in order to utilize these ideas in a commercial device. In general, the reduction of diffusion from the reference electrode solution to that of the sample, compatibility with standard semiconductor processing techniques and the lifetime or stability of attempted reference systems have prohibited most techniques from aiding in the miniaturization of the complete ISFET sensing device.

Although these reference electrode issues have hindered significant successful commercialization in many instances, the ISFET field has also experienced a great deal of success. Despite the declared uncertainty regarding initial physiological recording results, important verification has been presented in addition to a great deal of further progress concerning the understanding of the cleft interface between the cell and sensor surface and, as a result, the physical phenomena affecting or affected by this interface [193, 195]. Commercialization has also taken place, especially in disciplines in which the measurement conditions require higher stability then that offered by the standard glass pH meter. An assortment of related sensor structures has been developed over the past 35 years as well, which may be grouped into general categories; however there is some slight discrepancy which exists related to the terminology. This is attributable to competition between Bergveld, who originally published the idea of the ISFET and Janata, who claimed the first patent on these structures [192, 203]. In one case the ISFET and the related enzymatically selective field effect transistor (ENFET), ImmunoFET (IMFET), work-function field-effect transistor (WF-FET) and other related FETs are grouped into the general category referred to as chemically sensitive field-effect transistors (CHEMFETs) [4]. This term indicates the modulation of the measured signal by chemical species, which is certainly the case for all included devices. In the other classification of devices the ISFET is defined as a device in which the bare oxide is used at the interface with an electrolyte in order to measure modulation of the oxide/electrolyte interface potential, whereas the CHEMFET incorporates a membrane at this interface to achieve selectivity for specific chemical species. Although neither definition is technically incorrect, here the overall category of ISFETs will be used, encompassing the subgroup of CHEMFETs and thus the related devices also described by this classification.

3.4.2.1 Si-based ISFETs for pH Measurement

The ISFET is essentially a MOSFET with the gate contact replaced by solution and a reference electrode. This liquid/insulator interface, i.e. hydrated SiO_2 in the case of the initial ISFET based on silicon, allows for the measurement of the analyte concentration. A comparison between the typical Si-based MOSFET structure and that of the ISFET is demonstrated in figure 3.14.

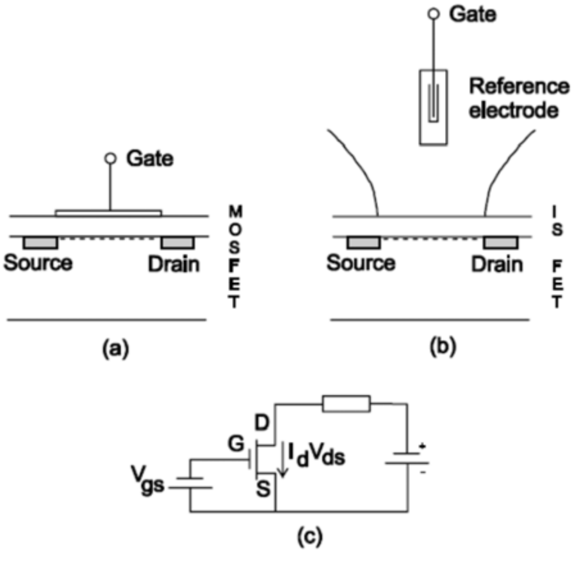

Figure 3.14: Comparison of a) MOSFET vs b) ISFET [194]

The similarities as well as the differences between the two structures become apparent upon observation of the visual structural comparison in figure 3.14a and b. Although the basic transistor structures are very similar, and even the equivalent electrical schematic diagram corresponds to both structures, there are significant issues, measurement demands and process difficulties which arise when working with the open gate structure. Due to the issue of stability in liquid, in particular for aggressive fluids such as biological media, encapsulation of the ISFET devices is an area of major importance. A portion of this work deals with the optimization of passivation materials and the non-destructive structuring process for this purpose; details concerning this are addressed in Chapter 5.

As the foundation for the theoretical ISFET operation is based on that of the MOSFET, the fundamentals and their relation to the solution-gated system will be discussed briefly, based mainly on the theory presented in *Physics of Semiconductors* by Sze as well as various literature sources which have dealt with the application of these concepts to the ISFET [204, 205, 206, 207]. The linear regime will be the point of interest in our case for the operation of the ISFET, thus the theoretical equations in this operation mode will primarily be considered. The general description of the drain current of the MOSFET, as well as the ISFET, in the non-saturation regime is as follows

$$I_d = C_{ox}\mu\frac{W}{L}\left(\left(V_{gs} - V_t\right)V_{ds} - \frac{1}{2}V_{ds}^2\right), \qquad 3.30$$

where C_{ox} is the oxide capacitance per unit area, W and L represent the channel width and length, respectively, and μ is the mobility of the charge carriers. The threshold voltage, V_t, of the MOSFET is defined as the gate to source voltage (V_{gs}) necessary to create a conducting channel between the source and drain contacts. The mobility, gate oxide capacitance and channel geometry parameters may be grouped into a term, β, the geometric sensitivity parameter

$$\beta = C_{ox}\mu\frac{W}{L}. \qquad 3.31$$

It becomes clear that, for the MOSFET, V_{gs} is the only variable input parameter when β is taken into consideration as a design parameter which remains constant, in addition to V_{ds} which is held constant by the applied electronic circuit. The value of V_t depends somewhat on fabrication processes, however these are under precise control, particularly for silicon semiconductor technologies, therefore making V_t constant as well [194]. Following the development of the ISFET, the determination of whether the additional input variable due to variations in the ion concentration of the electrolyte should be viewed as a modulation of V_t or V_{gs} was necessary. Various theories and models were presented to describe the interactions at the electrolyte/oxide interface, dealing with differences in the mechanism of pH sensitivity such as surface adsorption versus diffusion into the oxide creating a thin hydrated “gel” layer comparable to that of the glass electrode [206, 207, 208, 209]. Comparison with the glass electrode, and therefore the attempted correlation of a value such as the chemical potential of H^+ ions in the insulator, $\mu_{H^+}^{ox}$, originates from the initial use of SiO_2 as the gate insulator of the ISFET. An improved model was found, however, in the application of the site-dissociation model, proposed by Yates in 1974, to the ISFET by Siu and Cobbald as a colloid chemistry model of the oxide-aqueous electrolyte interface [210]. Verification of this treatment was given later by Bousse in a detailed description of the site-dissociation theory in combination with the Gouy-Chapmann theory of the EDL and the consequent application of these to the ISFET [207]. The response time of the sensors was taken into account along with the analysis of gate insulators which are not porous, i.e. Si_3N_4, in order to verify that the charging behavior of the metal oxide occurs at the surface and not through diffusion of H^+ into the oxide [207, 210]. Accurate definition of the surface potential and the modulation of this through the interaction with the potential determining (p.d.) ions was the main goal of the developed models for the ISFET. In these models for the initial ISFET the p.d. ions, and additionally the most often studied in the decades following, are H^+ and OH^- [211]. As the equilibrium between the AOH surface sites and the H^+ ions in solution takes place it is generally accepted that the following reactions are occurring

$$AOH \rightleftharpoons AO^- + H^+ \tag{3.32}$$

$$AOH_2^+ \rightleftharpoons \mathrm{AOH} + H^+. \tag{3.33}$$

The surface hydroxyl groups may therefore be neutral, protonated, or deprotonated, depending on the H^+ concentration and the equilibrium constants for the relevant dissociation reactions. This leads to a pH-dependent net surface charge and an additional voltage drop at the solid/liquid interface. In order to quantify the variations in this surface potential the equation for the MOSFET threshold voltage is taken into consideration

$$V_t = \frac{\Phi_{M-}\Phi_{Si}}{q} - \frac{Q_{ox}+Q_{ss}+Q_B}{C_{ox}} + 2\phi_f, \tag{3.34}$$

where Φ_M and Φ_{Si} correspond to the work functions of the metal and silicon, Q_{ox}, Q_{ss} and Q_B are the accumulated charge in the oxide and at the oxide-silicon interface and the depletion charge of the silicon, respectively, and the final term, $2\phi_f$, deals with the amount of doping in the silicon bulk and the consequent onset of inversion at the channel. As stated, this is dependent on fabrication processes as all involved terms are physical parameters [194]. In order to apply this to the ISFET two additional terms must be added to incorporate the effects of the reference electrode and the oxide/electrolyte interface

$$V_t = E_{ref} - \Psi + \chi^{sol} - \frac{\Phi_{Si}}{q} - \frac{Q_{ox}+Q_{ss}+Q_B}{C_{ox}} + 2\phi_f. \tag{3.35}$$

Here the potential of the reference electrode is given by E_{ref}, while $\Psi + \chi^{sol}$ represents the interfacial surface potential. χ^{sol} is the surface dipole potential of the solvent and is therefore constant, whereas Ψ represents the chemical input parameter of the system and has been demonstrated to be pH dependent for gate materials which react in an amphoteric nature, as described for the AOH surface groups of many of the gate oxides/nitrides considered during ISFET research. Although pH sensitive, many of these gate materials demonstrate sub-Nernstian sensitivities and/or substantial dependence on the overall ionic concentration, in particular SiO_2 which also shows a large hysteresis in comparison to other materials [211]. Investigations aimed at explaining the inability to attain the theoretical Nernstian sensitivities of gate materials were carried out by Bousse, et al., resulting in a theory involving two additional terms in the definition of the input parameter [207]

$$\Psi = 2.3\frac{kT}{q}\frac{\beta}{\beta+1}\left(pH_{pzc} - pH\right). \tag{3.36}$$

These supplementary parameters are pH_{pzc}, the value of pH for which the surface is electrically neutral, and β, a parameter characterizing the sensitivity of the surface. β was shown to be only surface dependent at high ionic strengths where the capacitive double layer reduces to the Stern capacitance. As may be seen from equation 3.36 this sensitivity factor accounts for the deviation from theoretical Nernstian limits when the value of β is not large [194, 207]. In order to confirm modeling results, Van den Berg, et al. carried out an extensive study in 1985 based on the theoretical sensitivities of SiO_2, Si_3N_4, Al_2O_3 and Ta_2O_5 to ions, especially H^+ [211]. In this work the equilibrium of surface OH groups of the various materials with the activity of H^+ at the electrolyte/insulator interface is considered. The typical approximation of $[H^+]$ in place of the hydronium ion activity is employed and one utilized approach involves relating the surface hydroxyl groups to the bulk hydronium ion concentration, $[H^+]_B$, which is then related to the concentration directly at the surface, $[H^+]_S$, through the Nernst equation

$$[H^+]_S = [H^+]_B exp(-q\psi_0/kT) \tag{3.37}$$

where q is the elementary charge and k is the Boltzmann constant. This approach was further developed by van Hal resulting in an improved model and a clarification of the importance of

$[H^+]_S$ [209]. Here the dissociation constants for the equilibrium conditions of the surface OH sites are as follows

$$K_a = \frac{v_{AO^-}[H^+]_S}{v_{AOH}} \tag{3.38}$$

$$K_b = \frac{v_{AOH}[H^+]_S}{v_{AOH_2^+}} \tag{3.39}$$

where v_i represents the number of sites per unit area. Utilizing the difference in the number of surface sites carrying positive and negative charge the surface charge density, σ_0, may be defined. From this it may be derived that the variation in the number of charge carrying surface groups for a small change in the pH at the surface, pH_S, is the intrinsic buffering capacity

$$\frac{\partial \sigma_0}{\partial pH_S} = -q\beta_{int}. \tag{3.40}$$

The equal but opposite charge of the EDL may then be employed to relate the insulator/electrolyte potential to this intrinsic buffering capacity. The final result is a general expression for the sensitivity of the electrostatic potential to bulk pH variations

$$\frac{\partial \psi_0}{\partial pH_B} = -2.3\frac{kT}{q}\alpha \tag{3.41}$$

with the dimensionless sensitivity parameter

$$\alpha = \frac{1}{\left(\frac{2.3kTC_{dif}}{q^2\beta_{int}}\right)+1} \tag{3.42}$$

where C_{dif} is the differential capacitance, which can be described as the ability of the electrolyte to store charge in response to a change in the electrostatic potential. Additional details on the full derivation of these terms may be found in [103] and [206]. The value of α varies between 1 and 0 with the theoretical Nernstian limit attained at a value of 1. As may be observed in equation 3.42 this ideal response of $\alpha=1$ is only possible for gate insulator with a high surface buffering capacity value and a low double layer capacity [194]. Experiments were carried out with various typical ISFET gate materials demonstrating the highest surface buffering capacity for Ta_2O_5 as well as giving an explanation for the deviation from the previously expected Nernstian behavior (fig 3.15).

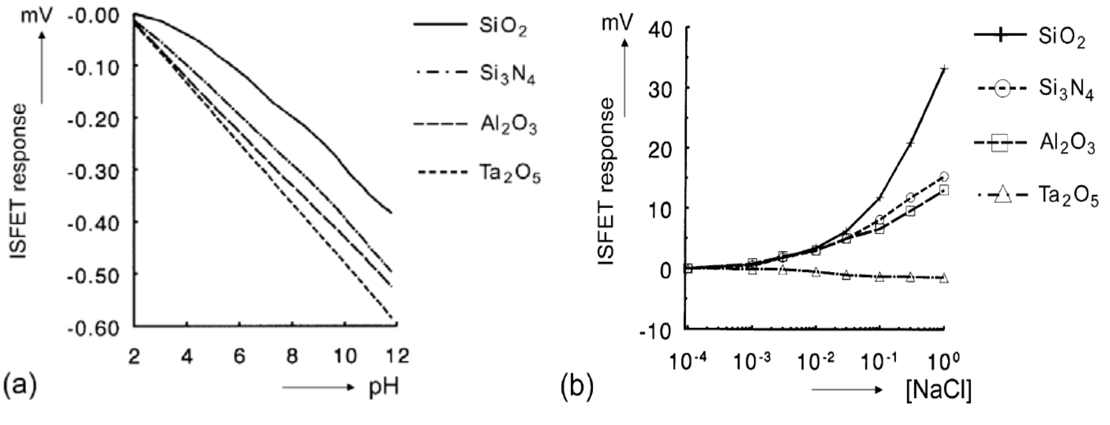

Figure 3.15: Response of various ISFET gate materials to (a) variation of pH in constant 0.1 M TABCl (b) variation of NaCl concertation at constant pH of 5.8 [194]

It is clear that the performance of SiO_2 is sub-Nernstian as well as varying a great deal with ionic concentration, while the very high surface buffering capacity of Ta_2O_5 may be recognized through observation of figure 3.15b where the response scarcely varies over the entire ionic concentration range.

The clear understanding of the variables affecting the mechanism by which the ISFET functions also made further improvement with related ChemFETs possible. Taking the importance of the surface buffering capacity into account development of various ion sensors could be better optimized by ensuring that materials which buffer the ion of interest are utilized, some of which will be discussed in Section 3.4.3. Beforehand, however, the deviation from Si-based ISFETs will be covered in terms of research involving ISFETs based on III-Nitride material systems.

3.4.2.2 GaN and AlGaN-based ISFETs for pH Measurement

Over the past 10-15 years ISFETs and related applications based on III-Nitride material systems have developed, particularly due to the interest in the advantageous material and chemical properties of these devices. Exploitation of the chemical stability is extremely attractive due to the challenging requirements for measurement in liquid environments while the optical transparent nature of these structures when grown on sapphire substrates is additionally very advantageous for biological applications where simultaneous monitoring of electronic and microscopic processes is critical [7, 197]. In 2003 the initial demonstration of an AlGaN/GaN based heterostructure for pH sensitive ISFETs was presented by Steinhoff, et al. [7]. In this case the 2DEG (described in Chapter 2) of transistor structures based on GaN:Si/GaN:Mg double layers and AlGaN/GaN heterostructures is utilized as the channel of the device, modulated by ion induced variations in the surface potential due to surface sites which are neutral, protonated or deprotonated, as described for the Si-ISFET [197]. In these preliminary studies of III-Nitride ISFETs the surface was analyzed in order to realize optimal sensitivity, taking into account the previous Si-ISFET studies on surface buffering capacity and effects of the double layer. As may be seen in figure 3.16a, in the initial report three variations on the GaN surface were fabricated and the interface potential change as a result of variation of the pH value was measured and compared. Two devices were measured as grown, while sample B was thermally oxidized prior to measurement [212].

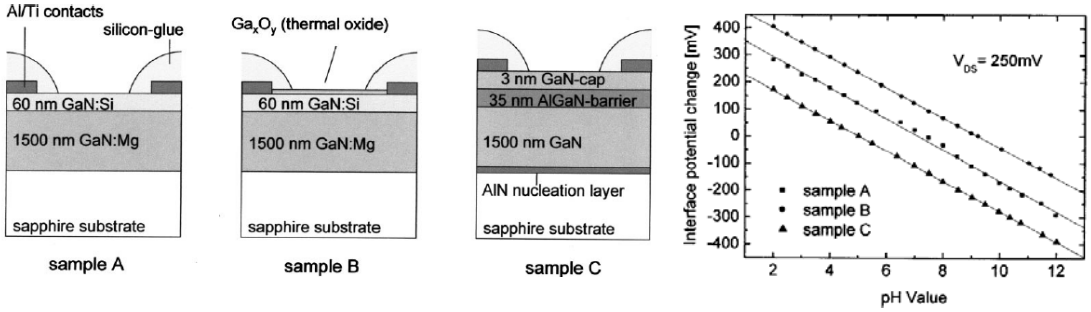

Figure 3.16: AlGaN/GaN based ISFET: a) Heterostructure variations and b) Comparison of the interface potential change vs pH variation - a constant offset value was introduced to facilitate comparison [212]

Due to the nearly identical sensitivities of all samples it may be concluded that the pH response is a surface effect. Additionally, it may be inferred that this surface effect occurs according to the site-binding model with sites on a Ga_xO_y surface layer resulting from a native oxide or from the thermally grown oxide. The mechanism by which the H^+ sensitivity is brought about is then analogous to that of the systematically studied metal oxide surfaces of Si-based ISFETs. Here the surface reactions take place as follows

$$GaOH \rightleftharpoons GaO^- + H^+ \tag{3.43}$$

$$GaOH \rightleftharpoons \mathrm{GaOH}_2^+ + H^+ \qquad 3.44$$

with dissociation constants, K_a and K_b, intrinsic surface buffering capacity, β_{int}, and the differential capacitance, C_{dif}, dominating the definition of surface sensitivity as demonstrated in the previous section. Although the amphoteric nature of the surface and the theoretical definition of the insulator/electrolyte potential correspond to that of the Si-based device, the underlying heterostructure here is quite different. To understand the influences of this system and the dissimilarities with respect to Si-based ISFETs several studies regarding heterostructure variation have been performed [7, 53, 212, 213, 214, 215, 216]. In these, the accumulation or depletion of the 2DEG channel according to the pH dependent variations of surface potential is taken into account. Details regarding the general processes of heterostructure growth and transistor fabrication for the analyzed systems will be given in the following chapter, here the 2DEG, pictorially depicted in figure 3.17a-c, may simply be considered as the conducting channel within the semiconductor for which the charge carrier concentration and electrical conductivity are of interest.

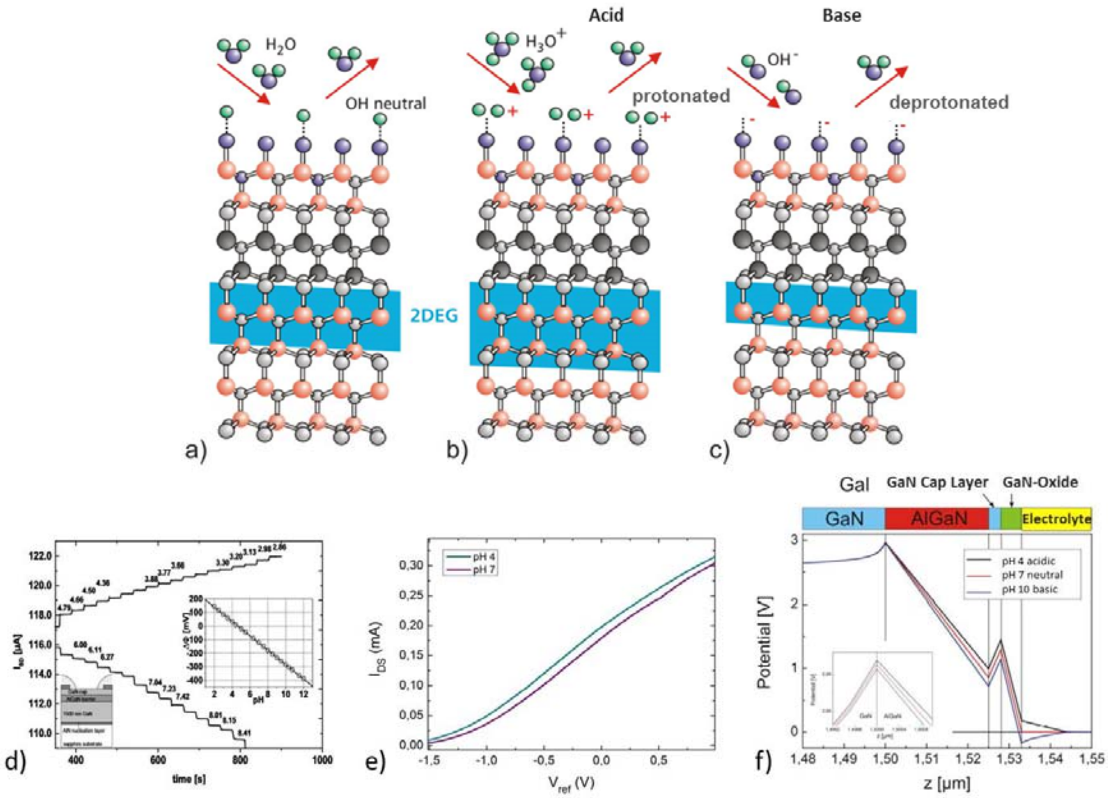

Figure 3.17: Crystal structure of GaN/AlGaN/GaN heterostructures with a schematic representation of the 2DEG for the case of a) neutral surface charge b) protonated or positive surface charge and c) deprotonated/dissociated or negative surface charge. Monitoring pH value dependent 2DEG variation though d) channel current modulation during transient modification of the electrolyte pH value and e) threshold voltage shift of transfer characteristic curves. f) Depiction of surface potential change due to pH variation and the ensuing interface potential shifts throughout the heterostructure, including effects on the 2DEG charge density [16, 212]

The GaN/AlGaN/GaN crystal structure is shown in this figure with the 2DEG represented by the blue area at the lower AlGaN/GaN interface. In this representation a) depicts the case for which the surface is neutral with a specific charge carrier concentration within the 2DEG. Upon protonation of the surface hydroxyl sites (fig 3.17b) as the pH value of the electrolyte lowers (i.e. the H^+ ion concentration increases) accumulation of charge within the 2DEG takes place due to the variation of surface potential. In the case of an increase in the pH (i.e. decrease in the H^+ concentration) the surface sites are deprotonated resulting in a more negative net surface charge and depletion of the 2DEG, as demonstrated in figure 3.17c. The pH dependent modulation of surface potential and the resulting variation in the charge within the 2DEG may be quantified by monitoring the drain-source current during transient adjustment of the H^+ concentration (figure 3.17d) or through threshold voltage shifts of the transfer characteristic curves upon modification of the pH level, as displayed in figure 3.17e [212]. This may also be viewed in terms of surface potential modulation and the ensuing alteration at each interface within the heterostructure, including the effects on charge carrier concentration within the 2DEG at the lower AlGaN/GaN interface, as shown in figure 3.17f [16]. This relationship between the polarization induced interface charges within the heterostructure and the way in which these may be modulated at the electrolyte/insulator boundary may also be further understood through the help of figure 3.18. This corresponds to the discussion in Chapter 2 regarding the development of the 2DEG due to spontaneous and piezoelectric polarization within the heterostructure. A cross-sectional view of a typical heterostructure is provided with fixed charges which accumulate at the interfaces resulting from the spontaneous and piezoelectric fields within the heterostructure. The interface charge densities are found by employing theoretical calculations along with correlation to the measurement of interface charges throughout the heterostructure by photoreflectance, polar optical scattering, acoustic scattering, piezoelectric scattering, and ionized impurity scattering [217, 218, 219, 220, 221]. This heterostructure is very similar to that used for other GaN sensors as well as those in this work, consisting of a 5 nm oxide at the electrolyte interface, a 3nm GaN cap layer, 35nm $Al_{0.28}Ga_{0.72}N$ barrier and a 1.5 μm GaN bulk layer on a sapphire substrate [212, 217, 218].

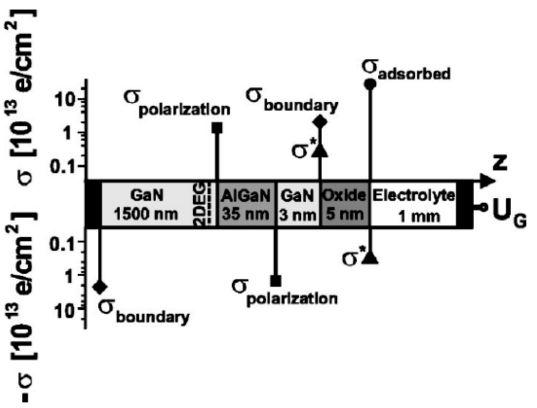

Figure 3.18: Simulated charge and potential distribution within the AlGaN/GaN heterostructure [218]

Several publications deal specifically with the study of the electrolyte/insulator interface to determine the number of hydroxyl sites, the dissociation constants and the effects of heterostructure modifications on these [222, 223]. In order to make quantitative calculations for the electrolyte/insulator interface of this system, evidence that the Ga_xO_y surface behaves similarly to that of Al_2O_3 was taken into account and the density of surface sites, n_S, and the dissociation constants for Al_2O_3 were thus used as a starting point [7, 218]. Solving the Poisson-Boltzmann equation utilizing these values to determine the interface potential, using the site-binding model for the surface charge density, and taking n_S as an adjustable parameter it was demonstrated that the calculated values could be well correlated experimental data of Steinhoff, et al. where a sensitivity of 55.7 mV/pH was found [212, 218]. Through variation of the modelling parameters and comparison with experimental results, determination of the dissociation constants and concentration of surface oxide sites could be achieved. Additionally, it was demonstrated that reduction of the distance between the amphoteric insulating surface and the 2DEG leads to an improvement in the transduction of the surface potential/charge interaction to the monitored modulation of channel conductivity [218]. This has been seen in the case of N-faced GaN which is less stable, however the 2DEG exists closer to the surface. This reduction of the distance may also be taken into account advantageously, as is the case in this work with a thinner barrier layer of 10nm and a GaN cap layer which is varied between 2-10nm [56].

Regardless of the heterostructure growth method, thickness of the barrier or GaN cap layer, surface oxidation techniques, as well as Si-doping (to an extent) within the heterostructure, little variation in the experimental pH sensitivity of the AlGaN/GaN surface has been observed. This has been demonstrated through various analysis methods, typically exhibiting near Nernstian sensitivities of 52-58 mV/pH [53, 212, 213, 214, 215, 216]. Measurement techniques which have been utilized to show this response include flatband potential determination of GaN through electrochemical impedance spectroscopy (EIS), potentiometric measurement of GaN FETs and AlGaN/GaN electrolyte-gated HEMTs, and the analysis of transfer characteristics for bare AlGaN surfaces [212, 213, 215]. Very recently further verification of the consistency of the pH-dependent surface potential modulation for these material systems has been carried out through potentiometric measurement of N-face GaN and also the evaluation of HEMT transfer characteristics with simultaneous x-ray radiation to demonstrate simultaneous measurement possibilities of biochemical and radiation responses [214, 216].

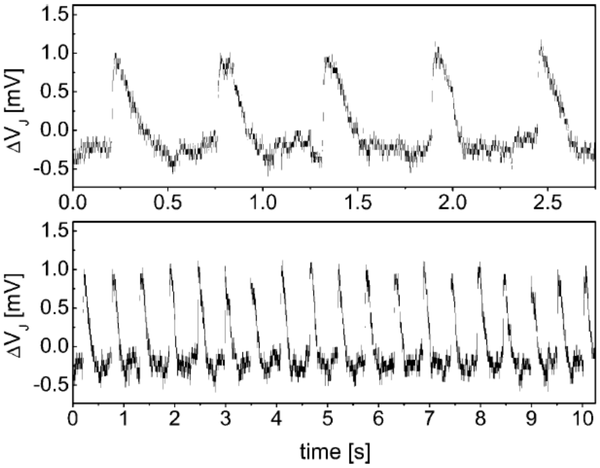

Figure 3.20: Extracellular potential of spontaneously beating rat heart muscle cells recorded with an AlGaN/GaN EGFET. The cells were cultivated on the device surface [197].

The establishment of III-Nitride based systems for stable and sensitive detection of H^+ ions led quickly to experimentation concerning biocompatibility and the potential to measure cell activity, similar to the extracellular potential recording results for Si-ISFETs. This investigation proved successful through the extracellular recording of spontaneously beating rat heart muscle cells cultured on the device [197]. Figure 3.20 shows the recorded tonic firing of these cardio myocytes using an AlGaN/GaN EGFET. This, in addition to a study on the effect of the surface oxidation process and variation of Al content in the Al_xGa_yN layer (x = 0, 0.22, 1) on the adhesion of 3T3 fibroblasts (fig 3.21) may additionally may be seen as an examples of the desired biocompatibility of the devices [7, 197].

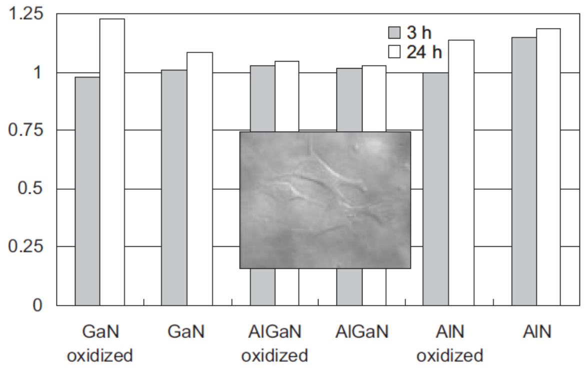

Figure 3.21: Comparison of adhered 3T3 fibroblasts on different untreated and wet thermally oxidized (2h, 700°C) Ga-face $Al_xGa_{1-x}N$ (x=0, 0.22, 1) surfaces after 3h and 24h. The inset shows the image of adherent cells on an untreated $Al_{0.22}Ga_{0.78}N$ surface after 24h. [7]

As the understanding of the III-Nitride heterostructure has progressed and the biocompatibility and bio-sensing possibilities of the fundamental systems have been demonstrated, various bio-sensing functionalization techniques have been developed based on these devices. An overview of pertinent sensors based on related systems will be given in the following section.

3.4.3 AlGaN/GaN Bio-functionalized HEMTs

The measurement of various analytes is desired over an extremely broad range of applications. The focus in this work involves biomarkers, which are used in life science to signal the onset of specific biological events. Biomarkers may include any biologically relevant molecule which has meaning in biological, medical, physiological, pathophysiological, disease diagnosis applications and so on. This field is extremely wide-ranging with many different sensing techniques based on a wide-variety of platforms. Here we will focus mainly on the development of bio-functionalized III-Nitride HEMTs, however many Si-based ISE or ISFET examples exist, many of which are well summarized in a detailed overview of by Izquierdo, et al. for continuous flow systems in an assortment of disciplines [224]. One Si-based example which is quite interesting lies in the relatively early development of an ISFET array for detection of multiple ions, indicating the desire for simultaneous monitoring of varying substances over exceedingly contrasting fields.

Already in 1992 Vlekkert demonstrated one of the first multi-analyte ISFET systems for flow injection analysis of pH and potassium concentration for horticulture applications [225]. In this investigation typical Si-based ISFET structures were utilized with modifications at the alumina gate consisting of a hydrogel as the inner solution for the ion of interest and an ion selective membrane on top of this, both covalently anchored to the substrate to maintain stability [237]. This demonstration of the possibility to monitor multiple analytes is widely desired over a variety of fields, particularly for physiological or pathophysiological measurement which can greatly benefit from this prospect. In this case, as has been previously stated, the stability and/or biocompatibility of Si-based technologies become problematic. When taking these concerns into consideration, the proclaimed chemical stability and demonstrated improvement in biocompatibility of the AlGaN/GaN material system is extremely attractive, particularly in comparison to SiO_2. The necessity for development of surface functionalization techniques for biosensors based on this heterostructure, however, becomes apparent for numerous applications. In many cases biological molecules such as enzymes or antibodies and/or their complementary binding partners, antigens or haptens, are employed in the functionalization of biosensors in order to achieve selective sensitivity towards a particular analyte. To achieve the immobilization of the desired selective biomolecule, a controllable chemical surface modification must be achievable.

In 2005 Kang, et al. demonstrated an example of 3-Aminopropyl triethoxysilane (APTES) surface treatment on GaN, resulting in an exposed amine (NH_3) surface functional group which facilitates covalent linkage with proteins [226]. Verification of this functionalization technique was accomplished by the binding of N-hydroxysulfosuccinimidobiotin (sulfo-NHS-biotin) to the surface amine groups. Sulfo-NHS-biotin possesses an extremely high affinity to bind streptavidin or avidin proteins [227, 228]. The initial binding of sulfo-NHS-biotin at the amine functional groups, as well as the following exposure to streptavidin is demonstrated in figure 3.22a. Exposure to BSA coated nanoparticles was utilized as a negative control, with no response in the source-drain current of the AlGaN/GaN HEMT, validating immobilization of streptavidin at the gate surface. Although evidence for the ability to functionalize the surface of the gate region with a bioreceptor was given through this work, covalent immobilization of the silane was not directly shown. The covalently bonded organosilane functionalization on GaN and AlN surfaces was, however, demonstrated shortly afterward [229]. X-ray photoelectron spectroscopy (XPS) and atomic force microscopy (AFM) were employed along with temperature-programmed desorption measurements to show Octadecyltrimethoxysilane (OCS) and APTES self-assembled monolayers (SAMs) following wet chemical hydroxylation of the GaN and AlN surfaces (fig 3.22b). This verification of covalent bonding strongly supports the possibility for the realization of stable chemical biofunctionalization techniques by providing a monolayer of functional groups. These may then be used to bind specific molecules for sensing or strands of deoxyribonucleic acid (DNA) to sense hybridization due to DNA matching, some examples of which are discussed in the following [229, 230, 231, 232].

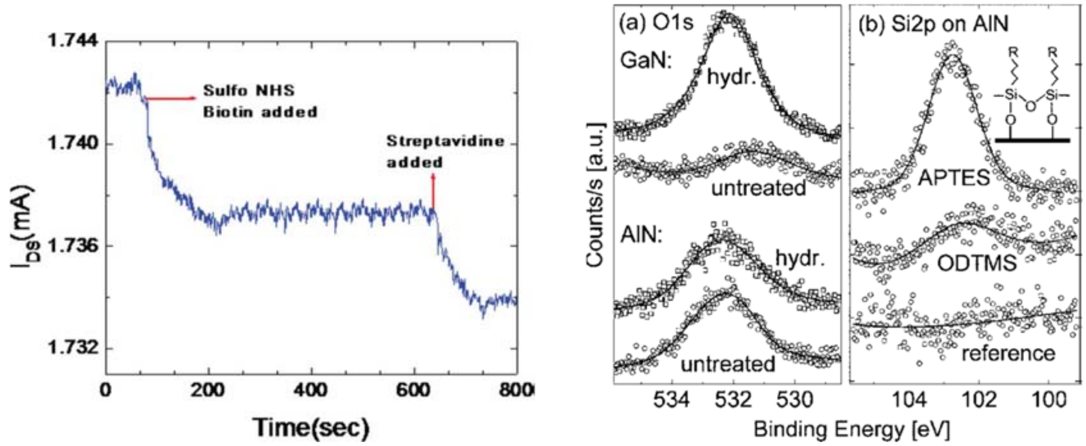

Figure 3.22: Demonstration of surface functionalization techniques through a) the change in HEMT drain-source current as a result of interaction between NHS-biotin and streptavidin introduced to the gateless HEMT surface and b) O 1s core-level XPS-Spectra of untreated (circles) and hydroxylated (squares) AlN and GaN. For GaN, an enhanced surface oxidation is observed. b) Si 2p core-level peaks for hydroxylated as well as APTES- and ODTMS-modified AlN. The inset shows a schematic of SAM formation on the surface (R: Remaining alkyl chain for ODTMS, amino group for APTES) [229, 230]

Following initial studies exhibiting the possibility for functionalization, an assortment of III-Nitride BioFET chemical surface modification techniques have been developed over the past decade for the detection of various biological analytes. Several examples of these include deoxyribonucleic acid (DNA) detection, early identification of kidney injury using kidney injury molecule-1 (KIM-1) antibody, prostate specific antigen (PSA) sensing for prostate cancer detection and the monitoring of glucose levels using exhaled breath condensate (EBC); summarized in a review from Kang, et al. in 2008 [230, 231, 232]. The assorted biofunctionalization techniques for these devices are presented in figure 3.23. Despite the possibility to make use of the ionic boding between Ga and N to allow for direct DNA or protein attachment at the open gate surface, here a thin 5nm Au layer was employed to provide a more stable functionalization method. In the case of DNA tethering this interaction with Au surfaces has been carefully investigated [229, 233]. As shown in figure 3.23a the Au-coated gate area is functionalized with 15-mer 3'-thiol-modified oligonucleotides. This immobilized DNA strand is then utilized to detect the formation of duplex DNA through oligomer hybridization when matched target DNA is introduced to the system. An observed decrease in the drain-source current upon introduction of matched DNA to the gate surface indicated the successful tethering of DNA at the Au surface, while lack of response to mismatched DNA verified the absence of non-specific binding (fig 3.23d) [232].

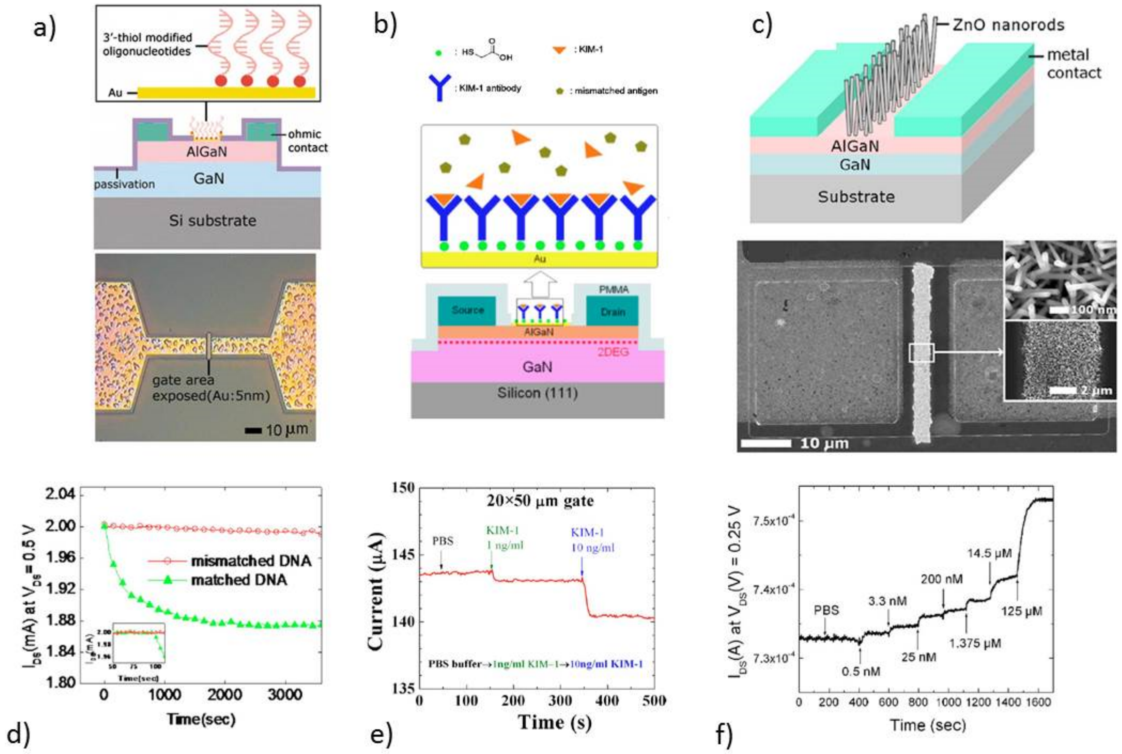

Figure 3.23: Biofunctionalization of AlGaN/GaN HEMTs for a) DNA matching b) antibody detection and c) glucose monitoring and corresponding measurement results for introduction of d) matched or mismatched DNA, e) KIM-1 molecule and f) various EBC glucose concentrations [230, 231, 232]

AlGaN/GaN based detection of disease biomarkers with immunosensor-based analytical platforms has also been demonstrated through the use of antibodies, as presented in figure 3.23b. The KIM-1molecule is concerned in this example, which has been proven to be an indicator of acute kidney injury (AKI) as well as showing a dramatic increase in the post ischemic kidney [234]. For the gate modification here, a thin Au layer is also employed. This allows for the self-assembly of a thioglycolic acid molecule (HSCH2COOH) monolayer due to a strong interaction between the thiol group and gold. The antibody immobilization may then be realized by making use of the interaction between the carboxyl group of thioglycolic acid and the amine group on the KIM-1 antibody. Subsequently, modification of the drain-source current may be observed due to varying concentrations of KIM-1 molecule (fig 3.23e). This demonstration of a non-invasive technique for pathogen detection is promising for disease diagnostic applications based on analogous systems.

In figure 3.23c the development of an enzymatic sensor is shown, created through the immobilization of glucose oxidase (Gox) on ZnO nanorods [231]. Very low detection limits were demonstrated for this sensor, achieving 0.5 nanomolar sensitivities (fig 3.23f). Although extremely low detection limits may not be necessary or even desired for *in vitro* or *in vivo* applications where the background glucose concentration is in the millimolar range, when working with EBC much lower concentrations are present. These may be correlated to the concentration in blood, however lower detection limits may in fact be required [75]. In this situation the AlGaN/GaN ISFET functionalized with ZnO nanorods and Gox immobilization could provide a non-invasive and adequately sensitive technique, particularly advantageous in regard to diabetic measurement in which the persistent necessity for phlebotomy can be very uncomfortable for patients [235].

Although many innovative bio-sensing techniques have been and are being developed on the III-Nitride platform, some basic issues are still at hand. Among these are the economic considerations in general as Si-based technologies are typically significantly cheaper. Applications which desire optical transparency or better biocompatibility, however, look to solutions such as III-Nitride systems. FET devices offer many positive aspects, especially for measurement of weak signals and/or high impedance applications, making them particularly suited for biosensing [236]. Miniaturization of the sensors is continuously desired; however the reference system continues to pose problems in this respect. A great deal of research has been devoted to this issue, as discussed, and continual is being made. A stable passivation is essential for measurement of any sort in a fluid environment. This topic has been generally problematic for ISFETs, and must be regarded carefully with III-Nitride systems in order to avoid damage to the underlying 2DEG. This must all be reconsidered when establishing new material or chemical functionalization techniques at the gate surface. In the following chapters the fabrication of devices utilized in this study is discussed, in addition to a developed technique to generate a stable passivation layer and the use of this with the nitric oxide sensor functionalization developed on the AlGaN/GaN technology.

4. Materials and Methods

The AlGaN/GaN based heterostructure has been a subject of investigation for approximately 20 years for a variety of applications, including high frequency, high power microwave devices as well as biochemical sensors. Much of the fabrication process has been thoroughly studied and optimized for heterostructure growth utilizing both molecular beam epitaxy (MBE) and metal organic chemical vapor deposition (MOCVD). All fabricated samples for this work were grown using MOCVD, as this technique is available as an industrial option and additionally the process has been optimized during previous work [15, 16, 54]. This growth method, as well as the following fabrication steps used to create the ISFETs or other test structures, will be discussed here in order to provide an understanding of the complete process. This will also facilitate the explanation of optimization or functionalization steps involving various stages of sample production.

4.1 Wafer Growth

Two-inch [0001] c-plane sapphire wafers were used as the substrate for AlGaN/GaN heterostructure growth. The sapphire substrate provides a hard, chemically inert, monoaxial crystal material with excellent thermal stability and optical properties. Depending on the optical requirements of the intended final application or measurements, the wafers are polished on either one or both sides. Additionally, quality epitaxial growth of GaN and AlGaN layers may be achieved due to the acceptable lattice mismatch of 13.9% between sapphire and GaN. SiC substrates provide a much improved mismatch of only 3.5%, however the trade-off of material cost makes sapphire currently more attractive when the heterostructure growth quality suffices. At a pressure of 15 mbar the MOCVD process is carried out, beginning with a thin (~20nm) AlN nucleation layer utilized to alleviate the lattice mismatch issues and to increase structural integrity. The AlN deposition is carried out at low temperature (460°C) followed by a high temperature anneal (1120°C) and the subsequent deposition of the following layers. Utilized precursors for GaN and AlGaN MOCVD growth include triethylgallium (TEG), trimethylaluminium (TMA), and ammonia (NH_4). Through variation of the ratio of TEG to TMA the Al content of the $Al_xGa_{1-x}N$ barrier layer may be adjusted.

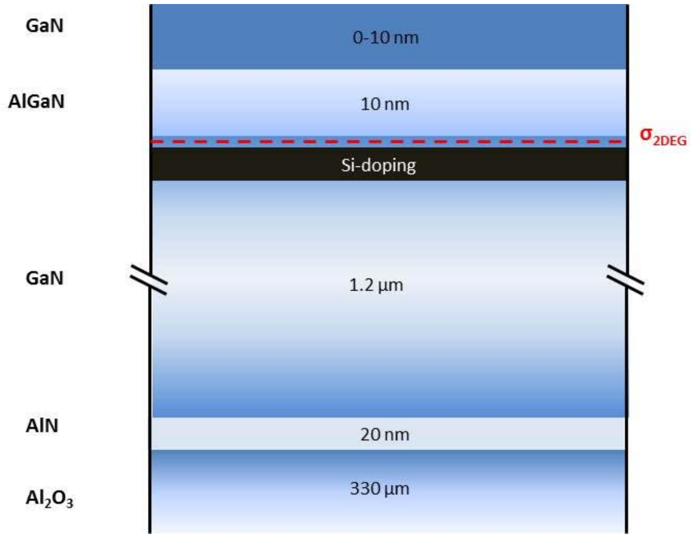

Figure 4.1: AlGaN/GaN MOCVD Heterostructure [56]

The heterostructure depicted in figure 4.1 is typical of that utilized throughout this work. The sapphire substrates are 330 µm thick and the following AlN nucleation layer is typically 20 nm thick. Subsequently, a 1.5 µm GaN buffer layer is grown and afterward the 10 nm $Al_xGa_{1-x}N$ barrier and 0-10 nm GaN cap layers were deposited. The $Al_xGa_{1-x}N$ barrier layer Al content was typically 30% and Si-doping (2 x 10^{13} cm^{-3}) is used just below the $Al_xGa_{1-x}N$ barrier layer. This Si-doping aides in the reduction of undesired light sensitivity of the final structures [16, 15]. Further specific details on the MOCVD process and optimization of the AlGaN/GaN heterostructures based both on sapphire as well as on SiC may be found in [54].

4.2 Sensor Fabrication

Once the MOCVD heterostructure growth has been finished, sensor fabrication is carried out at the wafer level, resulting in 64 sensor chips per 2” wafer, 5 mm x 5 mm in size. An example image of a finished sensor chip is shown in figure 4.4, while a schematic showing an example of the components of a single completed ISFET is given in figure 4.2. The fabrication steps necessary to reach this stage will be covered in this section as well as an explanation of each of the components shown here. The extra fabrication steps utilized for sensor functionalization will be addressed in the following section.

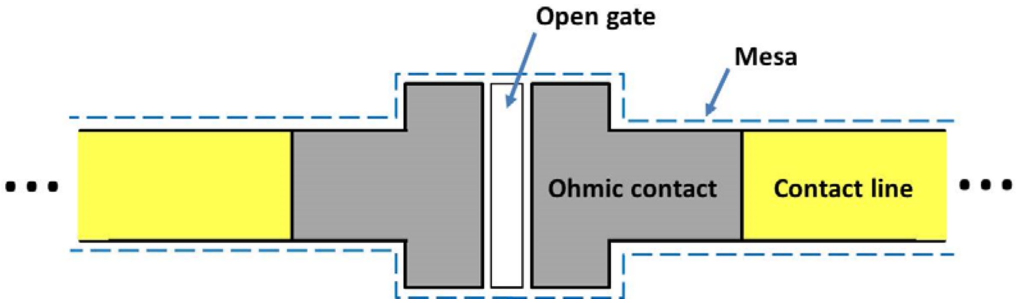

Figure 4.2: ISFET Schematic demonstrating the outcome of four main fabrication processes

The first step required in the fabrication process involves establishing ohmic contact to the 2DEG within the heterostructure. In order to realize this task, a technique involving a multi-layer metal stack of Ti/Al/Ti/Au (20/80/30/100 nm) is utilized. Previous research has been carried out in order to determine optimal metals, ratios of these and annealing temperatures to achieve low resistance contact to the charge carrying electron gas [164, 238, 239]. The first two metals of this stacking system have been shown to dominate the process of actually contacting the 2DEG while the second Ti layer (which is often replaced with Ni or Mo) provides a diffusion barrier. The final Au layer improves the ability to contact this metal stack as well as reducing the contact resistance. Other metals and contact systems have also been investigated, for example TiN which provides a much smoother contact surface, however these are in the developmental phase and were not taken advantage of for the devices here. Patterning of the ohmic contacts is performed through a typical photolithography lift-off process using a standard positive photoresist. This indicates that the areas of photoresist exposed to UV light and developed will be removed (fig 4.3a), allowing for patterning of the metal the contacts as desired (fig 4.3b). Once the photoresist has been patterned, an Ardenne® tool with multiple magnetron sputter sources is used to create the Ti/Al/Ti/Au stack. This tool achieves the deposition of multiple materials with minimum contamination since all sputtering is done within one chamber continuously under vacuum. Following this a rapid thermal process (RTP) anneal is carried out under N_2 atmosphere for 45 seconds at 825°C. It is through this high temperature procedure that the metal diffuses through the GaN cap and AlGaN barrier to create a low resistance contact to the 2DEG (fig 4.3c).

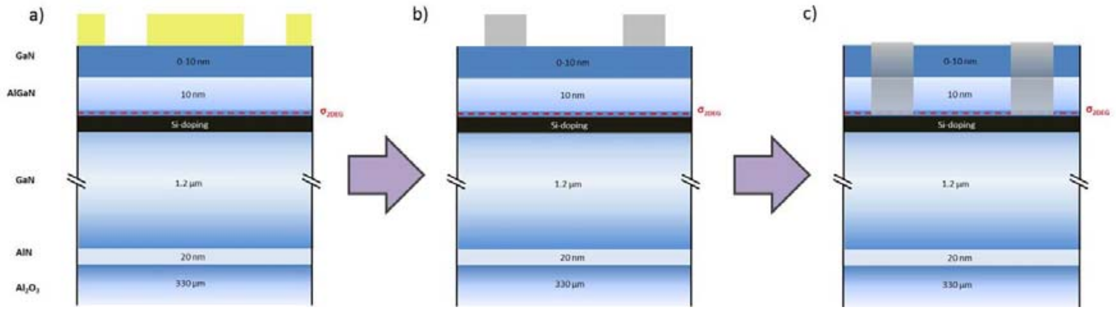

Figure 4.3: (a) Photolithography patterning and (b) lift-off structuring of ohmic contacts. (c) Ohmic contact to the underlying 2DEG following an RTP anneal.

Specifically, the lower Ti layer reacts with the underlying nitrogen of the heterostructure resulting in the formation of interfacial nitrides [54]. In this case a thin TiN layer is formed which, along with the ensuing reduction of the Schottky barrier, generates nitrogen vacancies, which act as donors producing a highly doped n^+-AlGaN layer beneath the thin metal layer. At the same time, the sputtered Al of the metallization sequence diffuses along dislocations in the semiconductor providing good conductive paths to the underlying 2DEG [54]. Once the 2DEG has successfully been contacted, all contacts on this substrate are then connected to one another via this charge carrying channel. In order to create electrical separation between the channels of various transistors an inductively coupled plasma (ICP) Cl_2 etch step is implemented. By etching the heterostructure deeper than the level of the 2DEG, unwanted electrical contact between separate transistor channels is eradicated. This structuring of the 2DEG is achieved using a thick photoresist, patterned in such a way to mask the ohmic contacts and the area between them, which will then be the channel of the ISFET. Although difficult to perceive in the optical microscopy image in figure 4.4, the mesa is defined as indicated by the white dotted line; etching the area outside of the ohmic contacts and the open gate of the transistor.

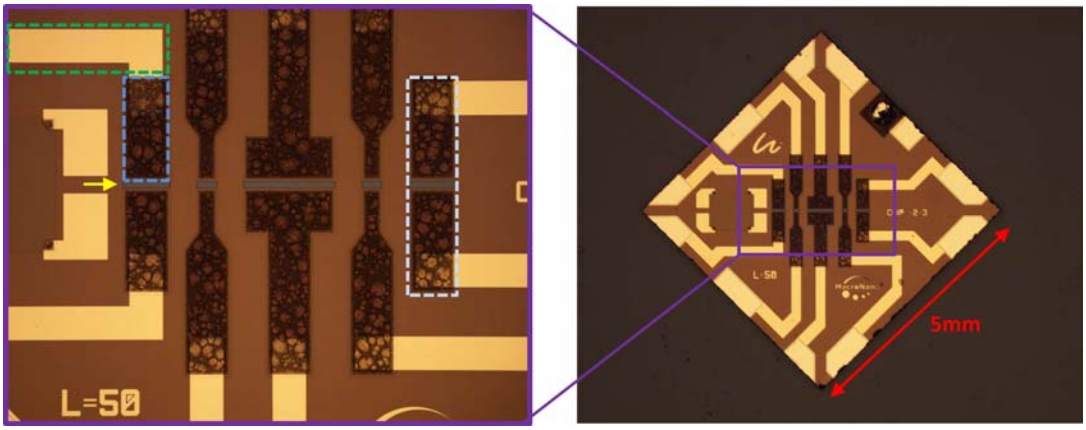

Figure 4.4: Completed sensor chip example, 5mm x 5mm size. An ohmic contact is indicated by the blue dotted line, unetched mesa area within the white dotted line, metal contact line by the green dotted line and the open gate area with a yellow arrow.

Once the 2DEG for each structure is confined to the desired location and electrical contact has been made, a second metallization is carried out in order to produce metal lines which provide the possibility for metal boding upon completion of the sensor chip or simply to probe the contact pads for electrical characterization of the device. The optical difference between the surface morphology of the annealed ohmic contact (blue dotted line) and the subsequently deposited contact lines (green dotted line) may be readily observed in figure 4.4. The contact lines are defined using a positive photoresist and lift-off, analogous to the first metallization process. In this case a thin 30 nm Ti adhesion layer is deposited followed by 200 nm of Au, providing a highly conductive contact line with a very flat surface.

At this point in the fabrication process each structure has been electrically isolated from one another and contact to the 2DEG has been established, in the presented figures these contacts represent the source/drain of the ISFET. As the operating conditions for these devices involves a fluid working environment, insulation of all metal contacts must also take place. This is a generally problematic area, often referred to as the weak link due to the numerous requirements of the passivation layer. This must be a chemically and mechanically stable layer with high electrical insulation properties. Additionally, the passivation layer must adhere well to the surface of the device and, one of the biggest obstacles, structuring this layer must be possible without damaging the underlying 2DEG. This patterning issue maybe be better visualized through observation of figure 4.5a in which the etch mask is indicated; the blocking or protection of the insulating layer is achieved with this mask while the gate region is etched free of this dielectric material. Other processes may be utilized in addition to this method of etching, some of which will be further discussed in Chapter 5. At this point, however, with the aid of this sketch it is straightforward to imagine the possibility of detrimental effects to the 2DEG due to physical etching through ion bombardment, as this conducting channel lies only 20 nm beneath the surface.

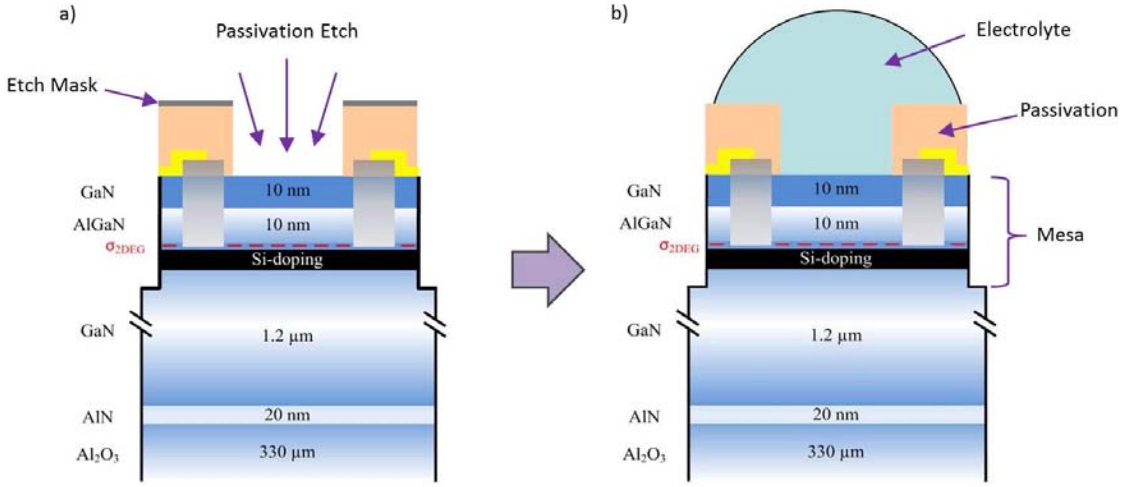

Figure 4.5: a) Example of passivation structuring by etching using an etch mask b) Completed ISFET with patterned passivation to allow measurement in a fluid environment

Upon successful structuring of the insulation layer, and in the case of a utilized etch mask, this material must be removed. The passivation etch process was predominantly carried out for the devices used here through the use of an Al etch mask. Care must be taken here in order to complete this fabrication step within a short period of time, typically 1-3 days, due to the development of a native oxide upon contact of the Al with ambient air. Holding the sample under vacuum obviously may aid in the prevention this issue. In any case, the Al mask is removed prior to use of the fabricated ISFETs. The individual sensor chips are then separated through a wafer dicing process utilizing a mechanical saw. The resulting 5 mm x 5 mm chips, the example of which was shown in figure 4.4, may be employed at this point in an appropriate measurement setup with integrated contact, sealing and fluidic system. The chip may also be mounted onto a ceramic (fig 4.6a) or printed circuit board with contact pads which are bonded to the bond pads of the sensor chip. The bond wires in this case are subsequently insulated using a silicon rubber paste which may be accurately dispensed over the wires while leaving the center of the chip exposed to allow contact with the electrolyte. This may be perceived in figure 4.6a and b as the transparent square covering the indicated contact pads as well as the edge of the chip, where the bond pads for the ISFETs are located. This encapsulation process allows for the entire chip and board to be immersed into fluid, apart from the connection pads seen at the bottom edge of the blue ceramic in figure 4.6a.

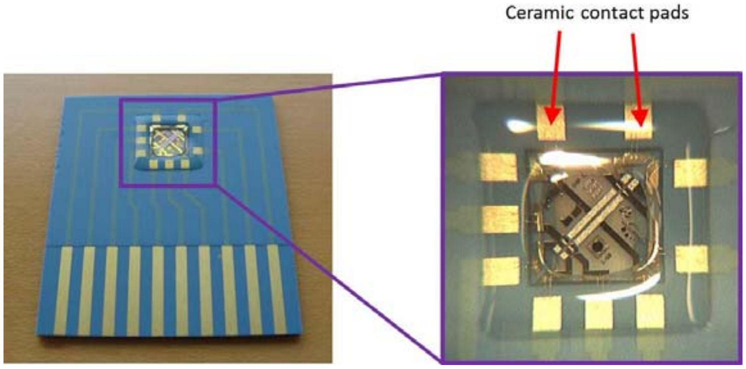

Figure 4.6: Mounted, bonded and encapsulated sensor chip

Once the sensor chip has been packaged in this way, measurement may take place, however a contamination due to photoresist or incomplete removal of the passivation layer is often present. This was typically dealt with in previous work by employing a 24 h watering process in addition to (partial) physical removal of the contamination layer utilizing a cotton applicator and acetone to reduce sensor drift [15]. Following this procedure stable measurement conditions were achieved via repetitive measurements (for approximately 5 h) and further DI water cleansing steps. This topic will be further analyzed in the following chapter as it again pertains to the development of a stable passivation system, which was one of the main goals in this work.

Without further modification to the structure during or following the process the resulting pH sensor has been shown to be stable as well as precise and accurate over a broad pH range. In order to work towards the objective of a multi-purpose sensor chip, and specifically to attain the desired goal of nitric oxide sensing, various functionalization layers were developed and tested. In the following section the details regarding the utilized materials and processes necessary will be discussed.

4.3 Functionalization for Nitric Oxide Measurement

As discussed in chapter 3, nitric oxide is important biological molecule due to its function as an intracellular messenger, vasodilator and in the immune system. In this section the discussion will focus on the functionalization of ISFETs to attain NO sensitivity. The materials utilized include tungsten trioxide (WO_3), graphene, porphyrin, and aluminum oxide or 'alumina' (Al_2O_3).

4.3.1 Tungsten Trioxide (WO_3)

Tungsten trioxide (WO_3), an n-type indirect wide band gap semiconductor, has found use in various applications including gas sensing, photocatalysis and electrochromic devices [240, 241]. Environmental monitoring of various gases, particularly pollution related substances such as NH_3, CO, CO_2, and NO_x, has brought about the exploration of various metal oxide semiconductors. As early as 1991 work involving the use of WO_3 for NO and NO_2 detection in air at elevated temperatures clearly demonstrated superior sensitivity in comparison to other oxide films [222, 242, 243]. However, this film has seldom been studied regarding NO_x

sensitivity in fluid environments. Here compatible fabrication techniques were developed to allow for functionalization of the gate area of AlGaN/GaN ISFETs with WO_3 thin films.

In general, tungsten oxide films have been realized through the use of several deposition techniques including reactive sputtering, chemical vapor deposition (CVD), evaporation, anodization, and sol-gel techniques [241, 244, 245, 246, 247, 248, 249]. Many studies have also been conducted regarding various nano-structuring possibilities, resulting in plate-like, slab-like or cube-like structures, various sizes of grain-like morphologies, nanowires, nanorods and nanoneedles [241, 250 251]. For the devices used in this work, two methods were developed and employed to achieve WO_3 thin films. The first is based on the inexpensive method from Widenkvist, et al., which is also easily incorporated into the AlGaN/GaN ISFET fabrication process. Initially sputter deposition of a 20 nm W layer is carried out followed by a subsequent immersion of this layer in nitric acid (HNO_3) at a temperature of 50 °C. It is believed that the resulting reaction involves an initial oxidation of tungsten to WO_4^{-2} due to the strong oxidizing nature of HNO_3. Subsequently, it is expected that the WO_4^{-2} should precipitate to tungstite according to the following reaction

$$WO_4^{-2} + 2H^+ \rightarrow WO_3 \cdot H_2O. \qquad 4.1$$

The resulting surface structure for a 20 nm W film processed under these fabrication conditions was similar to the plate-like structures in literature. A schematic demonstrating this method is depicted in figure 4.7 and the corresponding SEM image portraying the obtained morphology is given in figure 4.8a. This result is an example of the nanostructured surface, which may be interesting for many applications, here mainly due to the surface area increase of the transducer of the system.

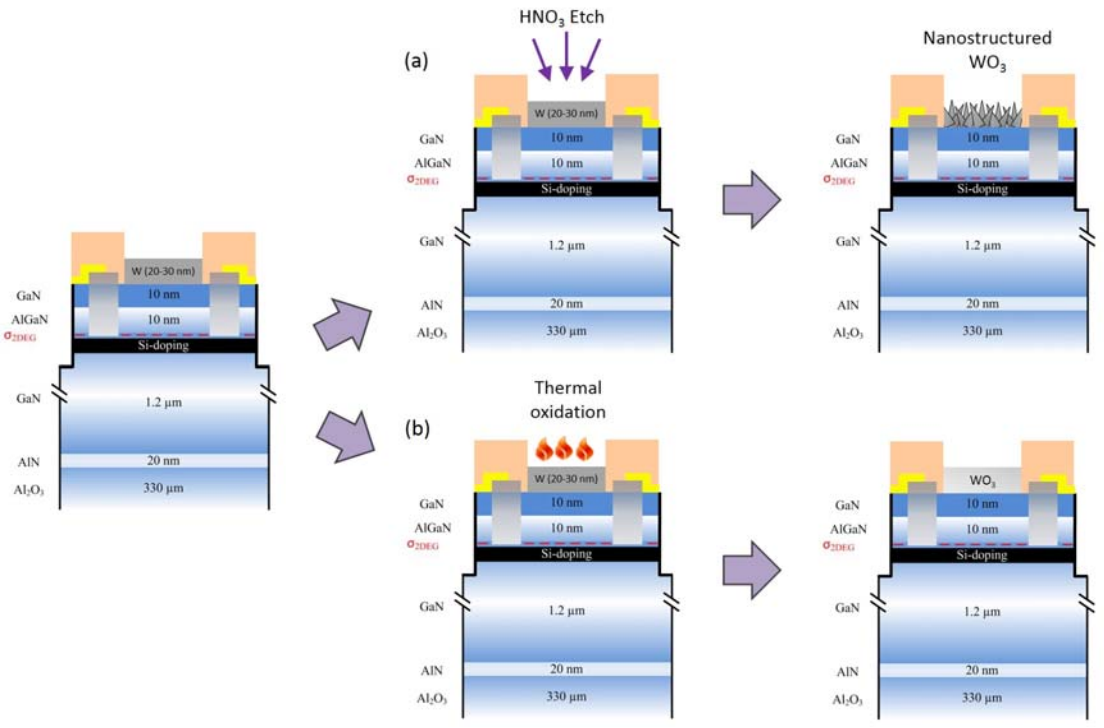

Figure 4.7: Processes for the formation of WO_3 through a) chemical etching of W to create a nanostructured surface or b) thermal oxidation of W forming a smooth surface

The second utilized method also involves an initial patterning of the sputtered tungsten film through photolithography and lift-off techniques. 20 and 30 nm films were deposited, which were then oxidized by RTP at a temperature of 600 °C for 90 seconds in oxygen atmosphere, resulting in a smooth surface of the WO_3 films. Similar annealing processes, converting the deposited amorphous film to a polycrystalline film, have been demonstrated to produce a more robust layer, increasing chemical and electrochemical stability [252]. A schematic of this method is also depicted in the illustration in figure 4.7 as well as an example of the acquired WO_3 surface morphology in figure 4.8b; a particle is included in this SEM image to demonstrate focus at the surface.

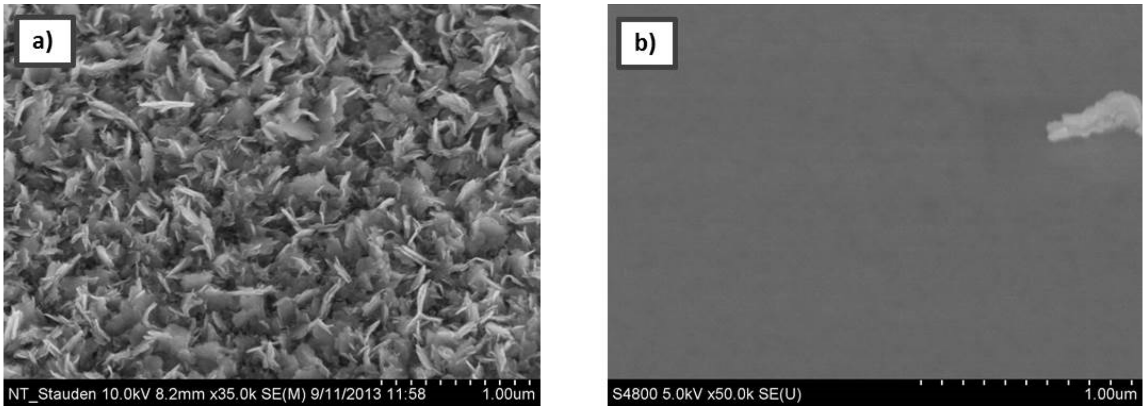

Figure 4.8: SEM images of the gate functionalization surface morphology for a) HNO_3 nanostructured WO_3 and b) thermally oxidized WO_3 by RTP

In order to confirm that the produced films are indeed comprised of the WO_3 stoichiometry, XPS was carried out following oxidation. A reference sample was prepared simultaneously with the WO_x samples, however without intentional oxidation and was transferred as quickly as possible to vacuum conditions in the XPS tool to avoid prolonged contact with ambient air. A comparison of the measured spectra for these materials is given in figure 4.9.

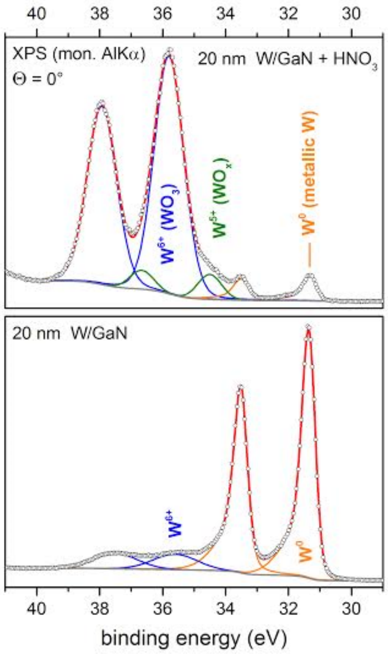

Figure 4.9: XPS confirmation of WO_3 structure for oxidized W layers (top) vs a reference W layer (bottom)

XPS is carried out through the irradiation of a sample with X-ray photons which transfer energy to electrons within the sample. These electrons may then be emitted from their initial state with a kinetic energy and intensity dependent on material type, atomic orbital, energy of the incident X-ray and the binding energy. The elements present as well as their concentration may then be identified through analysis of the emitted photoelectrons. In this case, examination of the W4f peaks of the film without oxidation (figure 4.9, bottom) shows mainly the response due to emission of electrons corresponding to the metallic tungsten film (contribution shown by the yellow curve); however a thin native oxide is also present due to the contact with air (blue curve). Utilizing the relationship between the assessed oxidation state and the ratio of metallic to oxidized content, this was estimated to be approximately 0.7 nm. The measured spectrum for the unknown mixed-phase WO_x film is shown in the upper portion of figure 4.9; the peaks for various binding energies demonstrate the various material species present. In this case the predominating WO_3 stoichiometry is revealed (oxidation state of W^{6+}, blue curve), with a small amount of an additional oxidation subspecies. This has been identified as the W^{5+} oxidation state, which has also been observed in literature as an often present additional species for various methods of W oxidation [253, 254, 255, 256]. Finally, a small part of the film remains in the metallic state as may be observed by the small peaks corresponding to the yellow W curve. These variations in existing oxidation states and resulting material properties represent an area in which a great deal of optimization could take place to maximize sensitivity for a specific analyte. Here the initial demonstration of the use of $WO_{3/x}$ films for NO detection was carried out.

4.3.2 Graphene

Since the preliminary preparation of two dimensional graphene sheets [257] and the initial demonstration of the electronic properties, research in the field has exploded with applications ranging from much focus in the realm of FETs [258, 316] to utilization for electrochemical sensors, biosensors [259, 260], and energy storage and production [261, 262]. Many possible applications of the two-dimensional sheets of carbon atoms are conceivable when taking into consideration the superior electronic transport and biocompatibility properties, as well as the high flexibility while simultaneously exhibiting exceptional material stiffness and strength [262]. In order to make the employment of this material possible, a great deal of advancement has taken place, including the development of a variety of techniques to yield an assortment of graphene materials. The commencement of this progress dates back to the mid-1900s when B. C. Brodie carried out work involving the technical terminology for various substances referred to as 'graphite' and methods to oxidize this material. He conducted experiments with graphite from several sources, physically grinding the materials into small plate-like structures and subsequently purifying the substance by boiling the graphite in acid. The chemical and thermal treatment described in this work provided the foundation for many current graphite oxidation techniques, including that of Hummers, et al., which was published exactly one century after Brodie and which is the basis for the process utilized in this work [263]. The two other mainly utilized over the past few decades in an endeavor to achieve single sheets of graphene include exfoliation of graphite by tape-transfer to the desired substrate and CVD growth, typically on nickel (Ni) substrates with subsequent transfer to the target substrate via a poly(methyl methacrylate) (PMMA) sacrificial layer [264].

As chemical sensing is the main topic of this work, graphene related sensing applications are of particular interest here. Various graphene structures have been studied over the past decade in relation to structural quality and sensing properties; pristine, intentionally doped or defective graphene have often been researched theoretically as well as practically [265, 266, 312]. This practice spans a variety of sensing applications, especially for systems similar to thin-film gas sensing due to the high surface area to material volume ratio, demonstrating achievements such as detection of single gas molecules [270, 271, 316]. This is relevant, for example, in order to successfully sense a small amount of environmental pollutant or toxic gas molecules such as NH_3, NO_2, which has been shown in practice to significantly affect conductance of single wall carbon nanotubes (SWCNTs) [269]. Several studies have been carried out regarding the atomic interactions and the gas adsorption-induced modifications of the electronic properties of graphene and related materials [266, 267]. Whether the molecular interaction which takes place is due to charge transfer or physiosorption is a point of discrepancy among graphene-based sensing reports. Additionally, the quality of the graphene sheet and presence of contamination or dopants is another major point of discussion with numerous groups reporting the observed sensitivity to a given analyte to be a result of contamination or doping, while pristine graphene may demonstrate a much lower or completely insensitive response [267, 268, 317]. Recently several investigations have taken place in which the quality and/or doping of the graphene sheets has been specifically considered. Zhang, et al. carried out a theoretical study on the differences between the small molecule interactions of NH_3, NO_2, CO and NO with pristine, boron-doped, nitrogen-doped and defective graphene sheets (P-, B-, N-. and D-graphene) [266]. Here the most favorable adsorption configurations were sought by placing the molecule of interest at various positions and orientations in reference to the graphene film (similar modeling to the following example of Chen, et al., shown in figure 4.10). Theoretically relevant values are extracted for each molecule and graphene type. Their findings are summarized in the following table, where the significant variation in adsorption energy (E_{ad}), atomic spacing (d) and Mulliken charge (Q) may be seen for each gas molecule studied, depending on dopant or defect presence in the graphene sheet [266].

Table 4.1: Adsorption energy (E_{ad}), equilibrium graphene-molecule distance (d) defined as the shortest atom-to-atom distance) and Mulliken charge (Q) of small molecules adsorbed on different graphene sheets [266]

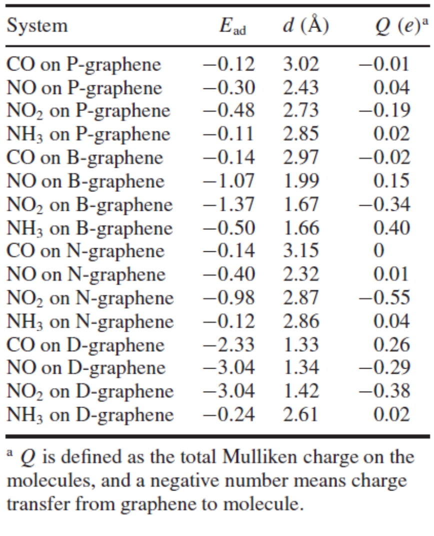

System	E_{ad}	d (Å)	Q (e)[a]
CO on P-graphene	−0.12	3.02	−0.01
NO on P-graphene	−0.30	2.43	0.04
NO_2 on P-graphene	−0.48	2.73	−0.19
NH_3 on P-graphene	−0.11	2.85	0.02
CO on B-graphene	−0.14	2.97	−0.02
NO on B-graphene	−1.07	1.99	0.15
NO_2 on B-graphene	−1.37	1.67	−0.34
NH_3 on B-graphene	−0.50	1.66	0.40
CO on N-graphene	−0.14	3.15	0
NO on N-graphene	−0.40	2.32	0.01
NO_2 on N-graphene	−0.98	2.87	−0.55
NH_3 on N-graphene	−0.12	2.86	0.04
CO on D-graphene	−2.33	1.33	0.26
NO on D-graphene	−3.04	1.34	−0.29
NO_2 on D-graphene	−3.04	1.42	−0.38
NH_3 on D-graphene	−0.24	2.61	0.02

[a] Q is defined as the total Mulliken charge on the molecules, and a negative number means charge transfer from graphene to molecule.

A related study was carried out by Chen, et al. examining the differences in the interaction between similar small gaseous molecules (NO, N_2O and NO_2) and either pristine graphene or Si-doped graphene [267]. Here the variation in atomic spacing and molecular orientation may additionally be visualized through the diagrams in figure 4.10 (the C, N, O and Si atoms are represented by grey, blue, red and yellow balls, respectively) [267]. Figure4.10 1a, b and c demonstrate the interaction of adsorbed NO, N_2O and NO_2 on pristine graphene with given bond distances (in Ångstroms) and angles (in degrees). To acquire these values each adsorbed molecule was placed in various orientations, perpendicular or parallel to the graphene film and at various locations with regard to the carbon atoms, i.e. on top of a carbon atom, in the honeycomb ring structure or at a C-C bond. The most stable adsorption configuration was found through this procedure and the pertaining values were extracted. Similar modeling and computations were carried out upon introduction of Si atoms into the graphene sheet lattice. The results for molecular interaction with NO are provided in figure 4.10, 2a, b and c where the two most stable configurations of a single NO atom are given in a and b with the N- or O-atom bound to the Si-atom. Here the increase in the adsorption energy (E_{ads}) by 0.755 eV for the case of the bound N-atom (fig 4.10, 2a), compared with the intrinsic graphene system, theoretically demonstrates this configuration to be the most stable. Fig4.10, 2c provides the most favorable geometry configuration in the case of two NO molecules binding to the identical Si-atom. Here it may be noted that the adsorption energy of the two NO molecules is slightly larger than that on the single molecule, indicating that the dimerization configuration is preferred [267].

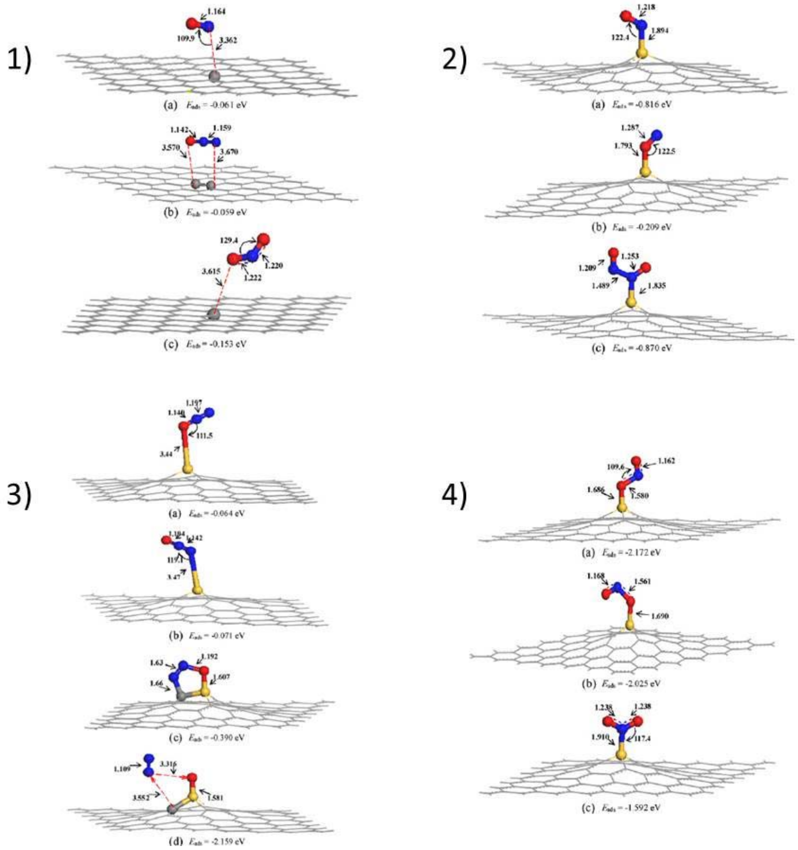

Figure 4.10: 1) Most favorable molecular configuration for a) NO, b) N_2O and c) NO_2 in relation to pristine graphene sheet. 2, 3, 4a, b, c, (d)) Possible, most stable, adsorption configurations for NO, N_2O and NO_2 on Si-doped graphene. Bond lengths are given in Ångstroms and angles in degrees [267].

Figure 4.10, 3a, b, c, d and 4a, b, c show the resulting most stable geometries and adsorption orientations for N_2O and NO_2 through analogous analysis techniques. Figure 4.10, 3a and b reveal only physical adsorption of the N_2O molecules with variations in E_{ads} stemming from van der Waal's attraction. As may be understood from the increase in E_{ads}, the most stable case for the interaction of N_2O with graphene is observed when an O-atom is left bound to the Si-atom while an N_2 molecule escapes from the sheet. Finally, in the case of adsorbed NO_2 the most stable configuration is found when one O-atom is bound to Si in a nitrite configuration. This type of analysis may provide a great deal of insight into the molecular interactions. In this way the described studies, as well as related theoretical and practical studies, have brought the potential of graphene-based sensing capabilities to a higher level through the improvement in the characterization of utilized films and, thus, the better understanding of the transpiring molecular interactions.

Based upon the presented possible interactions of small gas molecules and graphene, especially that of NO, this type of functionalization was also developed for the sensors here. Most of the discussed results from literature deal with environmental gas monitoring, therefore, in the case of practical sensing studies, measurement conditions are typically in air. For the sensing applications considered in this work, detection of NO must take place in a fluid environment. The primary goal was, therefore, to initially develop a compatible fabrication technique and assess the potential for NO sensing based on the AlGaN/GaN ISFET. As stated above, the Hummers method was utilized here for the formation of graphitic oxide, followed by the reduction of this material and dispersion in deionized water (DIW). To complete the functionalization process the produced graphene sheets must be positioned at the gate of the ISFET. Realization of this task was achieved through a developed "spray-on" technique of the graphene dispersion. This process is schematically depicted in figure 4.11.

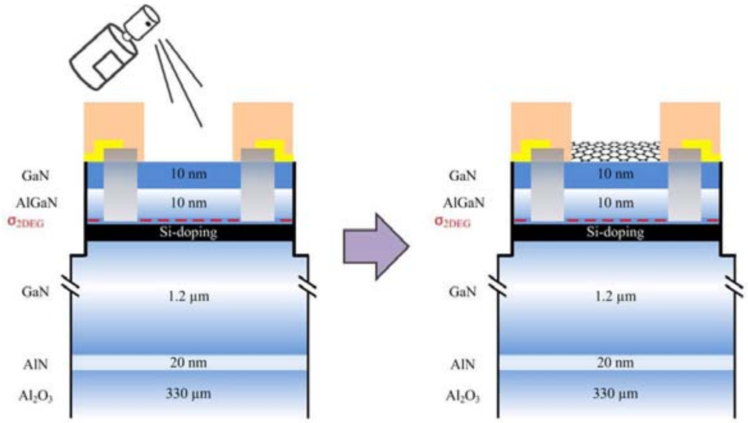

Figure 4.11: Schematic depiction of reduced GO spray-on technique

Following the application of graphene to the sensor-chip surface, thorough rinsing of the sensor-chip surface was carried out following a short drying period of approximately 2-3 minutes. This results in a distribution of the graphene flakes across the GaN surface which may be seen in the SEM images in figure 4.12. Here the typical wrinkled structure of the graphene sheet may be observed.

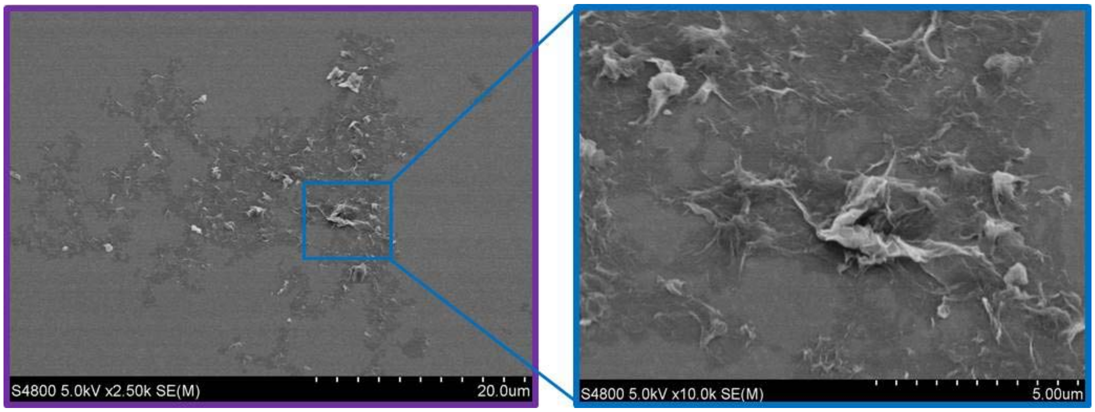

Figure 4.12: SEM images of graphene flakes on the GaN gate surface following spray-on deposition.

Two final techniques were evaluated in addition to the tungsten oxide and graphene films. These include porphyrin attachment and an Al_2O_3 layer. These will be covered here only briefly as arising issues with fabrication processes or passivation damage hindered stable measurement utilizing these techniques.

4.3.3 Porphyrin

Nitric Oxide sensing based on porphyrinic films is one of the original and most well-known techniques to date, for example the detection of NO from a single-cell by Malinski, et al., only a few years after the discovery of NO, was covered in Chapter 3. In this case a microelectrode was utilized and electrochemical deposition was carried out using differential pulse voltammetry (DPV) [151]. Porphyrin based sensing stems from the advantageous electron transfer capabilities in addition to allowing the possibility to control the redox chemistry of the central metal. This may be better understood upon examination of the general porphyrin structure in figure 4.13a as well as that of the metalloporphyrin with Ni as the central metal, Nickel (II) tetrakis(3-methoxy-4-hydroxyphenyl) porphyrin (Ni(II)TMHPP), in figure 4.13b.

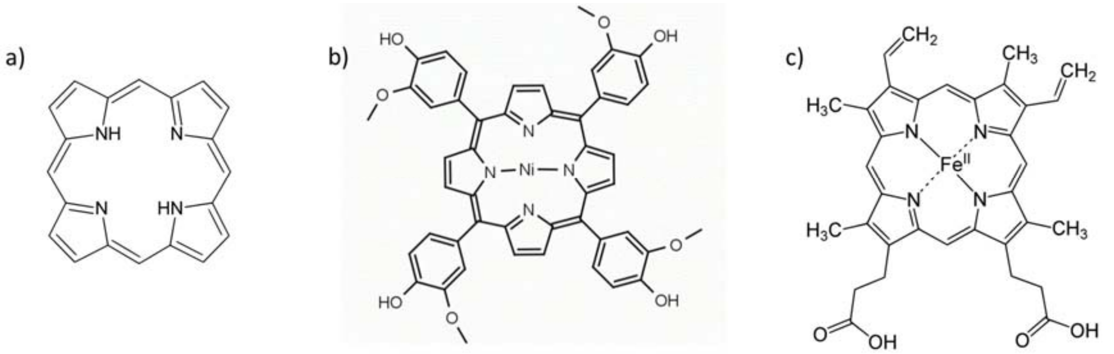

Figure 4.13: a) Simplest porphyrin structure b) Nickel (II) tetrakis(3-methoxy-4-hydroxyphenyl) porphyrin c) Heme B, well known porphyrin and cofactor of hemoglobin [275]

This central metal may be varied through chemical processes, including examples such as iron (Fe^{2+}), zinc (Zn^{2+}), tin (Sn^{4+}), chromium(Cr^{2+}), manganese (Mn^{2+}), copper (Cu^{2+}), magnesium (Mg^{2+}). The naturally occurring and most well-known metalloporphyrin, heme B, contains Fe^{2+} as may be seen in figure 4.13c. This heme is found is proteins such as hemoglobin, myoglobin, the peroxidase enzyme family and endothelial nitric oxide synthase. Metalloporphyrins modeled on this iron-containing heme are particularly interesting in regard to the NO scavenging behavior of hemoglobin due to the heme B cofactor [133, 158]. This concept, along with the demonstration of good catalytic behavior of polymetric metalloporphyrin films for the electrochemical oxidation of small molecules, has led to their use for a variety of sensing applications.

To facilitate the use of porphyrins or films incorporating porphyrins, deposition techniques must be established. Currently, functionalization of electroactive surfaces with porphyrin has been demonstrated by chemisorption, attachment to previously functionalized electrodes through chemical reactions, chemical reactions with a functionalized polymer, incorporation of the porphyrin with the polymer film, and electrochemical polymerization electrochemical techniques [186]. As the surface to be functionalized in the case of this study is not an electrode surface, electrochemical deposition methods must be disregarded. Chemical interaction with the target surface through simple drop-casting or dip-coating methods was therefore taken into consideration as a reasonable potential approach. The intended chemical interaction was to achieve direct surface attachment through the use of surface hydroxyl groups (fig. 4.14).

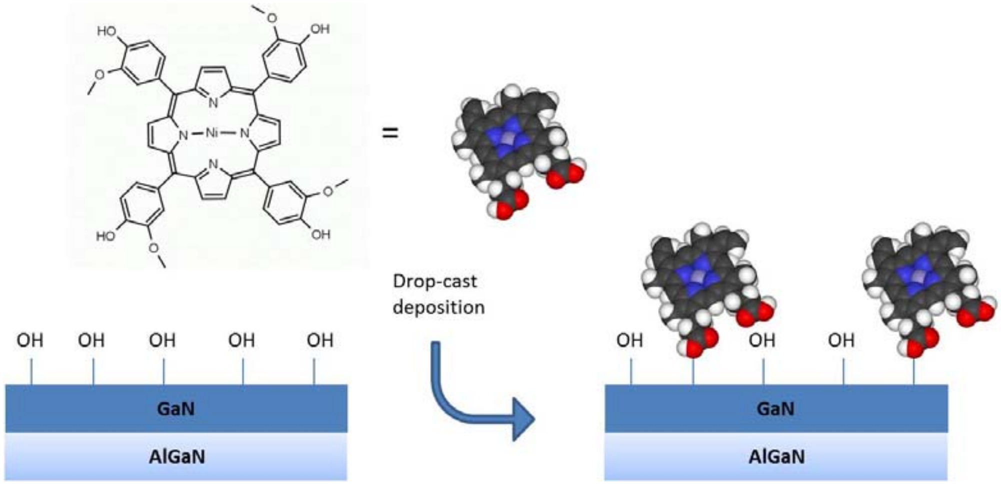

Figure 4.14: Surface functionalization through metalloporphyrin attachment [274]

The Ni(II)TMHPP was dissolved, utilizing ethanol as the solvent and drop-cast onto the sensor surface. This was allowed to dry for at least 30 minutes at room temperature before a thorough rinsing of the sensor. A diminished sensitivity was, however, demonstrated through the use of this technique as will be presented in Chapter 6. It may therefore be concluded that the surface attachment was unsuccessful and/or inhibition or blocking of the catalytic center of porphyrin took place. Additionally, as was visually observed in several instances, passivation damage occurred or contamination remained on the GaN gate area, reducing the effective surface area.

4.3.4 Aluminum Oxide (Al_2O_3)

Aluminum oxide (Al_2O_3) or *alumina* is a potentially useful material, particularly when the compatibility with the utilized material system is taken into account. Al_2O_3 forms the foundation of the device as the AlGaN/GaN heterostructure growth takes place on sapphire wafers. Due to the often proclaimed interaction of NO with metal oxides, in addition to specific sensing applications based on nano-alumina, a process to functionalize the GaN gate surface with Al_2O_3 was developed here [252, 253, 272, 273]. Atomic layer deposition (ALD) was employed to deposit an amorphous 20 nm Al_2O_3 film across the entire substrate. An etch-resistant photoresist is utilized to mask the areas in which the alumina layer is desired and a hydrofluoric acid dip is carried out to etch the superfluous material (fig 4.15). Following this structuring of the Al_2O_3 layer a thermal annealing at a temperature of 700 °C may be employed to achieve polycrystalline films and to increase the dielectric constant.

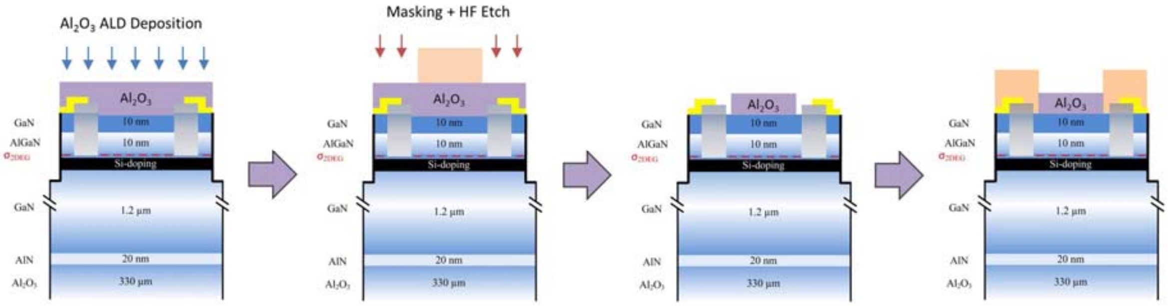

Figure 4.15: Functionalization of sensor surface with aluminum oxide

This technique was relatively unsuccessful with low NO sensitivity for the experiments carried out in this study; additionally, arising fabrication issues provided obstacles in some cases. The problematic processability may be recognized in figure 4.16 by the peeling appearance of the alumina layer (with blue tint) at the gate region.

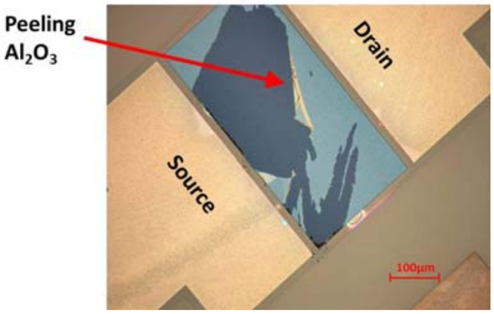

Figure 4.16: Fabrication difficulty with Al_2O_3 layer structuring

This problem typically occurred on samples with thicker (>100nm) Al_2O_3 films. Nevertheless, the possibility to overcome these issues through optimization exists and sensitivity testing was carried out here on samples with thinner films, despite imperfect structuring. As stated, the results, which will be covered in Chapter 6, show relatively low NO sensitivity. This procedure is therefore mentioned only as a side note as Al_2O_3 is known to demonstrate good pH sensitivity, therefore the reduced NO sensitivity could provide useful for simultaneous monitoring of NO and pH (or other analytes), as is the desired goal for the sensor array presented in Chapter 7.

4.4 Measurement Procedure

Due to the piezoelectric nature of the heterostructure as well as the light sensitivity issues covered in Chapter 2, care must be taken in order to achieve a stable measurement set-up. Chronoamperometry techniques were applied for the majority of measurements carried out in this research. These measurements were carried out inside a metal box-like structure which could be grounded proving a quasi-faraday cage. This aids in reducing electrical noise from the environment as well as providing a lower level of "light pollution" from ambient sunlight. Prior to amperometry measurements, initial testing is also carried out to ensure that good contact to the 2DEG has been made and to determine the maximum sensitivity regime is known and utilized.

4.4.1 Material and Device Characterization

Before reaching the final testing stage of developed sensors, various film or process characterization steps take place. Test structures are often employed in these instances to ensure achievement of necessary electrical properties, such as whether the 2DEG has been effectively contacted and individual ISFETs have been electrically separated during etching processes. Furthermore, material properties such as resistivity, sheet carrier density and mobility of the charge carriers may be determined. To quantify the latter three properties, hall structures are commonly employed; examples of those used in this work are shown in figure 4.17. Representations of Van der Pauw geometries are indicated by the yellow circle (rectangular structure), green circle ('clover-leaf'), and orange circle ('Greek cross') structure; variations which have been demonstrated to provide more accurate results depending on material system and fabrication constraints such as contact size [276]. In the case of the AlGaN/GaN heterostructures in this research, the uniform thickness of the 2DEG may be assumed and additionally the contact size typically does not present a major complication, making the rectangular and Greek-cross structures the most useful. Detailed information on the theory for hall measurements may be found in [276] as well as a detailed analysis of the AlGaN/GaN material system in [54]. As stated, hall measurements were employed in this work to determine charge carrier concentration and to ensure structural quality; often results are also correlated to the obtained values through the use of the capacitance-voltage (CV) structures, one of which is indicated by the blue circle in figure 4.17.

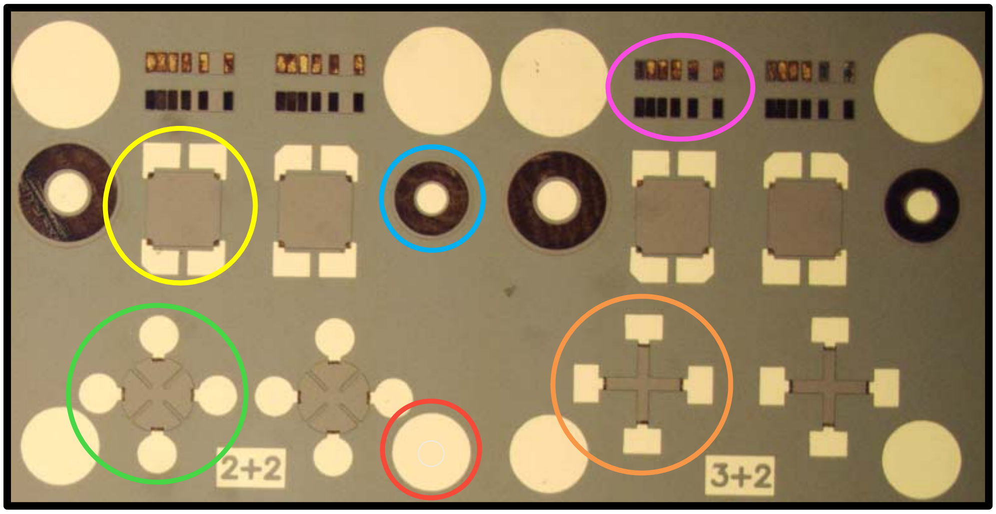

Figure 4.17: AlGaN/GaN test structure chip for the characterization of heterostructure growth and fabrication processes. Yellow, green, and orange circles represent various Van der Pauw hall structure geometries. A TLM structure is indicated by the pink oval, and CV measurement structure by the blue circle and an IV or CV test structure by the red circle.

The CV method may be utilized to derive the depth profile and charge carrier concentration of the barrier(/cap) layer(s) and 2DEG, respectively, through the use of assumptions based on the plate capacitor model, as has been shown by Ambacher, et al. and elaborated on by Donahue, et al. [11, 56]. A cross-sectional view of this structure, along with the typical Si-based metal insulator semiconductor (MIS) CV counterpart structure for comparison, is given in figure 4.18 [56]. The upper metal Schottky contact is the inner gold circular contact in this microscope image. The outer darker torus shaped portion is the contact to the underlying 2DEG which acts as the "back electrode"; this may be better visualized through the cross-sectional schematic in figure 4.18. In this portrayal the "inner 2DEG" is understood as the area found directly under the Schottky contact, and the "outer 2DEG" is found in the region between the edge of the Schottky contact and the ohmic contact to the 2DEG.

Figure 4.18: Typical Si-based MIS structure in comparison to the AlGaN/GaN structure [56].

Fabrication of structures which allow for utilization of the transfer length method (TLM) was also carried out. These may be utilized to determine contact resistance and, as mentioned above, to simply validate that contact to the 2DEG has been achieved. Finally, CV or IV structures, such as the example indicated by the red circle in figure 4.17, may also be utilized for various purposes. In this thesis this type of structure was typically employed to test preliminary structuring possibilities for passivation materials, as well as to examine the electrical integrity of these insulating materials. A cross sectional view of this layout, corresponding to the structure shown in this red circle, is presented in figure 4.19. A lower round metal contact is structured via lift-off, followed by deposition of the insulating layer to be assessed. An etch mask is deposited and structured in order to define the dielectric circular area (alternatively lift-off or direct photostructuring may be used if the material is compatible or photosensitive, respectively). Lastly, the upper contact is defined, once more through photolithography techniques. After completion of the structure, resistivity and break-down information on the dielectric film can be obtained. The upper and lower contacts are connected to a probe station (Keithley 2400) and a voltage range is scanned while observing leakage current through the insulating material. Utilizing the film thickness, characteristic dielectric properties and breakdown information with dependence on the applied electric field may be extracted from the resulting IV characteristics.

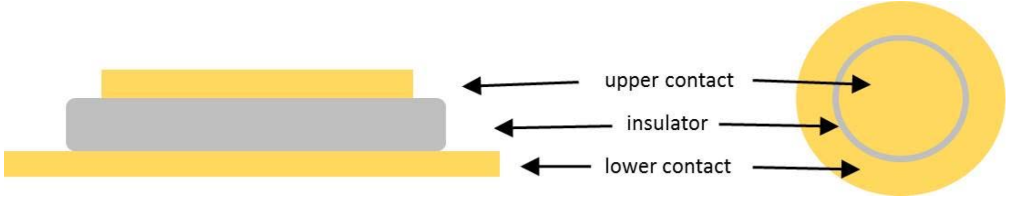

Figure 4.19: IV test structure for characterization of dielectric film integrity

Once a stable foundation has been established and fabrication/necessary packaging of the sensor chip has taken place (fig 4.6), characterization of the ISFET may be carried out. In this case the source, drain and reference electrode are connected as schematically shown in figure 4.20. Typical transistor curves such as the transfer and transconductance characteristics may be measured utilizing this same measurement setup and the appropriate analysis tool and software again in this case a Keithley 2400 with two source measure units (SMUs) and LabVIEW® programs to apply desired drain-source or reference potentials and read out the current.

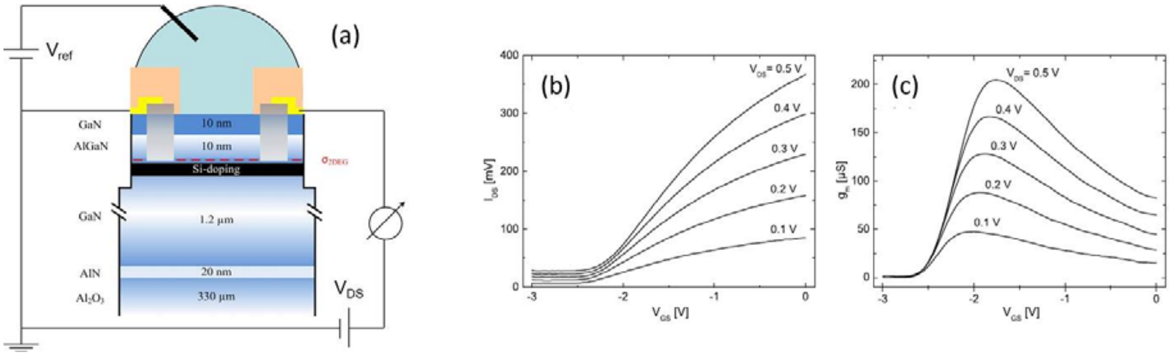

Figure 4.20: (a) Measurement connections showing source-drain bias (V_{DS}), gate bias through the use of a reference electrode (V_{ref}) as well as the readout of drain-source current I_{DS}. Representative transfer (b) and transconductance characteristics of a single AlGaN/GaN ISFET [197]

Diverse information such as proper operation of the transistor (this is relevant when examining contamination concerns as discussed in Section 4.2), and specific properties like transfer and transconductance characteristics or threshold voltage (fig 4.20 b, c) In the case of EGFETs the corresponding the variation of surface potential may also be measured or derived to determine analyte sensitivity. Conversely, the reference potential may be held constant and transfer IV curves may be recorded over various concentrations of the analyte; this has been well demonstrated for pH by Bergveld, et al. [194, 197].

4.4.2 Sensor Characterization and Solution Preparation

Simple phosphate buffer solutions were employed to maintain stable fixed pH values. These buffering systems are prepared using monopotassium phosphate (KH_2PO_4), disodium phosphate (Na_2HPO_4), and dipotassium phosphate (K_2HPO_4), to attain approximate desired pH values with the subsequent addition of hydrochloric acid (HCl) to adjust the pH to the exact value if necessary. The phosphate buffer solutions utilized for sensor characterization include blends which yield pH values of 6.5 (PB6.5), 7.0 (PB7.0), 7.4 (PB7.4), and 8.5 (PB8.5). These may be used to determine H^+ sensitivity of the ISFET as well as to provide the basis (typically PB7.0) for preparation of solutions used to analyze NO sensitivity.

As NO is rapidly destroyed though reaction with oxygen, one option which can be used for measurement in and/or calibration of sensor systems involves the careful pre-preparation of solutions which must be carefully deoxygenated prior to bubbling with NO gas. The storage of the samples must also be done cautiously to prevent reintroduction of oxygen into the solution. One possibility to accomplish this task entails working under oxygen-free conditions during the preparation of fluid samples followed by rapid sealing of and freezing of the solutions using liquid nitrogen [165]. A more convenient option, particularly for the initial functionalization testing presented here, involves the use of a nitric oxide complex which releases NO into solution in a controlled manner. This allows for the preparation of various concentrations necessary for cascade measurements to assess NO sensitivity. The employed complex is a type of NONOate, which are compounds with the chemical formula $R^1R^2N\text{-}(NO^-)\text{-}N{=}O$, where R^1 and R^2 are alkyl groups as shown in figure 4.21a. The production of such adducts relies on the long-known reaction of NO with primary and secondary amines to form salts with this structure [277, 278]. The specific NONOate employed here is diethylenetriamine/nitric oxide (DETA/NO) adduct or 2,2′-(Hydroxynitrosohydrazono)bis-ethanimine from Sigma-Aldrich® (figure 4.21b). Calculated concentrations were prepared in solutions of PB7.0 and half-life times were calculated based on the work of Beckerman, et al. (table 3.2), which specifies the NO to be in solution saturated with air at room temperature, i.e. $[O_2] = 225\ \mu M$ [133].

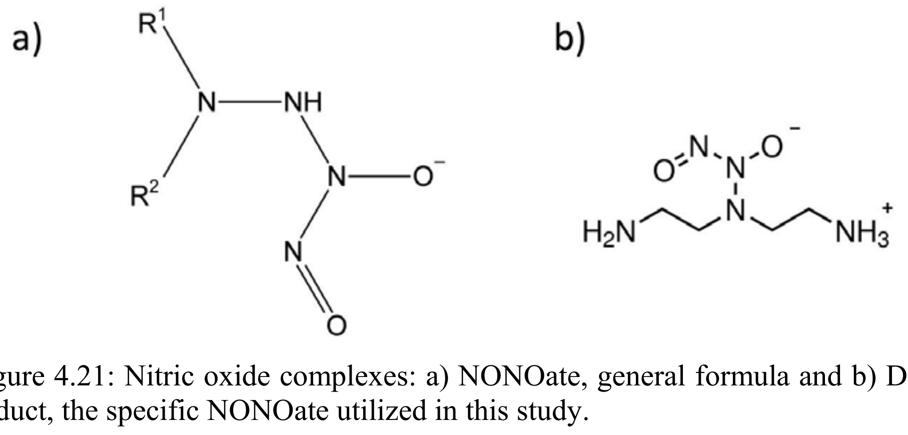

Figure 4.21: Nitric oxide complexes: a) NONOate, general formula and b) DETA/NO adduct, the specific NONOate utilized in this study.

Once preparation of pH and NO solutions is taken care of chronoamperometric measurement was typically made use of to examine sensitivity characteristics. The measurement cell is constructed from polyether ether ketone (PEEK) to allow for a fluid volume of approximately 7mL. The two-piece cell provides an opening for the surface of the sensor chip in the center at the bottom of the reservoir and a sealing ring which fits around this chip and prevents fluid leakage. From one side the contact lines on the ceramic circuit board are accessible to make electrical connection feasible. A schematic demonstrating this measurement setup is given in figure 4.22.

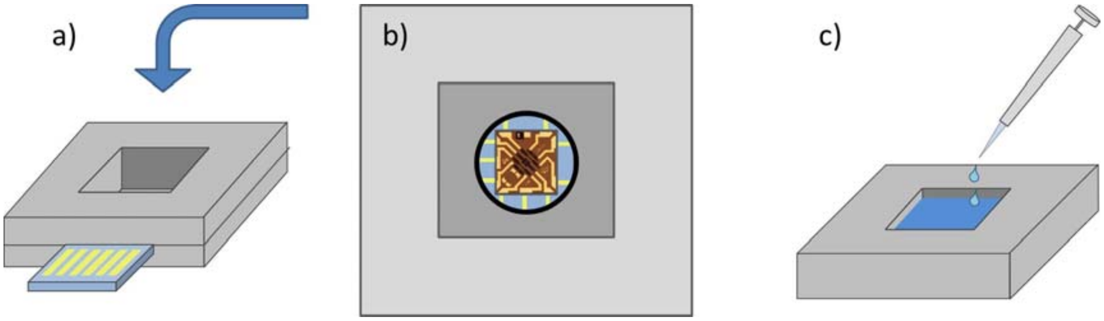

Figure 4.22: PEEK measurement cell a) side-view, b) top-view with sealing ring shown in black and c) depiction of pipetting during chronoamperometric measurements

After enclosure in this measurement cell and electrical connection to the ISFET, the reservoir is filled with the initial buffer solution. IV transistor characteristics are recorded to ensure proper connection as well as to analyze the general performance of the device. By exchanging the buffer for varying pH values the H^+ sensitivity may be found through analysis of the transfer characteristics and quantification of the threshold voltage. Similarly, chronoamperometry may be utilized by setting a constant V_{DS} and measuring I_{DS} as a function of surface potential or applied reference potential, V_{ref} or V_{GS}. In this research a 0 V reference potential was typically utilized and various concentrations of the analyte of interest were pipetted into the reservoir. This is fairly straightforward for pH measurement through calculation utilizing given phosphate buffer pH levels and the volume of the solution in the measurement cell and the solution to be added. In the case of NO measurement the time of the NONOate in solution must also be taken into account due to the discussed half-life of this molecule. The results of such experiments and a comparison of the functionalization methods will be presented in Chapters 6 and 7.

5. Passivation/Contamination Study

As discussed in the previous chapters, the passivation of the ISFET is a critical step, which has posed problems throughout the development of these devices due to comprised integrity after encapsulation and packaging [279]. Operation in a fluidic environment entails distinct requirements much different from the encapsulation of typical FETs or electronic devices in general. The utilized material (1) must provide good insulation of the metal contact lines to avoid leakage current, (2) must be stable over time, and (3) the patterning of this layer without damaging the underlying heterostructure or sensitive gate surface must be possible. Additionally, the resulting exposed surface defined through the structuring process must be completely free of the passivation material as the sensitivity of the ISFET is defined by this surface. In an effort to stabilize this issue for the AlGaN/GaN based system presented here, various passivation materials and techniques were investigated and characterized. Leakage current, fabrication issues and stability in solution were taken into account. The structural integrity after introducing the devices into a fluidic environment, and finally the effects of patterning on the 2DEG and surface contamination were considered.

5.1 Passivation Investigation

Several dielectric materials were considered to improve the passivation of III-nitride ISFETs. These include polyimide, SiO_xN_y, SiO_2, Si_3N_4, stacking techniques involving the latter two, Al_2O_3 and cyclotene. Polyimide is a well-known insulating material utilized in state-of-the-art devices such as implantable devices for biological applications including retina, neural implants [280, 281]. The relative dielectric constant of the final film depends on the specific polyimide, but typically ranges from approximately 2.9 to 3.5, with the variety utilized here lying at the lower end of this range. Advantages of this film include the known biocompatibility and various possibilities which exist involving the deposition and patterning [282, 283]. Polyimide films were therefore initially considered based on the given properties and the highly compatible nature of the deposition with the device fabrication process in this work. The specific utilized process firstly involves the spin-on deposition of an aminosilane based adhesion promoter to enhance adhesion of the subsequent polyimide (VM651 - HD Microsystems^{TM}). Spin speeds, as well as baking temperatures and times were selected according to the company specifications on the data sheet and were optimized in previous work [54]. Following application of the primer, the polyimide film (PI 2610 - HD Microsystems^{TM}) is then spun on at a speed of 800 rpm followed by 2750 rpm, resulting in a film thickness of approximately 1.8 µm. A temperature annealing step must then be carried out in order to cure the material, driving out the carrier solvent (N-Methyl-2-pyrrolidone - NMP) and obtaining the best possible electrical and mechanical properties. The optimal established conditions for this temperature anneal include a steady increase to 200 °C at 4 °C/min under ambient atmosphere, a 30 min holding step at 100 °C, and a subsequent ramp to 350 °C at 2.5 °C/min under nitrogen atmosphere. The substrate is held at 350 °C for 2.5 hours and brought slowly back to room temperature to avoid cracking of the film. At this point the resulting polyimide layer is fully imidized producing a stable passivation film which must then be patterned. To carry this structuring process out, a metal (Al or Ni) etch mask was first patterned through photolithography techniques and the exposed polyimide windows (fig 4.5, 4.6) were etched via various plasma processes which will be covered in the following section.

One of the known drawbacks of polyimide is that the advantageous encapsulation properties are compromised by water uptake and degradation [284]. Although the polyimide film used in this study demonstrates an improvement in these areas over previous polyimide varieties (0.5% moisture uptake vs 2-3%), SiO_2, Si_3N_4, and blends or stacking methods involving these materials were additionally considered in an effort to explore supposed “hard passivation” materials [286]. Dielectric constants of these films range from approximately 3.9 to 7-8, higher than that of polyimide or other available polymer films, however the possible reduction of fluid uptake along with the ensuing increase in leakage current is quite attractive [285]. Unstressed (62 MPa) films were deposited as well as introducing tensile (841 MPa) or compressive (-412 MPa) stress into these films through variations of growth conditions in an attempt at reduction of recognized issues such as development of pinholes in Si_3N_4 and SiO_2 [287, 288]. Stress measurements were carried out utilizing analogously deposited material layers on a standard Si wafer. Additional methods to suppress problematic film growth such as alternating material type to create a dielectric stack, or the inclusion of short etching steps throughout the growth phase, were also employed. Finally, a hybrid of the Si_3N_4 and SiO_2 was tested, producing a SiO_xN_y film. All films containing Si were deposited using plasma enhanced chemical vapor deposition (PECVD). This procedure will be described in the following section, in which a brief overview of various plasma techniques will be given. All hard passivation layers were deposited to result in a total thickness of approximately 200 nm. In the case of $Si_3N_4/SiO_2/Si_3N_4$ the deposition time for each layer was adjusted to give ~66 nm per layer, for a final thickness of 200 nm.

Structuring the passivation material through wet chemical methods as well as dry plasma etching was investigated. However, it must be taken into account (also in the case of polyimide) that etch processes utilizing fluorine ion (F-) bombardment, or ion bombardment in general, may affect the electrical properties of the 2DEG. In fact, F^- ion effects have even been positively exploited in the past to modify transistor properties with physical dependence such as threshold voltage [289, 290]. This effect will be further considered as well in the following sections.

Additional insulation materials were also taken into consideration including sol-gel, Cyclotene®, and Al_2O_3, however fabrication issue or immediate dielectric breakdown of the produced film hindered further investigation. Therefore, the following will cover only results and achievements regarding polyimide and Si-based passivation films.

5.1.1 Plasma Etch Processes

The physics of plasma processes is an extremely complicated subject within itself. Since the beginning of the seventies plasma processes have been developing; etch processes as well as sputter deposition or PECVD have made considerable progress. However, many factors take part in the ignition of plasma as well as the ensuing additive or subtractive processes. Included in these factors are plasma process parameters (gas, flow, pressure, power) as well as less influential factors such as chamber geometry, material of the reactor, and so on [291, 292, 293, 294].

The development of plasma takes place through the ionization of neutral atoms/molecules through the dissociative processes occurring due to collision with free electrons. This results in a partially ionized gas with a wide range of properties dependent on the stated process parameters. In general, capacitively coupled RF plasmas are the most common in dry etching [293]. The most well-known system used to accomplish this task is reactive ion etching (RIE) as a result of the simple design. Alternative methods including inductively coupled plasma (ICP) and electron cyclotron resonance (ECR) may also be employed, particularly when low pressure environments or reduction of ion bombardment are desired. Schematics of each of these plasma chambers are given in figure 5.1. Typically, power is applied to the upper or lower electrode at a frequency of 13.45 MHz, at which the free electrons can follow the variations of the electric field and, if collision is avoided, gain considerable energy while the positive ion movement is much lower as they gain most of this through thermal energy as their movement is much slower [294]. Due to the longer ranging movement of the electrons, they collide more often with the electrodes and reactor walls, resulting in the development of a DC electric field in order to maintain charge neutrality and to repel these electrons from the walls/electrodes. The capacitor shown in each schematic between the electrode and the power generator aids in the formation of this DC charge. Usually the DC bias is controlled by the various factors influencing the plasma itself and etching or deposition processes. The AC signal is then superimposed onto this DC bias.

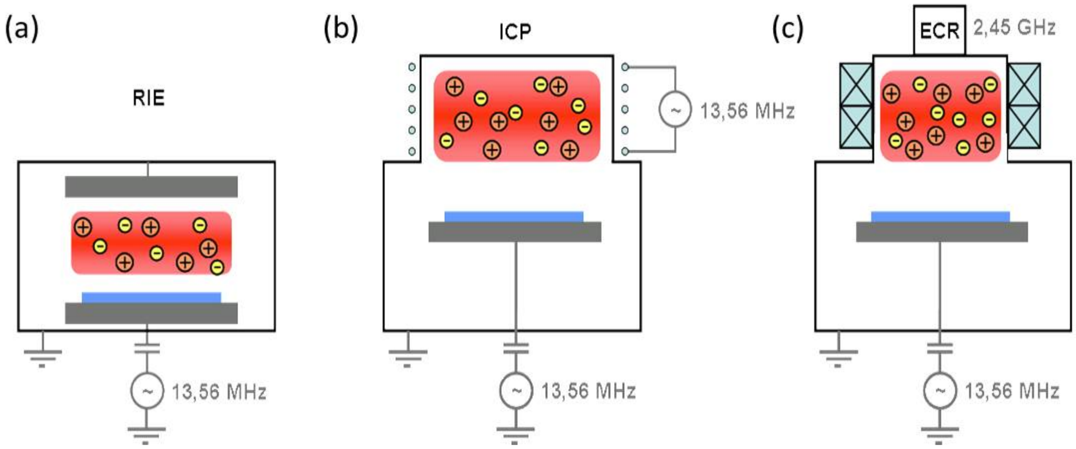

Figure 5.1: Example reactor construction for RIE, ICP, and ECR plasma chambers [295]

Reactive ion etching

Reactive ion etching is commonly employed in research institutes as well as industrial applications to accomplish dry etching tasks. This is a result of the simple design of the parallel plate reactor. Although the straightforward reactor construction provides a significant advantage, there are disadvantages as well regarding this technique. As discussed above, capacitive coupling is utilized to couple energy into the system and create reactive species through collision of free electrons with molecules of the utilized gases. This manner of energy coupling restricts the possibilities for etching or material deposition since the resulting plasma density is limited. This issue becomes more prominent at lower pressures, which are often desired in order to improve anisotropic etching and thus the material aspect ratios. ICP and ECR techniques provide alternative options in which low pressure plasmas may be realized.

Inductively coupled plasma

ICP techniques achieve higher plasma densities by means of power transfer through magnetic fields brought about by inductive coupling. This magnetic field, and the subsequent plasma generation, is induced as an RF voltage is applied to the coil wrapped around the chamber through which the used gases are introduced. This coil is represented in figure 5.1b by the circles on either side of the reactor section containing the plasma depiction. Once the plasma is formed, an electric field is formed within the reactor according to Faraday's Law which essentially relates the rate of change of the magnetic field, B, to the electric field, E:

$$\nabla x E = -\frac{1}{\mu}\frac{\delta H}{\delta t} \qquad 5.1$$

where μ is equal to $\mu_r\mu_o$, the relative permeability and the permeability constant ($4\pi \times 10^{-7}$ H·m^{-1}), respectively. To sustain ICP high RF power is necessary, typically on the order of 100 W. However, by employing this high power the desired high density plasma at low pressure may be obtained. In this research ICP processes are utilized only to achieve the mesa etching fabrication step. This anisotropic etch of GaN and AlGaN has previously been optimized and provides the electrical separation of the specific ISFETs [15, 16, 54]. This process has been discussed briefly in Chapter 4, and as the ICP has no further relevance and the standard etching processes were employed it will not be discussed further.

Electron cyclotron resonance

Electron cyclotron resonance (ECR) is a technique less often utilized in industrial practice, however may be quite useful for specific applications or requirements in research and development settings [291]. The main disadvantage, particularly relevant for industrial applications, has to do with lack of uniformity with increasing substrate size. As substrates employed here are relatively small ($\emptyset = 2"$), this does not impose a problem and the possibility for process variation may be exploited. The working principle involves a magnetron, located at the label 'ECR' in figure 5.1c from which a 2.45 GHz signal is produced and directed through the use of a waveguide in the direction of the substrate. This microwave generation along with the deflection of electrons through the use of a magnet allows for ECR to be attained. Plasma is generated through the coupling of the AC electric field with the frequency, *f*, at which the electrons rotate in the applied constant magnetic field, *B*:

$$2\pi f = \frac{eB}{m}. \tag{5.2}$$

Although the chamber design can impact the produced plasma, in some cases resulting in less density at the substrate level, in general a main advantage of the ECR plasma is a more dense plasma in relation to RF capabilities. This is possible at low pressures of less than 10 mTorr, but high magnetic fields of approximately 875 G are required at a magnetron frequency of 2.45 GHz.

In this case, the ECR method is interesting for the developed technology due to the reduction of ion bombardment while maintaining film removal during plasma etching. Specifically, this relates to the process step in which the passivation layer is patterned. This patterning takes place at the sensitive surface of the device, where the underlying 2DEG integrity is at risk when plasma-induced damage may occur due to ion bombardment. Observable damage to the 2DEG, measureable through variations in sheet resistance (R_s), demonstrates the delicate nature of this step. This type of effect has also been shown by Basu, et al. and later by Linkohr, et al. in studies looking into the electron transport properties of AlGaN/GaN heterostructures following plasma treatment [289, 296]. In these studies, the effects of fluorine (F) adsorption into the barrier layer and the resulting ion-induced damage or etching of the GaN surface were understood to have detrimental effects on 2DEG properties. Although some recovery of transport properties could be attained through annealing, in some cases with a slight increase in sheet carrier concentration, N_s, due to a shift in the surface potential, avoiding physical ion bombardment and/or etching of the surface altogether would be optimal. Therefore, the realization of this type of process was one of the main objectives of this work in order to achieve a reliable process with controllable sensor results. In order to achieve this goal practically, potential process variations were considered, some of which are included in table 5.1 (etch rates in this table are specific to polyimide).

Decreasing the RF bias as much as possible to avoid accelerating ions towards the substrate surface is desired. As the plasma density and ion energy are strongly connected in capacitively coupled plasmas, and additionally tend to linearly increase with RF power, alternative systems such as the ICP or ECR were considered. The concept of utilizing DC bias only and avoiding RF altogether was developed, which is possible in the case of ICP or ECR as the plasma induced through inductive or resonance coupling. The further possibility to modify the specific ECR used in this study presented itself, thus this was employed to carry out a comparison of DC vs RF along with process variations such as employing a gas ring which provides a more homogeneous introduction of gas into the chamber as well as utilization of a raised substrate holder, bringing the substrate approximately 10 cm closer to the plasma. All processes in table 5.1 are therefore carried out in the ECR system. This portion of the study resulted in a successful extremely stable O_2 etch process for polyimide which creates little or no measureable effect on the 2DEG. The etch rate is somewhat low, approximately 33 nm/min, however the lack of ion bombardment and/or adsorption onto/into the AlGaN/GaN barrier and cap layers proves to be very consistent. This process allows for complete material etching across the entire wafer, despite non-uniform thickness of the polyimide due to spin-on deposition edge effects, without damaging centrally located chip which are exposed to the plasma for longer periods of time.

Table 5.1: Overview of ECR plasma etch process variations

Process Nr	O_2 %	CF_4 %	Other %	Pressure ($*10^{-3}$ mbar)	Bias	Etch Rate polyimide (nm/min)
1	100			2.5	-50V DC	10
2	80	20		2.5	-50V DC	37
3	80		20(SF_6)	2.5	-50V DC	25
4	80		20(CHF_3)	2.5	-50V DC	27
5	80	20		1.25	-50V DC	30
6	80	20		5	-50V DC	24
7	20	80		2.5	-50V DC	19
8	100			2.5	-100V DC	33
9	80	20		2.5	-100V DC	42
10	80	20		2.5	5W (-110V)	124
11	100			2.5	20W (-205V)	139
12	92	8		2.5	20W (-205V)	187
13	88	12		2.5	20W (-205V)	186
14	80	20		2.5	20W (-205V)	177
15	70	30		2.5	20W (-205V)	186
16	60	40		2.5	20W (-205V)	184
17	0	100		2.5	20W (-215V)	65

Lastly, for dielectric material comparison *not* carried out on the AlGaN/GaN heterostructure, plasma etching may be utilized to structure the Si_3N_4, SiO_2, and related passivation systems. However, in the case where the 2DEG is present, all plasma processes which provide reasonable etch rates for these materials created permanent damage. Wet chemical processes were therefore investigated as a means to pattern Si-based dielectric films.

5.1.2 Wet Chemical Etch Processes

As a result of ion-induced damage generated by plasma etch processes the use of wet chemical etching was explored in the case of Si-based materials. Established recipes with well-defined etch rates exist for standard SiO_2 or Si_3N_4 films in literature. Hydrofluoric acid (HF) dips are often employed in etching process steps for oxides, particularly in the form of buffered oxide etchants (BOEs). This type of BOE solution consists of diluted HF buffered with ammonium fluoride (NH_4F); the role of the NH_4F being to replenish the fluoride ions as they are consumed during the etching process. BOE has a very high selectivity against Si, and is thus often utilized to etch SiO_2 layers while leaving the Si substrate or layer intact. Etch rates depend, to some point, on the strength of HF within the BOE solution [322]. Phosphoric acid (H_3PO_4), on the other hand, etches Si_3N_4 with high selectivity against SiO_2. This etch selectivity may be further enhanced through the use of additives to the solution [323]. These etch solutions were starting point to develop potential etch recipes for the film variations investigated in this thesis. Modifications were made according to the passivation technique (blended SiO_xN_y films or stacks of differing SiO_2/$Si3N_4$ layers). However, partially due to the isotropic etching of SiO_2, in most cases the wet chemical method was far less reliable for the required etching processes (the underetching due to this effect may be observed below in figure 5.5a). Additionally, significant contamination often remained on the sensor surface making measurement/characterization impossible. This structuring difficulty, along with material issues which will be presented in Section 5.3, rendered the hard passivation variations rather impractical for the final ISFETs, therefore these processes will not be discussed in great detail.

5.2 Material Comparison

Once the generated films were successfully deposited and patterned, test structures were employed in order to analyze the dielectric properties. As discussed in Chapter 4 (fig 4.17, 4.19), these consisted of circular metal contacts underneath and on top of structured passivation layers. The contacts were probed and IV characteristic curves were recorded. After analysis of the acquired data several materials could be ruled out due to immediate dielectric breakdown (fig 5.2a). PECVD of Si_3N_4 was performed in two separate tools in order to compare these films. The nitride layer with the lowest dielectric strength was deposited in the chamber of “tool 2” as may be observed from the much higher currents throughout the applied voltage range (dark green line fig 5.2a, b). This early breakdown may be attributed to the issue of pinholes mentioned above for films of Si_3N_4. This assumption is further supported by the fact that this utilized PECVD process demonstrating the earliest breakdown is improved slightly by incorporating short etching steps during the Si_3N_4 growth (light green, fig 5.2b). However, in the case of this film, the etching method did not improve the material quality sufficiently to contend with the further dielectrics. Most likely this has to do with process optimization for the specific tool, particularly since Si_3N_4 films from the first PECVD tool exhibited a much better performance.

Analysis of materials demonstrating useful results (fig 5.2c) reveals that the Si-based films perform relatively similarly to one another while polyimide (pink curve) outperforms all other materials, withstanding applied fields of *at least* 0.2 MΩ/cm. Additionally, throughout the scanned voltage range, observed currents in the polyimide films remained at least an order of magnitude below the next best performers. This is consistent with literature, where higher breakdown fields are often reported as well, up to 1-5 MΩ/cm [297]. In this case, the quantified field value simply represents the magnitude of the electric field at the highest applied voltage, 30 V. The polyimide film was not pushed to dielectric breakdown as 30 V is more than an order of magnitude above the voltage bias at which the ISFETs are operated. This initial material comparison based on the insulating properties alone set polyimide as the best performer. However, this does not include further significant constraints when employed as the ISFET passivation.

Due to the unique requirement of the ISFET to perform in a stable manner in a fluid environment, this aspect of the investigated materials was examined. The test structures were soaked in ionic solutions (PB8.5 or PB4) for one hour or more and were measured again immediately following removal from solution and a brief drying step to remove excess liquid

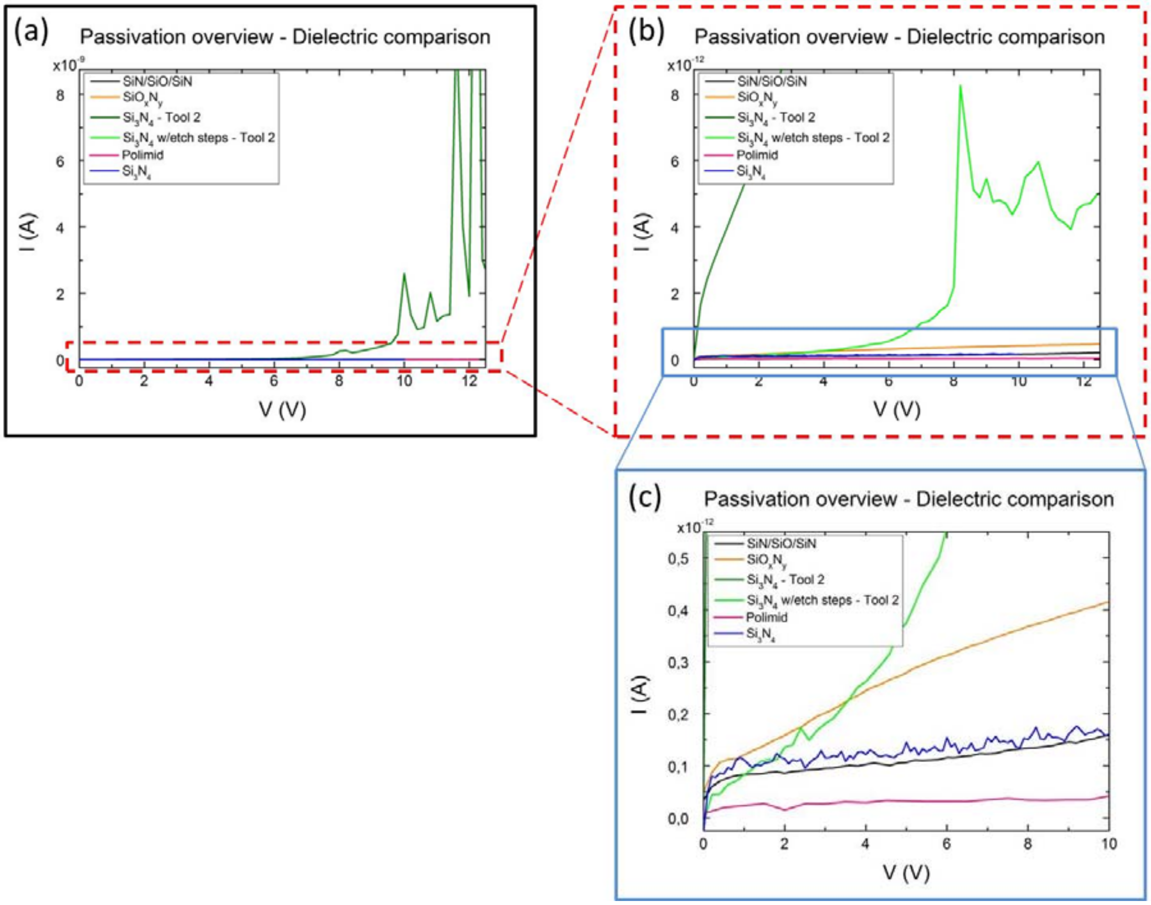

Figure 5.2: Comparison of various passivation materials through the use of IV measurements. a) Breakdown of low quality Si_3N_4 films b) Zoomed in view showing dielectric breakdown of the secondary Si_3N_4 film and c) Suitable films for further investigation: SiO_xN_y, $Si_3N_4/SiO_2/Si_3N_4$, Si_3N_4, and polyimide. Note: variations in the multiplication factor for the current magnitude are given at the top of the y-axis.

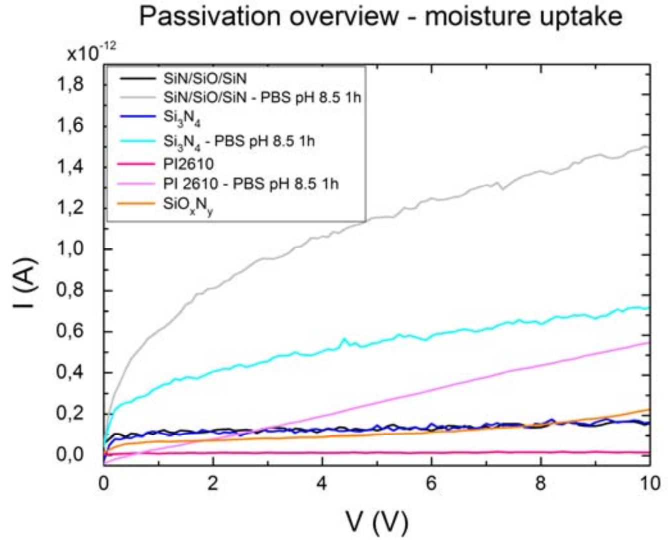

Figure 5.3: Passivation material comparison including exposure of each film to PBS pH 8.5 for 1 hour

at the outer surfaces. Negligible differences were observed for materials soaked in solutions with varying pH values, therefore only one variation (PB8.5) is displayed here. Surprisingly, fluid uptake was exhibited by all utilized films. Polyimide is known to demonstrate this effect; however, the "hard passivation" layers were expected to display this behavior at least to a lesser degree [298, 284]. This expectation stems from the reported lower porosity and utilization of films such as Si_3N_4 as a capping layer to hinder moisture adsorption [299]. Uptake by films involving SiO_2 on the other hand could be anticipated based on the studies of the 'gel-like' interface described in Chapter 3 with regard to the glass electrode and pH measurement principle. Indeed, the Si_3N_4 based films do outperform those containing SiO_2. As may be observed in figure 5.3, the resulting current in all films more than doubled, with an increase of an order of magnitude or more in $Si_3N_4/SiO_2/Si_3N_4$, SiO_xN_y, and polyimide. In this respect Si_3N_4 exhibits the best performance when looking specifically at moisture uptake. However, in the voltage range of interest and considering issues discussed in the following section, **polyimide prevails as the material with the most advantageous characteristics**. These characteristics, along with the developed **straightforward ECR etch process presented in Section 5.1**, provides solid evidence for **the advantages of polyimide utilization for standard AlGaN/GaN ISFET passivation.**

Additional silicon oxide/nitride based passivation issues

Further issues regarding the use of oxide or nitride based passivation films were additionally revealed during this investigation. The general lack of stability of SiO_2 in solution is fairly well-known. Chemical dissolution of oxides has been described in many instances [298, 300]. In an attempt to evade this problem SiO_2 was always placed at the inner location of a stack when utilized. Nevertheless, as demonstrated in the previous section, water uptake is still present in all films, meaning that the potential for this type of reported dissolution is still possible.

A secondary effect was recognized through the loss of electrical separation between individual ISFETs following deposition of the passivating layer. Typically, the ISFETs are electrically separated through the use of the discussed ICP mesa etching step (Section 4.2). This step results in the physical removal of cap, barrier, and some tens of nm of the bulk material between sensors, eliminating 2DEG electrical conduction between ISFETs on the same substrate. Deposition of silicon oxide or nitride passivation layers, however, resulted in a counterproductive induction of conductivity at the interface of the upper GaN layer and the passivation layer. This reintroduction of electrical connection or crosstalk between the ISFETs was observed to some extent for all oxide or nitride materials, presenting an additional issue for their consideration. The interface at which this issue is present may be seen in figure 5.4a for the example of the $Si_3N_4/SiO_2/Si_3N_4$ stacked passivation system. In this cross-section the interface where Si_3N_4 is in contact with the surface of the GaN cap layer appears quite minimal, although this is obviously not to scale. After examination of figure 5.4b it may be seen that the contact at this interface is in fact present over the majority of the surface, either with the upper GaN cap surface or (for the most part) with the etched sidewalls and lower GaN bulk layer. Only the labeled 'open gate' portion of the device etched during the final passivation etch does not have this material on top. Therefore, induced electrical conduction at the passivation/GaN interface creates a major problem due to cross-talk between transistors (fig 5.4b, red double-headed arrow).

Although such oxides and nitrides are often utilized as capping or passivation layers, a limited number of reports existing regarding the band offsets at the GaN/dielectric interface for SiO_2 or Si_3N_4 [205]. After observation of the induced conductivity once silicon nitride or oxide was deposited on the exposed GaN surface in this research, an explanation was sought, firstly through literature research to examine previously reported effects.

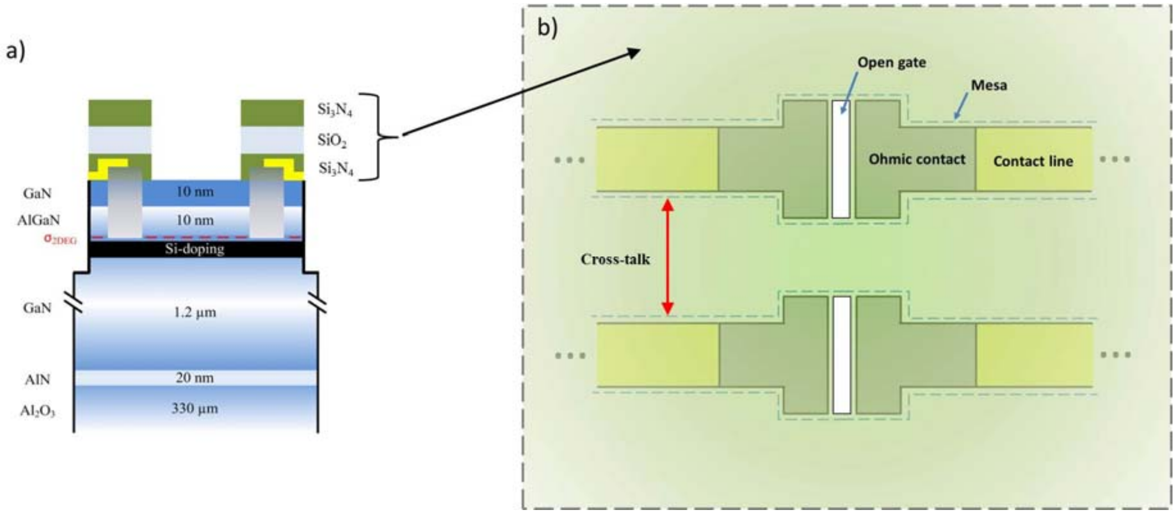

Figure 5.4: a) Cross-section and b) top view demonstrating passivated regions and possible crosstalk issues

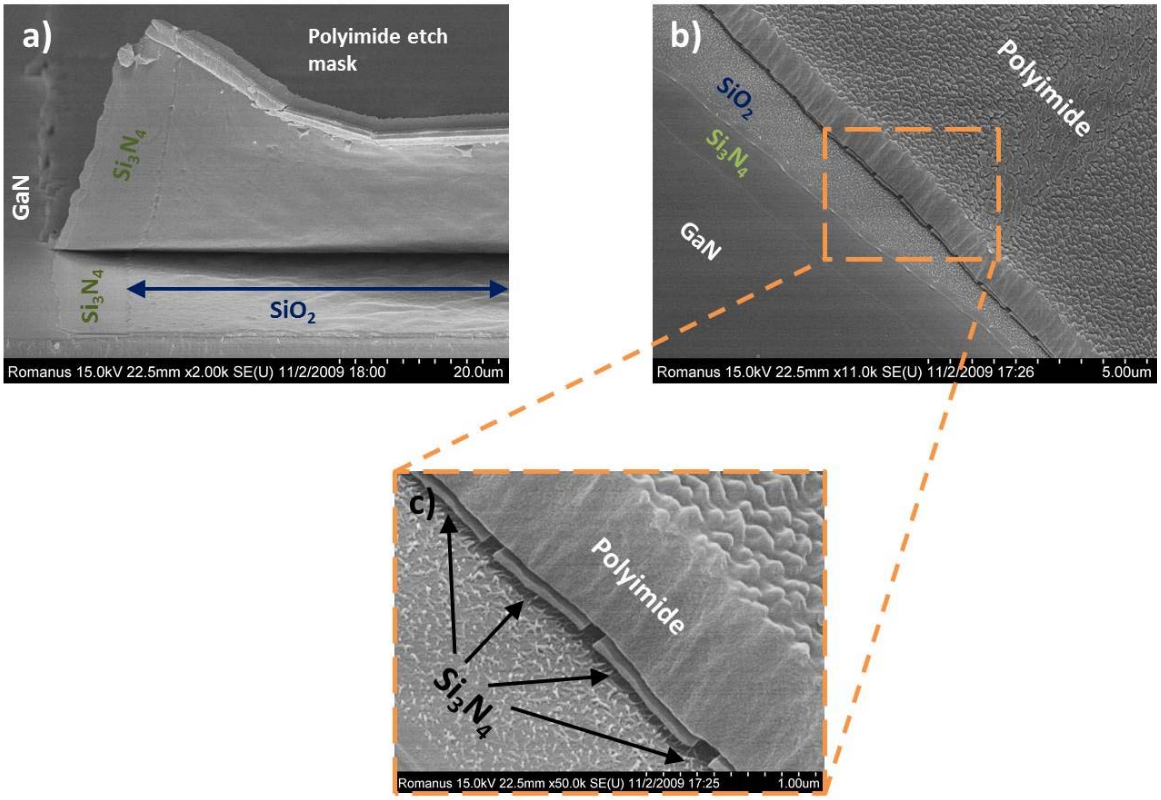

Figure 5.5: SEM visual demonstration of extremely stressed Si_3N_4 layers. a) Cross-sectional side view with the GaN gate surface (left) and passivation layers partially peeling due to mechanical stress of sample preparation. b) Angled view showing the polyimide (used as an etch mask in this case) and $Si_3N_4/SiO_2/Si_3N_4$ layers with c) zoomed view emphasizing the lower Si3N4 layer, including high tensile stress which is optically evident as the material physically splits in the horizontal plane without underlying contact/support.

The presence of electronic states at the GaN/dielectric interface seems to provide a reasonable clarification through the effects of electron trapping [250]. The influence of band offset due to interaction at the interface was shown to be particularly pronounced for the case of extremely strained Si_3N_4. Conductivity in nitride films was about an order of magnitude higher than those with GaN/SiO_2 heterojunctions. This corresponds well to the existing literature in which flatband voltage (V_{FB}) offset variations for GaN/Si_3N_4 or GaN/SiO_2 interfaces are considered [250, 300]. The flatband voltage is defined as the voltage at which the transition between the depletion regime and the inversion regime of a transistor or MIS/EIS capacitor structure occurs [205]. This is closely related to the threshold voltage through

$$V_t = V_{FB} - \frac{Q_B}{C_{ox}} + 2\phi_f$$

which was discussed in Section 3.4.2.1 due to the dependence of V_t, and thus V_{FB}, on the surface potential. In an MIS structure, V_{FB} is the potential at which there is no charge on the plates of the capacitor and thus no electric field is present across the insulator is present. Based on variations in V_{FB} information may be obtained regarding surface states, bulk trap states within the insulator or interface trap states at the dielectric/semiconductor interface [205, 300]. In the relevant studies for this research, ΔV_{FB} was shown to be 3-10 times higher for Si_3N_4 with the suggestion that interface traps cause the offset in oxide films, while bulk trap states are the source in nitride films. Consideration of this final issue regarding induced conductivity in nitride or oxide ‘hard passivation’ options gave enhanced support for the use of polyimide.

5.3 Surface Contamination

A final requirement in addition to the extreme importance of patterning the passivation layer without damaging the underlying 2DEG involves the complete removal of the insulating material from the sensitive surface. This has presented significant issues in previous studies involving the AlGaN/GaN heterostructure in a fluid environment. The AlGaN or GaN surface (more precisely the native or thermal oxide present at the surface) bestows the ion sensitivity of the device for standard ISFETs based on this material system. Remaining insulating material on this surface thus presents a significant issue through the reduction or complete blocking of the sensitive area. In previous work, a DI water soaking step of at least 24 hours in addition to mechanical removal utilizing a cotton applicator in addition was carried out to partially remove this contamination. Subsequently, approximately 5 h or more of electrical measurement was also necessary before the sensor surface was ready to be utilized in a stable manner. The latter treatment step may be carried out through continuous measurement until proper transistor transfer characteristics are obtained and depletion of the 2DEG is possible. This will be further described below regarding the results in figure 5.7.

Initial consideration of this issue brought about the use of various cleaning methods following process steps in which photoresist is in contact with the gate surface. The considered supplementary cleaning solutions were AZ100 and TechniStrip Micro D350 (dimethyl sulfoxide, DMSO), both supplied by MicroChemicals GmbH [286]. These options offer alternatives with lower vapor pressure in comparison to acetone, the standard utilized solvent for resist removal. The extremely fast evaporation of acetone may result in re-deposition of resist residue onto the substrate. AZ100, on the other hand, is a remover based on an amine-solvent mixture which has been specialized for the stripping of photoresist and has a much lower evaporation rate. Additionally, due to the relatively high boiling point, this remover may be heated to 60-80 °C, further improving the removal of photoresist. An additional promoted feature is its low attack on aluminum, which could prove beneficial in this case due to the presence of Al within the heterostructure. DMSO is a photoresist stripper which has developed as a non-toxic alternative to the powerful stripper, NMP (1-Methyl-2-pyrrolidon). This polar solvent may also be used at elevated temperatures due to it high boiling point and may be employed as a stripper or lift-off media. For the described fabrication process (Chapter 4), experiments with DMSO were performed at a temperature of 80 °C in place of acetone for lift-off steps to pattern metal contacts (ohmic contacts as well as contact lines). AZ100 was utilized at a temperature of 65 °C as a remover for the photoresist etch mask during the mesa etch when structuring the 2DEG.

In order to evaluate the potential benefit of these procedures, the Auger effect utilized. This is a material surface study technique which relies on ionizing radiation which causes a core electron to be ejected from an atom. This leaves a hole in the core level, which is rapidly filled by another electron. Through this process energy is emitted, either in the form of an X-ray or a secondary electron, the Auger electron. As this electron is dependent on the binding energies of the atomic energy levels and not on the energy of the incident radiation, elemental analysis along with analysis of bonding information may be performed [301]. This technique on its own is very specific to the surface atoms, with resolution down to sub-monolayer thickness and 20nm surface spatial area. The possibility to analyze hundreds of nm into the film is available as well when elemental depth profiling is carried out through the use of ion sputtering in conjunction with Auger analysis. This type of depth profiling was made use of in this study to analyze contamination level at the sensor surface. After comparison of the Auger spectra for the AZ100 sample and that of the sample fabricated under typical (acetone-based) conditions **it is clear that the carbon (C, black curve) levels are indeed lower for the device utilizing the AZ100 remover.** This signifies that the surface contamination is indeed organic and that the mesa etching step represents one process point, in which surface contamination is produced. Uncertainty regarding this step was previously present due to the temperature and unknown effects of the plasma on the cross-linking behavior of the resist mask.

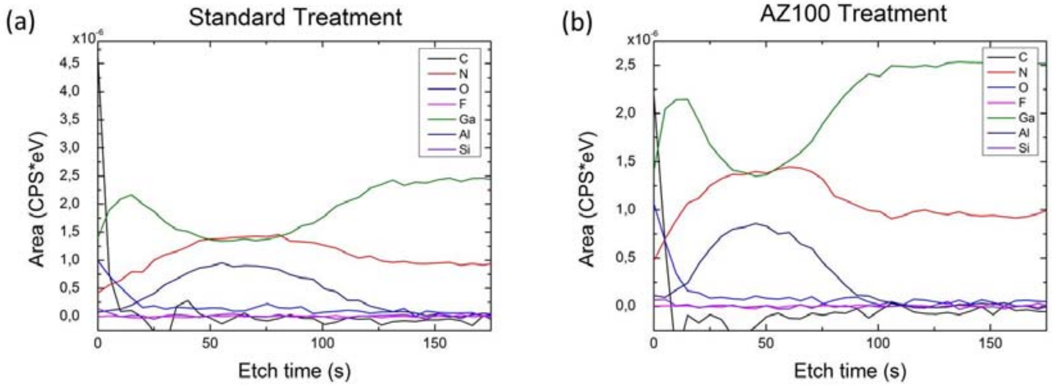

Figure 5.6: Auger spectra of samples with a) standard and b) AZ100 remover surface cleaning treatment. Higher carbon levels may be observed at the surface for the standard process.

In addition to the quantification of contamination levels on the surface by Auger techniques, electrical characterization was carried out through continuous measurement methods. This procedure was achieved through the use of ISFET transfer characteristics. Contamination at the surface shields the functional OH groups as well as acting as a quasi-dielectric layer creating an additional potential drop and preventing typical depletion of the 2DEG. This may be visualized in figure 5.7 where the transfer characteristic curves are presented to demonstrate effectiveness of cleaning procedures and the positive effect of the developed ECR plasma process. The measurements are carried out with the drain-source voltage is held constant, in this case at 1V. At V_{ref} values less than about -1V the ISFET should be “off” under proper operating conditions as the 2DEG is depleted in this case and pA I_{DS} values are observed. When V_{ref} is scanned to higher voltages the channel turns "on," the 2DEG accumulates, and mA range I_{DS} values are reached. As stated, contamination present on the gate surface prevents complete depletion of the 2DEG resulting in only about an order of magnitude variation between the on and off state. After continuous measurement of the ISFET this contamination layer is slowly decomposed until the transistor reaches a stable state and switches correctly. This reduction of contamination may be observed in figure 5.7 as the on/off ratio increases with measurement repetition. Figure 5.7a demonstrates the results using the described DMSO cleaning process, figure 5.7b that of AZ100, and figure 5.7c represents the effects of the ECR O_2 plasma clean.

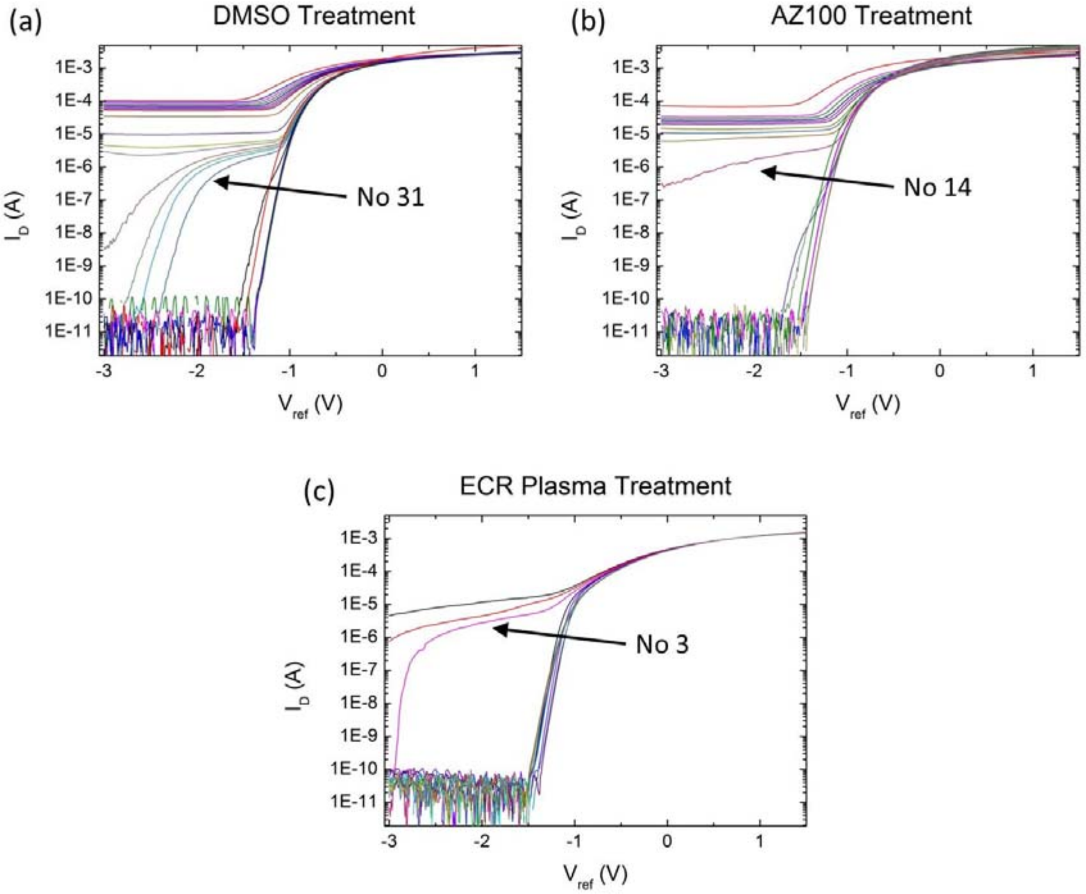

Figure 5.7: Demonstration of reduced surface contamination through repeated IV transistor measurement cycling for a) DMSO treatment, b) AZ100 treatment, and c) extended O_2 ECR plasma structuring. The data are plotted to demonstrate on/off ratio and, in the case of surface contamination, the inability to deplete the 2DEG resulting in the 'off' state

From these results it is easily observed that the AZ100 procedure results in a functional sensor in about half the time of the DMSO process (14 transfer curve measurements for AZ100 vs 31 recorded curves for DMSO). **Advantageously, the O_2 plasma clean results almost immediately in an ISFET which functions stably, only 3 measurements are necessary before proper on/off behavior is attained.** This is further demonstrated in Chapter 7 where sensitivity measurements for the miniaturized ISFET array drift only slight from the first measurement (without any continuous measurement procedure beforehand) and show very stable results after approximately 5-7 measurements. All cleaning procedures display significant improvement over the previous 24-48 *hour* contamination removal process, with the least efficient DMSO-only variant requiring less than 2 hours of measurement.

A final benefit of the developed ECR plasma etch process entails the highly anisotropic resulting profile. As one of the final goals is to develop a multi-sensor array (see Chapter 7), miniaturization of devices becomes necessary with increasing number of desired ISFETs. This logically requires the individual dimensions to be reduced. Isotropic etching can create significant fabrication issues when attempting to define small structures. Figure 5.8 demonstrates the highly anisotropic nature of the DC-biased ECR O_2 plasma etch process.

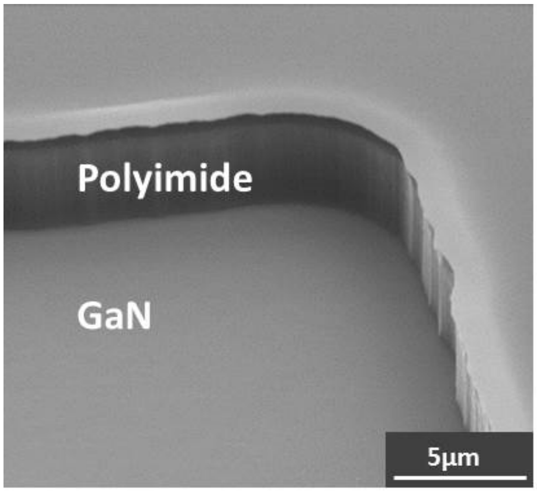

Figure 5.8: SEM image following ECR O_2 polyimide etch, demonstrating anisotropic etching resulting in near 90° sidewalls

This aspect ratio, in addition to the previously describe benefits of the developed DC bias O_2 ECR etch process provide a stable low-leakage passivation for the AlGaN/GaN ISFETs. With this solution a reliable basis is formed and the development of further sensing (or other) concepts may be researched and tested. This was exploited to investigate the possibilities for nitric oxide detection, the second main goal of this research which will be covered in the following chapter.

Key accomplishments demonstrated in this section include:

- realization of a stable passivation process through the use of polyimide, which demonstrates the best insulating properties in comparison to Si_3N_4 or SiO_2 based 'hard passivation' materials as well as offering a more biocompatible system
- development of a unique ECR plasma process developed to accomplish isotropic polyimide etching without measureable 2DEG damage
- contamination free sensitive open gate surface ensuring good device functionality from the initial measurement state of the ISFET, without need of additional cleaning procedures
- achievement of stable process conditions allowing for further functionalization and testing of AlGaN/GaN ISFET sensors for further analytes.

6. Nitric Oxide Sensitivity Study

The diverse biological roles of nitric oxide have made this molecule a subject of study since its recent discovery in the late 1980s [17, 110, 112]. In Chapter 3 a discussion on the significance of NO in neuroscience, immunology, and cardiovascular fields was presented. The ongoing desire to study NO within these fields and understand its influence in living systems drives the need for new and improved sensing possibilities. Various AlGaN/GaN ISFET functionalization techniques utilized in this research to develop NO sensors compatible with the fabrication of pH sensors on the same substrate were presented in Chapter 4. In this chapter the application of these functionalization methods and the ensuing measurement results are demonstrated.

6.1 Functionalization Sensitivity Comparison and Verification of NO Presence/ Sensitivity using Hemoglobin

Initially, in order to compare the performance of sensors with different functionalization materials, a standard I_{DS} vs time curve for various NO concentrations was measured (fig 6.1). This measurement was carried out separately for sensors employing each type of functionalization technique. For the results discussed here, square gate areas (W/L = 1) were used with an area of 500 µm x 500 µm. The measurement cell described in Chapter 4 was employed in order to bring the sensor in contact with the solution of interest. The beginning solution was PBS with a pH value of 7.4 (PBS7.4). V_{DS} in these measurements was set to 1 V and V_{ref} was held at 0 V. The sensor response was allowed to settle prior to the initial control measurements, which consisted of PBS7.4 additions into the measurement bath. These controls provide an idea of the stability of the sensor signal and ensure that this signal does not vary upon addition of fluid with a composition identical to that present in the bath. In figure 6.1 the initial control additions were made at approximately 300 s and 600 s. Subsequently, NO solutions were prepared using the previously discussed NONOate in the same PBS7.4 solution used for filling the preliminary measurement cell. Addition of NO solutions were made at 1000 s, 1300 s, 1700 s, 2700 s, and 3000 s to result in a final concentration of 750 nM, 1 µM, 1.1 µM and 1.2 µM, respectively. During this procedure further control measurements were also carried out at 2200 s and 3200 s to continually ensure that the sensor response was not affected by PBS7.4 additions. In figure 6.1 the signal drift due to decomposition of NO and diffusion out of the solution (see Section 3.3.1 and table 3.2) was calculated out in order to make the material comparison more visually straightforward. This diffusion and variation in concentration over time, however, was taken into account when calculating the final bath concentration. The normalized response of each curve was calculated, resulting in ΔI_{DS} on the y-axis. Each functionalization method is color coded and marked in the legend in the inset of the graph.

From this overall material comparison it may be concluded that the graphene and WO_3-based functionalization methods provide the only viable solutions of the examined techniques. Porphyrin, Al_2O_3 and the bare GaN gate surface were comparable in performance, although porphyrin has been often used in literature for NO sensing applications. The lack of good sensitivity in this case probably has to do with blocking of the catalytic center as a result of the deposition method or insufficient electrochemical potential to catalyze the reaction with NO (Section 4.3.3). The largest sensor response is provided by the nanostructured WO_3 layer due to the increase in NO sensitivity along with the large surface area. However, signal instability is also introduced as may be observed from the I_{DS} fluctuation. Therefore, further characterization was typically carried out using either the RTP oxidized WO_3 layers or the graphene functionalization method. The measured signal utilizing these methods is significantly higher as well as very stable. In further work, the nanostructured variant could be further optimized in order to combine the advantages of sensitivity and surface area enhancement.

In order to demonstrate the measurement result when the drift due to NO decomposition is not removed, an example of the raw data is given in figure 6.2. This measurement corresponds to that in figure 6.1, made using a 500 µm x 500 µm sensor with graphene functionalization at a V_{DS} of 0.25 V and V_{ref} = 0 V. The NO and control additions, as well as the resulting final concentrations, are therefore the same as those in figure 6.1.

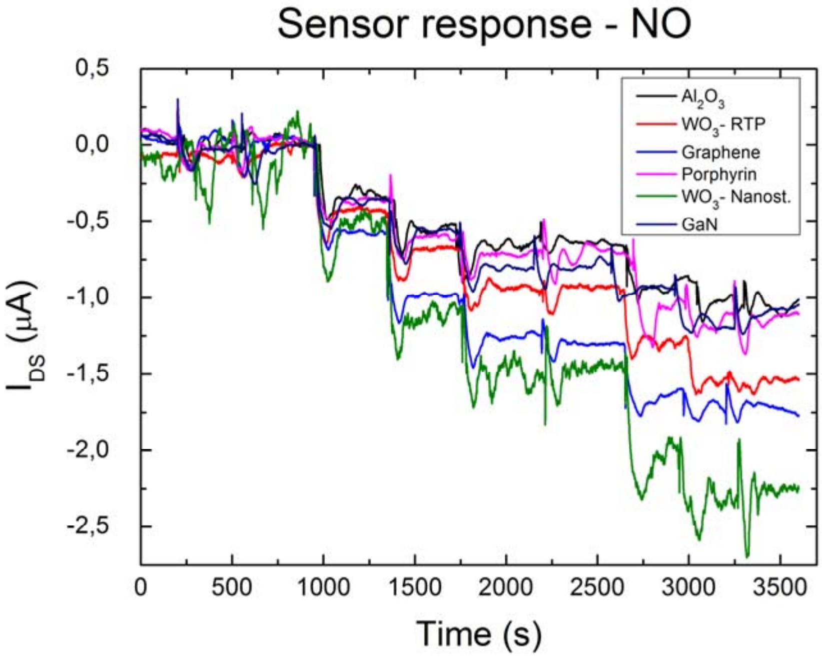

Figure 6.1: Normalized drain current response (I_{DS}) of various functionalization layers to nitric oxide additions.

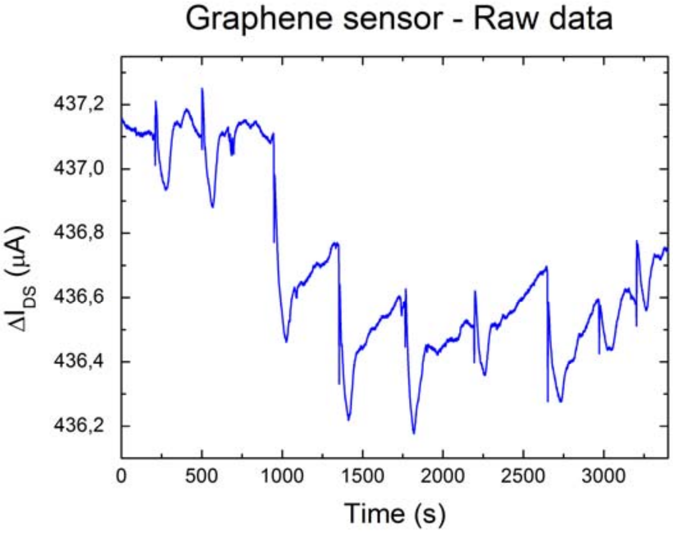

Figure 6.2: Raw measurement data for NO sensor with graphene functionalization demonstrating I_{DS} fluctuation as a result of NO decomposition upon reaction with O_2

It may be observed here as time progresses that the sensor signal fluctuates towards the initial baseline value following the addition of NO to the target solution. This "drift" of I_{DS} due to the decomposition of NO and the diffusion out of the solution may be beneficial. This provides initial evidence that the sensor response is in fact due to NO sensitivity. This proof may be quantified through the addition of a single concentration of NO into the measurement bath. By subsequently allowing the signal to fluctuate back towards the baseline value as NO reacts with O_2 (equation 3.24), the time at which the drain-source current reaches half of the initial response can be observed. The expected half-life of NO in the solution could additionally be calculated based on the initial concentration. Correlation of these values allows for the conclusion that the drift towards baseline values agrees with the expected decay due to $t_{1/2}$ of NO. This is depicted in figure 6.3 utilizing a 500 µm x 500 µm sensor with graphene functionalization at a V_{DS} of 1 V and V_{ref} of 0 V. The NO concentration in the measurement bath was adjusted to 0.9 µM corresponding to a half-life of approximately 620 s in solution exposed to air, thus assuming an O_2 concentration of 225 µM [133]. This clearly agrees well with the time at which [NO] falls to half its initial value, which occurs about 650 s after the addition.

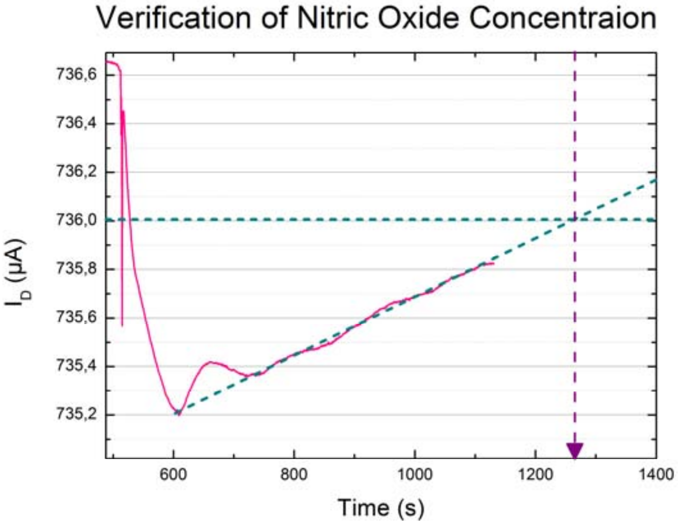

Figure 6.3: Nitric oxide decomposition demonstrating half-life in solution as well as sensor response to NO

This experiment was repeated for other concentrations of NO as well. The results are presented in figure 6.4 with concentrations of 650 nM and 2 µM represented by the cyan and purple curves, respectively. In this case the calculated concentrations correspond to a theoretical $t_{1/2}$ of approximately 870 s (650 nM) and 275 s (2 µM). These times correlate well to the extracted $t_{1/2}$ values from the measurement, showing ~820 s for the 650 nM addition and slightly over 400 s for the 2 µM concentration. The inaccuracy of $t_{1/2}$ for the higher concentration is most likely a result of slight timing errors while mixing the NO adduct in PBS and making dilutions. **Overall, these experiments provide excellent evidence of NO sensitivity utilizing the theory of NO decomposition and observing the corresponding signal "drift."**

An additional method utilized in this research to verify the sensor response to NO involves the use of hemoglobin. As discussed in Section 3.3, the NO is rapidly scavenged by hemoglobin (free or in red blood cells). This occurs under physiological conditions as NO diffuses from the point of production into the blood stream [133, 151, 161]. This interaction of NO with hemoglobin may be taken advantage of in sensitivity experiments to ensure that the sensor response is due to the presence of NO [133].

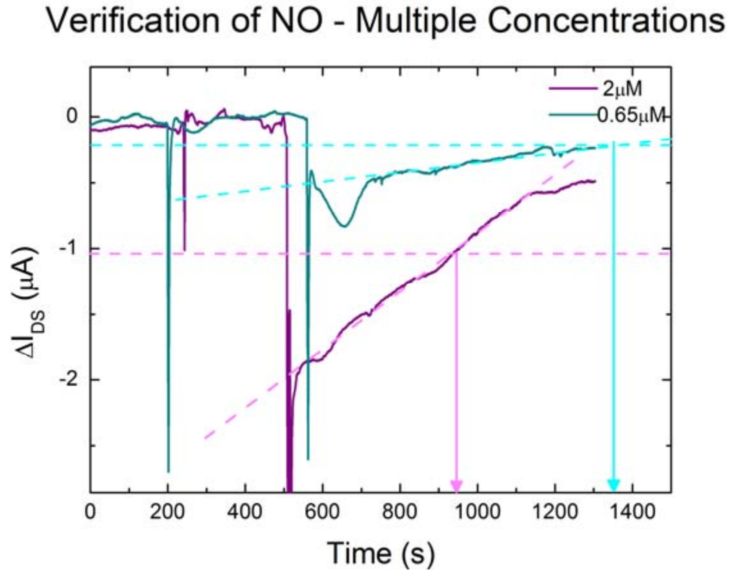

Figure 6.4: Confirmation of $t_{1/2}$ dependence on NO concentration for [NO] = 650 nM (cyan) and 2 μM (purple)

This verification test was carried out in two separate manners as a result of the light sensitivity issues present with AlGaN/GaN based sensors. The light sensitivity (discussed in Chapter 2) is present due to photo-induced charge carriers. These cause a significant variation in I_{DS} upon modification of the amount of light to which the sensor chip is exposed. Solutions containing hemoglobin (Sigma-Aldrich® Hemoglobin from bovine blood) were prepared in PBS7.4, a pH value at which hemoglobin is soluble. Due to this presence of hemoglobin, the test solutions are inherently a reddish-brown color. Addition of this solution to the measurement bath causes the molar attenuation coefficient – or light adsorption characteristic – of the fluid to be modified and thus the number of photo-induced charge carriers. Therefore, the variation in I_{DS} must be carefully inspected in order to understand the effects of light transmission property modulation versus those due to the presence of hemoglobin. The first experiment, presented in figure 6.5a, makes use of the I_{DS} fluctuation towards baseline values following the initial sensor response to NO. The green, black, and blue arrows in figure 6.5a indicate additions of control PBS7.4, hemoglobin, and NO, respectively. In the first measurement the control addition (PBS7.4) was made at 700 s to ensure signal stability. The second noticeable fluctuation in the I_{DS} level is due to the addition of a small amount of hemoglobin giving a concentration in the cell of approximately 0.1 μM. The current level decreases as expected due to the increased adsorption of light within the fluid and the consequent reduction of photo-induced charge carriers. The subsequent two additions consist of NO resulting in a total concentration of 250 nM and 500 nM in the measurement bath. The drift towards the baseline current value is evident due to the decomposition of NO, in this case partially by the low concentration of hemoglobin as well as through the discussed reaction with O_2. The influence of scavenging by hemoglobin is evident via observation of the fluctuation of I_{DS}. In this instance the $t_{1/2}$ value is (or will be) attained much more quickly than expected. A final higher concentration of hemoglobin (~1 μM) is added at 1500 s. It may be may be understood from the flat, steady I_{DS} response that the measurement bath is at this point free of NO, while the overall reduction in current at this addition is once again due to the increased molar attenuation coefficient.

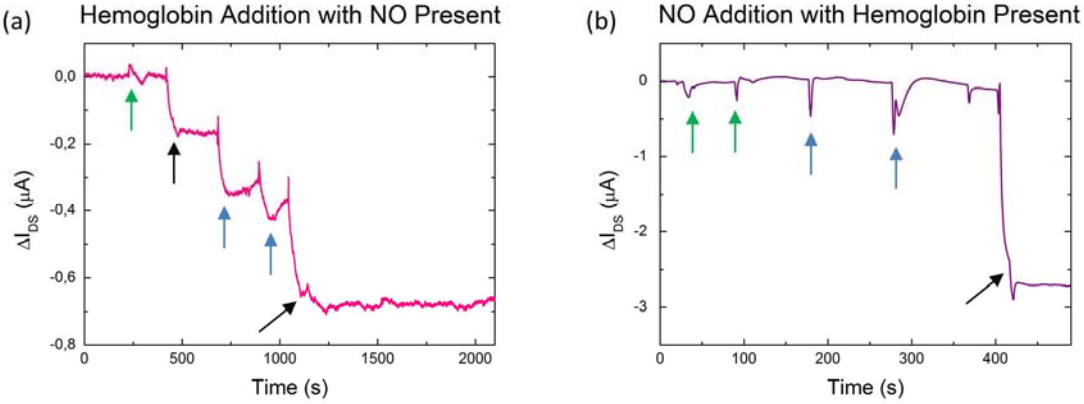

Figure 6.5: Verification of NO detection though the addition of hemoglobin a) following NO addition and b) prior to NO addition.

In figure 6.5b a similar technique was utilized; however with hemoglobin (~1 μM) present from the beginning of the measurement. In this case it is expected that the addition of NO should not create a sensor response due to the fast scavenging of this molecule. The first two additions in figure 6.5b at 40 s and 90 s are PBS7.4 control measurements, exhibiting no variation in I_{DS}. At 175 s the first NO addition is made, resulting in a final concentration of 500 nM, as anticipated with no significant sensor response. The second NO addition at 290 s results in a final concentration of 4 μM. Here the concentration is high enough to produce an initial sensor response; however as expected, the NO is quickly scavenged and the initial I_{DS} value is obtained. At 400 s additional hemoglobin is added, resulting in a decrease in I_{DS} as observed in the previous measurement due to photo-induced charge carrier reduction.

6.2 NO Sensitivity Tests

With the completion of experiments ensuring that the desired NO sensitivity has been attained, in contrast to that of other interfering substances, further experiments were carried out to evaluate the developed sensors. The limit of detection (LOD) and sensitivity range were examined within this evaluation – to the extent possible considering the half-life of NO in solution. When working with sensing applications in general, various operating regimes may be considered for optimal measurement conditions. V_{ref} (or V_{GS}) is typically set to a value which avoids electrochemical reactions when possible and not desired, does not approach level at which hydrolysis becomes a risk, and remains within a range where the device sensitivity is not compromised. Two main operating regimes are utilized in the realm of FET-based biosensors: subthreshold and peak transconductance (g_m). In Section 3.4.2.1 the drain-source current dependence on specific material properties and bias voltages was given, which can be further simplified in the linear regime where $V_{DS} << V_G - V_T$ as follows:

$$I_D = C_i \mu_n \frac{W}{L}\left((V_{GS} - V_T)V_{DS}\right). \qquad 6.1$$

In the saturation regime ($V_{DS} > V_G - V_T$) the drain current is given by:

$$I_D = C_i \mu_n \frac{W}{2L}(V_{GS} - V_T')^2, \qquad 6.2$$

with V_T in both cases incorporating information about the interfacial surface potential as discussed in Chapter 4 [302, 194]. V_T' may also be approximated to V_T depending on fabrication related conditions. The conditions which result in deviation from this approximation will not be discussed as the topic of interest is the amplification of the system which may be described as:

$$g_m = C_i\mu_n\frac{W}{L}V_{DS} \quad or \quad g_m = C_i\mu_n\frac{W}{L}(V_G - V_T') \tag{6.3}$$

in the linear or saturation regime, respectively [205, 303]. In both cases this may be found through the derivation of the drain current with respect to gate bias

$$g_m = \frac{\delta I_{DS}}{\delta V_{GS}}. \tag{6.4}$$

The value of g_m provides a quantification of the amplification delivered by the transistor, with the peak value giving the V_{GS} at which this signal amplification (or change in I_{DS} due to change in V_{GS}) will be highest for a specific V_{DS}. This is related to the concept of the subthreshold swing operation regime in which the maximum slope may be found from the same I_{DS} vs V_{GS} transfer curve. However, in this case I_{DS} is plotted on a log scale due its exponential dependence on the applied gate potential at subthreshold conditions:

$$I_{DS,sub} \propto exp\left(\frac{V_{GS}}{nV_T}\right). \tag{6.5}$$

The inverse of this slope is termed the subthreshold swing, *S*, and may be derived to be

$$S = nV_T ln(10) \tag{6.6}$$

with the term *n* accounting for deviation from ideal conditions under which n = 1 and the theoretical thermodynamic limit of ~60 mV/$I_{DS,decade}$ would be attained [304]. This value represents the best-case when looking into I_{DS} on/off ratio, however typical, non-ideal values lie above this and are often dependent on the bulk capacitance and therefore also the charges within this layer. Although this regime has also been reported to demonstrate high sensitivity, these results are frequently shown in terms of $\Delta I_{DS}/I_{DS}$ which inherently make this ratio much greater due to lower current values [305]. Perhaps in some cases this may be the more beneficial operation mode; however, it has been demonstrated often in literature for bio-FET sensing applications that optimal signal-to-noise ratios (SNR) are generally attained when operating under peak transconductance conditions [306]. Accordingly, this operation mode is utilized within this research for the majority of sensing experiments; indeed for all of those presented in this thesis.

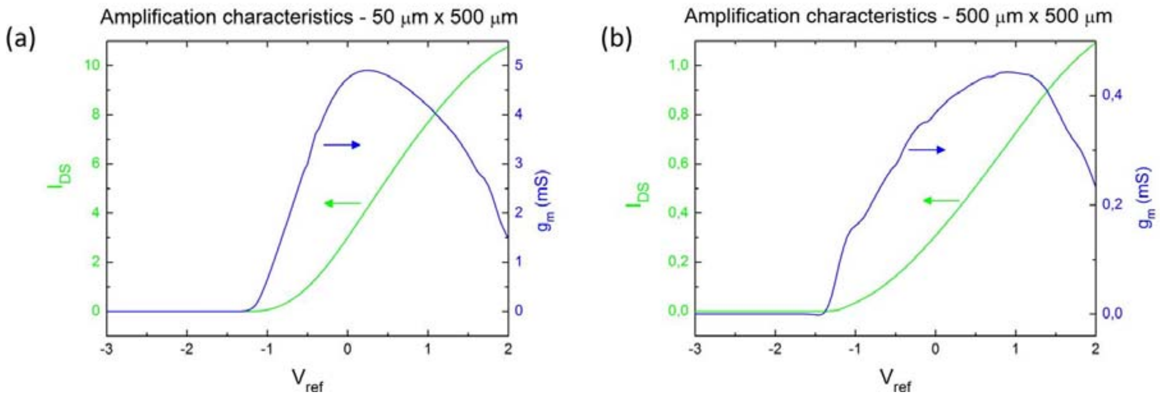

Figure 6.6: AlGaN/GaN ISFET transfer and transconductance characteristics of a typical device utilized in this work for gate area geometries of a) 50 μm x 500 μm and b) 500 μm x 500 μm

In order to practically determine g_m, transfer characteristics of each device are recorded (I_{DS} vs V_{GS}) and the first derivative of this measurement is calculated. Representative resulting curves for AlGaN/GaN ISFETs are given in figure 6.6. The demonstrated **amplification characteristics with g_m values of up to 5 mS (normalized g_m = 9800mS/mm)** are excellent in comparison to ISFETs reported in literature. Reported devices on this scale typically exhibit lower amplification properties, with transconductance values of 0.05 – 0.5 mS (normalized g_m = ~5500 mS/mm) for III-Nitride based ISFETs, while higher values such as 0.4 – 3.5 mS (normalize g_m = 350000 mS/mm) are achieved when employing unique fabrication techniques, i.e. nanowires, or when attaining excellent C_i values [197, 307]. The results in this work demonstrate advantageous g_m values at a low V_{ref} of 0 V for V_{DS} values within the range of interest. This V_{ref} bias was therefore utilized for the constant current (i.e. V_{DS} = const) measurements in the following NO sensitivity experiments.

Further testing regarding the transconductance was carried out with the employed functionalization materials. These results are presented in figure 6.7 for the GaN surface in comparison to graphene and WO_3 (RTP oxidized) at a V_{DS} bias of 0.25 V and 1 V. Here it may be observed that the general depletion linear and saturation ranges, and therefore that of increased g_m, are comparable. The ISFET with graphene functionalization exhibits an increase in g_m, presumably due to the increased surface area and improved impact of gate voltage on the channel. The WO_3 surface supports this assumption of increased surface area as the maximum in this case is comparable to that of the GaN surface. For WO_3, however, it may be noted that there are two distinct peaks in g_m. This is supposed to occur due to the development of an additional charge carrier region or channel. Similar dual peaks have been seen in previous studies regarding multiple 2DEG (or 2DEG and 2DHG) channels created by stacking techniques of materials such as AlN, AlGaN and GaN [308, 309, 310].

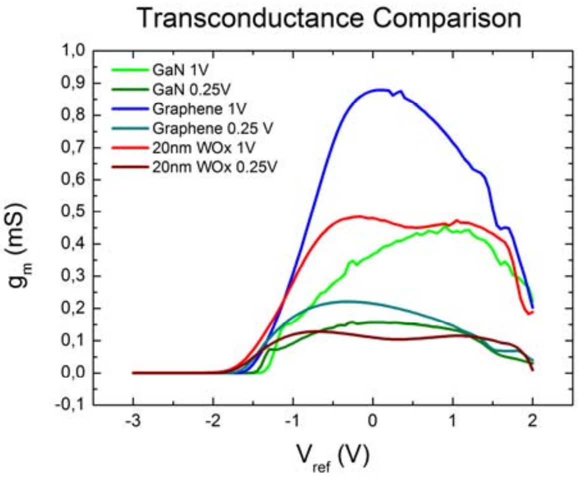

Figure 6.7: Transconductance comparison of ISFET gate surfaces consisting of GaN, graphene and WO_3 at V_{DS} = 0.25 V and 1 V

Based on the results of the g_m measurements, the remaining NO sensitivity experiments were carried out at V_{ref} = 0 V. The LOD was determined through pipetting experiments utilizing various concentrations of NO. The results of these concentration experiments are plotted in the main graphs of figure 6.8 with the actual measurement curves from which the data points were (partially) acquired presented in the insets. The measurements seen in these insets were carried out in order to test lower concentrations and extract the LOD. This LOD may be found using the intersection of the line approximating the linear range and the baseline current level with no NO in solution or a very low concentration which is not detectable with these sensors. As also indicated within the figure, **the determined LODs for the graphene and WO_3 functionalization techniques are 235 nM and 9 nM**, respectively. Although an initial interpretation of the LOD values makes the WO_3 technique appear more advantageous, the increased noise in the signal is clear upon inspection of the inset graphs. This is a potential disadvantage of the WO_3 material system, possibly thermal-related due to the (relatively) high V_{DS} used within these tests. Experiments with tissue or cell cultures based on similar AlGaN/GaN heterostructures avoid a V_{DS} bias above 0.5 V to prevent tissue damage [311]. Additionally, the initial comparison (fig 6.1) as well as the following discussed experiment shows a much lower noise level when operating at 0.25 V. Further advantages and disadvantages of each functionalization technique will be discussed in the conclusion of this chapter.

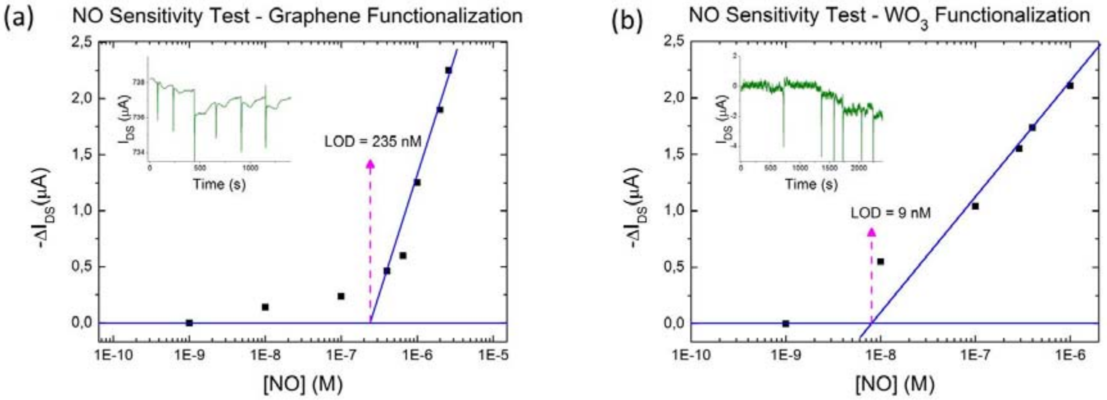

Figure 6.8: Sensitivity results for a) graphene and b) WO_3 functionalization layers

A final experiment regarding the sensitivity of the functionalized ISFETs was implemented in order to examine the effects of variation of V_{DS}. In these measurements (fig 6.9) a single concentration of NO was pipetted into the bath yielding an overall concentration of 1 μM. This was carried out at V_{DS} = 0.25 V and 1 V, following stabilization of the measurement signal. At V_{DS} = 0.25 V a similar response of graphene and WO_3 is observed, not surprising based on the previous sensitivity investigation of all materials. In the case of V_{DS} = 1 V however, the response of WO_3 is 4-5 times that of the graphene sensor. The mechanism responsible for this large increase is not certain, but may be due to redox activity within the film when larger electric fields are present.

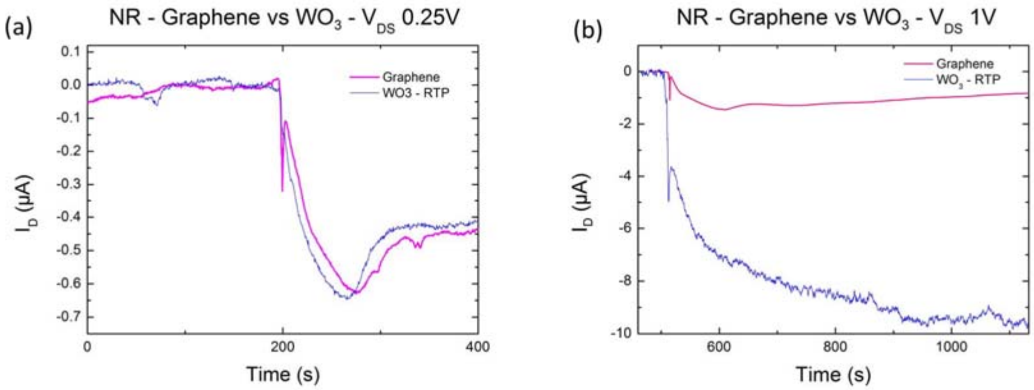

Figure 6.9: Effect of V_{DS} variation (0.25 V or 1 V) as well as increased response without LED

As previously briefly discussed, higher V_{DS} values may also lead to heating of the substrate, potentially catalyzing reaction between NO and WO_3, which is well known to increase at elevated temperatures [252, 242]. As WO_3 has been often employed in fields such as the automotive industry for NO sensing to ensure safe environmental conditions, many studies involving reactions at various temperatures have been carried out. Typically, the sensing mechanism involves WO_3 acting as an oxidizing agent through the reaction

$$2NO + 2e^- \rightarrow N_2 + 2O^-(ad) \qquad 6.7$$

creating an increase in the resistivity of the film due to a decrease of free carrier concentration. In the case of this reaction for the WO_3 ISFET based sensor, this decrease of charge carriers and adsorbed O^- theoretically induces a more negative potential at the interface with the electrolyte. This shift causes the observed reduction of I_{DS} when NO is introduced into the measurement cell.

In the case of the graphene-based sensing mechanism, the type of modeled interaction discussed in Chapter 4 is presumed. Here the atomic interactions and the gas adsorption-induced modifications of the electronic properties of pristine and defective graphene were examined [265, 266, 312]. The sensitivity demonstrated here is most likely due to pi-pi electron interaction between graphene and NO upon such atomic proximity. This interaction is not expected to vary significantly due to substrate heating as V_{DS} increases. Thus, good agreement to the variation in sensor response shown in figure 6.9 is achieved through this explanation as the expected channel current increase due to greater signal amplification is seen, yet no additional signal increase due to thermal catalytic behavior is observed.

6.3 Possibility for Simultaneous pH and NO Measurement

As the realization of a miniaturized sensor array for the simultaneous measurement of NO and pH was one of the main goals of this work, the effect of pH variation on the developed NO sensors was investigated. When working under biological conditions the pH value (in blood) should not deviate from the typical range of 7.35-7.45, otherwise a problem with acid-base homeostasis is likely present, which may indicate respiratory or metabolic issues. The AlGaN/GaN ISFETs (with GaN upper surface) have been optimized to be very sensitive to such small variations in pH levels. The effect of these pH fluctuations on the functionalized sensors must however be assessed. This investigation provides understanding of possible interference issues and information to assist in finding methods to obtain the desired information.

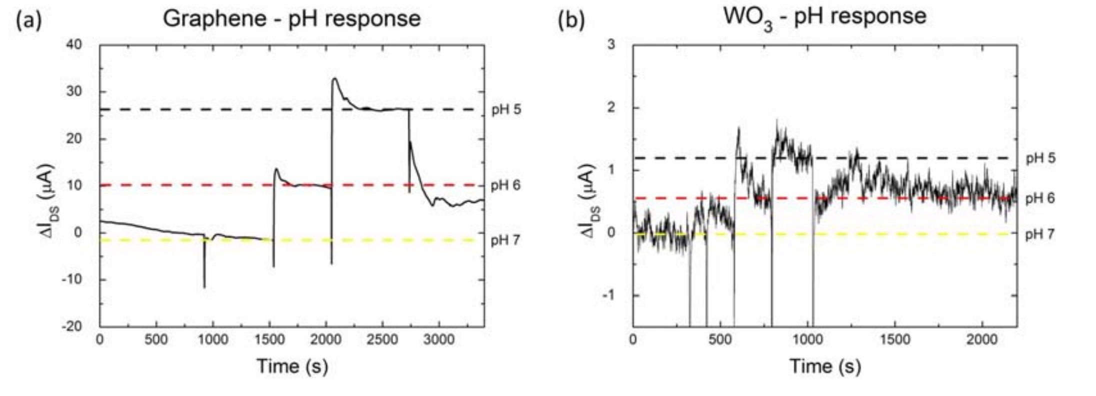

Figure 6.10: Reduced pH sensitivity of a) graphene and b) WO_3 functionalization layers

The majority of the measurements in this work were carried out with W/L = 1 (often W = 500 µm, however also 10 µm or 50 µm in Chapter 7) and at V_{DS} = 1V. Analogous device geometry and operating conditions were utilized in these measurements to ensure straightforward comparison. The initial pH value of the measurement bath was 7, while subsequent additions of PBS4 brought the overall level to pH 5 and pH 6. A final addition of PBS8.5 was carried out to result in an overall pH of 6.

For the case of graphene the pH sensitivity is reduced in comparison to the bare GaN surface. As may be seen in figure 6.10a, the **graphene surface demonstrates approximately -(10-12) µA/pH (12-17 mV/pH) in comparison to -(35-40) µA/pH (or 49-54 mV/pH)** for a device with comparable amplification properties operated under analogous measurement conditions (Section 7.2). This pH sensitivity of the GaN surface will be presented and further discussed in the following chapter as the results are obtained from the developed sensor array. Figure 6.10b shows the greatly reduced pH sensitivity of the WO_3 functionalization technique. In this case, variation in I_{DS} amounts to only about **-0.55 µA/pH (or ~1.1 mV/pH), presenting a suitable solution of simultaneous pH and NO measurement**.

The low pH sensitivity of WO_3 poses an interesting question based on the origin of this effect. Multiple publications exist on the good sensitivity of WO_3 to variations in pH, however a multitude of literature sources also exist on the highly differing properties depending on what phase of tungsten oxide is present. Studies have been carried out to investigate the surface termination properties of both bulk and thin film WO_3. This was done using first principles calculations based on density functional theory (DFT), demonstrating WO_2 planar surface, bare oxygen surface, and hydrogenated oxygen surface [313, 314]. Separate investigations look into the Lewis acidity and dehydroxylation/dehydration of the WO_x surface as a function of evacuation temperature as well as under aqueous conditions [272, 315]. Possibly the low sensitivity to pH found in this study results from a material structure which does not result in a significant number of surface hydroxyl groups accessable for the described site-binding behavior of SiOH or GaOH (Chapter 3). An involved materials study on the deposition and thermal or chemical WO_3 formation could be carried out in order to find optimal sensitivity conditions. In the case of graphene, the possibility to further reduce the pH sensitivity of the graphene functionalization layer may exist through an improved dispersion and deposition of the flakes. The gate surface coverage on the sensors utilized here varied significantly, often with results such as that shown in figure 6.11. This is certainly an example in which there is large room for improvement through further reduction of the pH sensitivity and improvement of that of NO. This notion is supported by examples in literature of low pH sensitivity of pristine graphene [317]. A variety of sensitivities are obtained depending on the type of graphene and possible post-treatment techniques to further passivate the surface or, conversely, to induce defects. Ozone induced defects have been shown to raise the pH-sensitivity, reinforcing the concept of defect-related sensitivity.

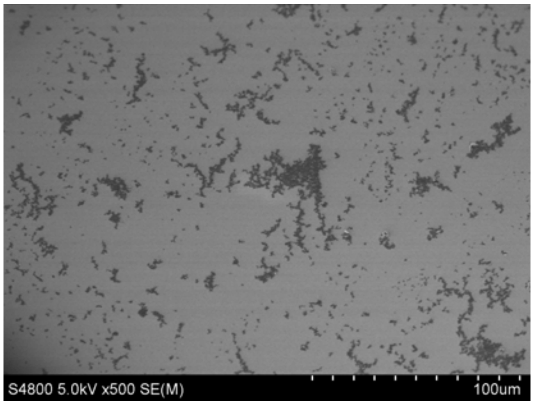

Figure 6.11: Example of mediocre graphene gate surface coverage. Graphene flakes are visibly darker, while the (most likely) free GaN surface is lighter

For pristine (or low defect density) graphene, low sensitivities of ~9 mV/pH were reported, which may be further reduced through fluorobenzene passivation, resulting in effective sensitivities of ~0 mV/pH [317, 318]. Thus, with improved coverage of graphene flakes on the GaN surface, further reduction of the pH sensitivity while additionally improving the impact of NO presence on the channel current is a clear possibility.

6.4 Cell Growth – Control, Graphene and WO_3

A final experiment for the graphene and WO_3 functionalization methods involves an assessment of the biocompatibility of these materials. In this investigation initial biocompatibility assessment was performed simply though the analysis of cell growth on the substrates of interest. Control glass substrates as well as sensor chips with graphene and WO_3 functionalization layers were sterilized in 70% ethanol for 15 minutes, rinsed three times with DIW, dried in the sterile fume hood placed into a Greiner CELLSTAR® 24-well culture plate. 35000 L929 (mouse fibroblasts) were seeded per well and cultured over 7 days in 10% RPMI+Pen/Strep+1%Glutamin at 37°C/5%CO_2. 1 mL cell medium was used per well and media changes were carried out 3 and 5 days post-seeding. On day 7 the metabolic activity was confirmed utilizing an AlamarBlue® test.

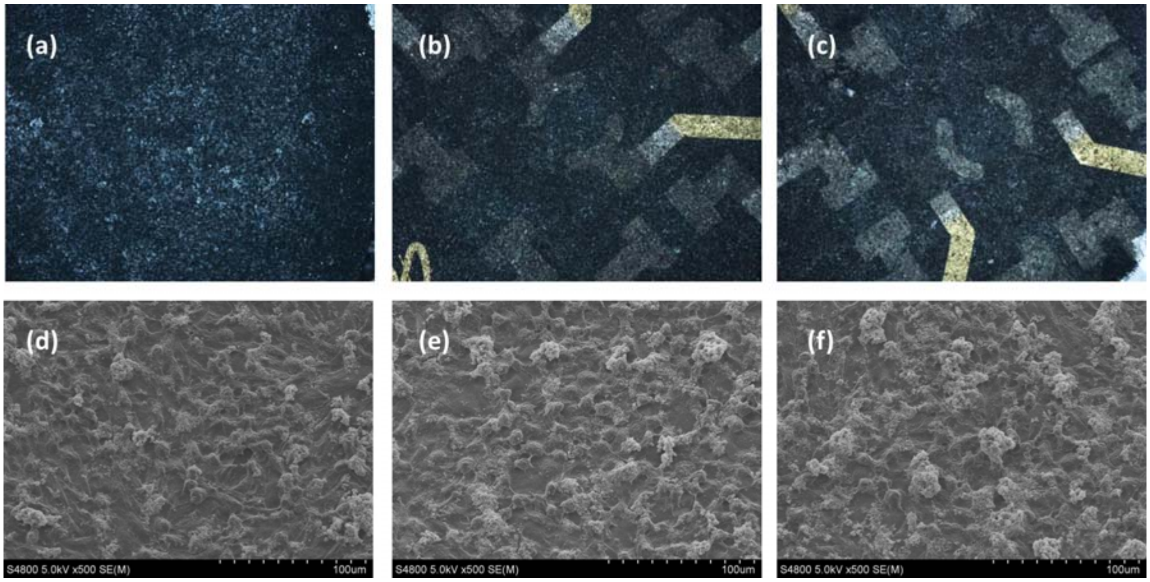

Figure 6.12: Initial biocompatibility demonstration via homogeneous cell growth observed in optical microscope and SEM images for a,d) a control glass substrate, b,e) graphene functionalization and c,f) WO_3 functionalization methods.

Figure 6.12 demonstrates the cell growth through optical (top row) and corresponding SEM (bottom row) images. It may be observed that the cells are homogeneously distributed, as well as exhibiting a healthy appearance, on the control glass substrate (left) as well as on those with graphene (middle) and WO3 (right) functionalization layers. The positive results pertaining to biocompatibility are significant as many of the existing questions related to the study of NO involve its roles *in vivo*. Applications utilizing sensors such as these therefore inherently often necessitates direct contact with tissue or the possibility to culture cells on the device for *in vitro* characterization.

In summary, functionalization methods to produce sensors capable of detecting low levels of NO have been developed. These levels are pertinent for the levels of NO produced under healthy, as well as critical, biological conditions. Initial results demonstrate advantages and disadvantages of both functionalization techniques. WO_3 exhibits a lower LOD and a low characteristic pH sensitivity, along with ease of deposition due to standard fabrication processes which are very compatible with those utilized for the standard AlGaN/GaN ISFET. However, high noise levels and the not well defined sensing mechanism bring uncertainty into this method. Graphene possess the potential for a more stable film; however the process remains to be optimized.

The key results demonstrated in this chapter consist of:

- development of new technological processes involving AlGaN/GaN ISFET gate area functionalization to enable nitric oxide measurement
- analysis of sensor performance based on the utilized functionalization methods
- verification of nitric oxide sensitivity opposed to that of interfering substances
- suitable reduction of pH sensitivity to make simultaneous (pH and NO) measurement possible
- initial demonstration of biocompatibility using L929 (mouse fibroblast) cells on control, graphene, and WO_3 substrates.

Various possibilities to further investigate the developed sensors exist, including: an improved measurement system to reduce the effects of incident light, full coverage of the graphene functionalization layer, improved mechanical stability/electrical noise level of the WO_3 RTP annealed and nanostructured layer, and an in depth study on the effects of various biasing conditions on the redox behavior of the system and sensitivity, as well as the effects of lighting conditions.

7. Miniaturization of ISFET pH/NO Sensor Arrays

Most advancements in miniaturization and sensor array technology for studies on neuronal or other types of cells are still based on silicon technologies due to the wider availability and proliferation of silicon fabrication processes. However, as discussed in previous sections, III-Nitride devices have great advantages over Si-based technology in many cases, particularly for applications requiring chemical stability and good biocompatibility [21, 197]. In the following, progress related to miniaturization of the presented pH and NO ISFET sensors based on the AlGaN/GaN heterostructure and the related results are presented. This includes comparison to the current literature status in which:

- claims have been made about the overall reduction of sensor size; however sizes remain relatively large (between 4 and 50 μm)

- an increase in the number of sensor sites is often discussed, yet typically irrelevant because
  - the increased number of sites are unnecessary to be of applicable use
  - the pitch between sites of existing sensors remains large, requiring a considerable overall surface to compensate the site increase

Recent advances in ISFET arrays, similar to those developed in this research, include pH sensing and DNA detection based on CMOS source-drain follower circuits employing Si-technology, Al_2O_3/Si nanowires, distributed Si-based ISFETs and gold electrodes for stimulation and monitoring of metabolism, and AlGaN/GaN ISFETs for pH sensing and recording of cell activity [319, 320]. The first mentioned study, reported by Nakazota, showed a clear advantage, with the primary benefit being in the direct integration of interface circuitry through the use of CMOS technology. Contact to the electrolyte is made by an 'extended gate' with the integrated circuitry embedded below within the substrate. An additional advantage entails the large number of possible sensors, with a goal of one million per chip quoted in this publication. Such a large number of sensors is excessive in almost all possible applications, fitting into the classification described by Dahlin as "nanohype in sensor research," or reducing size unnecessarily and often introducing additional issues [322]. Additionally, the sensitive areas of the employed CMOS Si-based ISFETs are only relatively small, at about 4.2 μm x 4.2 μm, with a measurement cell pitch of more than 100 μm. Furthermore, the pH ISFETs in their work only demonstrate sensitivity up to 41 mV/pH [319]. The Al_2O_3 coated Si-nanowires (Si-NWs) reported by Chen, et al. on the other hand demonstrate very near Nernstian sensitivities of up to 57.8 mV/pH (at 22 °C). Although the term "nanoISFET" is utilized to describe these sensors, 15 μm x15 μm windows in the insulating film are still used to bring the Si-NWs in contact with the electrolyte [320].

The investigation carried out by Martinoia, et al. occurred about a decade before the previous two publications; however it also demonstrated very good pH sensitivity, 56 mV/pH, along with the attractive addition of stimulation electrodes on some of the developed chips. This possibility to stimulate cultured neurons and also monitor metabolic activity is indeed interesting. However, this chip is again limited by size and pitch [321]. Finally, and most relevant, is the study carried out by Steinhoff, et al., already mentioned within this thesis due to the comparable AlGaN/GaN heterostructure basis. In this work the ISFETs discussed in the biosensor section of Chapter 4 were employed in an array with 35 μm x 35 μm sensitive gate areas for pH and cardiomyocyte recording. This array is indeed very similar, with 16 ISFETs and a high pH sensitivity of up to 56.6 mV/pH [197]. The sensitive gate area of the ISFET array in this work was reduced slightly further to 10 μm x 10 μm. Even for a large number of analytes, the micrometer scale of many of the discussed arrays will typically suffice. Regarding improvements, the size of the sensor area could be reduced and the pitch between sites could still be reduced. Essentially, the ISFET array demonstrated here is competitive or demonstrates an improvement over existing options with:

- standard sensor size of 10 µm x 10 µm
- 16 sensors with a standard pitch between sensors of 100 µm

producing a suitable option for biologically relevant studies as well as the possibility to further reduce sensor size or increase sensor number for applications in which this may be useful.

7.1 Array Fabrication

Aside from difficulties associated with reduction of size, the corresponding variations for the layout and the resulting complications there is not a great deal of dissimilarity in the fabrication process for the sensor array. For initial experiments, two ISFET layout designs were developed, both containing 16 sensors with a W/L = 1 and open gate lengths reduced to either 50 µm or 10 µm. Examples of these array layouts are depicted in figure 7.1. The sensor chip size is held at 5 mm x 5 mm, as with all other discussed layouts in this work, and the number of bond pads around the outer edge is increased to 22

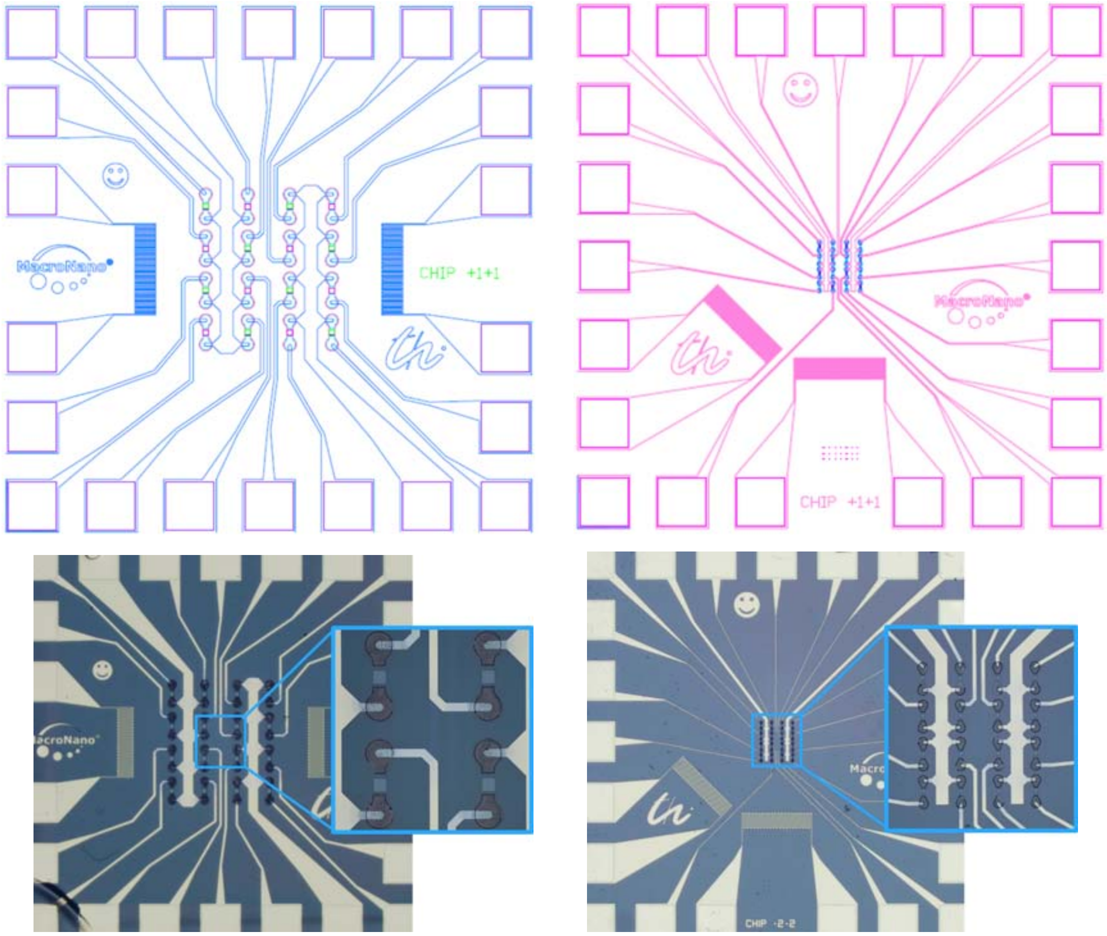

Figure 7.1: 16 ISFET array layout (top) and completed sensor chip (bottom) with open gate sizes of a) 50 µm x 50 µm and b) 10µm x 10µm

The first new consideration for this layout involves the metal lines to provide contact to the ISFET source and drains. To make the 4 x 4 sensor array possible a common source arrangement was chosen with two source contacts per chip, each supplying contact to 8 transistors. The 16 drain contacts are individually addressable. The much wider source contact is visible both in the layout and the fabricated arrays between, running vertically between first/second and third/fourth columns of individual ISFETs. The remaining contact lines address each drain contact along with four additional lines connected to two gold meander structures, which may be employed to monitor temperature fluctuations. Attention to line width and avoiding sharp corners were the only other major points of concern for the contact lines.

As the creation of the ohmic contacts and the mesa etching steps were not expected to cause major issues due to size reduction, the dimensions were simply scaled down keeping metal lines wide enough to avoid introduced issues if higher current levels are reached. These steps were indeed carried out without complication, resulting in good 2DEG contact and characteristic channel resistance values. Slightly higher *R* was observed for the reduced ISFET size which is reasonable when taking into account the space between the edge of the etched window and that of the ohmic contact. This gap is typically 5 - 10 µm, depending on the layout. In the case of the 500 µm x 500 µm gate area, this extra length is negligible. ON the other hand, in the case of the 10 µm x 10 µm ISFET this gap increases the channel by a factor of 2. When taking this into consideration the observed channel resistance falls into the expected range. Regarding miniaturization, the only other potential issue had to do with the passivation of the metal lines. However, as a result of the passivation study (discussed in detail in Chapter 5) and the developed isotropic polyimide plasma etch process, this step also could be scaled down without considerable difficulties. The 10 µm x 10 µm were opened effectively with clean gate surfaces free of contamination or residue.

The final alteration to the array layout involves an additional mask to provide the additional possibility to functionalize every other gate area, as demonstrated in figure 7.2. This fabrication process is extremely compatible for any lithography based technique, such as WO_3. Other functionalization methods may also be carried out utilizing this mask, however compatible processes may need to be developed depending on the material.

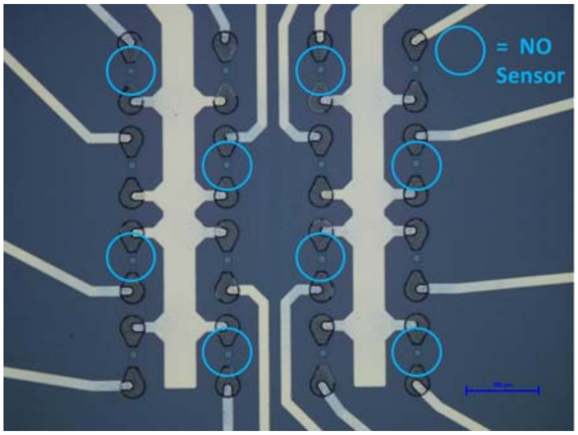

Figure 7.2: Example of sensor array for simultaneous pH and NO measurement. Gate areas of the ISFETs marked with blue circles are functionalized for NO sensing, those unmarked have the upper GaN pH sensitive surface.

7.2 Characterization of W/L = 1

Initial characterization of pH sensitive ISFETs with W/L =1 was first carried out on larger devices prior to array fabrication. Sensitivity variation over a range of V_{DS} and V_{ref} potentials was investigated in order to find a range in which this geometry may be successfully employed. pH sensors with W = 500 µm were utilized in the preliminary analysis, measured directly following fabrication and encapsulation - i.e. no further cleaning processes were used. Twenty measurements were carried out consecutively, alternating between PBS4 and PBS7 solutions. The measured sensor current (I_{DS}) and obtained sensitivity are plotted in figure 7.3a. **The ability to carry out measurements directly following fabrication again reinforces the great benefit of the developed ECR passivation etch process** described in Chapter 5. Only a slight drift in I_{DS} is noticeable over the first 6-8 measurements, which then settles and the current signal remains stable. In this case the higher I_{DS} (upper blue line 600 – 700 µA) corresponds to the sensor current in the presence of pH 4, while the lower I_{DS} corresponds to pH 7. The sensitivity in µA/pH is displayed by the green curve, also showing good stability which settles further after the first measurements. In figure 7.3b the sensitivity results are shown in terms of mV/pH. Utilizing this format, comparison to the theoretical Nernstian limit (58.2 mV/pH at 20 °C) may be made. **High sensitivities are attained with this consideration as well, stable over the entire measurement series with values up to 55.0 mV/pH**.

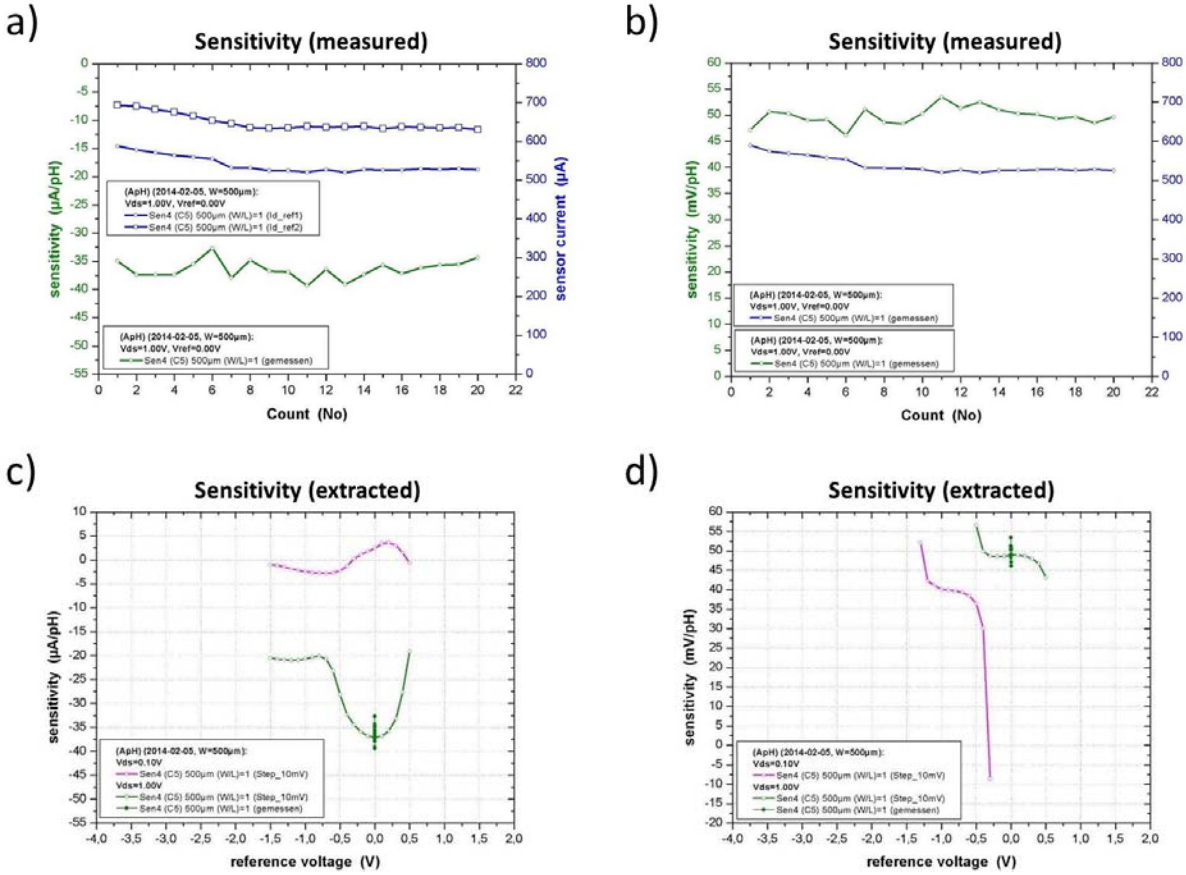

Figure 7.3: Characterization of W/L = 1 ISFETs to determine a) stabilization time, b) sensitivity in µA/pH and mV/pH during stabilization, and sensitivity dependence on drain-source current through measurement at V_{DS} = 0.1 V and 1 V, displayed in c) µA/pH and d) mV/pH

In the lower portion of figure 7.3 the sensitivities are compared for V_{DS} = 1 V and 0.1 V, shown in µA/pH (fig 7.3c) and mV/pH (fig 7.3d). The pinks curves represent the measurement series utilizing V_{DS} = 0.1 V, while the green curves demonstrate the sensitivity results at V_{DS} = 1 V. The large variations in the sensitivity between the two V_{DS} values portrayed in µA/pH are clear, as well as expected based on the characteristic amplification properties.

From standard FET theory, along with a brief description in the previous chapter, it is known that g_m increases with V_{DS} until the saturation regime is reached. As the variations of the surface potential are dependent on the ion activity, and thus limited by the Nernst relationship, this amplification is observed through the increased I_{DS} response. The sensitivity variations presented in mV/pH, on the other hand, may be directly compared. Therefore, from figure 7.3d it is easily observed that the increase in the operating drain-source bias to V_{DS} = 1 V brings about higher and more stable sensitivities, as well as demonstrating this behavior in the desired range for V_{ref}. **These results are beneficial from the viewpoint of possibly attaining high sensitivities with W/L = 1 in the desired sensor array, in addition to the goal of concurrent monitoring of various analytes under biological conditions – in this case pH and NO – for which low V_{ref} values are advantageous**.

10 µm x 10 µm ISFET Array

With the stable measurement possibility employing the W/L = 1 ISFET geometry and the controlled fabrication process, experiments with the reduced gate size could be carried out. The smaller 10 µm x 10 µm was investigated as miniaturization to this size range was the goal for the array. Similar sensitivity testing was performed resulting in the excellent sensitivities shown in figure 7.4. This is presented through the modulation of I_{DS} when the sensor is brought into contact with PBS4 or PBS at various V_{ref} values, as presented in figure 7.4a. The corresponding sensitivities for these measurements in mV/pH are displayed in figure 7.4b. **These results demonstrate the prospect of exceptional sensing capability for the measurement array, with comparable values (up to 55.1 mV/pH) to the previous example with W = 500 µm**. The lower overall drain current variation while attaining good sensitivities may be understood by referring to the discussion of signal amplification, specifically transconductance. The dependence on C_i makes the reduction of g_m clear, although the W/L ratio remains at 1. However, in the case of reduced size ISFETs, the better sensitivity range is found at lower V_{DS} values

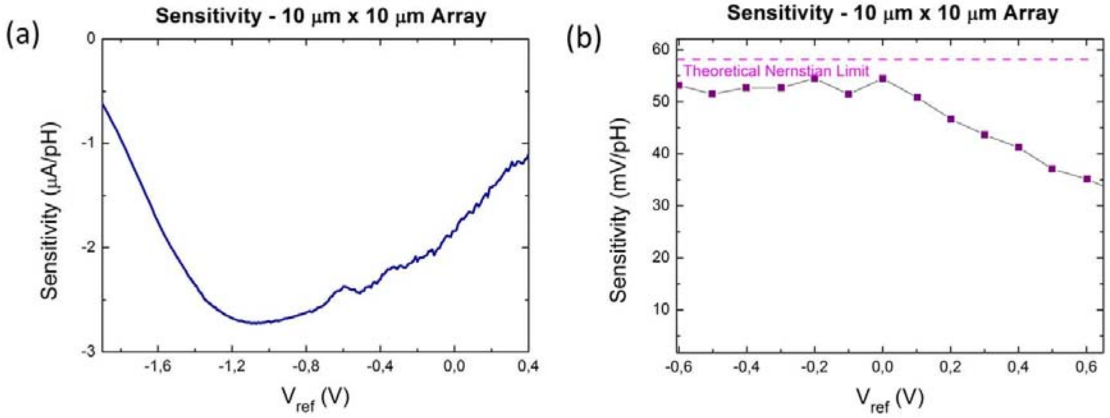

Figure 7.4: 10 µm x 10 µm array ISFET sensitivity study with results given in a) µA/pH and b) mV/pH demonstrating near Nernstian values

To further investigate this sensitivity variation, a final comparison was made at differing drain-source voltages. This variation is shown in figure 7.5 for the 10 µm x 10 µm ISFET array sensor.

A clear trend is observed from these results with improved sensitivities demonstrated with decreasing V_{DS}. This trend is opposite to that of the 500 µm x 500 µm sensor size. As a result of the variation with sensor size, this effect is likely to be due to the resulting modulation of the electric field. In order to develop a complete understanding of the sensitivity and its dependence on sensor size and applied V_{DS} a comprehensive study utilizing a range of ISFET geometries should be carried out. This variation in analyte sensitivity at differing values of V_{DS} could perhaps additionally be exploited in order to reduce or enhance pH/NO sensitivity when endeavoring to detect concentration changes simultaneously.

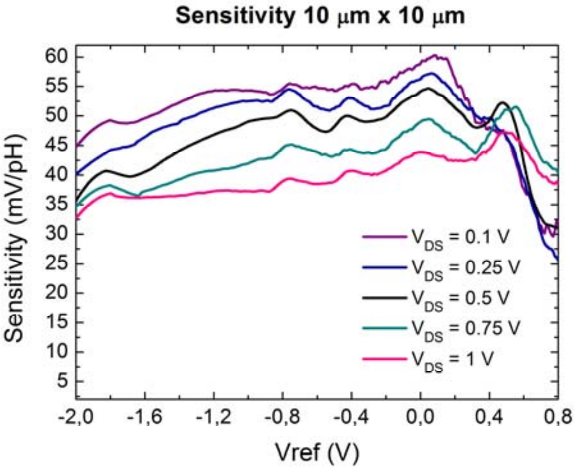

Figure 7.5: Sensitivity variation with dependence on V_{DS} for a 10 µm x 10 µm array ISFET

The successful size reduction of AlGaN/GaN ISFETs opens possibilities for interesting biological and physiological investigations. The capability to attain accurate sensitivity measurements utilizing the miniaturized ISFET array makes the prospect of taking advantage of the chemical stability and biocompatibility of AlGaN/GaN based biosensors an attractive possibility.

In summary, the significant achievements for the ISFET array related research include:

- development of a miniaturized AlGaN/GaN ISFET array, competitive in size and performance to comparable reduced sensor size arrays reported in literature
- sensor size reduction and pitch size to 10 µm x 10 µm and 100 µm x 100 µm, respectively to improve precision for *in vitro* cell culture or tissue related experiments
- immediate suitable ISFET response as well as rapid stabilization, attributable to the developed ECR passivation plasma etch process
- sensitivities of up to 55.7 mV/pH attained for W/L = 1 at V_{DS} = 1V for larger scale devices, as well as the reduced 10 µm x 10 µm gates; values extremely near the theoretical Nernstian limit of 58.2 mV/pH (at 20 °C)
- small scale array gate area functionalization possibility to enable nitric oxide measurement

8. Conclusions

At the onset of this research the overall goal of nitric oxide (NO) detection to further expand biologically or physiologically significant sensing possibilities was established. Previous work dealt with accurate pH measurement with the application to extremely small amounts of fetal blood – or fetal blood sampling (FBS). This resulted in a system capable of successfully determining the blood pH level with volumes of less than 10 µL. In order to further take advantage of this system, additional analyte detection presents one beneficial option. As a consequence of its broad cellular functions, NO represents a key parameter in biosensing, whose concentration levels may provide information in diverse physiological and pathological processes. NO plays roles in the control of vascular tone and blood pressure, as well as being involved in the pathogenesis and control of infectious disease and tumors and performing intracellular messenger functions in neurotransmission. From this point of view, NO is an extremely interesting molecule working both as a toxin and cellular messenger. Analytical issues arise however when attempting to detect this gaseous messenger in solution. The instability in the presence of oxygen and its high reactivity with other molecules present difficulties regarding the development of sensing platforms. Here the demonstration of sensing possibilities based on the AlGaN/GaN ISFET have been presented, however prior to investigations regarding these advances, improving the stability of the foundation was necessary.

A great deal of work has been carried out of the past 10-15 years within the field of III-Nitride development and specifically for AlGaN/GaN based ISFETs as well. Specifically, within our institution a great deal of success regarding advancement in the quality of heterostructure growth and the following fabrication processes has been achieved. A point which has posed continuous problems throughout the development has been the final fabrication step providing passivation of the metal lines. This must offer good insulating properties to reduce leakage current, while additionally providing stability within fluidic environments and at the same time giving access to the sensitive gate surface without remaining residue and without damaging the underlying heterostructure. To realize a suitable passivation technique various materials were researched and tested with respect to dielectric properties and effects due to i.e. swelling upon introduction to liquid. Polymer based materials (polyimide, cyclotene) as well as "hard passivation" systems such as Si_3N_4, SiO_2, various stress or stacking techniques involving these, and metal oxides were considered. The performance of polyimide superseded that of the remaining materials, even in experiments regarding water uptake where nitride or oxide films were expected to excel. All films displayed some level of increased leakage current due to swelling and thus introduction of ions into the material; however polyimide remained the most insulating under these conditions.

Once suitable candidates for passivation material were acquired, the process to pattern these on the ISFET structures was also investigated. This was primarily carried out for polyimide as preliminary results showed the promising nature of this material. A variety of wet chemical and dry plasma etch processes were explored in order to structure the passivation films. Care must be taken however, as the underlying heterostructure and 2DEG providing the channel of the ISFET must remain undamaged during this process. Additionally, residue or contamination must not be left behind on the surface following this structuring process; another problem often encountered in past work with such devices. In this research a reliable, yet unusual O_2 plasma etch process was established utilizing DC bias to avoid plasma damage to the 2DEG. This process proved to avoid bombardment of the GaN surface to the point that the total etch time could be slightly prolonged to ensure complete etching of polyimide across the entire substrate – despite non-uniform thickness due to spin-coating effects – and ultimately drastically reduce surface residue. Typical transistor characteristic curves could be obtained directly following fabrication. Good sensitivities were observed in the first measurements as well, with some slight drift from the initial I_{DS} value (approximately 7% of the original I_{DS}). Through the selection of the most stable passivation material and the development of a corresponding ECR plasma process, a stable foundation was provided enabling further development on the AlGaN/GaN ISFET basis.

As previously stated, one of the main goals of this work was to expand sensing options; in this case for NO detection. In order to investigate this idea, new technological processes involving AlGaN/GaN ISFET gate area functionalization were conceived. Based on current information in literature, various materials were sought out and possible processes developed. Graphene, porphyrin, Al_2O_3, and thermally annealed as well as nanostructured WO_3 were considered. Fabrication processes were developed for each material and NO sensitivity testing was carried out upon successful sensor functionalization. Graphene and WO_3 provided the best response as well as demonstrating initial positive results regarding biocompatibility. Additional testing was carried out to confirm the presence of NO in contrast to interfering substance or other unknown effects. Good detection limits were attained along with the potential to implement NO sensor functionalization within a reduced ISFET array layout.

In order to realize an ISFET array containing dimensions desirable to provide the resolution necessary for *in vitro* investigations, characterization of ISFET gate area geometry was carried out. Single ISFET dimensions of 10 µm x 10 µm were chosen with a pitch of 100 µm x 100 µm between neighboring sensors. This W/L = 1 geometry was initially characterized using 500 µm x 500 µm sensors, followed by the miniaturized 10 µm x 10 µm device within in the actual array, once successful fabrication was accomplished. In both cases good results were attained, however only after examining sensitivity variations in relation to applied V_{DS}. When a lower V_{DS} bias was employed less modulation of the surface potential was observed with variation of pH value, in addition to significant drop off of sensitivity at quite low V_{ref} bias. However, at higher V_{DS} excellent sensitivities were found, ranging up to near Nernstian values of 55.7 mV/pH across a good range surround $V_{ref} = 0$ V. This characterization, along with the development of NO sensors with functionalization techniques compatible for integration into the ISFET array, provides the basis for simultaneous sensing of these analytes. Through the use of various tissue types or cell cultures, interesting physiological or pathophysiological information may be obtained by correlating fluctuations in pH or NO levels. Additionally, this may be combined with the low sample volume measurement system to provide a solution for pharmaceutical and clinical applications, e.g. the high-throughput screening of medicaments or the development of point-of-care systems.

References

[1] Beckman, A. O., & Dickinson, R. G. (1928). The products of the photochemical decomposition of hydrogen azide. *Journal of the American Chemical Society*, *50*(7), 1870-1875.

[2] Beckman, A. O. *J. Optical Soc. Amer.* 1928, *16,* 276–277.

[3] Clark, L. C., & Lyons, C. (1962). Electrode systems for continuous monitoring in cardiovascular surgery. *Annals of the New York Academy of sciences*, *102*(1), 29-45.

[4] Janata, J. (2004). Thirty years of CHEMFETs–a personal view. *Electroanalysis*, *16*(22), 1831-1835.

[5] Abe, H., Esashi, M., & Mats, T. (1979). ISFET's using inorganic gate thin films. *Electron Devices, IEEE Transactions on*, *26*(12), 1939-1944.

[6] Arquint, P., Koudelka-Hep, M., van der Schoot, B. H., van der Wal, P., & de Rooij, N. F. (1994). Micromachined analyzers on a silicon chip. *Clinical chemistry*, *40*(9), 1805-1809.

[7] Steinhoff, G., Purrucker, O., Tanaka, M., Stutzmann, M., & Eickhoff, M. (2003). AlxGa1–xN—A new material system for biosensors. *Advanced Functional Materials*, *13*(11), 841-846.

[8] Yoshida, S.; Misawa, S.; Gonda, S. (1982): Properties of $Al_xGa_{1-x}N$ films prepared by reactive molecular beam epitaxy. In: J. Appl. Phys. 53 (10), S. 6844–6848.

[9] Yoshida, S., Misawa, S., & Gonda, S. (1983). Improvements on the electrical and luminescent properties of reactive molecular beam epitaxially grown GaN films by using AlN-coated sapphire substrates. *Applied Physics Letters*, *42*(5), 427-429.

[10] Strite, S., Lin, M. E., & Morkoc, H. (1993). Progress and prospects for GaN and the III–V nitride semiconductors. *Thin Solid Films*, *231*(1), 197-210.

[11] Ambacher, O. (1998). Growth and applications of group III-nitrides. *Journal of Physics D: Applied Physics*, *31*(20), 2653.

[12] Jakobson, C., Bloom, I., & Nemirovsky, Y. (1998). 1/f noise in CMOS transistors for analog applications from subthreshold to saturation. *Solid-State Electronics*, *42*(10), 1807-1817.

[13] Ambacher, O., Foutz, B., Smart, J., Shealy, J. R., Weimann, N. G., Chu, K., ... & Dimitrov, R. (2000). Two dimensional electron gases induced by spontaneous and piezoelectric polarization in undoped and doped AlGaN/GaN heterostructures. *Journal of applied physics*, *87*(1), 334-344.

[14] Steinhoff, G., Baur, B., von Ribbeck, H. G., Wrobel, G., Ingebrandt, S., Offenhäusser, A., ... & Eickhoff, M. (2006). AlGaN/GaN electrolyte-gate field-effect transistors as transducers for bioelectronic devices. In *Advances in Solid State Physics* (pp. 363-374). Springer Berlin Heidelberg.

[15] B. Lübbers. AlGaN-based pH-Sensors: Impedance Characterisation, Optimisation and Application for Foetal Blood Sampling. PhD thesis, Technische Universität Ilmenau, Ilmenau, 2013.

[16] G. Kittler. GaN-basierte pH-Sensoren: Empfindlichkeit, Drift und Passivierungstechnologien. PhD thesis, Technische Universität Ilmenau, Ilmenau, 2007.

[17] Furchgott, R. F., Khan, M. T., & Jothianandan, D. (1987, March). Comparison of endothelium-dependent relaxation and nitric oxide-induced relaxation in rabbit aorta. In *Federation proceedings* (Vol. 46, No. 3, pp. 385-385). 9650 ROCKVILLE PIKE, BETHESDA, MD 20814-3998: FEDERATION AMER SOC EXP BIOL.

[18] Garcia, M. A., Losurdo, M., Wolter, S. D., Lampert, W. V., Bonaventura, J., Bruno, G., ... & Brown, A. S. (2008). Comparison of functionalized III–V semiconductor response for nitric oxide. *Sensor Letters*, *6*(4), 627-634.

[19] Nakamura, S. (1991). GaN growth using GaN buffer layer. *Japanese Journal of Applied Physics*, *30*(10A), L1705.

[20] Khan, M. A., Chen, Q., Sun, C. J., Shur, M., & Gelmont, B. (1995). Two-dimensional electron gas in GaN–AlGaN heterostructures deposited using trimethylamine-alane as the aluminum source in low pressure metalorganic chemical vapor deposition. *Applied physics letters*, *67*(10), 1429-1431.

[21] Ambacher, O., Smart, J., Shealy, J. R., Weimann, N. G., Chu, K., Murphy, M., ... & Stutzmann, M. (1999). Two-dimensional electron gases induced by spontaneous and piezoelectric polarization charges in N-and Ga-face AlGaN/GaN heterostructures. *Journal of Applied Physics*, *85*(6), 3222.

[22] Khan, M. A., Skogman, R. A., Van Hove, J. M., Krishnankutty, S., & Kolbas, R. M. (1990). Photoluminescence characteristics of AlGaN-GaN-AlGaN quantum wells. *Applied physics letters*, *56*(13), 1257-1259.

[23] Potts, H. R., & Pearson, G. L. (1966). Annealing and arsenic overpressure experiments on defects in gallium arsenide. *Journal of Applied Physics*, *37*(5), 2098-2103.

[24] Mizuta, M., Fujieda, S., Matsumoto, Y., & Kawamura, T. (1986). Low temperature growth of GaN and AlN on GaAs utilizing metalorganics and hydrazine. *Japanese journal of applied physics*, *25*(12A), L945.

[25] Lei, T., Fanciulli, M., Molnar, R. J., Moustakas, T. D., Graham, R. J., & Scanlon, J. (1991). Epitaxial growth of zinc blende and wurtzitic gallium nitride thin films on (001) silicon. *Applied physics letters*, *59*(8), 944-946.

[26] Powell, R. C., Tomasch, G. A., Kim, Y. W., Thornton, J. A., & Greene, J. E. (1990). Diamond, silicon carbide and related wide band gap semiconductors. In *MRS symposia proceedings* (No. 162).

[27] Strite, S., Ruan, J., Li, Z., Salvador, A., Chen, H., Smith, D. J., ... & Morkoc, H. (1991). An investigation of the properties of cubic GaN grown on GaAs by plasma-assisted molecular-beam epitaxy. *Journal of Vacuum Science & Technology B*, *9*(4), 1924-1929.

[28] Khan, M. A., Bhattarai, A., Kuznia, J. N., & Olson, D. T. (1993). High electron mobility transistor based on a GaN-AlxGa1− xN heterojunction. *Applied Physics Letters*, *63*(9), 1214-1215.

[29] Amano, H., Kito, M., Hiramatsu, K., & Akasaki, I. (1989). P-type conduction in Mg-doped GaN treated with low-energy electron beam irradiation (LEEBI). *Japanese Journal of Applied Physics*, *28*(12A), L2112.

[30] Osamura, K., Naka, S., & Murakami, Y. (1975). Preparation and optical properties of Ga1− xInxN thin films. *Journal of Applied Physics*, *46*(8), 3432-3437.

[31] Brunner, D., Angerer, H., Bustarret, E., Freudenberg, F., Höpler, R., Dimitrov, R., ... & Stutzmann, M. (1997). Optical constants of epitaxial AlGaN films and their temperature dependence. *Journal of applied physics*, *82*, 5090-5096.

[32] Bremser, M. D., Perry, W. G., Zheleva, T., Edwards, N. V., Nam, O. H., Parikh, N., ... & Davis, R. F. (1996). Growth, Doping and Characterization of Al x Ga 1− x N Thin Film Alloys on 6H-SiC (0001) Substrates. *MRS Internet Journal of Nitride Semiconductor Research*, *1*, e8.

[33] Koide, Y., Itoh, H., Khan, M. R. H., Hiramatu, K., Sawaki, N., & Akasaki, I. (1987). Energy band-gap bowing parameter in an AlxGa1− x N alloy. *Journal of applied physics*, *61*(9), 4540-4543.

[34] Kim, K. S., Saxler, A., Kung, P., Razeghi, M., & Lim, K. Y. (1997). Determination of the band-gap energy of Al1− xInxN grown by metal–organic chemical-vapor deposition. *Applied physics letters*, *71*(6), 800-802.

[35] Guo, Q., Ogawa, H., & Fstritida, A. (1995). Growth of Al x In 1− x N single crystal films by microwave-excited metalorganic vapor phase epitaxy. *Journal of crystal growth*, *146*(1), 462-466.

[36] Nakamura, S., Mukai, T., & Senoh, M. (1994). Candela-class high-brightness InGaN/AlGaN double-heterostructure blue-light-emitting diodes. *Applied Physics Letters*, *64*(13), 1687-1689.

[37] Taniyasu, Y., Kasu, M., & Makimoto, T. (2006). An aluminium nitride light-emitting diode with a wavelength of 210 nanometres. *Nature*, *441*(7091), 325-328.

[38] Fujii, T., Gao, Y., Sharma, R., Hu, E. L., DenBaars, S. P., & Nakamura, S. (2004). Increase in the extraction efficiency of GaN-based light-emitting diodes via surface roughening. *Applied physics letters*, *84*(6), 855-857.

[39] Watanabe, S., Yamada, N., Nagashima, M., Ueki, Y., Sasaki, C., Yamada, Y., ... & Kudo, H. (2003). Internal quantum efficiency of highly-efficient InxGa1− xN-based near-ultraviolet light-emitting diodes. *Applied physics letters*, *83*(24), 4906-4908.

[40] Fujioka, A., Misaki, T., Murayama, T., Narukawa, Y., & Mukai, T. (2010). Improvement in output power of 280-nm deep ultraviolet light-emitting diode by using AlGaN multi quantum wells. *Applied physics express*, *3*(4), 041001.

[41] Yamada, M., Mitani, T., Narukawa, Y., Shioji, S., Niki, I., Sonobe, S., ... & Mukai, T. (2002). InGaN-based near-ultraviolet and blue-light-emitting diodes with high external quantum efficiency using a patterned sapphire substrate and a mesh electrode. *Japanese journal of applied physics*, *41*(12B), L1431.

[42] Nakamura, S., Pearton, S., & Fasol, G. (2013). *The blue laser diode: the complete story*. Springer Science & Business Media.

[43] Cich, M. J., Aldaz, R. I., Chakraborty, A., David, A., Grundmann, M. J., Tyagi, A., ... & Krames, M. R. (2012). Bulk GaN based violet light-emitting diodes with high efficiency at very high current density. *Applied Physics Letters*, *101*(22), 223509.

[44] Gebinoga, M., Mai, P., Donahue, M., Kittler, M., Cimalla, I., Lübbers, B., Klett, M., Lebedev, V., Silveira, L., Singh, S. and Schober, A., 2012. Nerve cell response to inhibitors recorded with an aluminum–galliumnitride/galliumnitride field-effect transistor. *Journal of neuroscience methods*, *206*(2), pp.195-199.

[45] Schober, A., Fernekorn, U., Lübbers, B., Hampl, J., Weise, F., Schlingloff, G., Gebinoga, M., Worgull, M., Schneider, M., Augspurger, C. and Hildmann, C., M. Kittler and M. Donahue, 2011. Applied nano bio systems with microfluidics and biosensors for three-dimensional cell culture. *Materialwissenschaft und Werkstofftechnik*, *42*(2), pp.139-146.

[46] Hashizume, T., Saiki, A., & Terayama, K. (2011, October). Fabrication of Tantalum nitride thin film using the low vacuum magnetron sputtering system. In *IOP Conference Series: Materials Science and Engineering* (Vol. 18, No. 9, p. 092032). IOP Publishing.

[47] Bykhovski, A. D., Gelmont, B. L., & Shur, M. S. (1997). Elastic strain relaxation and piezoeffect in GaN-AlN, GaN-AlGaN and GaN-InGaN superlattices. *Journal of Applied Physics*, *81*(9), 6332-6338.

[48] Sun, C. J., Kung, P., Saxler, A., Ohsato, H., Haritos, K., & Razeghi, M. (1994). A crystallographic model of (00· 1) aluminum nitride epitaxial thin film growth on (00· 1) sapphire substrate. *Journal of applied physics*, *75*(8), 3964-3967.

[49] Sasaki, T., & Zembutsu, S. (1987). Substrate-orientation dependence of GaN single-crystal films grown by metalorganic vapor-phase epitaxy. *Journal of applied physics*, *61*(7), 2533-2540.

[50] Murphy, M. J., Chu, K., Wu, H., Yeo, W., Schaff, W. J., Ambacher, O., ... & Eustis, T. J. (1999). Molecular beam epitaxial growth of normal and inverted two-dimensional electron gases in AlGaN/GaN based heterostructures. *Journal of Vacuum Science & Technology B*, *17*(3), 1252-1254.

[51] Ambacher, O., Dimitrov, R., Stutzmann, M., Foutz, B. E., Murphy, M. J., Smart, J. A., ... & Green, B. (1999). Role of Spontaneous and Piezoelectric Polarization Induced Effects in Group-III Nitride Based Heterostructures and Devices. *physica status solidi (b)*, *216*(1), 381-389.

[52] C. Buchheim. Dielektrische Funktion und elektrooptische Eigenschaften von (Al,Ga)N/GaN-Heterostrukturen. PhD thesis, Technische Universität Ilmenau, Ilmenau, 2010.

[53] Köhler, K., Müller, S., Aidam, R., Waltereit, P., Pletschen, W., Kirste, L., ... & Mikulla, M. (2010). Influence of the surface potential on electrical properties of AlxGa1− xN/GaN heterostructures with different Al-content: Effect of growth method. *Journal of Applied Physics*, *107*(5), 053711.

[54] K. Tonisch. AlGaN/GaN-Schichtsysteme für piezoelektrisch angeregte Resonatoren. PhD thesis, Technische Universität Ilmenau, Ilmenau, 2009.

[55] F. Niebelschuetz. Mikrostrukturierungstechniken zur Herstellung von MEMS aus Halbleitern großer Bandlücke. PhD thesis, Technische Universität Ilmenau, Ilmenau, 2010.

[56] Donahue, M., Lübbers, B., Kittler, M., Mai, P., & Schober, A. (2013). Impedance characterization of AlGaN/GaN Schottky diodes with metal contacts. *Applied Physics Letters*, *102*(14), 141607.

[57] Lang, D. V., Logan, R. A., & Jaros, M. (1979). Trapping characteristics and a donor-complex (DX) model for the persistent-photoconductivity trapping center in Te-doped Al x Ga 1− x As. *Physical Review B*, *19*(2), 1015.

[58] Lang, D. V., Petroff, P. M., Logan, R. A., & Johnston Jr, W. D. (1979). Recombination-enhanced interactions between point defects and dislocation climb in semiconductors. *Physical Review Letters*, *42*(20), 1353.

[59] Chen, H. M., Chen, Y. F., Lee, M. C., & Feng, M. S. (1997). Persistent photoconductivity in n-type GaN. *Journal of applied physics*, *82*(2), 899-901.

[60] Li, J. Z., Lin, J. Y., Jiang, H. X., Khan, M. A., & Chen, Q. (1997). Persistent photoconductivity in a two-dimensional electron gas system formed by an AlGaN/GaN heterostructure. *Journal of applied physics*, *82*(3), 1227-1230.

[61] Beadie, G., Rabinovich, W. S., Wickenden, A. E., Koleske, D. D., Binari, S. C., & Freitas Jr, J. A. (1997). Persistent photoconductivity in n-type GaN. *Applied physics letters*, *71*(8), 1092-1094.

[62] Johnson, C., Lin, J. Y., Jiang, H. X., Khan, M. A., & Sun, C. J. (1996). Metastability and persistent photoconductivity in Mg-doped p-type GaN. *Applied physics letters*, *68*(13), 1808-1810.

[63] Qiu, C. H., & Pankove, J. I. (1997). Deep levels and persistent photoconductivity in GaN thin films. *Applied physics letters*, *70*(15), 1983-1985.

[64] Dang, X. Z., Wang, C. D., Yu, E. T., Boutros, K. S., & Redwing, J. M. (1998). Persistent photoconductivity and defect levels in n-type AlGaN/GaN heterostructures. *Applied physics letters*, *72*(21), 2745-2747.

[65] Minsky, M. S., White, M., & Hu, E. L. (1996). Room-temperature photoenhanced wet etching of GaN. *Applied physics letters*, *68*(11), 1531-1533.

[66] Youtsey, C., Adesida, I., & Bulman, G. (1997). Broad-area photoelectrochemical etching of GaN. *Electronics Letters*, *33*(3), 245-246.

[67] Peng, L. H., Chuang, C. W., Ho, J. K., Huang, C. N., & Chen, C. Y. (1998). Deep ultraviolet enhanced wet chemical etching of gallium nitride. *Applied physics letters*, *72*, 939.

[68] Youtsey, C., Romano, L. T., & Adesida, I. (1998). Gallium nitride whiskers formed by selective photoenhanced wet etching of dislocations. *Applied physics letters*, *73*(6), 797-799.

[69] Yang, B., & Fay, P. (2006). Bias-enhanced lateral photoelectrochemical etching of GaN for the fabrication of undercut micromachined system structures. *Journal of Vacuum Science & Technology B*, *24*(3), 1337-1340.

[70] Weyher, J. L., & Van de Ven, J. (1983). Selective etching and photoetching of {100} gallium arsenide in CrO 3-HF aqueous solutions: I. Influence of composition on etching behaviour. *Journal of crystal growth*, *63*(2), 285-291.

[71] CLARK JR, L. C., & CLARK, E. W. (1987). A personalized history of the Clark oxygen electrode. *International anesthesiology clinics*, *25*(3), 1-29.

[72] Astrup, P., & Severinghaus, J. W. (1986). *The history of blood gases, acids, and bases*. Munksgaard.

[73] Lama, R. D., Charlson, K., Anantharam, A., & Hashemi, P. (2012). Ultrafast detection and quantification of brain signaling molecules with carbon fiber microelectrodes. *Analytical chemistry*, *84*(19), 8096-8101.

[74] Dubach, J. M., Lim, E., Zhang, N., Francis, K. P., & Clark, H. (2011). In vivo sodium concentration continuously monitored with fluorescent sensors. *Integrative Biology*, *3*(2), 142-148.

[75] Effros, R. M., & Widell, J. L. (2010). Acid-base balance. *Murray and Nadel's Textbook of Respiratory Medicine, 5th Ed., edited by Mason RJ, Broaddus VC, Martin T, King T Jr, Schraufnagel D, Murray JF, Nadel JA, Philadelphia, WB Saunders*, 135-156.

[76] Ebbing, D., & Gammon, S. D. (2010). *General chemistry*. Cengage Learning.

[77] Ehlers, C., Ivens, U. I., Møller, M. L., Senderovitz, T., & Serup, J. (2001). Comparison of two pH meters used for skin surface pH measurement: the pH meter 'pH900'from Courage & Khazaka versus the pH meter '1140'from Mettler Toledo. *Skin research and Technology*, *7*(2), 84-89.

[78] Bayram, F., Özerkan, K., Cengiz, C., Develioglu, O., & Cetinkaya, M. (2010). Perinatal asphyxia is associated with the umbilical cord nucleated red blood cell count in pre-eclamptic pregnancies. *Journal of Obstetrics & Gynaecology*, *30*(4), 383-386.

[79] Henderson, L. J., & Black, O. F. (1907). CONCERNING THE NEUTRALITY OF PROTOPLASM. *Am. J. Physiol*, *18*, 250-255.

[80] Henderson, L. J. (1908). Concerning the relationship between the strength of acids and their capacity to preserve neutrality. *American Journal of Physiology--Legacy Content*, *21*(2), 173-179.

[81] Ben-Yaakov, S., & Kaplan, I. R. (1968). High pressure pH sensor for oceanographic applications. *Review of Scientific Instruments*, *39*(8), 1133-1138.

[82] Thomas, G. W. (1996). Soil pH and soil acidity. *Methods of soil analysis. Part*, *3*, 475-490.

[83] Patterson, J. W. (1985). Industrial wastewater treatment technology.

[84] Severinghaus, J. W., & Astrup, P. B. (1985). History of blood gas analysis. I. The development of electrochemistry. *Journal of clinical monitoring*, *1*(3), 180-192.

[85] Severinghaus, J. W., & Astrup, P. B. (1985). History of blood gas analysis. II. pH and acid-base balance measurements. *Journal of clinical monitoring*, *1*(4), 259-277.

[86] Szabadváry, F. (2013). *History of Analytical Chemistry: International Series of Monographs in Analytical Chemistry*. Elsevier.

[87] Ostwald, W. (1890). *Über die Affinitätsgrössen organischer Säuren und ihre Beziehungen zur Zussammensetzung und Constitution derselben*. Hirzel.

[88] Nernst, W. (1888). Zur kinetik der in lösung befindlichen körper.

[89] Nernst, W. (1889). Die elektromotorische Wirksamkeit der Jonen.. (Doctoral dissertation).

[90] Sørensen, S. P. L. (1909). Über die Messung und die Bedeutung der Wasserstoffionenkonzentration bei enzymatischen Prozessen.

[91] Sørensen, S. P. L., & Linderstrøm-Lang, K. (1924). On the determination and value of π 0 in electrometric measurements of hydrogen ion concentrations. *Compt. rend. du Lab. Carlsberg*, *15*, 1-40.

[92] Feldman, I. (1956). Use and abuse of pH measurements. *Analytical Chemistry*, *28*(12), 1859-1866.

[93] Gillespie, L. J., & Hurst, L. A. (1918). HYDROGEN-ION CONCENTRATION-SOIL TYPE-COMMON POTATO SCAB. *Soil Science*, *6*(3), 219-236.

[94] Sharp, L. T., & Hoagland, D. R. (1919). NOTES ON RECENT WORK CONCERNING ACID SOILS. *Soil Science*, *7*(3), 197-200.

[95] Clark, W.M., The determination of hydrogen ions, Baltimore (1920).

[96] Hasselbalch, K. A. (1917). "Die Berechnung der Wasserstoffzahl des Blutes aus der freien und gebundenen Kohlensäure desselben, und die Sauerstoffbindung des Blutes als Funktion der Wasserstoffzahl*". Biochemische Zeitschrift* **78**: 112–144.

[97] Bray, J. J., Cragg, P. A., & Macknight, A. D. (1994). *Lecture notes on human physiology*. London: Blackwell Scientific Publications, 1994.

[98] Beckman, A. O. (1936). *U.S. Patent No. 2,058,761*. Washington, DC: U.S. Patent and Trademark Office.

[99] ©Mettler-Toledo Intl. Inc. (Jan. 2016). _LabX® for pH meter. Retrieved from: http://de.mt.com/de/de/home/microsites/labx/Instruments/phmeter.html

[100] Life: The Science of Biology 4th Edition by Purves, William K.; Orians, Gordon H.; Heller, H. C Raig; He, Sinauer Associates Inc (December 1, 1994).

[101] Basava-Reddi, L., Stalker, L., Noble, R., Pejcic, B., Leybourne, M., Hortle, A., & Michael, K. (2011, November). Feasibility of Monitoring Techniques for Substances Mobilised by CO2 Storage in Geological Formations. In 1st Sustainable Earth Sciences Conference & Exhibition (SES2011).

[102] Haber, F., & Klemensiewicz, Z. (1909). Über elektrische phasengrenzkräfte. *Z. phys. Chem*, *67*, 385-431.

[103] A.J. Bard and L.R. Faulkner, Electrochemical Methods Fundamentals and Applications, Wiley, New York, 1980.

[104] Bakker, E., & Pretsch, E. (2002). Peer Reviewed: The new wave of ion-selective electrodes. *Analytical chemistry*, *74*(15), 420-A.

[105] Bühlmann, P., & Chen, L. D. (2012). Ion-Selective Electrodes With Ionophore-Doped Sensing Membranes. *Supramolecular Chemistry: From Molecules to Nanomaterials*.

[106] "Glass electrode scheme-1" by Glass_electrode_scheme.jpg: Kaverinderivative work: Hidodu - Glass_electrode_scheme.jpg. Licensed under CC BY-SA 3.0 via Commons. Retrieved from: https://commons.wikimedia.org/wiki/File:Glass_electrode_scheme-1.jpg#/media/File:Glass_electrode_scheme-1.jpg.

[107] Newman, J., & Thomas-Alyea, K. E. (2012). *Electrochemical systems*. John Wiley & Sons.

[108] Trasatti, S. (1986). The absolute electrode potential: an explanatory note (Recommendations 1986). *Pure and Applied Chemistry*, *58*(7), 955-966.

[109] Shrestha, B. (April 2010). CHEM GUIDE – Electrochemical Cell. Retrieved from: http://chem-guide.blogspot.fr/2010/04/electrochemical-cell.html

[110] Moncada, S. R. M. J., Palmer, R. M. L., & Higgs, E. (1991). Nitric oxide: physiology, pathophysiology, and pharmacology. *Pharmacological reviews*, *43*(2), 109-142.

[111] Pearson, A. M., & Tauber, F. W. (1984). Processed meats. Westport, Connecticut, USA: Avi Publishing Company.

[112] Leroy, F., Geyzen, A., Janssens, M., De Vuyst, L., & Scholliers, P. (2013). Meat fermentation at the crossroads of innovation and tradition: a historical outlook. *Trends in Food Science & Technology*, *31*(2), 130-137.

[113] Ignarro, L. J. (2002). NITRIC OXIDE AS A UNIQUE SIGNALING MOLECULE IN THE. *Journal of physiology and pharmacology*, *53*(4), 503-514.

[114] Furchgott, R. F., & Zawadzki, J. V. (1980). The obligatory role of endothelial cells in the relaxation of arterial smooth muscle by acetylcholine. *Nature*, *288*(5789), 373-376.

[115] Furchgott, R. F., & Bhadrakom, S. (1953). Reactions of strips of rabbit aorta to epinephrine, isopropylarterenol, sodium nitrite and other drugs. *Journal of Pharmacology and Experimental Therapeutics*, *108*(2), 129-143.

[116] Katsuki, S., Arnold, W., Mittal, C., & Murad, F. (1977). Stimulation of guanylate cyclase by sodium nitroprusside, nitroglycerin and nitric oxide in various tissue preparations and comparison to the effects of sodium azide and hydroxylamine. *Journal of cyclic nucleotide research*, *3*(1), 23-35.

[117] Böhme, E., Graf, H., & Schultz, G. (1977). Effects of sodium nitroprusside and other smooth muscle relaxants on cyclic GMP formation in smooth muscle and platelets. *Advances in cyclic nucleotide research*, *9*, 131-143.

[118] Murad, F., Arnold, W. P., Mittal, C. K., & Braughler, J. M. (1978). Properties and regulation of guanylate cyclase and some proposed functions for cyclic GMP. *Advances in cyclic nucleotide research*, *11*, 175-204.

[119] Murad, F. (1986). Cyclic guanosine monophosphate as a mediator of vasodilation. *Journal of Clinical Investigation*, *78*(1), 1.

[120] Ignarro, L. J., Buga, G. M., Wood, K. S., Byrns, R. E., & Chaudhuri, G. (1987). Endothelium-derived relaxing factor produced and released from artery and vein is nitric oxide. *Proceedings of the National Academy of Sciences*, *84*(24), 9265-9269.

[121] Palmer, R. M., Ferrige, A. G., & Moncada, S. (1987). Nitric oxide release accounts for the biological activity of endothelium-derived relaxing factor.

[122] Nathan, C. F., & Hibbs, J. B. (1991). Role of nitric oxide synthesis in macrophage antimicrobial activity. *Current opinion in immunology*, *3*(1), 65-70.

[123] Nathan, C. (1992). Nitric oxide as a secretory product of mammalian cells. *The FASEB Journal*, *6*(12), 3051-3064.

[124] Garthwaite, J., Charles, S. L., & Chess-Williams, R. (1988). Endothelium-derived relaxing factor release on activation of NMDA receptors suggests role as intercellular messenger in the brain.

[125] Gillespie, J. S., Liu, X., & Martin, W. (1989). The effects of L-arginine and NG-monomethyl L-arginine on the response of the rat anococcygeus muscle to NANC nerve stimulation. *British journal of pharmacology*, *98*(4), 1080-1082.

[126] SoRelle, R. (1998). Nobel prize awarded to scientists for nitric oxide discoveries. *Circulation*, *98*(22), 2365-2366.

[127] Łowicka, E., & Bełtowski, J. (2006). Hydrogen sulfide (H2S)-the third gas of interest for pharmacologists. *Pharmacological reports: PR*, *59*(1), 4-24.

[128] Li, L., Hsu, A., & Moore, P. K. (2009). Actions and interactions of nitric oxide, carbon monoxide and hydrogen sulphide in the cardiovascular system and in inflammation—a tale of three gases!. *Pharmacology & therapeutics*, *123*(3), 386-400.

[129] Schmidt, H. H., & Walter, U. (1994). NO at work. *cell*, *78*(6), 919-925.

[130] Hibbs, J. B., Taintor, R. R., Vavrin, Z., & Rachlin, E. M. (1988). Nitric oxide: a cytotoxic activated macrophage effector molecule. *Biochemical and biophysical research communications*, *157*(1), 87-94.

[131] Nathan, C., & Xie, Q. W. (1994). Nitric oxide synthases: roles, tolls, and controls. *Cell*, *78*(6), 915-918.

[132] Green, L. C., De Luzuriaga, K. R., Wagner, D. A., Rand, W., Istfan, N., Young, V. R., & Tannenbaum, S. R. (1981). Nitrate biosynthesis in man. *Proceedings of the National Academy of Sciences*, *78*(12), 7764-7768.

[133] Beckman, J. S., & Koppenol, W. H. (1996). Nitric oxide, superoxide, and peroxynitrite: the good, the bad, and ugly. *American Journal of Physiology-Cell Physiology*, *271*(5), C1424-C1437.

[134] Pacher, P., Beckman, J. S., & Liaudet, L. (2007). Nitric oxide and peroxynitrite in health and disease. *Physiological reviews*, *87*(1), 315-424.

[135] Bredt, D. S., & Snyder, S. H. (1992). Nitric oxide, a novel neuronal messenger. *Neuron*, *8*(1), 3-11.

[136] Vanhoutte, P. M., Shimokawa, H., Tang, E. H., & Feletou, M. (2009). Endothelial dysfunction and vascular disease. *Acta Physiologica*, *196*(2), 193-222.

[137] Bredt, D. S., & Snyder, S. H. (1994). Nitric oxide: a physiologic messenger molecule. *Annual review of biochemistry*, 63(1), 175-195.

[138] Vanhoutte, P. M. (1998). Vascular biology: old-timer makes a comeback. *Nature*, *396*(6708), 213-216.

[139] Lowenstein, C. J., & Padalko, E. (2004). iNOS (NOS2) at a glance. *Journal of cell science*, *117*(14), 2865-2867.

[140] Spanagel, R. (2009). Alcoholism: a systems approach from molecular physiology to addictive behavior. *Physiological reviews*, *89*(2), 649-705.

[141] Cho, H. J., Xie, Q. W., Calaycay, J., Mumford, R. A., Swiderek, K. M., Lee, T. D., & Nathan, C. (1992). Calmodulin is a subunit of nitric oxide synthase from macrophages. *The Journal of experimental medicine*, *176*(2), 599-604.

[142] Guix, F. X., Uribesalgo, I., Coma, M., & Munoz, F. J. (2005). The physiology and pathophysiology of nitric oxide in the brain. *Progress in neurobiology*, *76*(2), 126-152.

[143] Hibbs, J. B. (1991). Synthesis of nitric oxide from L-arginine: a recently discovered pathway induced by cytokines with antitumour and antimicrobial activity. *Research in immunology*, *142*(7), 565-569.

[144] Burney, S., Caulfield, J. L., Niles, J. C., Wishnok, J. S., & Tannenbaum, S. R. (1999). The chemistry of DNA damage from nitric oxide and peroxynitrite. *Mutation Research/Fundamental and Molecular Mechanisms of Mutagenesis*, *424*(1), 37-49.

[145] Chabrier, P. E., Demerle-Pallardy, C., & Auguet, M. (1999). Nitric oxide synthases: targets for therapeutic strategies in neurological diseases. *Cellular and Molecular Life Sciences CMLS*, *55*(8-9), 1029-1035.

[146] Good, P. F., Hsu, A., Werner, P., Perl, D. P., & Olanow, C. W. (1998). Protein nitration in Parkinson's disease. *Journal of Neuropathology & Experimental Neurology*, *57*(4), 338-342.

[147] Smith, M. A., Harris, P. L. R., Sayre, L. M., Beckman, J. S., & Perry, G. (1997). Widespread peroxynitrite-mediated damage in Alzheimer’s disease. *The Journal of neuroscience*, *17*(8), 2653-2657.

[148] Cookson, M. R., & Shaw, P. J. (1999). Oxidative stress and motor neurone disease. *Brain pathology*, *9*(1), 165-186.

[149] Nagase, S., Takemura, K., Ueda, A., Hirayama, A., Aoyagi, K., Kondoh, M., & Koyama, A. (1997). A novel nonenzymatic pathway for the generation of nitric oxide by the reaction

of hydrogen peroxide and D-or L-arginine. *Biochemical and biophysical research communications*, *233*(1), 150-153.

[150] Maiese, K., Greenberg, R., Boccone, L., & Swiriduk, M. (1995). Activation of the metabotropic glutamate receptor is neuroprotective during nitric oxide toxicity in primary hippocampal neurons of rats. *Neuroscience letters*, *194*(3), 173-176.

[151] Malinski, T., & Taha, Z. (1992). Nitric oxide release from a single cell measured in situ by a porphyrinic-based microsensor. *Nature*, *358*(6388), 676-678.

[152] Malinski, T., Taha, Z. G. S. P. S. K. M. P., Grunfeld, S., Patton, S., Kapturczak, M., & Tomboulian, P. (1993). Diffusion of nitric oxide in the aorta wall monitored in situ by porphyrinic microsensors. *Biochemical and biophysical research communications*, *193*(3), 1076-1082.

[153] Malinski, T., Radomski, M. W., Taha, Z., & Moncada, S. (1993). Direct electrochemical measurement of nitric oxide released from human platelets. *Biochemical and biophysical research communications*, *194*(2), 960-965.

[154] Deinum, G., Stone, J. R., Babcock, G. T., & Marletta, M. A. (1996). Binding of nitric oxide and carbon monoxide to soluble guanylate cyclase as observed with resonance Raman spectroscopy. *Biochemistry*, *35*(5), 1540-1547.

[155] Selwood, D. L., Brummell, D. G., Budworth, J., Burtin, G. E., Campbell, R. O., Chana, S. S., ... & Hobbs, A. J. (2001). Synthesis and biological evaluation of novel pyrazoles and indazoles as activators of the nitric oxide receptor, soluble guanylate cyclase. *Journal of medicinal chemistry*, *44*(1), 78-93.

[156] Barker, S. L., Zhao, Y., Marletta, M. A., & Kopelman, R. (1999). Cellular applications of a sensitive and selective fiber-optic nitric oxide biosensor based on a dye-labeled heme domain of soluble guanylate cyclase. *Analytical chemistry*, *71*(11), 2071-2075.

[157] Henry, Y., Ducrocq, C., Drapier, J. C., Servent, D., Pellat, C., & Guissani, A. (1991). Nitric oxide, a biological effector. *European biophysics journal*, *20*(1), 1-15.

[158] Lancaster, J. R. (1997). A tutorial on the diffusibility and reactivity of free nitric oxide. *Nitric Oxide*, *1*(1), 18-30.

[159] Shaw, S. R. (1977). Restricted diffusion and extracellular space in the insect retina. *Journal of comparative physiology*, *113*(3), 257-282.

[160] Subczynski, W. K., Lomnicka, M., & Hyde, J. S. (1996). Permeability of nitric oxide through lipid bilayer membranes. *Free radical research*, *24*(5), 343-349.

[161] Lancaster, J. R. (1994). Simulation of the diffusion and reaction of endogenously produced nitric oxide. *Proceedings of the National Academy of Sciences*, *91*(17), 8137-8141.

[162] Schuman, E. M., & Madison, D. V. (1994). Nitric oxide and synaptic function. *Annual review of neuroscience*, *17*, 153-183.

[163] Leone, A. M., Furst, V. W., Foxwell, N. A., Cellek, S., & Moncada, S. (1996). Visualisation of nitric oxide generated by activated murine macrophages. *Biochemical and biophysical research communications*, *221*(1), 37-41.

[164] Liu, X., Miller, M. J., Joshi, M. S., Sadowska-Krowicka, H., Clark, D. A., & Lancaster, J. R. (1998). Diffusion-limited reaction of free nitric oxide with erythrocytes. *Journal of biological chemistry*, *273*(30), 18709-18713.

[165] Archer, S. (1993). Measurement of nitric oxide in biological models. *The FASEB journal*, *7*(2), 349-360.

[166] Bedioui, F., & Villeneuve, N. (2003). Electrochemical nitric oxide sensors for biological samples–principle, selected examples and applications. *Electroanalysis*, *15*(1), 5-18.

[167] Malinski, T., Bailey, F., Zhang, Z. G., & Chopp, M. (1993). Nitric oxide measured by a porphyrinic microsensor in rat brain after transient middle cerebral artery occlusion. *Journal of Cerebral Blood Flow & Metabolism*, *13*(3), 355-358.

[168] Ciszewski, A., & Milczarek, G. (2003). Electrochemical detection of nitric oxide using polymer modified electrodes. *Talanta*, *61*(1), 11-26.

[169] Clyne, M. A. A., Thrush, B. A., & Wayne, R. P. (1964). Kinetics of the chemiluminescent reaction between nitric oxide and ozone. *Transactions of the Faraday Society*, *60*, 359-370.

[170] Fontijn, A., Sabadell, A. J., & Ronco, R. J. (1970). Homogeneous chemiluminescent measurement of nitric oxide with ozone. Implications for continuous selective monitoring of gaseous air pollutants. *Analytical Chemistry*, *42*(6), 575-579.

[171] Archer, S. L., & Cowan, N. J. (1991). Measurement of endothelial cytosolic calcium concentration and nitric oxide production reveals discrete mechanisms of endothelium-dependent pulmonary vasodilatation. *Circulation research*, *68*(6), 1569-1581.

[172] Brien, J. F., McLaughlin, B. E., Nakatsu, K., & Marks, G. S. (1991). Quantitation of nitric oxide formation from nitrovasodilator drugs by chemiluminescence analysis of headspace gas. *Journal of pharmacological methods*, *25*(1), 19-27.

[173] Arroyo, C. M., & Kohno, M. (1991). Difficulties encountered in the detection of nitric oxide (NO) by spin trapping techniques. A cautionary note. *Free radical research communications*, *14*(2), 145-155.

[174] Greenberg, S. S., Wilcox, D. E., & Rubanyi, G. M. (1990). Endothelium-derived relaxing factor released from canine femoral artery by acetylcholine cannot be identified as free nitric oxide by electron paramagnetic resonance spectroscopy. *Circulation research*, *67*(6), 1446-1452.

[175] Wennmalm, Å., Lanne, B., & Petersson, A. S. (1990). Detection of endothelial-derived relaxing factor in human plasma in the basal state and following ischemia using electron paramagnetic resonance spectrometry. *Analytical biochemistry*, *187*(2), 359-363.

[176] Wang, J. F., Komarov, P., Sies, H., & de Groot, H. (1991). Contribution of nitric oxide synthase to luminol-dependent chemiluminescence generated by phorbol-ester-activated Kupffer cells. *Biochem. J*, *279*, 311-314.

[177] Westenberger, U., Thanner, S., Ruf, H. H., Gersonde, K., Sutter, G., & Trentz, O. (1990). Formation of free radicals and nitric oxide derivative of hemoglobin in rats during shock syndrome. *Free Radical Research*, *11*(1-3), 167-178.

[178] Kelm, M., Feelisch, M., Spahr, R., Piper, H. M., Noack, E., & Schrader, J. (1988). Quantitative and kinetic characterization of nitric oxide and EDRF released from cultured endothelial cells. *Biochemical and biophysical research communications*, *154*(1), 236-244.

[179] Gustafsson, L. E., Leone, A. M., Persson, M. G., Wiklund, N. P., & Moncada, S. (1991). Endogenous nitric oxide is present in the exhaled air of rabbits, guinea pigs and humans. *Biochemical and biophysical research communications*, *181*(2), 852-857.

[180] Shibuki, K. (1990). An electrochemical microprobe for detecting nitric oxide release in brain tissue. *Neuroscience research*, *9*(1), 69-76.

[181] Shibuki, K., & Okada, D. (1991). Endogenous nitric oxide release required for long-term synaptic depression in the cerebellum. *Nature*, *349*(6307), 326-328.

[182] Mao, L., Yamamoto, K., Zhou, W., & Jin, L. (2000). Electrochemical nitric oxide sensors based on electropolymerized film of M (salen) with central ions of Fe, Co, Cu, and Mn. *Electroanalysis*, *12*(1), 72-77.

[183] Topoglidis, E., Astuti, Y., Duriaux, F., Grätzel, M., & Durrant, J. R. (2003). Direct electrochemistry and nitric oxide interaction of heme proteins adsorbed on nanocrystalline tin oxide electrodes. *Langmuir*, *19*(17), 6894-6900.

[184] Wu, F. H., Zhao, G. C., & Wei, X. W. (2002). Electrocatalytic oxidation of nitric oxide at multi-walled carbon nanotubes modified electrode. *Electrochemistry Communications*, *4*(9), 690-694.

[185] Chang, D., Malinski, T., Ulman, A., & Kadish, K. M. (1984). Electrochemistry of nickel (II) porphyrins and chlorins. *Inorganic Chemistry*, *23*(7), 817-824.

[186] Malinski, T., Ciszewski, A., Bennett, J., Fish, J. R., & Czuchajowski, L. (1991). Characterization of Conductive Polymeric Nickel (II) Tetrakis (3-methoxy-4-hydroxy-phenyl) Porphyrin as an Anodic Material for Electrocatalysis. *Journal of The Electrochemical Society*, *138*(7), 2008-2015.

[187] Zhang, C., Hein, T. W., Wang, W., Miller, M. W., Fossum, T. W., McDonald, M. M., ... & Kuo, L. (2004). Upregulation of vascular arginase in hypertension decreases nitric oxide–mediated dilation of coronary arterioles. *Hypertension*, *44*(6), 935-943.

[188] Shao, S., Qiu, X., He, D., Koehn, R., Guan, N., Lu, X., ... & Grimes, C. A. (2011). Low temperature crystallization of transparent, highly ordered nanoporous SnO 2 thin films: application to room-temperature hydrogen sensing. *Nanoscale*, *3*(10), 4283-4289.

[189] Sberveglieri, G. (1995). Recent developments in semiconducting thin-film gas sensors. *Sensors and Actuators B: Chemical, 23*(2), 103-109.

[190] Sberveglieri, G. (1992). Classical and novel techniques for the preparation of SnO 2 thin-film gas sensors. *Sensors and Actuators B: Chemical, 6*(1), 239-247.

[191] Ogita, M., Higo, K., Nakanishi, Y., & Hatanaka, Y. (2001). Ga 2 O 3 thin film for oxygen sensor at high temperature. *Applied surface science, 175*, 721-725.

[192] Bergveld, P. (1970). Development of an ion-sensitive solid-state device for neurophysiological measurements. *IEEE Transactions on Biomedical Engineering*, *1*(BME-17), 70-71.

[193] Bergveld, P. (1972). Development, operation, and application of the ion-sensitive field-effect transistor as a tool for electrophysiology. *Biomedical Engineering, IEEE Transactions on*, (5), 342-351.

[194] Bergveld, P. (2003). Thirty years of ISFETOLOGY: What happened in the past 30 years and what may happen in the next 30 years. *Sensors and Actuators B: Chemical*, *88*(1), 1-20.

[195] Bergveld, P. (1976). Simple test for electrophysiologically tolerable parameters of artificial stimulation. *Medical and biological engineering*, *14*(5), 479-482.

[196] Janata, J. (1994). Historical review. Twenty years of ion-selective field-effect transistors. *Analyst*, *119*(11), 2275-2278.

[197] Steinhoff, G., Baur, B., Wrobel, G., Ingebrandt, S., Offenhäusser, A., Dadgar, A., ... & Eickhoffa, M. (2005). Recording of cell action potentials with AlGaN/GaN field-effect transistors. *environments*, *19*, 20.

[198] Offenhäusser, A., Rühe, J., & Knoll, W. (1995). Neuronal cells cultured on modified microelectronic device surfaces. *Journal of Vacuum Science & Technology A*, *13*(5), 2606-2612.

[199] Offenhäusser, A., Sprössler, C., Matsuzawa, M., & Knoll, W. (1997). Field-effect transistor array for monitoring electrical activity from mammalian neurons in culture. *Biosensors and Bioelectronics*, *12*(8), 819-826.

[200] Nakajima, H., Esashi, M., & Matsuo, T. (1982). The cation concentration response of polymer gate ISFET. *Journal of The Electrochemical Society*, *129*(1), 141-143.

[201] Bergveld, P., Van Den Berg, A., Van Der Wal, P. D., Skowronska-Ptasinska, M., Sudhölter, E. J. R., & Reinhoudt, D. N. (1989). How electrical and chemical requirements for REFETs may coincide. *Sensors and Actuators*, *18*(3), 309-327.

[202] Van Den Berg, A., Grisel, A., Van Den Vlekkert, H. H., & De Rooij, N. F. (1990). A micro-volume open liquid-junction reference electrode for pH-ISFETs. *Sensors and Actuators B: Chemical*, *1*(1), 425-432.

[203] Johnson, C. C., Moss, S. D., & Janata, J. A. (1977). *U.S. Patent No. 4,020,830*. Washington, DC: U.S. Patent and Trademark Office.

[204] Bergveld, P. (1981). The operation of an ISFET as an electronic device. *Sensors and Actuators*, *1*, 17-29.

[205] Sze, S. M., & Ng, K. K. (2006). *Physics of semiconductor devices*. John Wiley & Sons.

[206] Van Hal, R. E. G., Eijkel, J. C. T., & Bergveld, P. (1996). A general model to describe the electrostatic potential at electrolyte oxide interfaces. *Advances in colloid and interface science, 69*(1), 31-62.

[207] Bousse, L., De Rooij, N. F., & Bergveld, P. (1983). Operation of chemically sensitive field-effect sensors as a function of the insulator-electrolyte interface. *Electron Devices, IEEE Transactions on*, *30*(10), 1263-1270.

[208] Yates, D. E., Levine, S., & Healy, T. W. (1974). Site-binding model of the electrical double layer at the oxide/water interface. *Journal of the Chemical Society, Faraday Transactions 1: Physical Chemistry in Condensed Phases*, *70*, 1807-1818.

[209] Van Hal, R. E. G., Eijkel, J. C. T., & Bergveld, P. (1995). A novel description of ISFET sensitivity with the buffer capacity and double-layer capacitance as key parameters. *Sensors and Actuators B: Chemical*, *24*(1), 201-205.

[210] Siu, W. M., & Cobbold, R. S. (1979). Basic properties of the electrolyte—SiO 2—Si system: physical and theoretical aspects. *Electron Devices, IEEE Transactions on*, *26*(11), 1805-1815.

[211] Van den Berg, A., Bergveld, P., Reinhoudt, D. N., & Sudhölter, E. J. (1985). Sensitivity control of ISFETs by chemical surface modification. *Sensors and Actuators*, *8*(2), 129-148.

[212] Steinhoff, G., Hermann, M., Schaff, W. J., Eastman, L. F., Stutzmann, M., & Eickhoff, M. (2003). pH response of GaN surfaces and its application for pH-sensitive field-effect transistors. *Applied Physics Letters*, *83*(1), 177-179.

[213] Kocha, S. S., Peterson, M. W., Arent, D. J., Redwing, J. M., Tischler, M. A., & Turner, J. A. (1995). Electrochemical Investigation of the Gallium Nitride-Aqueous Electrolyte Interface. *Journal of the Electrochemical Society*, *142*(12), L238-L240.

[214] Tran Ba, K. H., Mastro, M. A., Hite, J. K., Eddy, C. R., & Ito, T. (2009). Nitrogen-polar gallium nitride substrates as solid-state pH-selective potentiometric sensors. *Applied Physics Letters*, *95*(14), 2501.

[215] Kokawa, T., Sato, T., Hasegawa, H., & Hashizume, T. (2006). Liquid-phase sensors using open-gate AlGaN/GaN high electron mobility transistor structure. *Journal of Vacuum Science & Technology B Microelectronics and Nanometer Structures*, *24*(4), 1972-1976.

[216] Hofstetter, M., Funk, M., Paretzke, H. G., Thalhammer, S., Howgate, J., Sharp, I. D., & Stutzmann, M. (2010). Real-time x-ray response of biocompatible solution gate AlGaN/GaN high electron mobility transistor devices. *Applied Physics Letters*, *96*(9).

[217] Buchheim, C., Winzer, A. T., Goldhahn, R., Gobsch, G., Ambacher, O., Link, A., ... & Stutzmann, M. (2004). Photoreflectance studies of (Al) Ga-and N-face AlGaN/GaN heterostructures. *Thin Solid Films*, *450*(1), 155-158.

[218] Bayer, M., Uhl, C., & Vogl, P. (2005). Theoretical study of electrolyte gate AlGaN⁄ GaN field effect transistors. *Journal of applied physics*, *97*(3), 033703.

[219] O'Clock Jr, G. D., & Duffy, M. T. (1973). Acoustic surface wave properties of epitaxially grown aluminum nitride and gallium nitride on sapphire. *Applied physics letters*, *23*(2), 55-56.

[220] Littlejohn, M. A., Hauser, J. R., & Glisson, T. H. (1975). Monte Carlo calculation of the velocity-field relationship for gallium nitride. *Applied Physics Letters*, *26*(11), 625-627.

[221] Bernardini, F., Fiorentini, V., & Vanderbilt, D. (1997). Spontaneous polarization and piezoelectric constants of III-V nitrides. *Physical Review B, 56*(16), R10024.

[222] Akiyama, T., Ujihira, Y., Okabe, Y., Sugano, T., & Niki, E. (1982). Ion-sensitive field-effect transistors with inorganic gate oxide for pH sensing. *Electron Devices, IEEE Transactions on*, *29*(12), 1936-1941.

[223] Fung, C. D., Cheung, P. W., & Ko, W. H. (1986). A generalized theory of an electrolyte-insulator-semiconductor field-effect transistor. *Electron Devices, IEEE Transactions on*, *33*(1), 8-18.

[224] Izquierdo, A., & de Castro, M. D. L. (1995). Ion-sensitive field-effect transistors and ion-selective electrodes as sensors in dynamic systems. *Electroanalysis*, *7*(6), 505-519.

[225] Van den Vlekkert, H. H., Verkerk, U. H., Van der Wal, P. D., Van Wingerden, A., Reinhoudt, D. N., Haak, J. R., ... & Holterman, H. A. J. (1992). Multi-ion sensing device for horticultural application based upon chemical modification and special packaging of ISFETs. *Sensors and Actuators B: Chemical*, *6*(1), 34-37.

[226] Kang, B. S., Ren, F., Wang, L., Lofton, C., Tan, W. W., Pearton, S. J., ... & Chow, P. P. (2005). Electrical detection of immobilized proteins with ungated AlGaN⁄ GaN high-electron-mobility Transistors. *Applied Physics Letters*, *87*(2), 023508.

[227] Chaiet, L., & Wolf, F. J. (1964). The properties of streptavidin, a biotin-binding protein produced by Streptomycetes. *Archives of biochemistry and biophysics*, *106*, 1-5.

[228] Smith, C. L., Milea, J. S., & Nguyen, G. H. (2005). Immobilization of nucleic acids using biotin-strept (avidin) systems. In *Immobilisation of DNA on Chips II* (pp. 63-90). Springer Berlin Heidelberg.

[229] Baur, B., Steinhoff, G., Hernando, J., Purrucker, O., Tanaka, M., Nickel, B., ... & Eickhoff, M. (2005). Chemical functionalization of GaN and AlN surfaces. *Applied Physics Letters*, *87*(26), 263901.

[230] Kang, B., Pearton, S. J., Chen, J. J., Ren, F., Johnson, J. W., Therrien, R. J., ... & Linthicum, K. J. (2006, January). Electrical detection of deoxyribonucleic acid hybridization with AlGaN/GaN high electron mobility transistors. In *MRS Proceedings* (Vol. 955, pp. 0955-I14). Cambridge University Press.

[231] Kang, B. S., Wang, H. T., Ren, F., Pearton, S. J., Morey, T. E., Dennis, D. M., ... & Linthicum, K. J. (2007). Enzymatic glucose detection using ZnO nanorods on the gate region of AlGaN/GaN high electron mobility transistors. *Applied Physics Letters*, *91*(25), 2103.

[232] Kang, B. S., Wang, H. T., Ren, F., & Pearton, S. J. (2008). Electrical detection of biomaterials using AlGaN/GaN high electron mobility transistors. *Journal of applied physics*, *104*(3), 031101.

[233] Petrovykh, D. Y., Kimura-Suda, H., Whitman, L. J., & Tarlov, M. J. (2003). Quantitative analysis and characterization of DNA immobilized on gold. *Journal of the American Chemical Society*, *125*(17), 5219-5226.

[234] Ichimura, T., Bonventre, J. V., Bailly, V., Wei, H., Hession, C. A., Cate, R. L., & Sanicola, M. (1998). Kidney injury molecule-1 (KIM-1), a putative epithelial cell adhesion molecule containing a novel immunoglobulin domain, is up-regulated in renal cells after injury. *Journal of Biological Chemistry*, *273*(7), 4135-4142.

[235] Smart, W. H., & Subramanian, K. (2000). The use of silicon microfabrication technology in painless blood glucose monitoring. *Diabetes technology & therapeutics*, *2*(4), 549-559.

[236] Sandifer, J. R., & Voycheck, J. J. (1999). A review of biosensor and industrial applications of pH-ISFETs and an evaluation of Honeywell's "DuraFET". *Microchimica Acta*, *131*(1-2), 91-98.

[237] Sudhölter, E. J., van der Wal, P. D., Skowronska-Ptasinska, M., van den Berg, A., Bergveld, P., & Reinhoudt, D. N. (1990). Modification of ISFETs by covalent anchoring of poly (hyroxyethyl methacrylate) hydrogel. Introduction of a thermodynamically defined semiconductor-sensing membrane interface. *Analytica chimica acta*, *230*, 59-65.

[238] Ruvimov, S., Liliental-Weber, Z., Washburn, J., Duxstad, K. J., Haller, E. E., Fan, Z. F., ... & Morkoc, H. (1996). Microstructure of Ti/Al and Ti/Al/Ni/Au Ohmic contacts for n-GaN. *Applied Physics Letters*, *69*(11), 1556-1558.

[239] Lin, M. E., Ma, Z., Huang, F., Fan, Z. F., Allen, L. H., & Morkoc, H. (1994). Low resistance ohmic contacts on wide band-gap GaN. *Applied Physics Letters*, *64*(8), 1003-1005.

[240] Miyauchi, M. (2008). Photocatalysis and photoinduced hydrophilicity of WO 3 thin films with underlying Pt nanoparticles. *Physical Chemistry Chemical Physics*, *10*(41), 6258-6265.

[241] Widenkvist, E., Quinlan, R. A., Holloway, B. C., Grennberg, H., & Jansson, U. (2008). Synthesis of nanostructured tungsten oxide thin films. *Crystal Growth and Design*, *8*(10), 3750-3753.

[242] Yamazoe, N., & Miura, N. (1994). Environmental gas sensing. *Sensors and Actuators B: Chemical*, *20*(2), 95-102.

[243] Yamazoe, N. (1991). New approaches for improving semiconductor gas sensors. *Sensors and Actuators B: Chemical*, *5*(1), 7-19.

[244] Hardee, K. L., & Bard, A. J. (1977). Semiconductor electrodes X. Photoelectrochemical behavior of several polycrystalline metal oxide electrodes in aqueous solutions. *Journal of the Electrochemical Society*, *124*(2), 215-224.

[245] Bittencourt, C., Landers, R., Llobet, E., Molas, G., Correig, X., Silva, M. A. P., ... & Calderer, J. (2002). Effects of oxygen partial pressure and annealing temperature on the formation of sputtered tungsten oxide films. *Journal of the Electrochemical Society*, *149*(3), H81-H86.

[246] Tägtström, P., & Jansson, U. (1999). Chemical vapour deposition of epitaxial WO 3 films. *Thin Solid Films*, *352*(1), 107-113.

[247] Antonaia, A., Polichetti, T., Addonizio, M. L., Aprea, S., Minarini, C., & Rubino, A. (1999). Structural and optical characterization of amorphous and crystalline evaporated WO 3 layers. *Thin Solid Films*, *354*(1), 73-81.

[248] Ho, C., Raistrick, I. D., & Huggins, R. A. (1980). Application of A-C Techniques to the Study of Lithium Diffusion in Tungsten Trioxide Thin Films. *Journal of The Electrochemical Society*, *127*(2), 343-350.

[249] Choi, Y. G., Sakai, G., Shimanoe, K., Teraoka, Y., Miura, N., & Yamazoe, N. (2003). Preparation of size and habit-controlled nano crystallites of tungsten oxide. *Sensors and Actuators B: Chemical*, *93*(1), 486-494.

[250] Baek, Y., & Yong, K. (2007). Controlled growth and characterization of tungsten oxide nanowires using thermal evaporation of WO3 powder. *The Journal of Physical Chemistry C, 111*(3), 1213-1218.

[251] Rajagopal, S.; Nataraj, D.; Mangalaraj, D.; Djaoued, Yahia; Robichaud, Jacques; Khyzhun, O. Yu. (2009): Controlled Growth of WO3 Nanostructures with Three Different Morphologies and Their Structural, Optical, and Photodecomposition Studies. In: *Nanoscale Res Lett 4* (11), S. 1335–1342.

[252] Marquis, B. T., & Vetelino, J. F. (2001). A semiconducting metal oxide sensor array for the detection of NO x and NH 3. *Sensors and Actuators B: Chemical*, *77*(1), 100-110.

[253] Siokou, A., Leftheriotis, G., Papaefthimiou, S., & Yianoulis, P. (2001). Effect of the tungsten and molybdenum oxidation states on the thermal coloration of amorphous WO 3 and MoO 3 films. *Surface science*, *482*, 294-299.

[254] Leftheriotis, G., Papaefthimiou, S., Yianoulis, P., & Siokou, A. (2001). Effect of the tungsten oxidation states in the thermal coloration and bleaching of amorphous WO 3 films. *Thin solid films*, *384*(2), 298-306.

[255] Szilágyi, I. M., Madarász, J., Pokol, G., Király, P., Tárkányi, G., Saukko, S., ... & Varga-Josepovits, K. (2008). Stability and controlled composition of hexagonal WO3. *Chemistry of Materials*, *20*(12), 4116-4125.

[256] Lee, J. S., Jang, I. H., & Park, N. G. (2012). Effects of oxidation state and crystallinity of tungsten oxide interlayer on photovoltaic property in bulk hetero-junction solar cell. *The Journal of Physical Chemistry C*, *116*(25), 13480-13487.

[257] Novoselov, K. S., Geim, A. K., Morozov, S. V., Jiang, D., Zhang, Y., Dubonos, S. A., ... & Firsov, A. A. (2004). Electric field effect in atomically thin carbon films. *science*, *306*(5696), 666-669.

[258] Schwierz, F. (2010). Graphene transistors. *Nature nanotechnology*, *5*(7), 487-496.

[259] Zhou, M., Zhai, Y., & Dong, S. (2009). Electrochemical sensing and biosensing platform based on chemically reduced graphene oxide. *Analytical Chemistry*, *81*(14), 5603-5613.

[260] Yang, Y., Asiri, A. M., Tang, Z., Du, D., & Lin, Y. (2013). Graphene based materials for biomedical applications. *Materials today*, *16*(10), 365-373.

[261] Huang, X., Qi, X., Boey, F., & Zhang, H. (2012). Graphene-based composites. *Chemical Society Reviews*, *41*(2), 666-686.

[262] Xiang, Q., Yu, J., & Jaroniec, M. (2012). Graphene-based semiconductor photocatalysts. *Chemical Society Reviews*, *41*(2), 782-796.

[263] Hummers Jr, W. S., & Offeman, R. E. (1958). Preparation of graphitic oxide. *Journal of the American Chemical Society*, *80*(6), 1339-1339.

[264] Dan, Y., Lu, Y., Kybert, N. J., Luo, Z., & Johnson, A. C. (2009). Intrinsic response of graphene vapor sensors. *Nano Letters*, *9*(4), 1472-1475.

[265] Fagan, S. B., Souza Filho, A. G., Lima, J. O. G., Filho, J. M., Ferreira, O. P., Mazali, I. O., ... & Dresselhaus, M. S. (2004). 1, 2-Dichlorobenzene interacting with carbon nanotubes. *Nano Letters*, *4*(7), 1285-1288.

[266] Zhang, Y. H., Chen, Y. B., Zhou, K. G., Liu, C. H., Zeng, J., Zhang, H. L., & Peng, Y. (2009). Improving gas sensing properties of graphene by introducing dopants and defects: a first-principles study. *Nanotechnology*, *20*(18), 185504.

[267] Chen, Y., Gao, B., Zhao, J. X., Cai, Q. H., & Fu, H. G. (2012). Si-doped graphene: an ideal sensor for NO-or NO2-detection and metal-free catalyst for N2O-reduction. Journal of molecular modeling, 18(5), 2043-2054.

[268] Goldoni, A., Larciprete, R., Petaccia, L., & Lizzit, S. (2003). Single-wall carbon nanotube interaction with gases: sample contaminants and environmental monitoring. *Journal of the American Chemical Society*, *125*(37), 11329-11333.

[269] Peng, S., & Cho, K. (2000). Chemical control of nanotube electronics. *Nanotechnology*, *11*(2), 57.

[270] Yavari, F., & Koratkar, N. (2012). Graphene-based chemical sensors. *The Journal of Physical Chemistry Letters*, *3*(13), 1746-1753

[271] Schedin, F., Geim, A. K., Morozov, S. V., Hill, E. W., Blake, P., Katsnelson, M. I., & Novoselov, K. S. (2007). Detection of individual gas molecules adsorbed on graphene. *Nature materials*, *6*(9), 652-655.

[272] Kanan, S. M., Lu, Z., Cox, J. K., Bernhardt, G., & Tripp, C. P. (2002). Identification of surface sites on monoclinic WO3 powders by infrared spectroscopy. *Langmuir*, *18*(5), 1707-1712.

[273] Afzal, A., Cioffi, N., Sabbatini, L., & Torsi, L. (2012). NO x sensors based on semiconducting metal oxide nanostructures: progress and perspectives. *Sensors and Actuators B: Chemical*, *171*, 25-42.

[274] "Haem-B-3D-vdW". Licensed under Public Domain via Commons - https://commons.wikimedia.org/wiki/File:Haem-B-3D-vdW.png#/media/File:Haem-B-3D-vdW.png

[275] "Porphyrin" by Lukáš Mižoch - Own work. Licensed under Public Domain via Commons - https://commons.wikimedia.org/wiki/File:Porphyrin.svg#/media/File:Porphyrin.svg

[276] Shore, L. 7500/9500 Series Hall System User's Manual. *Appendix A*.

[277] Drago, R. S., & Karstetter, B. R. (1961). The reaction of nitrogen (II) oxide with various primary and secondary amines. *Journal of the American Chemical Society*, *83*(8)

[278] Drago, R. S., & Paulik, F. E. (1960). The reaction of nitrogen (II) oxide with diethylamine. *Journal of the American Chemical society*, *82*(1), 96-98.

[279] Oelβner, W., Zosel, J., Berthold, F., & Kaden, H. (1995). Investigation of the dynamic response behaviour of ISFET pH sensors by means of laser Doppler velocimetry (LDV). *Sensors and Actuators B: Chemical*, *27*(1), 345-348.

[280] Rabilloud, G. (1999). *High-performance polymers: chemistry and applications* (Vol. 2). Editions Technip.

[281] Horch, K. W., & Dhillon, G. S. (2004). *Neuroprosthetics theory and practice*. World Scientific.

[282] Myllymaa, S., Myllymaa, K., Korhonen, H., Töyräs, J., Jääskeläinen, J. E., Djupsund, K., ... & Lappalainen, R. (2009). Fabrication and testing of polyimide-based microelectrode arrays for cortical mapping of evoked potentials. *Biosensors and Bioelectronics*, *24*(10), 3067-3072.

[283] Richardson, R. R., Miller, J. A., & Reichert, W. M. (1993). Polyimides as biomaterials: preliminary biocompatibility testing. *Biomaterials*, *14*(8), 627-635.

[284] Hsu, J. M., Kammer, S., Jung, E., Rieth, L., Normann, R. A., & Solzbacher, F. (2007, October). Characterization of Parylene-C film as an encapsulation material for neural interface devices. In *Conference on Multi-Material Micro Manufacture*.

[285] Gray, P., & Hurst, P. (2009). S. Lewis, and R. Meyer. *Analysis and Design of Analog Integrated Circuits*.

[286] HD MicroSystems™. (2009). PI-2600 Series – Low Stress Applications. Retrieved from: http://www.hdmicrosystems.com/HDMicroSystems/en_US/pdf/PI-2600_ProcessGuide.pdf.

[287] Blaauw, C. (1984). Preparation and Characterization of Plasma-Deposited Silicon Nitride. *Journal of The Electrochemical Society*, *131*(5), 1114-1118.

[288] Nguyen, S. V. (1986). Plasma assisted chemical vapor deposited thin films for microelectronic applications. *Journal of Vacuum Science & Technology B*, *4*(5), 1159-1167.

[289] Basu, A., Kumar, V., & Adesida, I. (2007). Study of fluorine bombardment on the electrical properties of AlGaN⁄ GaN heterostructures. *Journal of Vacuum Science & Technology B*, *25*(6), 2607-2610.

[290] Chung, J. W., Hoke, W. E., Chumbes, E. M., & Palacios, T. (2010). AlGaN/GaN HEMT with 300-GHz. *Electron Device Letters, IEEE*, *31*(3), 195-197.

[291] Manos, D. M., & Flamm, D. L. (Eds.). (1989). *Plasma etching: an introduction*. Elsevier.

[292] Lieberman, M. A., & Lichtenberg, A. J. (1994). Principles of plasma discharges and materials processing. *MRS Bulletin*, *30*, 899-901.

[293] Verdonck, P. (2006). Plasma etching. *Oficina de Microfabrição: Projeto e Construção de CI's MOS.*

[294] Goldston, R. J., & Rutherford, P. H. (1995). *Introduction to plasma physics*. CRC Press.

[295] Crystec Technology Trading GmbH. (March 2011).Plasma Technology. Retrieved from: https://www.crystec.com/triplae.htm

[296] Linkohr, S., Pletschen, W., Polyakov, V., Himmerlich, M., Lorenz, P., Krischok, S., ... & Cimalla, V. (2012). Influence of plasma treatments on the properties of GaN/AlGaN/GaN HEMT structures. *physica status solidi (c)*, *9*(3-4), 1096-1098.

[297] Diaham, S., Zelmat, S., Locatelli, M. L., Dinculescu, S., Decup, M., & Lebey, T. (2010). Dielectric breakdown of polyimide films: area, thickness and temperature dependence. *Dielectrics and Electrical Insulation, IEEE Transactions on*, *17*(1), 18-27.

[298] Schmitt, G., Schultze, J. W., Fassbender, F., Buss, G., Lüth, H., & Schöning, M. J. (1999). Passivation and corrosion of microelectrode arrays. *Electrochimica Acta*, *44*(21), 3865-3883.

[299] Fassbender, F., Schmitt, G., Schöning, M. J., Lüth, H., Buss, G., & Schultze, J. W. (2000). Optimization of passivation layers for corrosion protection of silicon-based microelectrode arrays. *Sensors and Actuators B: Chemical*, *68*(1), 128-133.

[300] Cook, T. E., Fulton, C. C., Mecouch, W. J., Davis, R. F., Lucovsky, G., & Nemanich, R. J. (2003). Band offset measurements of the Si3N4/GaN (0001) interface. *Journal of applied physics*, *94*(6), 3949-3954.

[301] O'Connor, J., Sexton, B. A., & Smart, R. S. (2003). *Surface analysis methods in materials science* (Vol. 23). Springer Science & Business Media.

[302] Janata, J. (2010). *Principles of chemical sensors*. Springer Science & Business Media.

[303] Diebold, A. C. (Ed.). (2001). *Handbook of silicon semiconductor metrology*. CRC Press.

[304] Y.P. Tsividis, *Operation and Modeling of the MOS Transistor*, McGraw-Hill, New-York, 1987.

[305] Gao, X. P., Zheng, G., & Lieber, C. M. (2009). Subthreshold regime has the optimal sensitivity for nanowire FET biosensors. *Nano letters*, *10*(2), 547-552.

[306] Rajan, N. K., Brower, K., Duan, X., & Reed, M. A. (2014). Limit of detection of field effect transistor biosensors: Effects of surface modification and size dependence. *Applied Physics Letters*, *104*(8), 084106.

[307] Chang, W. T., & Lin, Y. S. (2013). Performance Dependence on Width-to-Length Ratio of Si Cap/SiGe Channel MOSFETs. *Electron Devices, IEEE Transactions on*, *60*(11), 3663-3668.

[308] Cao, Yu, Kejia Wang, Guowang Li, Tom Kosel, Huili Xing, and Debdeep Jena. "MBE growth of high conductivity single and multiple AlN/GaN heterojunctions." *Journal of Crystal Growth* 323, no. 1 (2011): 529-533.

[309] Wille, A., Yacoub, H., Debald, A., Kalisch, H., & Vescan, A. (2015). AlGaN/AlN-GaN-SL HEMTs with Multiple 2DEG Channels. *Journal of Electronic Materials*, *44*(5), 1263-1267.

[310] Si, Q., Yue, H., Xiaohua, M., Pengtian, Z., & Yuanbin, X. (2010). AlGaN/GaN double-channel HEMT. *Journal of Semiconductors*, *31*(4), 044003.

[311] G. Steinhoff. Group III-Nitrides for Bio- and Electrochemical Sensors. PhD thesis, Technischen Universität München, 2008.

[312] Bai, L., & Zhou, Z. (2007). Computational study of B-or N-doped single-walled carbon nanotubes as NH 3 and NO 2 sensors. Carbon, 45(10), 2105-2110.

[313] Yakovkin, I. N., & Gutowski, M. (2007). Driving force for the WO 3 (001) surface relaxation. *Surface Science*, *601*(6), 1481-1488.

[314] Yuxiang, Q., Deyan, H., & Xiao, L. (2013). First principles study on the surface-and orientation-dependent electronic structure of a WO3 nanowire. *Journal of Semiconductors*, *34*(6), 062002.

[315] Contescu, C., Jagiello, J., & Schwarz, J. A. (1993). Chemistry of surface tungsten species on tungsten trioxide/alumina composite oxides under aqueous conditions. *The Journal of Physical Chemistry*, *97*(39), 10152-10157.

[316] He, Q., Wu, S., Yin, Z., & Zhang, H. (2012). Graphene-based electronic sensors. *Chemical Science*, *3*(6), 1764-1772.

[317] Fu, W., Nef, C., Knopfmacher, O., Tarasov, A., Weiss, M., Calame, M., & Schönenberger, C. (2011). Graphene transistors are insensitive to pH changes in solution. *Nano letters*, *11*(9), 3597-3600.

[318] Heller, I., Chatoor, S., Männik, J., Zevenbergen, M. A., Dekker, C., & Lemay, S. G. (2010). Influence of electrolyte composition on liquid-gated carbon nanotube and graphene transistors. *Journal of the American Chemical Society*, *132*(48), 17149-17156.

[319] Nakazato, K. (2009). An integrated ISFET sensor array. *Sensors*, *9*(11), 8831-8851.

[320] Chen, S., Bomer, J. G., Carlen, E. T., & van den Berg, A. (2011). Al2O3/silicon nanoISFET with near ideal Nernstian response. *Nano letters*, *11*(6), 2334-2341.

[321] Martinoia, S., Rosso, N., Grattarola, M., Lorenzelli, L., Margesin, B., & Zen, M. (2001). Development of ISFET array-based microsystems for bioelectrochemical measurements of cell populations. *Biosensors and Bioelectronics*, *16*(9), 1043-1050.

[322] Dahlin, A. B. (2012). Size matters: problems and advantages associated with highly miniaturized sensors. *Sensors*, *12*(3), 3018-3036.

[323] Seo, D., Bae, J. S., Oh, E., Kim, S., & Lim, S. (2014). Selective wet etching of Si 3 N 4/SiO 2 in phosphoric acid with the addition of fluoride and silicic compounds. *Microelectronic Engineering*, *118*, 66-71.

[324] El-Kareh, B. (2012). *Fundamentals of semiconductor processing technology*. Springer Science & Business Media.

[325] Hirayama, H. (2005). Quaternary InAlGaN-based high-efficiency ultraviolet light-emitting diodes. *Journal of applied physics*, *97*(9), 091101.

[326] Kneissl, M., Kolbe, T., Chua, C., Kueller, V., Lobo, N., Stellmach, J., ... & Johnson, N. M. (2011). Advances in group III-nitride-based deep UV light-emitting diode technology. *Semiconductor Science and Technology*, *26*(1), 014036.

Erklärung

Ich versichere, dass ich die vorliegende Arbeit ohne unzulässige Hilfe Dritter und ohne Benutzung anderer als der angegebenen Hilfsmittel angefertigt habe. Die aus anderen Quellen direkt oder indirekt übernommenen Daten und Konzepte sind unter Angabe der Quelle gekennzeichnet.

Bei der Auswahl und Auswertung folgenden Materials haben mir die nachstehend aufgeführten Personen in der jeweils beschriebenen Weise unentgeltlich geholfen:

1. Mario Kittler – LabVIEW Messprogramme und Unterstützung bei der Charakterisierung und Auswerten der Transistoren.

2. Thomas Stauden – Unterstützung bei der konstruktiven Entwicklung des Plasmaätzprozesses und bei der Charakterisierung unterschiedlichen Materialen.

Weitere Personen waren an der inhaltlich-materiellen Erstellung der vorliegenden Arbeit nicht beteiligt. Insbesondere habe ich hierfür nicht die entgeltliche Hilfe von Vermittlungs- bzw. Beratungsdiensten (Promotionsberater oder anderer Personen) in Anspruch genommen. Niemand hat von mir unmittelbar oder mittelbar geldwerte Leistungen für Arbeiten erhalten, die im Zusammenhang mit dem Inhalt der vorgelegten Dissertation stehen.

Die Arbeit wurde bisher weder im In- noch im Ausland in gleicher oder ähnlicher Form einer Prüfungsbehörde vorgelegt.

Ich bin darauf hingewiesen worden, dass die Unrichtigkeit der vorstehenden Erklärung als Täuschungsversuch angesehen wird und den erfolglosen Abbruch des Promotionsverfahrens zur Folge hat.

MSEE Mary Jocelyn Donahue

Ilmenau 11. Januar 2016